

# Modeling and Characterization of Friction Stir Fabricated Coatings on Al6061 and Al5083 Substrates

David T. Gray

Dissertation submitted to the faculty of the  
Virginia Polytechnic Institute and State University  
In partial fulfillment of the requirements for the degree of

Doctor of Philosophy

in

Materials Science and Engineering

Stephen L. Kampe

Jeffery P. Schultz

William T. Reynolds

Robert W. Hendricks

December 9<sup>th</sup>, 2009

Blacksburg, Virginia

Keywords: Friction Stir Fabrication, Aluminum 5083, Finite Difference Thermal Model

# Modeling and Characterization of Friction Stir Fabricated Coatings on Al6061 and Al5083 Substrates

David T. Gray

## Abstract

We have created a three-dimensional, implicit finite difference model that can accurately calculate temperatures within the bulk of a sample during a friction stir fabrication process. The model was written in Wolfram Mathematica<sup>®</sup> 7 for Students, and allows for time-efficient calculation of thermal profiles. The non-dimensionality of the model allows for accurate refinement of the temporospatial mesh, and provides portability across material types. The model provides insight as to the mechanism of heat generation by qualifying the fraction of mechanical energy converted to thermal energy for different material types and sample geometries. Finally, our model gives an understanding of the effects of the heat transfer at the boundaries of the workpiece and suggests a backside heat loss localized at the center of the tool due to a decrease in thermal contact resistance.

We have explored the effects of processing parameters on the performance of the friction stir fabrication process. The process has four stages; tool insertion, warm-up, bead formation, and steady-state translation. The tool insertion phase is characterized by a rapid increase in system horsepower requirements. During the warm-up phase, the mechanical energy of the rotating tip is converted to thermal energy. Once enough thermal energy has been transferred to the workpiece, the volume between the tip and the workpiece is filled by feedstock material. Finally, the tool is translated under relatively steady-state conditions. The success or failure of the process is dependent on adequate material delivery to the system. The horsepower requirements of the process depend on the material type and the rate of material delivery.

We have explored the effect of processing parameters on the microstructure of the processed samples. Optical microscopy shows that the stratification of layers within the weld and the depth of the weld are both dependent on the processing parameters. EBSD analysis coupled with Vicker's microhardness measurements of the processed pieces show that the grain size within the weld nugget is constant over the range of processing parameters available to the system. Data also show that pressure and heat inherent in friction stir processing of strain-hardened Al5083 counteract strengthening of the temper of the alloy.

## **Acknowledgements**

I would like to express my deep appreciation to my advisor, Dr. Stephen Kampe, who took a chance with me and provided me a second opportunity to perform this work. I am extremely grateful for the advice and assistance provided both before and after I became a member of the Kamposites group.

I would like to express my thanks to Dr. Jeffery Schultz who proved to be a good friend and who also took a risk in investing his time and resources in my abilities. I am proud to have performed my research with the guidance and advice of a friend and peer.

I am extremely grateful for the advice and assistance provided by Dr. Robert Hendricks throughout my tenure as a graduate student at Virginia Tech. His wisdom and sympathy were key in my decision to pursue a PhD.

I would like to express my thanks to Dr. Reynolds, especially in the area of mathematical modeling.

I am indebted to the Office of Naval Research for the funding provided to perform this work, as well as to the Materials Science and Engineering department at Virginia Tech for the funding and academic support provided during my tenure here as a student.

I owe a debt of gratitude to the multitude of colleagues that I have had in my tenure here, both graduate students and technical staff. The expertise in procedures, analysis, and equipment has been invaluable in filling in the gaps in my knowledge in the various to which I have been exposed during my research. In particular, this work would not have been possible without the hard work and intuition of Mr. Peter Ferek at Schultz-Creehan.

I would like to thank my parents for always encouraging my inquisitiveness as a child, and for continuing to nudge me along the path towards a PhD. The love and support made this journey possible.

As with all graduate students who have served in the MSE department of Virginia Tech between the year 2000 and today, it would be unthinkable for me not to acknowledge the selfless and untiring efforts of Mr. David Berry. I had planned on earning a degree from this department, but the gift of this friendship was an unexpected bonus along the way.

Finally I would like to my wife Nicole. I am where I am today because of the hard work, sympathy and encouragement that she provides on a daily basis. Since the first day of my enrollment in the department, and through the unending stream of hurdles and closed doors, Nicole always kept my perspective focused on the most important aspect of life. It is to Nicole that I dedicate this work.

# Contents

Acknowledgements.....	iii
Table of Figures.....	vi
1 Background.....	1
1.1 Friction Stir Welding.....	1
1.2 Friction Stir Processing.....	3
1.3 Friction Stir Fabrication.....	4
1.4 Thermomechanical Modeling of Friction Stir Welding.....	5
2 Thermal Model.....	8
2.1 Model Assumptions.....	9
2.1.1 Temperature-Independent Diffusivity.....	9
2.1.2 Mixed Boundary Conditions.....	9
2.1.3 Heat Source.....	10
2.2 Implicit Model Description.....	13
2.2.1 Justification of conversion to dimensionless model.....	13
2.2.2 Implicit versus Explicit Version.....	13
2.3 Determination of Heat Transfer Coefficients and Power Conversion Factor.....	16
2.4 Model Validation.....	22
3 Friction Stir Fabrication Process Characterization.....	26
3.1 Equipment Description.....	26
3.1.1 Motor and Controller.....	26
3.1.2 Feedstock Delivery System.....	26
3.1.3 Tool Description.....	27
3.1.4 Gantry Table Description.....	30
3.1.5 Temperature Monitoring.....	30
3.2 Process Description.....	31
3.2.1 Tool Insertion.....	32
3.2.2 Warm-up Stage.....	34
3.2.3 Bead Formation.....	35
3.2.4 Steady-State Operation.....	37

4	Effects of Processing Parameters on Microstructure and Hardness.....	50
4.1	General description of friction stir fabrication microstructures.....	50
4.1.1	Description of the weld nugget .....	52
4.1.2	Description of the thermomechanically affected zone .....	61
4.2	Effects of processing parameters on weld nugget macrostructure .....	67
4.2.1	Effect of $\omega/v$ ratio on weld nugget strata.....	67
4.2.2	Effect of feedstock compaction in the tool tip on weld macrostructure .....	70
4.2.3	Effect of processing parameters on depth of DRZ.....	74
4.3	Effects of processing parameters on grain size and hardness.....	80
4.3.1	Correlation of Vickers hardness to grain size .....	81
4.3.2	Vickers hardness maps of processed samples.....	82
5	Conclusions and Future Work .....	89
5.1	Thermal Model Conclusions.....	89
5.2	Thermal Model Future Work .....	89
5.3	Process Characterization Conclusions.....	90
5.4	Process Characterization Future Work .....	90
5.5	Process effects on Microstructure Conclusions.....	91
5.6	Process-Microstructure Future Work .....	92
6	References .....	93
Appendix A	Conversion from dimensional to dimensionless form of the heat equation.....	95
Appendix B	Derivation of Implicit, Dimensionless Boundary Conditions .....	97
Appendix C	3-D Implicit Model Mathematica® Code.....	101
Appendix D	3-D Explicit Finite Difference Model Mathematica® Code .....	133

## Table of Figures

Figure 1.1 Schematic representation of Friction Stir Welding[1] (used with permission) .....	1
Figure 1.2 Typical microstructure of FSW zones[3] (used with permission) .....	2
Figure 1.3 Friction Stir Fabrication schematic diagram .....	4
Figure 2.1 Model Schematic .....	9
Figure 2.2 Graphical representation of heat source at time t .....	12
Figure 2.3 Energy balance for internal node .....	14
Figure 2.4 Energy balance at a surface .....	15
Figure 2.5 Thermocouple locations within bulk of sample .....	17
Figure 2.6 Empirical and calculated thermal profiles for steady-state operation.....	18
Figure 2.7 Thermocouple locations in larger sample geometry.....	19
Figure 2.8 Empirical and calculated thermal profiles for larger sample geometry.....	19
Figure 2.9 Simulated temperature contour plot of top surface of 100mm X 100mm X 25 mm Al6061 .....	21
Figure 2.10 Thermal gradients with Al6061 workpiece.....	22
Figure 2.11 Comparison of empirical to calculated temperatures for Al6061 translated at 15 mm/min .....	23
Figure 2.12 Comparison of empirical to calculated temperatures for Al6061 translated at 25 mm/min .....	24
Figure 2.13 Comparison of empirical to calculated temperatures for Al5083 translated at 3.5mm/min .....	25
Figure 3.1 Schultz-Creehan friction stir fabrication tool .....	27
Figure 3.2 Optical micrograph of Al6061/NAB process run with focus on interface .....	28
Figure 3.3 Optical micrograph showing a depth profile for an NAB/NAB FSF run .....	29
Figure 3.4 Placement of three thermocouples used in early Al6061 experiments.....	30
Figure 3.5 Placement of four thermocouples used for Al6061 experiments .....	31
Figure 3.6 Placement of four thermocouples for Al5083 experiments.....	31
Figure 3.7 Output data from process monitor system showing four stages of a fabrication run; a. insertion, b. warm-up, c. bead formation, d. steady-state operation.....	32
Figure 3.8 Power, rotational speed, and force applied to system prior to insertion showing proportional response of power to rotational speed.....	33
Figure 3.9 Power, rotational speed and force applied to system prior to insertion showing relative insensitivity of power to feedstock force .....	34
Figure 3.10 Four stages of fabrication process for an Al6061 run -- a. tool insertion, b. warm-up, c. bead formation, d. steady-state.....	35
Figure 3.11 Four stages of fabrication run on Al5083 sample -- a. tool insertion, b. warm-up, c. bead formation, d. steady-state .....	36

Figure 3.12 Typical absolute material delivery rate for a. Al6061/Al6061, b. Al6061/Al5083, c. Al5083/Al6061 and d. Al5083/Al5083 .....	38
Figure 3.13 Area of overlap of circles with centers separated by distance d.....	39
Figure 3.14 Process parameters for Al5083 run with $v = 2.5\text{mm/min}$ .....	40
Figure 3.15 Volume of material delivered to bead normalized by effective depth of 2.7 mm for an Al5083/Al5083 process run with tool translation of 2.5 mm/min. ....	41
Figure 3.16 Examples of runs in which inadequate material was delivered to interface when $z_{\text{eff}} = 2.7\text{mm}$ , resulting in incomplete deposition layers .....	41
Figure 3.17 Examples of runs in which an excess of material was delivered to interface when $z_{\text{eff}} = 2.7\text{mm}$ , resulting in successful depositions .....	42
Figure 3.18 Graphs showing steady-state horsepower requirements for a. Al6061/Al6061, b. Al6061/Al5083, c. Al5083/Al6061, and d. Al5083/Al5083 .....	43
Figure 3.19 Graphs showing relationship between changes in feedstock delivery rate and instantaneous horsepower .....	44
Figure 3.20 Force applied to feedstock and resulting material delivery rate.....	45
Figure 3.21 Graphs depicting dependence of feedstock rate on applied force at constant rotation .....	46
Figure 3.22 Process run data demonstrating feedstock built-in resistance to motion of $\sim 675\text{ N}$ .....	46
Figure 3.23 Decrease in feedrate with increasing force signifying stock stuck in spindle a. for Al6061/Al6061 run, and b. for Al5083/Al5083 run.....	47
Figure 3.24 Horsepower and feedrate at various rotational frequencies without tool translation .....	48
Figure 3.25 Focus on step change in $\omega$ for stationary process run .....	49
Figure 3.26 Comparison of feedrate of runs with different rotational frequencies .....	49
Figure 4.1 Cross sectional micrograph of a typical process run (Al5083/Al5083, $\omega = 1200\text{ rpm}$ , $v = 2.5\text{mm/min}$ ) .....	50
Figure 4.2 Schematic representation of grain morphology in strain-hardened Al5083, as well as directions relative to FSF processing .....	51
Figure 4.3 Micrograph of the cross section of a FSF workpiece (Al5083/Al5083, $\omega = 1000\text{ rpm}$ , $v = 2.5\text{ mm/min}$ ) .....	52
Figure 4.4 Longitudinal view of advancing side (AS) of weld (Al5083/Al5083, $\omega = 1000$ , $v = 2.5\text{ mm/min}$ ) .....	52
Figure 4.5 Cross-sectional micrographs of FSF runs showing early, incomplete onion formation a. Al5083/Al5083, $\omega = 1200$ , $v = 2.5\text{mm/min}$ , b. Al5083/Al5083, $\omega = 1000$ , $v = 2.5\text{mm/min}$ .....	53
Figure 4.6 Optical micrograph of Al6061/Al6061 sample (2100 rpm, 25.4 mm/min) stained with NaOH.....	54

Figure 4.7 SEM image of advancing side nugget-to-TMAZ interface of sample (Al6061/Al6061, $\omega = 2100$ , $v = 21$ mm/min) etched using two step NaOH/HF etch.....	55
Figure 4.8 BSE image of the interface between the TMAZ and the DRZ of a FSF processed sample (Al5083/Al5083, $\omega = 2500$ rpm, $v = 2.5$ mm/min) .....	56
Figure 4.9 BSE image of Al5083/Al5083 sample etched with Keller's etch (Al5083/Al5083, $\omega = 1000$ rpm, $v = 3.56$ mm/min) .....	57
Figure 4.10 Backscatter image of Al5083 prior to processing showing insoluble precipitate chains oriented in the direction of rolling .....	58
Figure 4.11 BSE image of stirred area in Al5083 sample showing refinement of insoluble intermetallic particles (Al5083/Al5083, $\omega = 2500$ rpm, $v = 2.5$ mm/min).....	59
Figure 4.12 EBSD image showing band contrast and Euler space coloring for a region within the advancing wide of a processed Al5083 sample (Al5083/Al5083, $\omega = 1000$ rpm, $v = 2.5$ mm/min). .....	60
Figure 4.13 Micrograph of cross-section of processed sample with detail of TMAZ halo (Al5083/Al5083, $\omega = 850$ rpm, $v = 2.5$ mm/min) prepared with Keller's etch .....	61
Figure 4.14 Detail of material in TMAZ directly under tool nubs (Al5083/Al5083, $\omega = 800$ rpm, $v = 2.5$ mm/min) .....	62
Figure 4.15 Detail of grain motion to accommodate screw motion of weld nugget (Al5083/Al5083, $\omega = 1000$ rpm, $v = 2.5$ mm/min).....	63
Figure 4.16 Longitudinal view of weld nugget and TMAZ underneath nub on retreating side of workpiece (Al5083/Al5083, $\omega = 1000$ rpm, $v = 2.5$ mm/min) prepared with Keller's etch .....	64
Figure 4.17 Longitudinal view of weld nugget and TMAZ along centerline of workpiece (Al5083/Al5083, $\omega = 1000$ rpm, $v = 2.5$ mm/min) prepared with Keller's etch .....	64
Figure 4.18 Longitudinal view of weld nugget and TMAZ underneath nub on advancing side of workpiece (Al5083/Al5083, $\omega = 1000$ rpm, $v = 2.5$ mm/min) prepared with Keller's etch .....	65
Figure 4.19 EBSD image of TMAZ of AS of weld of an Al5083 sample (Al5083/Al5083, $\omega = 1000$ rpm, $v = 2.5$ mm/min).....	66
Figure 4.20 EBSD pattern of heat affected zone of Al5083 workpiece (Al5083/Al5083, $\omega = 1000$ rpm, $v = 2.5$ mm/min).....	67
Figure 4.21 Optical micrograph of two Al6061 samples showing difference in onion strata a. $\omega/v = 207$ rev/mm, b. $\omega/v = 83$ rev/mm.....	68
Figure 4.22 Optical micrograph comparing onion layer thickness across material type a. Al6061/Al6061, $\omega/v = 83$ rev/mm, b. Al5083/Al5083, $\omega/v = 394$ rev/mm .....	69
Figure 4.23 Optical micrograph of two Al5083 samples showing difference in onion strata a. $\omega/v = 394$ rev/mm, b. $\omega/w = 472$ rev/mm .....	70
Figure 4.24 Micrograph of a FSF run without feedstock delivery (Al6061/Al6061, $\omega = 2100$ rpm, $v = 10.16$ mm/min).....	71

Figure 4.25 Al5083 processed samples showing varying degrees of void in the onion a. no void, b. void initiation on AS of nugget, c. void across center of nugget .....	72
Figure 4.26 Detail of micrograph of void in Al5083 sample (Al5083/Al5083, $\omega = 2500$ rpm, $v = 2.54$ mm/min) .....	73
Figure 4.27 Incomplete void exhibiting a fully developed TMAZ and fine layer above the void line (Al5083/Al5083, $\omega = 2250$ rpm, $v = 2.54$ mm/min) .....	74
Figure 4.28 Comparison of depth of weld nugget for Al5083/Al5083 samples processed under different conditions a. $\omega = 1200$ rpm, $v = 3.56$ mm/min, depth = 3.167 mm b. $\omega = 1000$ rpm, $v = 3.56$ mm/min, depth = 2.717 mm.....	75
Figure 4.29 Weld depth versus feedstock force for Al6061 and Al5083 samples.....	76
Figure 4.30 Depth of weld versus a. translational velocity and b. rotational frequency .....	77
Figure 4.31 Depth of weld versus ratio of rotational frequency to translation speed including samples that show evidence of feedstock delivery problems.....	78
Figure 4.32 Depth versus $\omega/v$ ratio excluding compacted stock samples.....	79
Figure 4.33 Average steady-state power versus depth of weld for Al6061/Al6061 and Al5083/Al5083 samples .....	80
Figure 4.34 Depth profile of Vickers hardness of an Al5083/Al5083 sample ( $\omega = 1000$ rpm, $v = 2.54$ mm/min), dashed line corresponds to the depth of the weld nugget.....	81
Figure 4.35 Hardness versus grain size relationship for friction stir processed Al5083 [26] (used with permission) .....	82
Figure 4.36 Optical micrograph showing location of hardness indents and corresponding hardness map (Al5083/Al5083, $\omega = 1200$ rpm, $v = 3.56$ mm/min) .....	83
Figure 4.37 Optical micrograph showing location of hardness indents and corresponding hardness map (Al5083/Al5083, $\omega = 1000$ rpm, $v = 2.54$ mm/min) .....	83
Figure 4.38 Optical micrograph showing location of hardness indents and corresponding hardness map (Al5083/Al5083, $\omega = 2500$ rpm, $v = 2.54$ mm/min) .....	84
Figure 4.39 Relative hardness of sample with process parameters .....	85
Figure 4.40 Calculated grain size for material in the weld nugget for different processing parameters.....	87
Figure 4.41 Calculated grain size for material in the weld nugget for different processing parameters with error in HVN-d propagation .....	88

# 1 Background

## 1.1 Friction Stir Welding

Friction stir welding is a derivative of traditional friction welding[1] (see Figure 1.1). In friction stir welding, a rotating tool is translated across the abutting edges of sheets or plates to be joined. The frictional contact of the shoulder with the top surface of the workpiece, along with the plastic deformation caused by the pin, act to locally heat the workpiece[2]. The heat softens the material and, coupled with the motion of the tool, acts to move the material from the front of the tool to the back of the tool in the solid state.

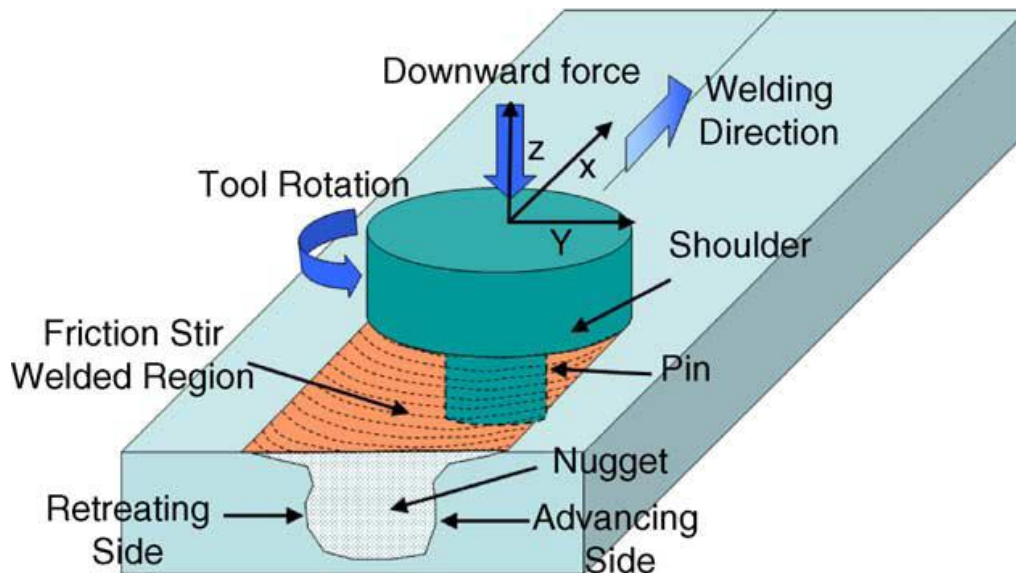


Figure 1.1 Schematic representation of Friction Stir Welding[1] (used with permission)

Friction stir welding results in a characteristic microstructure in the workpiece. Traditionally there are three distinct 'zones' in the weld; the weld nugget (or dynamically recrystallized zone, DRX), the thermo-mechanically affected zone (TMAZ) and the heat affected zone (HAZ) (Figure 1.2). Due to the asymmetric and dynamic nature of the process, the three zones have quite different microstructures and properties.

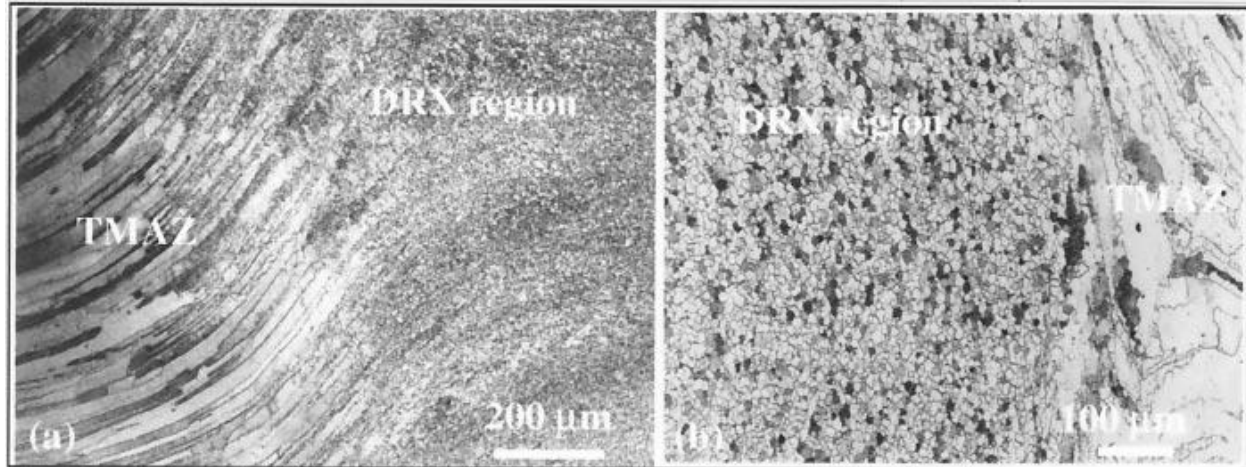


Figure 1.2 Typical microstructure of FSW zones[3] (used with permission)

The weld nugget itself experiences high strain at an elevated temperature (relative to the bulk of the workpiece). A fine grain structure with high-angle grain boundaries are typically seen in the weld nugget. The absence of a dendritic structure means that melting does not occur, but rather that the process is a continuous dynamic recrystallization process brought on by deformation and subsequent annealing of the workpiece[4]. Due to the dynamic aspect of the recrystallization, the microstructural history of the workpiece plays little role in the final microstructure of the weld zone. It is rather the processing parameters, in particular rotation and translation speeds of the tool on the workpiece surface, that dictate the final weld zone morphology[5].

In aluminum alloys that rely on precipitation hardening for strength, the temperature in the weld nugget during FSW may reach temperatures high enough to cause the precipitates to go into solution. In such alloys, re-precipitation occurs once the workpiece cools sufficiently. This can be seen by a change in the morphology of precipitates from an oriented (stringered) arrangement to a randomly dispersed configuration[6].

Material in the TMAZ zone experiences a lower temperature and less strain than the weld nugget. The microstructure in the TMAZ can exhibit a wide range of dislocation densities and grain size distributions. In the portions of the TMAZ that are far from the tool shoulder (far TMAZ), grains show higher dislocation densities and significant grain growth. The material in this area is deformed due to plastic deformation of the workpiece but does not experience sufficient time at elevated temperature for full recovery of the deformation. The temperature is high enough for some grain growth, but not for the migration of dislocations to grain boundaries[7].

Subgrains in the far TMAZ show low angle grain boundaries. The microstructure closer to the weld nugget (near TMAZ) shows different degrees of recovery and absorption of dislocations

into the grain boundaries. Grains here experience such a degree of deformation and heat that dynamic recovery dominates resulting in small subgrains with low angle boundaries[8].

In precipitate hardened aluminum alloys, the state of the precipitates varies widely in the TMAZ as well. Due to the difference in temperature ranges, precipitates in the far TMAZ are only partially dissolved, while those in the near TMAZ appear to be completely dissolved[8]. The state of the precipitates in the TMAZ under standard FSW process parameters (350 rpm and 15 mm/min) on Al 7075, suggest maximum temperatures of 350C and 400C for the far and near TMAZ respectively.

The HAZ experiences no deformation, but is subject to diffusive heat from the tool. In the HAZ zone of the weld, there is not typically sufficient thermal energy to allow for significant grain growth. There is however enough thermal energy to allow for precipitate growth (in applicable alloys). The effect of the precipitate growth depends on the thermal history of the base metal, but as a general rule acts to soften the metal.

Little work has been reported in the literature of the effects of FSW on the microstructure of aluminum alloys that do not exhibit precipitate hardening, other than to qualitatively demonstrate grain refinement in the mechanically affected zones[9, 10]. Due to the insensitivity of the mechanical properties with respect to elevated temperature, these alloys are good candidates for traditional fusion welding techniques. Much of the work on the dynamic recrystallization process suggests that intragranular dislocation generation is dependent on strain incompatibility of neighboring grains with different phases. The literature does suggest that significant grain refinement will occur in non-precipitate hardened aluminum alloys, although the specific mechanisms are not completely understood.

## **1.2 Friction Stir Processing**

Mishra was the first to apply FSW to a monolithic workpiece as a general microstructural refinement method[11, 12]. All of the process-structure-properties relationships developed for FSW are applicable to Friction stir processing (FSP). In FSP however, problems associated with joining two or more workpieces (thinning of pieces at the joint line, etc) are avoided.

In particular, much work has been done on using FSP to increase superplasticity in aluminum alloys[11]. Superplasticity is dependent on a fine grain structure and on the stability of that grain structure with respect to temperature. The FSP process results in microstructures with grains sizes between 0.1  $\mu\text{m}$  and 15  $\mu\text{m}$ . Furthermore, the grain size of the resulting microstructure can be manipulated by controlling the rotational speed and translational velocity of the tool on the workpiece or by the addition of quenching mechanisms on the back side of the tool[2].

Friction stir processing has also been used as an alternative to liquid phase surface modification techniques to create surface composite structures. Techniques such as high-energy laser melt, high-energy electron beam irradiation, and plasma spraying all operate at such high temperatures that it is difficult to avoid the interfacial reaction between reinforcement particles and the matrix. The solid-state, low temperature aspect of FSP allows for incorporation of ceramic reinforcement particles within the aluminum matrix with no risk of reaction between particles. Furthermore, FSP allows for an amply wide range of operating parameters such that detrimental properties such as porosity, low-density layers, poor adhesion or substrate surface oxidation can be avoided.

### 1.3 Friction Stir Fabrication

Friction stir fabrication (FSF) differs from FSP in the method of delivery of the material to be stirred into the workpiece. In typical FSP techniques, the material to be mixed into the workpiece is deposited onto the surface of the workpiece before stirring begins. Usually the material is deposited as a solution from which the solvent evaporates, leaving a coating on the surface of metal. A standard FSW tool with a shoulder and a pin is used to stir the material into the substrate.

In FSF however, the pin of the tool is replaced with the material to be deposited, as shown in Figure 1.3. As the tool is rotated, pressure is applied to the filler rod (or other form of feedstock) and the substrate is translated relative to the tool.

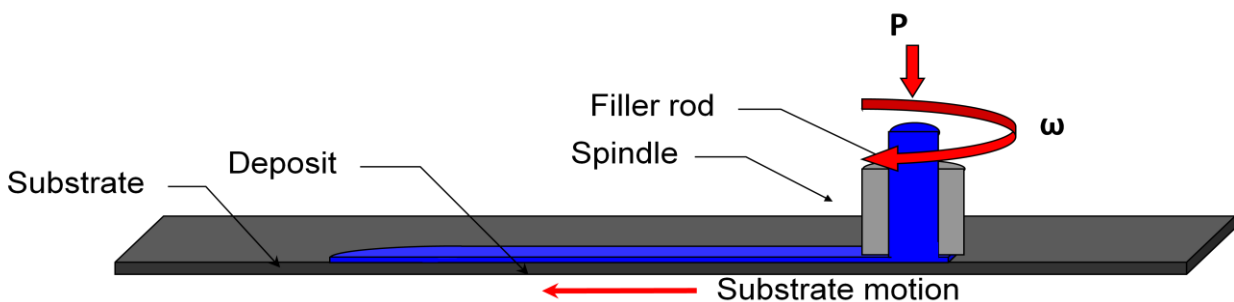


Figure 1.3 Friction Stir Fabrication schematic diagram

The feedstock must rotate relative to the workpiece, and not relative to the tool head. Rotation relative to the tool could lead to welding between the feedstock and the tool itself. In order to ensure that the feedstock rotates relative to the workpiece, the tool is either keyed, or has an asymmetric opening relative to the axis of rotation.

The feedstock material can be in solid, nugget, or even powder form. Furthermore, the feedstock material need not be of the same type or composition as the substrate. The main advantage of FSF is that different material types and compositions can be joined or introduced at low temperature, from aluminum to the components required for the *in-situ* formation of

discontinuously reinforced aluminum metal matrix composites (DRA MMCs). Since the feedstock is deposited as the tool moves, multiple passes maybe be made with relative speed. The ability for multiple passes leads to the possibility for higher in-plane uniformity (through rastering) and for very thick layers (by manipulation of the tool height with subsequent passes).

#### 1.4 Thermomechanical Modeling of Friction Stir Welding

Early work done on modeling in FSW was mainly of an analytical nature. Due to practical limitations in computing at the time, numerical modeling was too expensive and time consuming. Much of this early work was done by Myhr and Grong in Norway[13, 14]. The thermal history of workpieces undergoing FSW were modeled by a moving heat source along the surface of a thick, thin, or medium-thick slab of material[13]. Application of analytical solutions proved extremely difficult as the workpiece approximation (thick vs. thin) must be varied with distance from the weld center. Additionally, adaptation of these models to accommodate for different input parameters to the system required extensive reworking of the constitutive equations.

The first numerical model for the temperature profiles within the workpiece came in the form of a PhD thesis done by Øyvind Frigaard working under Grong[15]. Frigaard proposed what has become the basis for nearly all subsequent thermal models. Frigaard's model is a 3-D, finite-difference heat flow model written in MATLAB [16]. Frigaard assumes a moving point-source translating across the surface of the workpiece. The heat input from the system is limited to the friction between the tool shoulder and the workpiece, with no contribution from the pin. All of the mechanical energy involved in rotation of the tool is assumed to be converted into thermal energy via friction at the tool shoulder-to-workpiece interface. This leads to a radially dependent heat source[16]. In order to simplify calculation, the footprint of the tool is assumed to be rectangular as opposed to circular[16].

The heat input is given in as

$$q_0 = \frac{4}{3}\pi^2\mu PNR^3$$

or

$$q_0 = \frac{4}{3}\pi^2\mu PN \sum_{i=1}^n (R_i^3 - R_{i-1}^3)$$

where P is the pressure on the tool, N is the rotational speed (in rotations/second),  $\mu$  is the friction coefficient and R is the tool radius.

It is generally accepted that if the temperature under the tool reaches the melting point of the workpiece, the tool shoulder will ride on a cushion of liquid metal, and the heat input to the system will go to zero. In reality, the frictional coefficient varies with temperature and pressure. Measurement of the friction coefficient with respect to input parameters is quite difficult. Therefore, in order to restrict the heat input to the system corresponding to localized melting of the workpiece, Frigaard modeled the coefficient of friction as a step function[15]. Below the melting point of the workpiece the coefficient is unity, at the melting point it is assumed to be zero.

Later models attempted to improve on the accuracy of Frigaard's model by attempting to account for the tool pin[17], adjusting the heat loss through the backing plate[18], introducing a power efficiency factor to quantify the transformation of mechanical energy to frictional heat[19], or by attempting to account for heat from plastic deformation[20].

Thermal model accuracy is usually validated through comparison with empirical data. Thermocouples are inserted into the workpiece and the temperature at different points is recorded. Generally there is good agreement of the simple Frigaard model with experimental data[15], especially during the heating phase of the process. Most work in the literature beyond Frigaard attempts to vary the inputs to the system or the boundary conditions to the system to achieve a better match between the experimental and computed data[17-21].

Nearly all of the models in the literature take a two-stage approach to predicting the mechanical properties of the age-hardened aluminum workpiece after a weld. Temperature profiles are estimated using finite difference thermal models as described above. From these thermal histories, hardness profiles are calculated using models based on thermodynamics, kinetic theory and dislocation mechanics. Usually the metallurgical models consider dissolution of precipitates due to elevated temperature as the primary influence on strength change during the weld, with subsequent reprecipitation of the strengthening phases bringing some recovery of strength via artificial ageing[15, 18, 20, 22, 23].

According to Myhr and Grong[14], the fraction of dissolved precipitates is given by:

$$X_d = \left( \int_0^t \frac{dt}{t^*} \right)^{1/2}$$

where

$$t^* = t_r^* \exp \left[ \frac{Q_{eff}}{R} \left( \frac{1}{T} - \frac{1}{T_r} \right) \right]$$

where  $t_r^*$  represents complete dissolution of the precipitates at temperature  $T_r$ ,  $Q_{eff}$  is the effective activation energy for the dissolution mechanism, and  $R$  is the gas constant. A similar expression can be created to describe the age hardening precipitation of the particles in the matrix during subsequent ageing. Hardness profiles for a fusion weld can be generated if the temperature history has been measured or estimated[24].

Mechanical validation is performed by measuring microhardness across the weld and comparing the results to predicted values. The early work by Myhr and Grong on dissolution and reprecipitation gives quite good results[15]. Additionally, TEM results are often used to verify accurate predictions for the size and concentration of precipitates in the matrix[21].

The vast majority of metallurgical modeling in the literature consists of the two-stage thermo-mechanical model described above. No work has been found so far on modeling the effects of input parameters (such as rotation speed, translation speed, and tool pressure) on the resulting grain size of the affected regions. Grain refinement is understood to have a far lesser impact on material strength than does the change in precipitate structure in age-hardened alloys. The existing models in the literature focus mainly on the effects of temperature on the system and not on the effects of deformation. Furthermore, since aluminum alloys that are not age hardened typically can be fusion welded without significant loss in strength, little work has been done on modeling the FSW process on non age-hardened alloys.

## 2 Thermal Model

The modeling portion of this work was framed by a need to understand the thermal history of the friction stir workpiece. More specifically, the model was generated to calculate temperature profiles within an aluminum workpiece under specific processing conditions. The predictive nature of the model allows for a better understanding of how the different processing parameters can affect the power input to the system, as well as to explain the heat flow throughout the system. As a standalone work, the model provides insight into the effects boundary heat transfer and sample geometry on the process, and aids in guiding the selection of parameters for a friction stir fabrication. As a prerequisite work, the thermal model provides a foundation for the development of either a more complete second-generation thermal model, or a coupled thermomechanical model for friction stir processing of materials.

Previous modeling work done in the literature differs from our work in several key aspects. Firstly, the vast majority of the existing models assume a steady-state, semi-infinite regime [15, 16, 19]. The reduction in complexity that comes with such assumptions allows for focus not only on the temperature within the workpiece, but a coupling with mechanical modeling. For most work done in FSW, the mechanical properties of a heat-treatable aluminum alloy are of utmost importance in the processed sample [16, 18]. The goal of previous models is to understand the effects of the elevated temperature and high plastic deformation on the material properties of the processed sample, rather than characterization of the process itself. The purpose of our model is primarily to characterize the process, and secondly to provide insight into the mechanical properties of the resulting material. Our model therefore must be designed to take into account both the transient nature of a warm-up period and the subtle but important effects of boundaries on the process itself.

The thermal model generated for this work is a three-dimensional finite difference approximation to the solution of the heat equation;

$$\frac{\partial T}{\partial t} = \alpha \nabla^2 T + q_r$$

where  $\alpha$  is the thermal diffusivity in  $\text{m}^2/\text{s}$  of the material, and  $q_r$  represents the net volumetric heat generation within the solid (here in  $\text{K}/\text{s}$ ). For the friction stir fabrication process, the volumetric heat source represents the frictional and deformational heat generated by the tool shoulder and the portion of feedstock acting as a stirring pin. As the net energy input to the system is calibrated using empirical data (see Section 2.3), the quantity  $q_r$  accounts for heat generation due to friction between the tool shoulder and the workpiece, due to work done to deform the workpiece and feedstock materials, as well as the amount of energy stored in

dislocations and grain creation during processing. The heat source is translated across the surface of the workpiece at a constant velocity,  $v$  mm/min, as depicted in Figure 2.1.

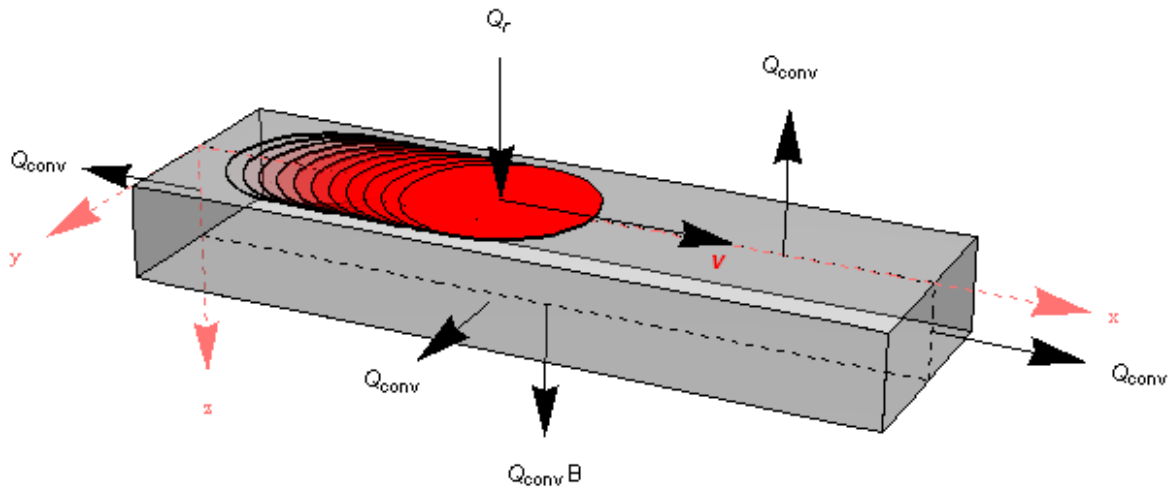


Figure 2.1 Model Schematic

## 2.1 Model Assumptions

In order to simplify the calculations involved in the model, as well as to allow for a sample geometries of finite dimension, certain assumptions were made concerning the material properties of the sample, the boundary conditions of the system, and the form of the heat input into the system.

### 2.1.1 Temperature-Independent Diffusivity

The explicit version of the model described in Appendix D allows for simple incorporation of a temperature-dependent diffusivity, as properties can be linked to a previously calculated temperature at a certain node. For the implicit version of the model however, incorporation of temperature-dependent thermal diffusivity adds a dimension of complexity to the model and increases computational requirements. Our model therefore assumes temperature independent materials properties. The thermal diffusivity used for all calculations in the implicit version of the model is that of the alloy under consideration at room temperature ( $9.44 \times 10^{-5} \text{ m}^2/\text{s}$  for Al5083).

### 2.1.2 Mixed Boundary Conditions

Most models reported in the literature [16, 18, 23] assume a semi-infinite sample geometry. For large workpieces, this is generally a valid assumption and simplifies the mathematics of the model with the assumption of either Neumann or Dirichlet boundary conditions. The small volume of workpiece relative to the tool geometry in our experiments requires that heat loss through the boundaries be factored into the finite difference solution. The physical setup of our FSF system is such that it is appropriate to assume a convective heat

transfer to ambient ( $T \cong 30^\circ\text{C}$ ) from the sides and the top of the workpiece during a run. A mask is applied mathematically to the heat transfer coefficient at the surface such that there is no convection through the tool. The backside of the sample is in direct contact with an actively cooled anvil. Although thermal conduction across a resistance is a more physically accurate assumption, we have simplified the boundary conditions by treating this transfer mechanism as an effective convection to a liquid. Experimentally, the temperature of the anvil varies during a fabrication run, but for our model is assumed to remain at  $100^\circ\text{C}$  for the duration of the simulation. A convective heat transfer at the surfaces requires mixed-boundary conditions for the system. Therefore, the form of the heat transfer at the boundaries is

$$q_{conv} = hA(T^\infty - T^P)$$

where  $h$  is a heat transfer coefficient in  $\text{W}/\text{m}^2\text{K}$ ,  $A$  is the area defined by the mesh in  $\text{m}^2$ , and  $T^\infty$  is the temperature of the fluid (or anvil on the backside of the workpiece).

Typical process runs involve a single pass of the tool down the centerline of the workpiece. The restriction of tool translation to motion along the centerline in the  $x$ -direction allowed for the assumption of a mirror plane along the centerline of the tool. The mirror plane acts to reduce the dimensionality of the boundary conditions at the center of the tool, as well as to reduce the number of nodes in the  $y$ -direction while maintaining adequate spatial refinement.

### 2.1.3 Heat Source

The heat input to the system during a friction stir fabrication run is due both to frictional heat at the tool shoulder as well as plastic deformation of the workpiece and feedstock within the stir zone. During deformation, a portion of the energy input to the system will be stored within the material and thus will not be released as heat input to the system.

The form of the heat input to the system is equivalent to a heat flux at the surface that is distributed through the uppermost layer of the mesh used to define the workpiece. Depending on the depth of penetration of the TMAZ of the stirred region and the width of the mesh in the  $z$ -direction, this assumption may or may not be completely accurate. However, as the variation in depth of penetration of the TMAZ into the workpiece with respect to process parameters is not completely understood, the model shall treat the heat source as a volumetric heat source distributed within the top layer of the workpiece.

Initially, we had hoped to assume a total power input to the system of the form

$$q_0 = P_f \frac{4}{3} \pi^2 \mu P N \sum_{i=1}^n (R_i^3 - R_{i-1}^3)$$

where  $P$  is the pressure on the tool,  $N$  is the rotational speed,  $\mu$  is the friction coefficient,  $R$  is the tool radius, and  $P_f$  represents the fraction of power that is converted from mechanical energy to thermal energy. Experimental observation showed that the net heat input to the system once a bead has been formed is not directly proportional to the rotational velocity of the tool, neither does the current setup have means to control or monitor tool pressure (see Section 3.1.2). However, the circularly paraboloidal shape of the heat input remains an accurate physical approximation. We therefore modeled our heat input to the system as

$$S(i, j) = P_{eff} \frac{[i - S_C(i)]^2 + [j - S_C(j)]^2}{\sum_{i=1, j=1}^{Mu, Mv} \{[i - S_C(i)]^2 + [j - S_C(j)]^2\}}$$

where  $S_C(i, j)$  is the location of the center of the tool on the surface, and  $P_{eff}$  represents the effective thermal power delivered to the system.  $P_{eff}$  is defined as

$$P_{eff} = P_{cont} P_f$$

where  $P_{cont}$  is the mechanical output power of the motor, and  $P_f$  is the fraction of mechanical power converted to thermal power.  $P_f$  therefore accounts for both frictional heat input as well as mechanical deformation work, and, albeit not quantitatively, the amount of energy stored within the materials. The above conditions hold true for when the node under consideration is within the radius of the tool, and the uppermost layer of the mesh;

$$[i - S_C(i)]^2 + [j - S_C(j)]^2 \leq R^2 \text{ and } k = 0$$

where  $R$  is the radius of the tool shoulder and  $k$  is the index of the  $z$  dimension of the node under question. The equation for  $S(i, j)$  given above describes a discretized circular paraboloid about the center of the tool. The magnitude of the individual nodes within the source is normalized such that the sum of the power of all of the nodes is the total effective power delivered to the system. The center of the heat source,  $S_C(i, j)$  is translated in the  $x$ -direction at a fixed rate. The magnitude of the volumetric heat input at each node in the top layer of the mesh is recalculated at each timestep. A graphical representation of the heat source at an arbitrary time is given in Figure 2.2.

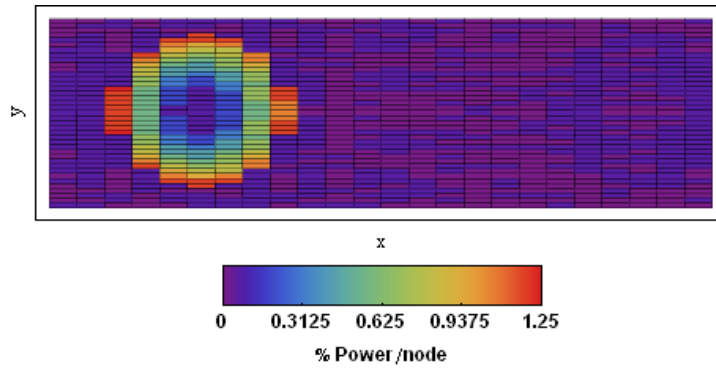


Figure 2.2 Graphical representation of heat source at time t.

## 2.2 Implicit Model Description

### 2.2.1 Justification of conversion to dimensionless model

Conversion of the model from a dimensional to a dimensionless problem strengthens the model in two ways. First, reducing the model to one without dimension provides for ease or portability across material type by facilitating reassignment of materials properties. Secondly, the division of time-space into an appropriate mesh becomes more straightforward with the implementation of a dimensionless model.

The conversion to a dimensionless model involves a substitution of variables for the parameters in the finite difference equations using characteristic parameters as system normalizers. For our model, characteristic parameters are the thermal diffusivity ( $\alpha$  in  $\text{m}^2/\text{s}$ ), the melting point of the alloy ( $T_m$  in K), and the length of the sample in the through-thickness direction ( $L_z$  in m).

The heat equation can then be transformed from

$$\frac{\partial T}{\partial t} = \alpha \nabla^2 T + q_r$$

to

$$\frac{\partial \theta}{\partial \tau} = \nabla^2 \theta + Q$$

where the dimensionless temperature,  $\theta$ , and the dimensionless power density,  $Q$ , are given by

$$\theta = \frac{T}{T_m}$$

$$Q = \frac{q_r L_z^2}{T_m \alpha}$$

A more thorough description of the dimensionless transformation is given in 0.

### 2.2.2 Implicit versus Explicit Version

The explicit method for approximating the solution to the partial differential equation allows for a simpler set of constitutive equations and requires less processing power to arrive at a solution. A first version of the model was therefore written following the explicit method. A description of the explicit version of the model, as well as derivation of the constitutive equations is given in Appendix D. The criteria for mathematical stability with the explicit

method require prohibitively small timesteps. In order to achieve an adequately refined spatial mesh, the division in time was on the order of tens of nanoseconds, and the computation time for typical runs was on the order of tens of hours on a dual core personal computer.

The limitations of the explicit version of the model led us to reformulate our model after the implicit method. The implicit method requires simultaneous solution of the equations at each node in the mesh for each time step. However, the universal stability of the model allows for a much coarser mesh in the time dimension, with minimal loss in accuracy. Furthermore, the coupling of commercial mathematical software and current level personal computing power great facilitate the process for solving the simultaneous equations.

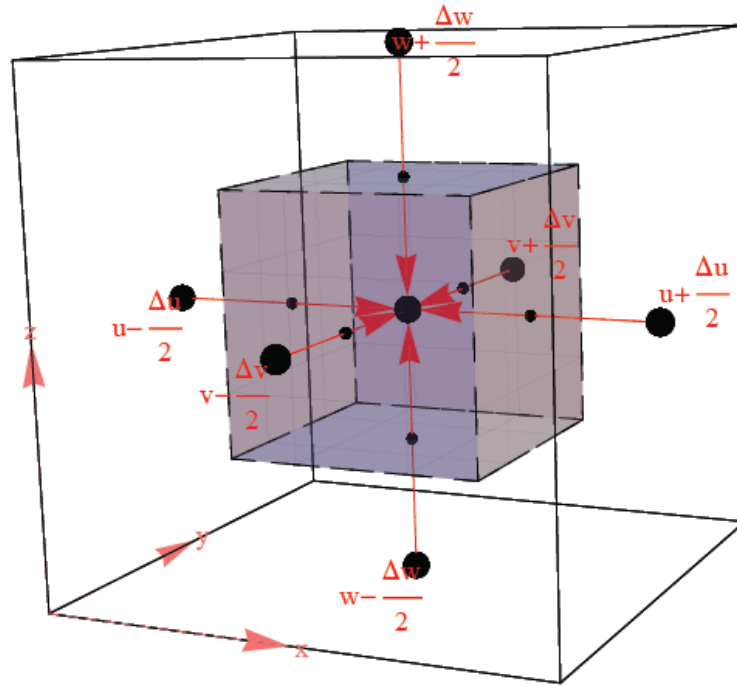


Figure 2.3 Energy balance for internal node

In general, assuming a rectilinear mesh, the implicit approximation to the dimensionless partial differential equation can be written as

$$\frac{1}{\Delta\tau}(\theta^P - \theta^0) = \frac{\theta^{u+1} - 2\theta^P + \theta^{u-1}}{\Delta u^2} + \frac{\theta^{v+1} - 2\theta^P + \theta^{v-1}}{\Delta v^2} + \frac{\theta^{w+1} - 2\theta^P + \theta^{w-1}}{\Delta w^2} + Q$$

where  $\theta^P$  is the dimensionless temperature at node P and dimensionless time  $\tau + \Delta\tau$ ,  $\theta^0$  is the dimensionless temperature at node P and time  $\tau$ , and  $\theta^{u+1}$  is the dimensionless temperature at the neighboring node in the +u direction at time  $\tau + \Delta\tau$ . Physically, this approximation can be thought of as an energy balance for an internal node P, as depicted in Figure 2.3. Here the temperature at the node under consideration is a function of the temperature gradients

between the neighboring nodes, the thermal diffusivity of the material, the internal energy stored in the node, and any energy created in the node.

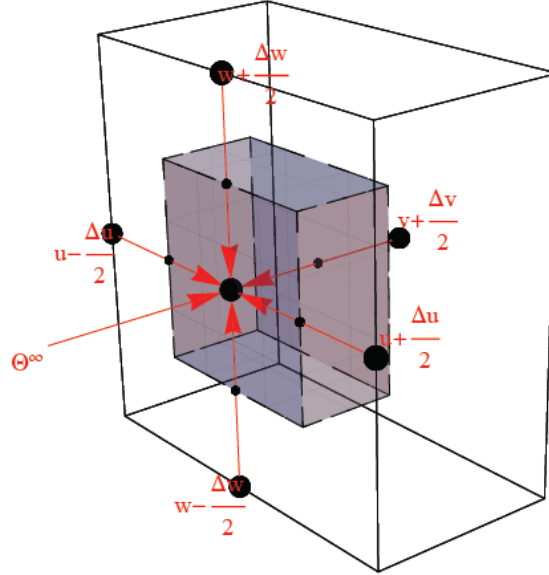


Figure 2.4 Energy balance at a surface

For nodes at surfaces, the mixed nature of the boundary conditions required to approximate convective heat transfer complicate nodal equations. For the case shown in Figure 2.4 for convection at a node on the  $wv$  plane the energy balance equation is

$$\frac{1}{\Delta\tau}(\theta^P - \theta^0) = \bar{h}(\theta^\infty - \theta^P)\Delta v\Delta w + \frac{\theta^{u+1} - \theta^P}{\Delta u^2} + \frac{\theta^{v+1} - 2\theta^P + \theta^{v-1}}{\Delta v^2} + \frac{\theta^{w+1} - 2\theta^P + \theta^{w-1}}{\Delta w^2} + Q$$

where  $\Delta v\Delta w$  is the area of the convection surface of the cell surrounding node,  $\theta^\infty$  is the dimensionless temperature to which heat is being transferred, and  $\bar{h}$  is a dimensionless heat transfer coefficient defined as

$$\bar{h} = h_r \frac{L_z^4}{\alpha}$$

Since our model allows for distinct heat transfer coefficients at any surfaces and a non-cubic mesh, we require twenty-six different boundary node equation types; six for the faces of the workpiece, eight for the corners of the workpiece, and twelve for the edges of the workpiece. The derivations of the boundary equations for the model are given in Appendix B.

The assumption of a mirror plane at  $v = 0$  allows for a reduction in the complexity of the boundary conditions, albeit a relatively trivial reduction.

The nodal equations for  $\theta$  are generated automatically based on the mesh selected by the user. The equations are solved simultaneously for each step in  $\tau$  and the value for  $\theta$  at each node is stored. Using the appropriate materials parameters and sample size, each  $\theta(u,v,w,\tau)$  can be translated into a  $T(x,y,z,t)$ . The data can be queried and displayed graphically in any of several formats, from thermal history profiles (Figure 2.6) to instantaneous thermal gradients within any plane in the sample (Figure 2.10). Thermal history profiles are essential for calibrating predicted temperature values, while in-plane contour maps assist in understanding heat flow during processes runs.

### **2.3 Determination of Heat Transfer Coefficients and Power Conversion Factor**

For the model to accurately predict the temperatures within the workpiece, the values of the heat transfer coefficients at the surfaces must be fairly accurate. Our model assumes free convective heat flow from the sides and top of the workpiece (except in the region directly under the tool shoulder). Typical values for free convection to air assume  $h \cong 100 \text{ W/m}^2\text{K}$ [25]. While thermal conduction across a resistive interface would be more physically accurate, for the purpose of this model, an effective heat transfer across an area between two fluids was found to be sufficient. Measurements made at the back surface of the workpiece showed that the steady-state temperature of the coolant block was approximately  $100^\circ\text{C}$ . The order of magnitude of the transfer coefficient to the coolant plate however needed to be estimated.

In addition to quantifying the heat losses from the workpiece, the effective heat input needed to be determined. Calculation of the power requirements of the system based on process parameters is not possible (see Section 3.2.4.3). However, as the purpose of this model is primarily to calculate of thermal profiles in order to characterize a process, an effective power input is sufficient. The motor controller used on the FSF machine outputs the instantaneous torque generated. Using the supplied torque and rotation frequency, the output power of the motor can be calculated from

$$P = \frac{\text{torque } \omega}{5252}$$

where  $P$  is the power in hp, torque is in foot pounds, and  $\omega$  is the rotational speed in rpm. As described previously, we assumed that only a fraction of the mechanical power generated by the motor was converted into thermal energy in the process. Conductive heat transfer to the spindle and convective heat transfer from the rotation of the tool are contained in the  $P_{\text{eff}}$  term

mentioned previously, as well as mechanisms of non-thermal energy loss (e.g. sidewall deformation).

To calibrate the heat transfer coefficients and the power conversion factor, the tool was rotated but was not translated across the surface of a 101.6mm × 31.75mm × 12.7mm Al6061 sample. The power output from the motor remained relatively constant at ~ 3.25hp for the duration of the run of approximately 30 minutes. The sample had thermocouples placed at four locations within the body of the workpiece, as depicted in Figure 2.5. The tool was positioned such that its center was aligned in x- and y- dimensions with the location of thermocouple one. The backside of the workpiece was cooled via a coolant block with internal ethylene glycol circulation.

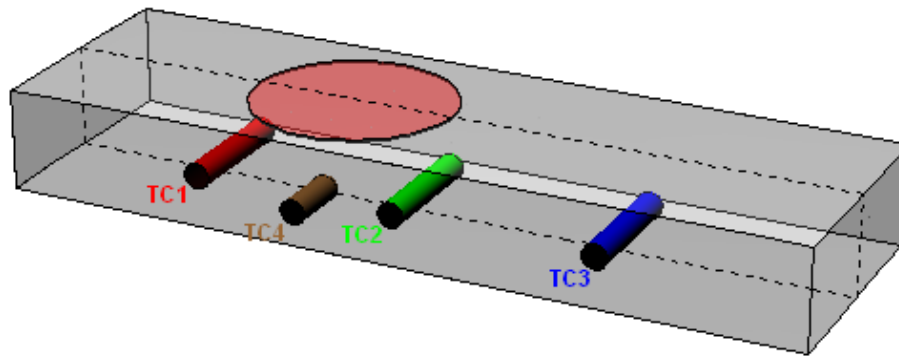


Figure 2.5 Thermocouple locations within bulk of sample

A simulation was run with a mesh of (24 X 5 X 5) nodes in the x, y, and z-directions respectively with a timestep of approximately 60s. The values of the heat transfer coefficients ( $h$  and  $h_b$ ) and the power conversion factor ( $P_f$ ) were varied and the temperatures simulated iteratively until satisfactory agreement was attained between the predicted and experimental values for temperatures at the thermocouple locations. Each simulation run took approximately fifteen minutes to run on a Gateway™ laptop with 4 GB RAM with a Core™2Duo processor running Windows Vista™ Home Premium.

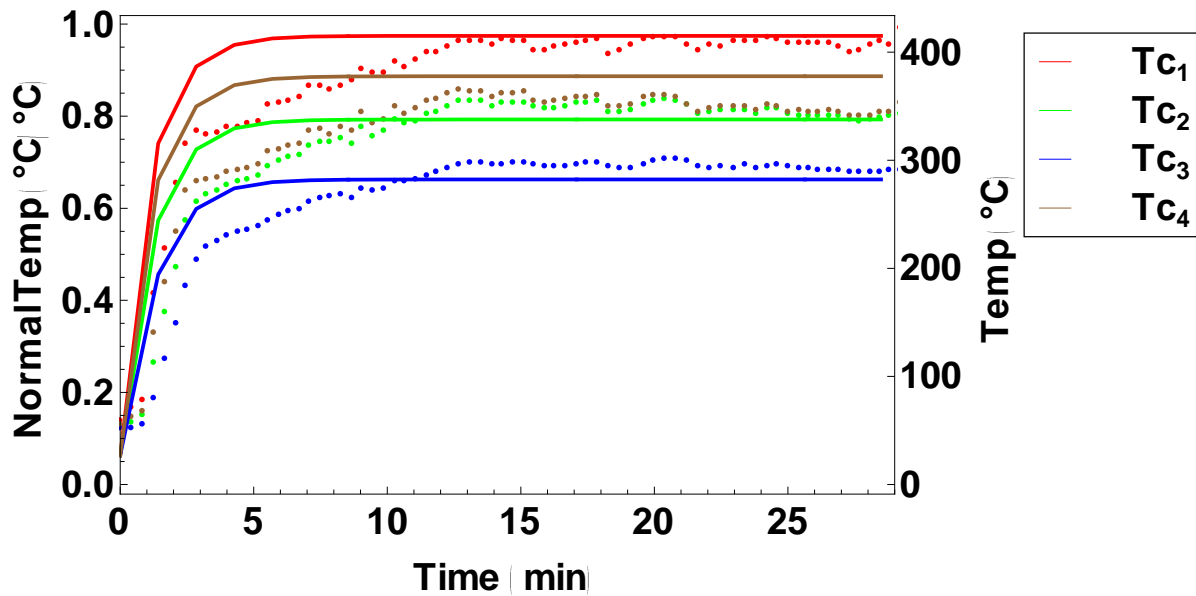


Figure 2.6 Empirical and calculated thermal profiles for steady-state operation

Figure 2.6 shows the empirical (dotted curves) and simulated (solid curves) temperatures for four locations within the sample. The optimal values for the heat transfer coefficients were found to be  $50 \text{ W/m}^2\text{K}$  out the sides and top of the workpiece, and  $1000 \text{ W/m}^2\text{K}$  to the backside anvil. The simulation shows good agreement with the thermocouples in the plane parallel to the anvil of the workpiece (TC1, TC2 and TC3) once a steady-state condition has been reached (after 12 minutes). The model results predict a steeper thermal gradient in the through thickness of the workpiece compared to the actual measured values.

In order to examine the discrepancy between the empirical and calculated temperature gradients in the through-thickness direction, a larger sample geometry was examined. The rationale for a larger sample geometry was to change the relative effects on the system of the heat losses at the surfaces. A  $101.6\text{mm} \times 101.6\text{mm} \times 25.4\text{mm}$  Al6061 sample was processed without tool translation. The tool was situated at a point on the surface equidistant from thermocouple 1 and thermocouple 2, as shown in Figure 2.7. In this scenario, thermocouple 4 was offset in the y-direction only, as opposed to an offset in both the y- and z-directions as in previously simulation. The tool was rotated at 2000 rpm, and the power output from the motor was relatively constant at  $\sim 5 \text{ hp}$  for the duration of the steady-state portion of the run (roughly four minutes).

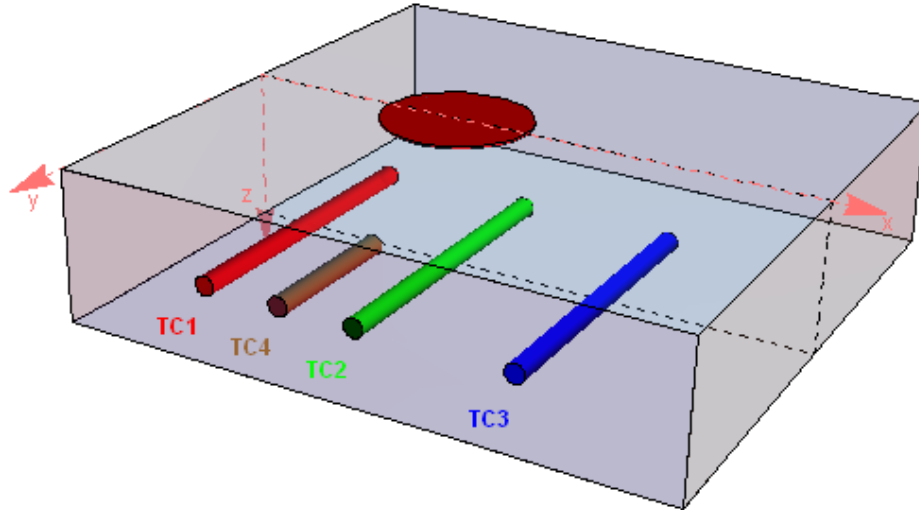


Figure 2.7 Thermocouple locations in larger sample geometry

A simulation was run on a 101.6mm × 101.6mm × 25.4mm Al6061 sample with a mesh of (24 X 7 X 7) nodes in the x, y, and z-directions respectively with a timestep of approximately 14s. The heat transfer coefficients and power factor were once again varied iteratively to optimize agreement between the model results and empirical data. The results shown in Figure 2.8 were obtained with a heat transfer coefficient at the backside anvil of 800 W/m<sup>2</sup>K, and a power factor of 0.75.

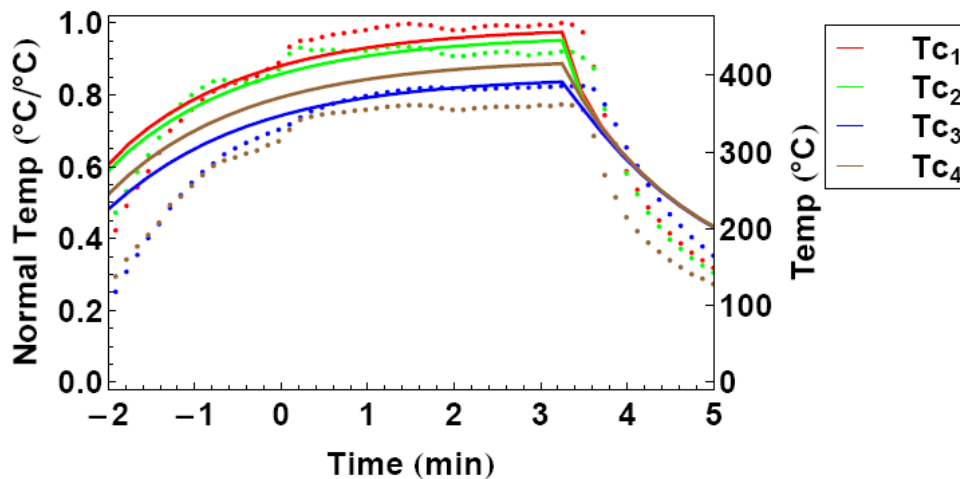


Figure 2.8 Empirical and calculated thermal profiles for larger sample geometry

The predicted values for temperatures of thermocouples 1, 2, and 3 show close agreement with the actual measured values, while the values at thermocouple 4 differ significantly. Part of the reason for this deviation lies in the change in heat transfer out of the backside of the larger sample. In order to achieve good agreement between experimental and predicted values, the heat transfer coefficient out the backside of the workpiece was lowered

from  $1000 \text{ W/m}^2\text{K}$  to  $800 \text{ W/m}^2\text{K}$ . We believe that this 20% reduction in effective heat transfer out of the anvil side of the sample is due to an inaccurate assumption as to the mode of heat transfer across the interface (i.e. convective to a fluid vs. conductive across a thermal resistance). The localized pressure of the feedstock acting upon the surface of the workpiece would act to reduce the thermal resistance between the workpiece and the anvil directly under the tool. An increase in the local heat transfer out the backside of the workpiece would work to change the nature of the gradient field in the sample. The isotherm lines shown in the contour plot in Figure 2.10 would change in shape from nearly spherical (as shown) to more a more cylindrical form (with the height of the cylinder parallel to the z-direction) under the influence of an increased localized heat transfer. Such a change would act to align the theoretical and empirical temperature values at thermocouple 4 in both Figure 2.6 and Figure 2.8.

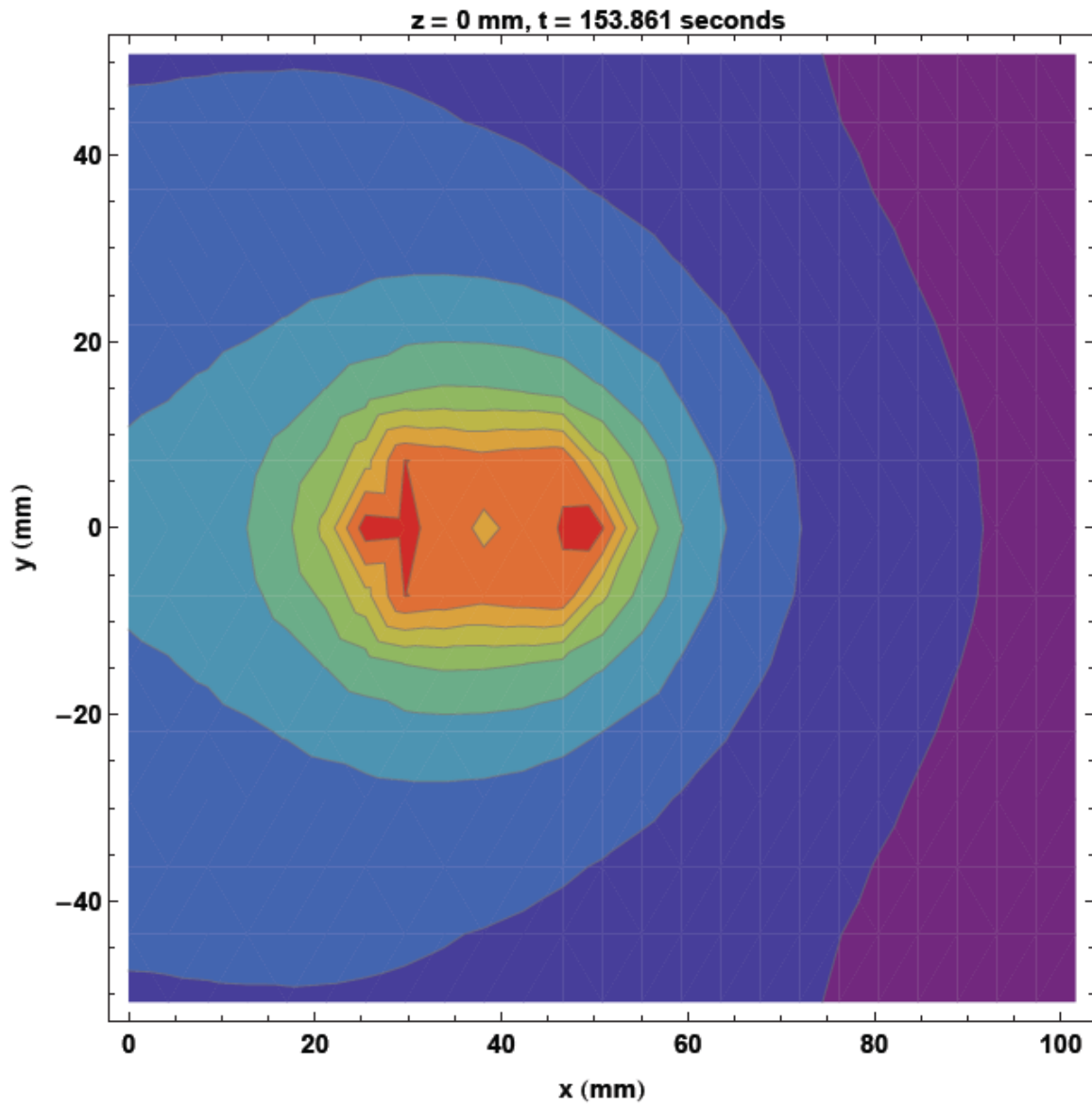


Figure 2.9 Simulated temperature contour plot of top surface of 100mm X 100mm X 25 mm Al6061

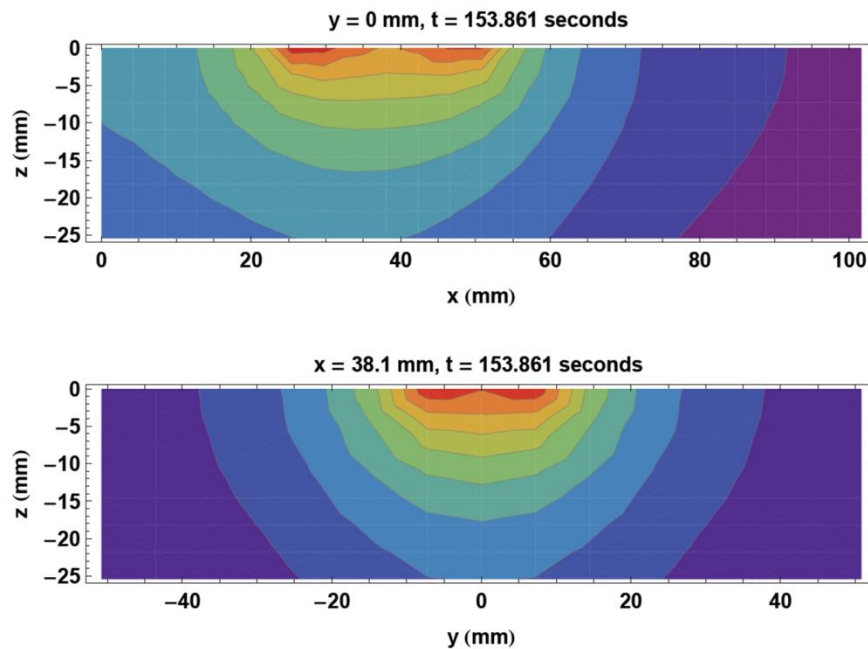


Figure 2.10 Thermal gradients with Al6061 workpiece

A second important piece of information gleaned from this experiment is the fact that the power conversion factor was increased from 35% in the smaller sample geometry to 75% in this larger sample. The smaller samples have a width roughly equal to that of the tool shoulder (31.75 mm sample vs. 25.4 mm tool shoulder). Upon processing, the sidewalls of the smaller samples are significantly deformed, especially on the advancing side of the stir zone. In a larger sample there is adequate material such that there exists a resistance to deformation directly adjacent to the stir zone resulting in a higher degree of conversion of mechanical energy to thermal energy.

## 2.4 Model Validation

The heat transfer coefficients and power factors calculated from the steady-state experiments described above were used to simulate temperature profiles in both Al6061 and Al5083 samples. Figure 2.11 and Figure 2.12 show empirical (dotted curves) and calculated (solid curves) temperature profiles for typical Al6061 process runs. The sample in Figure 2.11 was translated at 15 mm/min and that of Figure 2.12 at 25 mm/min. Included in the figures is a graph of the measured power input to the system (blue curve) with the approximated input power used for the calculations (purple curve). As shall be described in Section 3.2, the friction stir fabrication proceeds in a four-stage process. The power input to the system during these four stages can be treated as a step function, followed by a linear increase, and finally resulting in a plateau during the steady-state translation portion of the run.

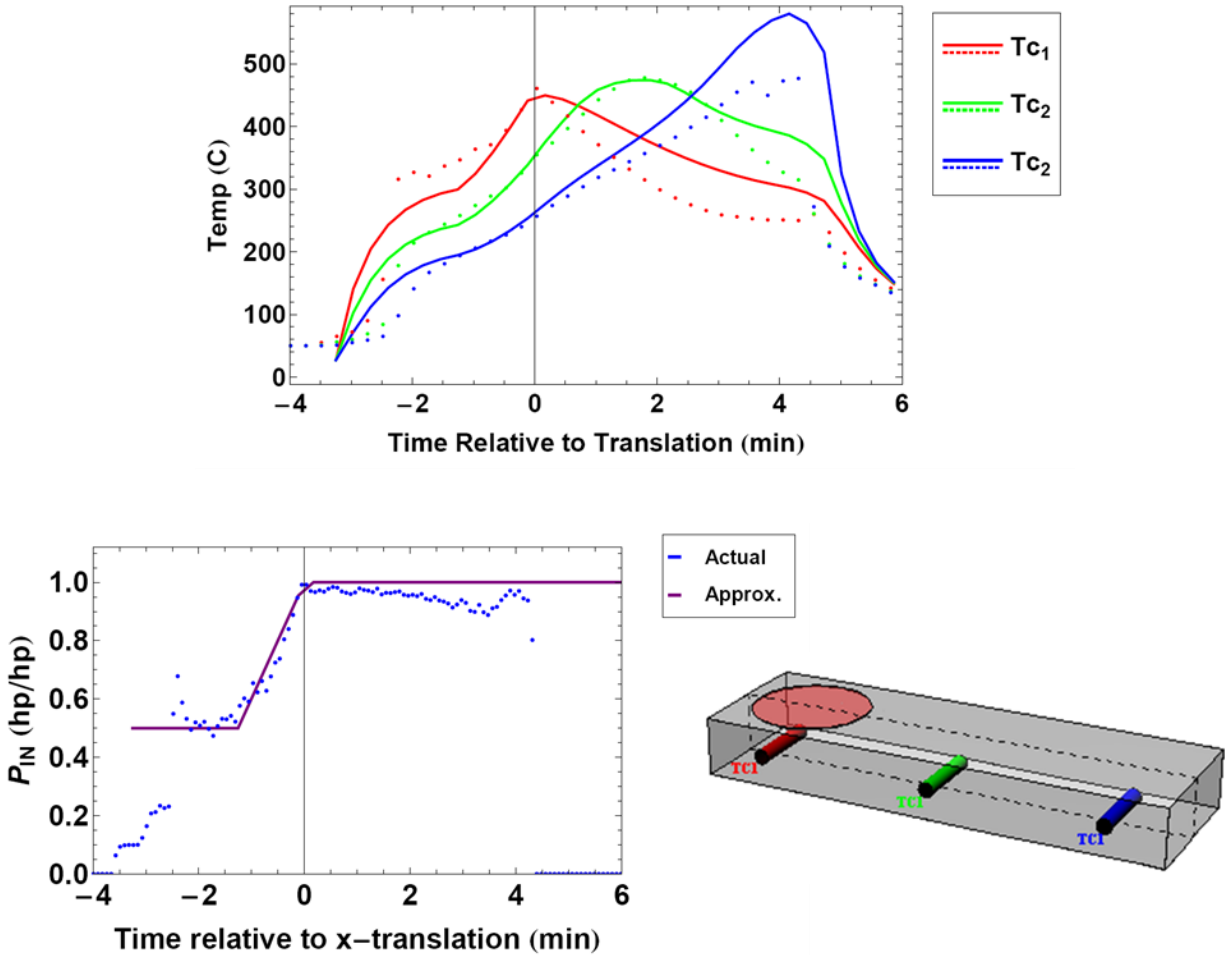


Figure 2.11 Comparison of empirical to calculated temperatures for Al6061 translated at 15 mm/min

As it exists, the Schultz-Creehan friction stir fabrication system has no active monitoring of the position of the workpiece with respect to the tool. Determination of the beginning of tool translation in the empirical data file is somewhat inexact. Typically tool translation begins immediately after bead formation (i.e. the second power plateau). However, the initiation of tool translation is manual and might be delayed slightly depending on system performance. Due to the difficulties in determining the zero on the time scale, there exist slight discrepancies in the locations of inflection points between empirical and calculated profiles. Despite the minor differences in the relative placement of the time axes, there is excellent agreement between empirical and calculated temperature values.

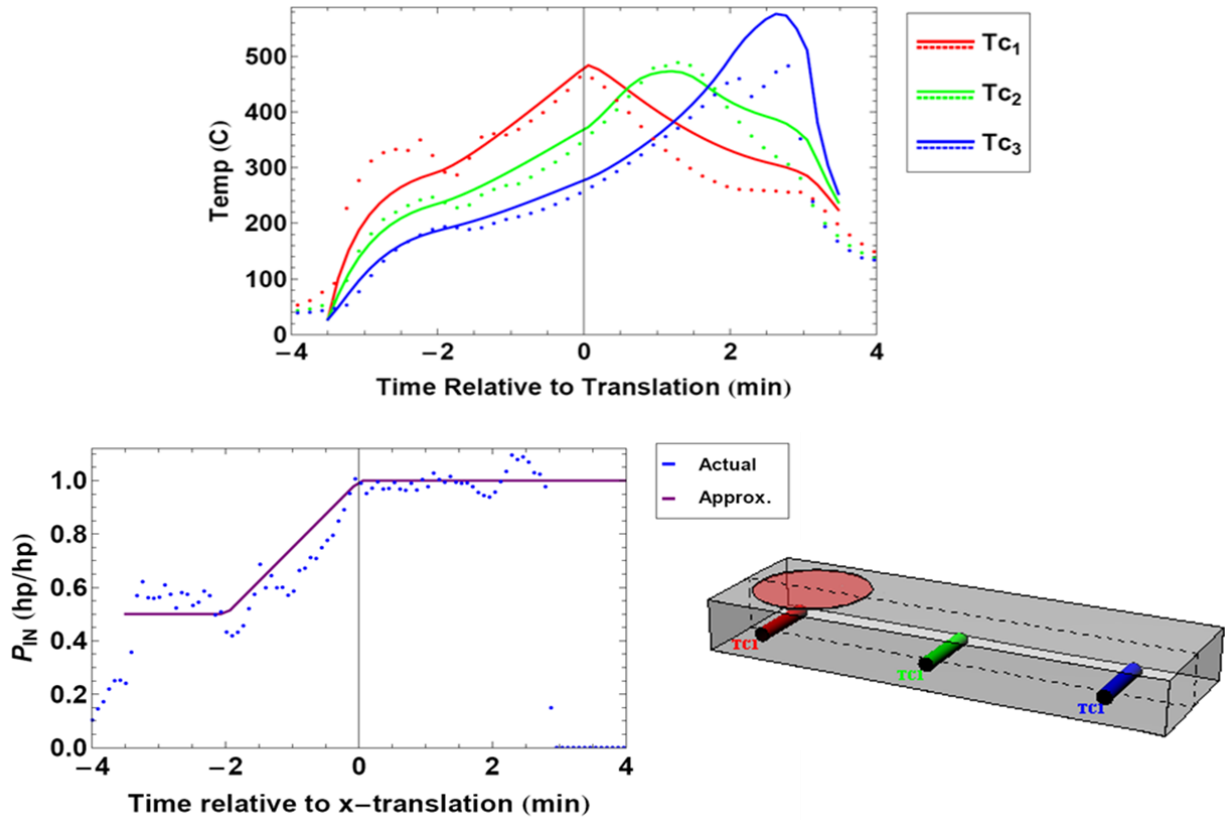


Figure 2.12 Comparison of empirical to calculated temperatures for Al6061 translated at 25 mm/min

Figure 2.11 and Figure 2.12 show that there is good agreement between calculated and empirical data for different processing parameters for Al6061 samples. Using the same heat transfer coefficients and power conversion factors, thermal profiles can also be calculated for Al5083 samples. Figure 2.13 shows the profiles calculated for four thermocouple positions within an Al5083 sample. The sample was processed with a constant input power, but a much slower translation speed of 3.5 mm/min (vs. 15 – 25 mm/min for Al6061). Figure 2.13 shows that our model can accurately calculate temperature profiles with the Al5083 sample, both in and out of the plane parallel to the top surface.

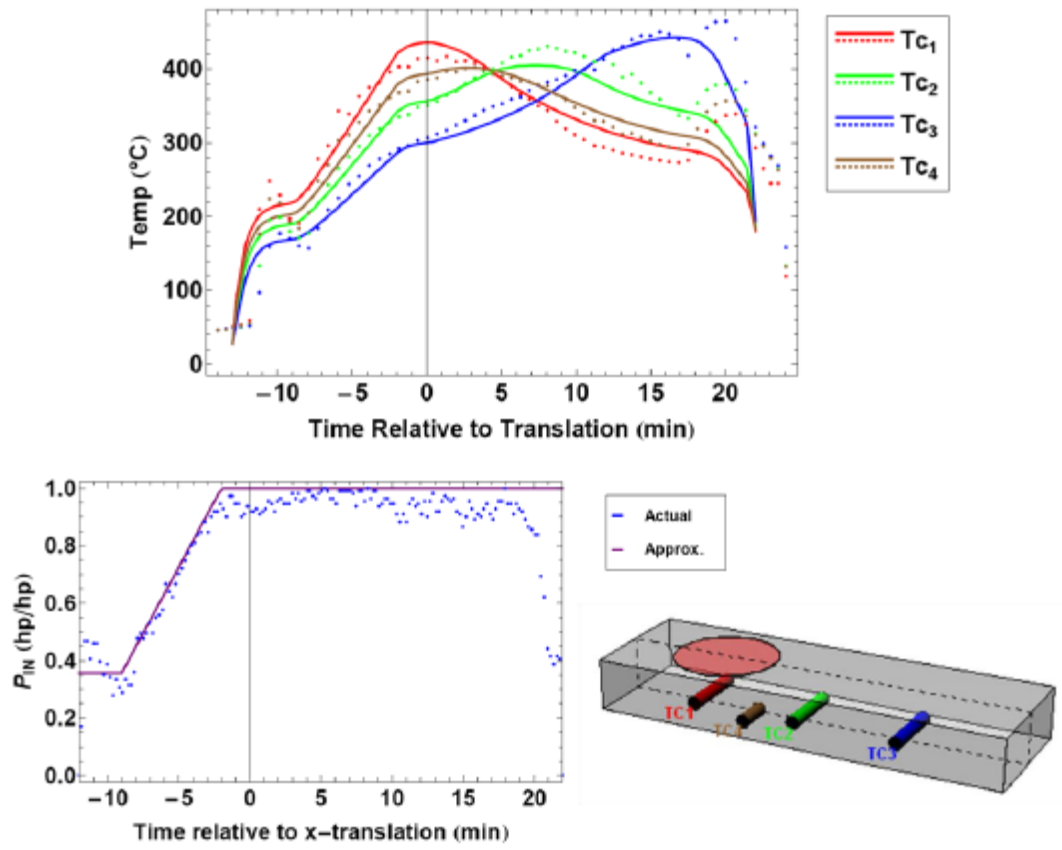


Figure 2.13 Comparison of empirical to calculated temperatures for Al5083 translated at 3.5mm/min

## **3 Friction Stir Fabrication Process Characterization**

### **3.1 Equipment Description**

The Schultz-Creehan FSF machine consists of four main subsystems; the motor and controller, the feedstock delivery system, the tool, and the temperature monitoring system.

#### **3.1.1 Motor and Controller**

A Baldor EM3218T high-efficiency 5 hp, 1750 rpm, synchronous AC motor drives the spindle via a pulley and belt system. The pulleys are matched such that the spindle-to-motor speed ratio is 1:1. Motor control is achieved by an ABB variable frequency drive motor controller operated via a custom-built LABView-based GUI. The system monitors motor torque and drive current in real time, which are recorded in a database through the LABView control software.

The synchronous nature of the AC motor restricts the motor efficiency at frequencies much lower than the synchronous frequency of 1750 rpm. The power requirements of the FSF process are such that it is not possible to operate the system at frequencies lower than 800 rpm.

#### **3.1.2 Feedstock Delivery System**

A 9.525 mm square feedstock rod is loaded into the backside of the spindle. The spindle and the tool have an aligned square channel through the center to accommodate the feedstock. The stock is square in order to ensure that rotational motion occurs between the feedstock and the workpiece as opposed to between the feedstock material and the inside walls of the spindle or tool tip (see Section 1.3).

A pneumatic piston supplies force to the backside of the feed rod to drive the feedstock through the tip and into the stir area. The force on the piston is controlled through the LABView control GUI, and has a maximum value of 8800 Newtons. The position of the backside of the feed rod is monitored with a Celesco Cable PT1A extension position transducer.

### 3.1.3 Tool Description

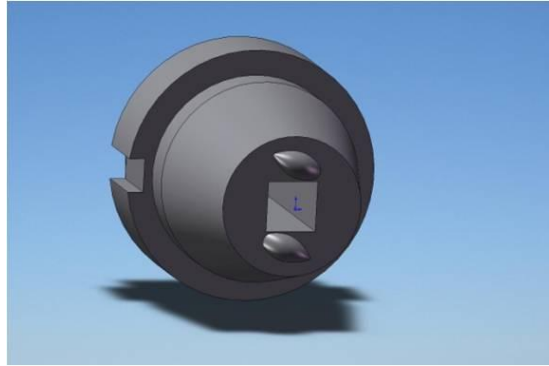


Figure 3.1 Schultz-Creehan friction stir fabrication tool

The Schultz-Creehan system has a detachable tool mounted to the end of the spindle, allowing for change in the design of the tool without changing other parts of the system. All experiments performed for this work were done using the tool shown in Figure 3.1. The tool has two tear-drop shaped nubs in a spiral arrangement on the tool shoulder. These nubs act to assist in warm-up heat generation, to break up surface oxides on the workpiece, to form part of the quasi-tip of the tool, and to guide the flow of material within the bead. Tool tips are designed by Schultz-Creehan using commercial CAD software and subsequently machined in-house from tool steel using a micromachining station.

The nubs are essential in forming a good bond between the workpiece and the deposited material. Al6061 was deposited onto nickel aluminum bronze (NAB) using the FSF machine. Prior depositions of NAB on NAB caused significant damage to the tool tip in the form of wear on the nubs. The deposition run essentially removed the nubs from the tip. To prevent damage to the tool tip during the Al6061/NAB process run, the tool was not inserted into the NAB workpiece. The resulting aluminum deposition layer did not mechanically bond to the surface.

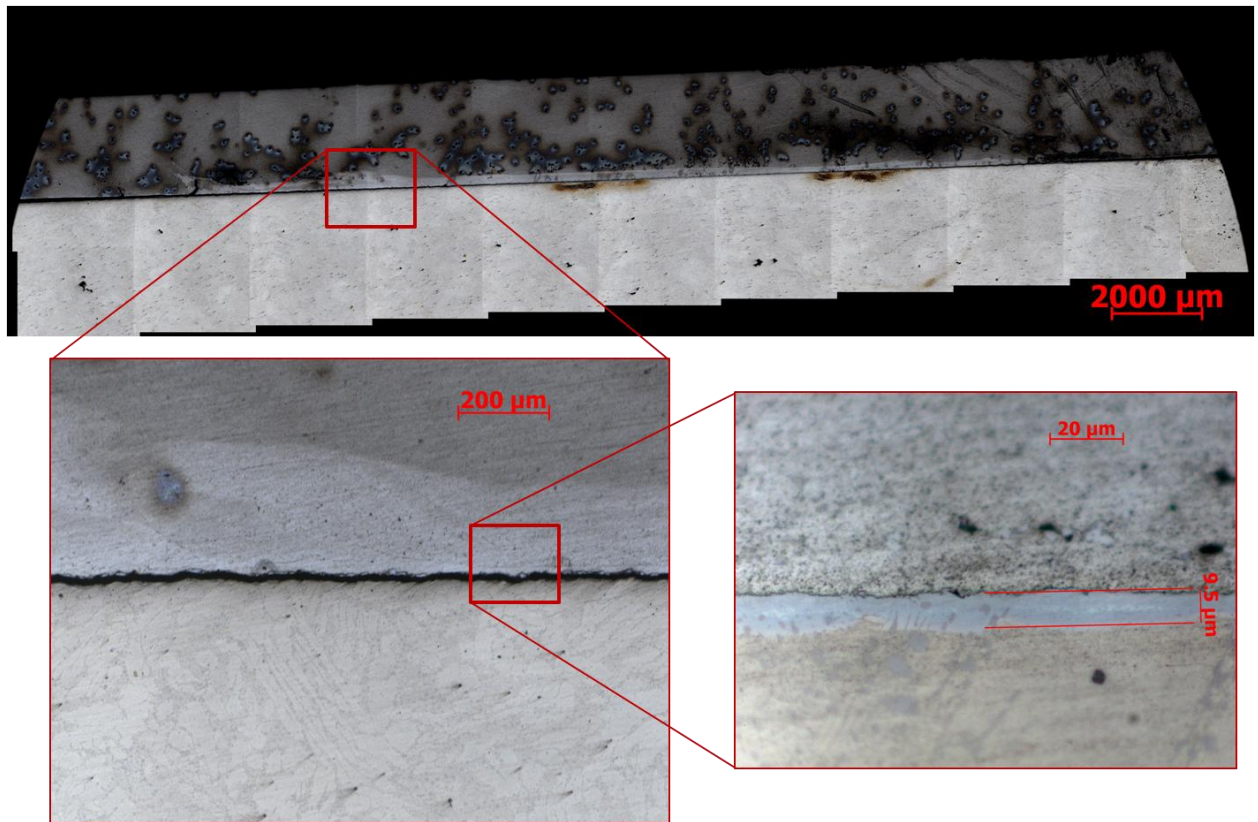


Figure 3.2 Optical micrograph of Al6061/NAB process run with focus on interface

The inset in Figure 3.2 shows what appears to be a wetting layer of aluminum in the top 10  $\mu\text{m}$  of the NAB workpiece. There is no mixing of the workpiece and the feedstock, and in fact there a gap between the deposited aluminum layer and the workpiece. In contrast, Figure 3.3 shows a depth profile of the NAB/NAB process run for which the tool was inserted to a depth of  $\sim 760 \mu\text{m}$ . With the nubs inserted into the workpiece, the feed material and the workpiece material show good mixing and an intimate interface. The effects that the nubs have in assisting to mix the material in the stir zone imply that the nubs can also be thought of as part of a pseudo FSF tool pin, determining the width of the weld (see Section 4.2.3).



Figure 3.3 Optical micrograph showing a depth profile for an NAB/NAB FSF run

### 3.1.4 Gantry Table Description

Motion of the tool relative to the workpiece is accomplished through motion of a gantry table to which the workpiece is attached. Ethylene glycol is circulated through a backside cooling block that is mechanically fixed to the gantry table. To prevent heat transfer to the table, the coolant block is thermally isolated from the table with refractory bricks.

The gantry table used for the FSF machine is the xyz stage of a Kondia knee mill. The table is equipped with stepper motors for automated control of the x and y axes of motion of the table. A Prototrak MX2 digital read out allows for entry of translation speed and distance in the x and y planes (CNC). The table does not have a z-direction motor, so motion in the vertical direction is controlled manually. Although the position of the table can be viewed on the controller, linkage to a PC is not possible due to the age of the table hardware. There is therefore no active monitoring or recording of position or translation speed with respect to time for FSF process runs.

### 3.1.5 Temperature Monitoring

To provide additional process monitoring capabilities, systems were developed to read and record temperature at various positions during the process. A Raytek RAYMID20LTCB3 infrared (IR) Pyrometer was mounted to the spindle housing and focused on the sidewall of the tool. The placement of the IR sensor was such that readings were made on the tip and not on the workpiece surface. The output of the IR sensor is read by the LABView GUI and values are sampled at 3Hz throughout process runs.

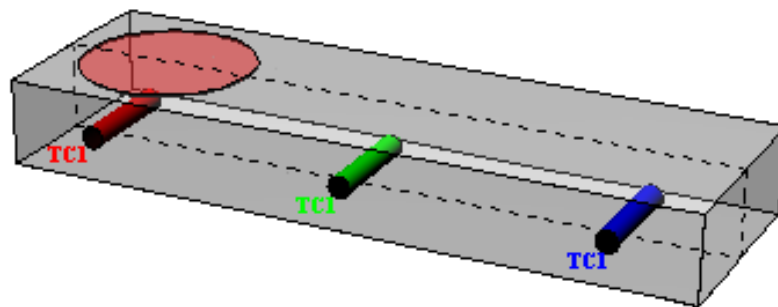


Figure 3.4 Placement of three thermocouples used in early Al6061 experiments

In addition to tip the IR tip temperature monitoring system, a thermocouple amplifier was constructed to allow for the addition of up to four thermocouples. Initially for Al6061 processes, three sleeved, type K thermocouples were inserted at various locations along the centerline of the workpiece, as shown in Figure 3.4. To further increase confidence in thermal model predicted values, a fourth thermocouple was placed at the center of the backside of the workpiece as shown in Figure 3.5.

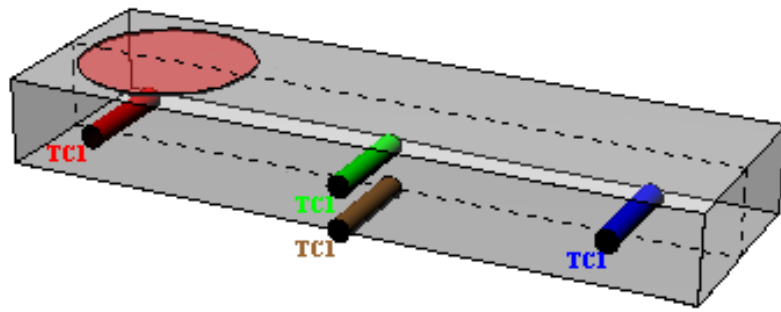


Figure 3.5 Placement of four thermocouples used for Al6061 experiments

Values measured at the backside of the thermocouple sample both the temperature of the workpiece and that of the cooling block. To avoid the inaccuracy in measurement directly at the backside interface, the final configuration of thermocouples used for all Al5083 runs places thermocouples at  $(0.25 L_x, 0.5 L_y, 0.5 L_z)$ ,  $(0.5 L_x, 0.5 L_y, 0.5 L_z)$ ,  $(0.75 L_x, 0.5 L_y, 0.5 L_z)$ , and  $(0.375 L_x, 0.3125 L_y, 0.75 L_z)$  as shown in Figure 3.6, where  $L_x$ ,  $L_y$ , and  $L_z$  correspond to the length of the workpiece in the x-, y-, and z-directions respectively. Reconfiguring the thermocouples such that the fourth thermocouple was offset from the other three thermocouples in both the y- and z-direction allows for a more rugged verification of model calculations (see Section 2.4). Furthermore, since typical process runs involved a net x-direction translation of  $\sim 64$  mm, positioning TC1 and TC3 closer to the center of the workpiece ensures temperature readings with the tool shoulder translating through the x-coordinate of all thermocouples.

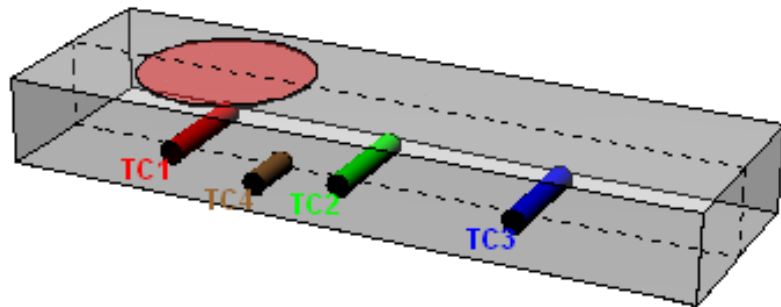


Figure 3.6 Placement of four thermocouples for Al5083 experiments

## 3.2 Process Description

A typical friction stir fabrication run has four stages of interest – tool insertion, material warm-up, bead formation, and steady-state translation. Each stage has signature characteristics in temperature, power input and feedstock delivery rate. Figure 3.7 shows a normalized graph of the data recorded during a typical process run on an Al6061 substrate.

Temperature values at the embedded thermocouples were recorded, but are not included in this graph. The defining characteristic for the tool insertion phase is the power drawn by the process. All other stages of the process run can be identified primarily through the rate of feed delivery to the bead.

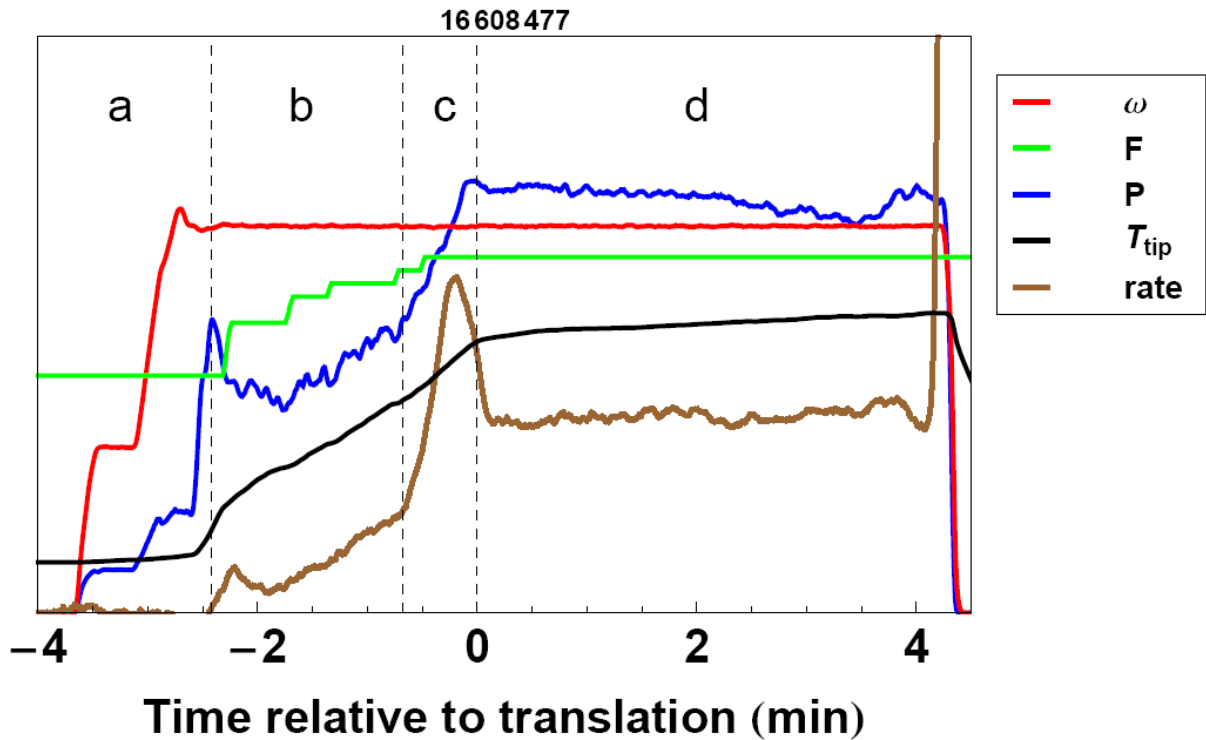


Figure 3.7 Output data from process monitor system showing four stages of a fabrication run; a. insertion, b. warm-up, c. bead formation, d. steady-state operation

### 3.2.1 Tool Insertion

The tool insertion phase of the run shown in Figure 3.7 lasts from  $t \cong -4.5$  minutes until  $t \cong -2.5$  minutes (stage a), and is characterized by a sharp increase in horsepower to a value roughly half of that of the steady-state phase. Prior to the start of a run, the tool is positioned such that the ends of the nubs are touching the surface of the workpiece, but are not penetrating. As the tool is brought up to speed, minimal force is applied to the feedstock both to prevent flow of workpiece material into the stock channel and to provide additional thermal energy. The power required to rotate the tool with a minimal level of feedstock force prior to insertion is relatively low (typically less than 1 hp). Once the tool rotation speed is achieved, the table on which the workpiece rests is manually raised, driving the nubs into the surface of the workpiece. The nubs are inserted to a depth of 7.6 mm, such that there remains a 7.6 mm gap between the tool shoulder and the workpiece surface. As the tool is inserted into the workpiece, the nubs act to mill material from the workpiece, increasing the power requirements of the system.

To explore the effect of rotational speed on the power requirements of the system prior to bead formation, the force on the feedstock was held constant at 1000 N while the rotational speed was increased from 500 rpm to 1750 rpm. As shown in Figure 3.8, the power requirement is proportional to the frequency of rotation prior to bead formation.

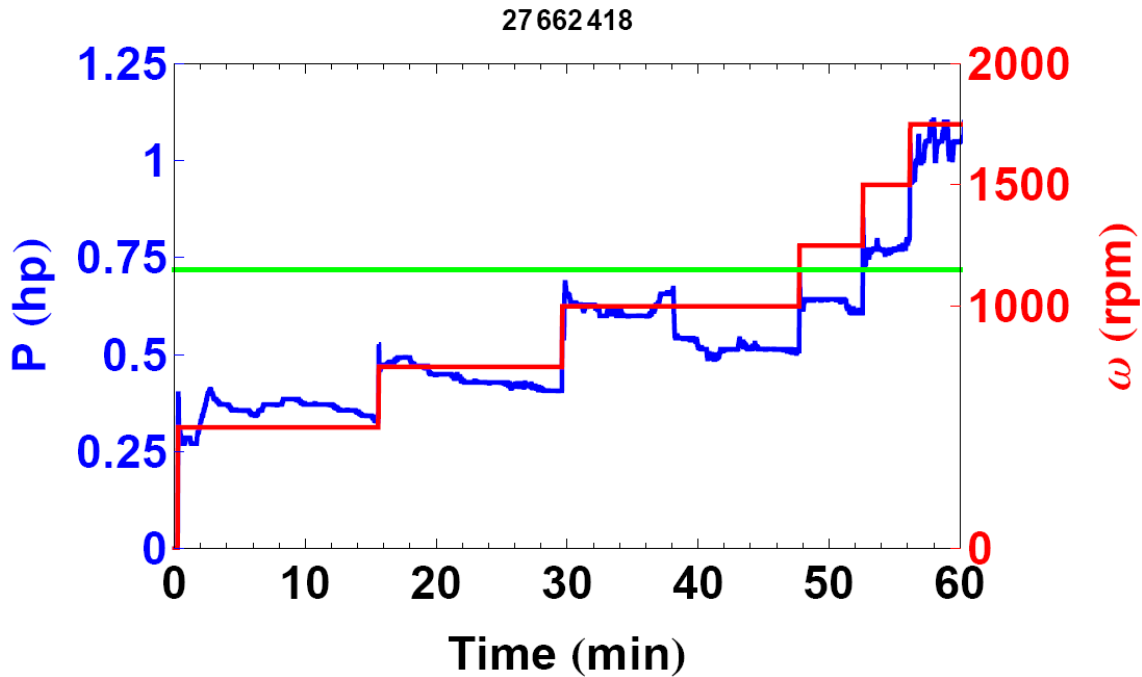


Figure 3.8 Power, rotational speed, and force applied to system prior to insertion showing proportional response of power to rotational speed

The force supplied to the backside of the feed rod however has little effect on the power requirements of the process prior to bead formation. When the rotational speed of the tool is held constant, increases in feedstock force from 220 to 2000 N have negligible effect on the power requirements of the system (Figure 3.9).

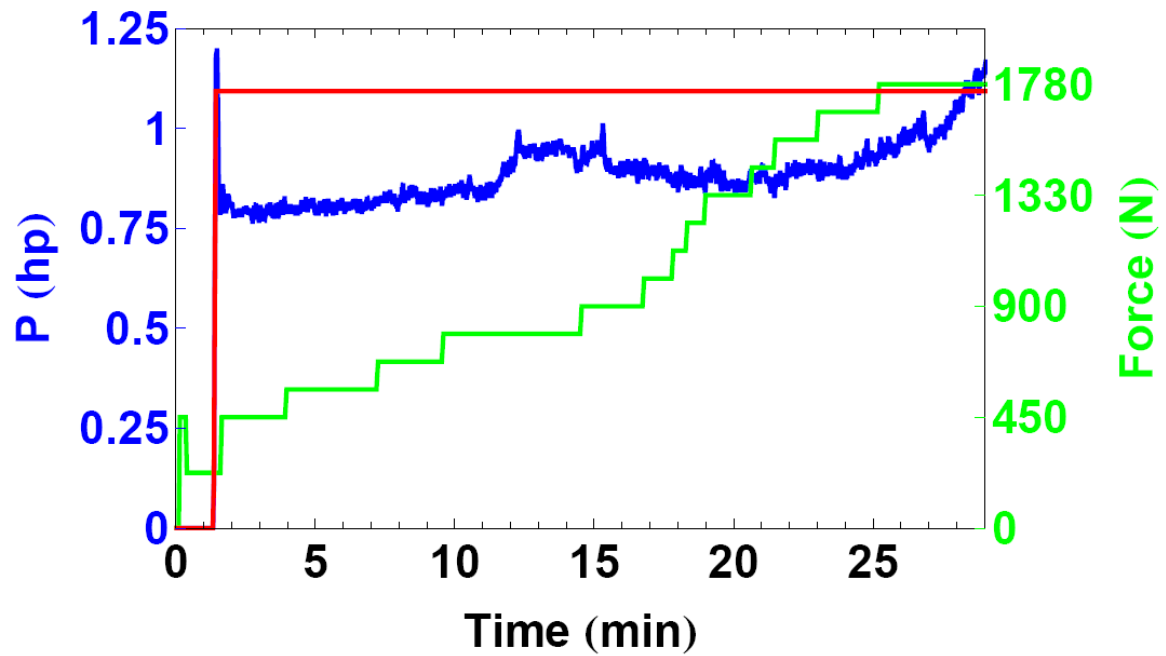


Figure 3.9 Power, rotational speed and force applied to system prior to insertion showing relative insensitivity of power to feedstock force

### 3.2.2 Warm-up Stage

The warm-up phase begins when the nubs have completed milling material from the workpiece and ends at bead formation. This start of this stage is characterized by leveling off of the power to the system (Figure 3.10) or a drop in power to the system (Figure 3.7).

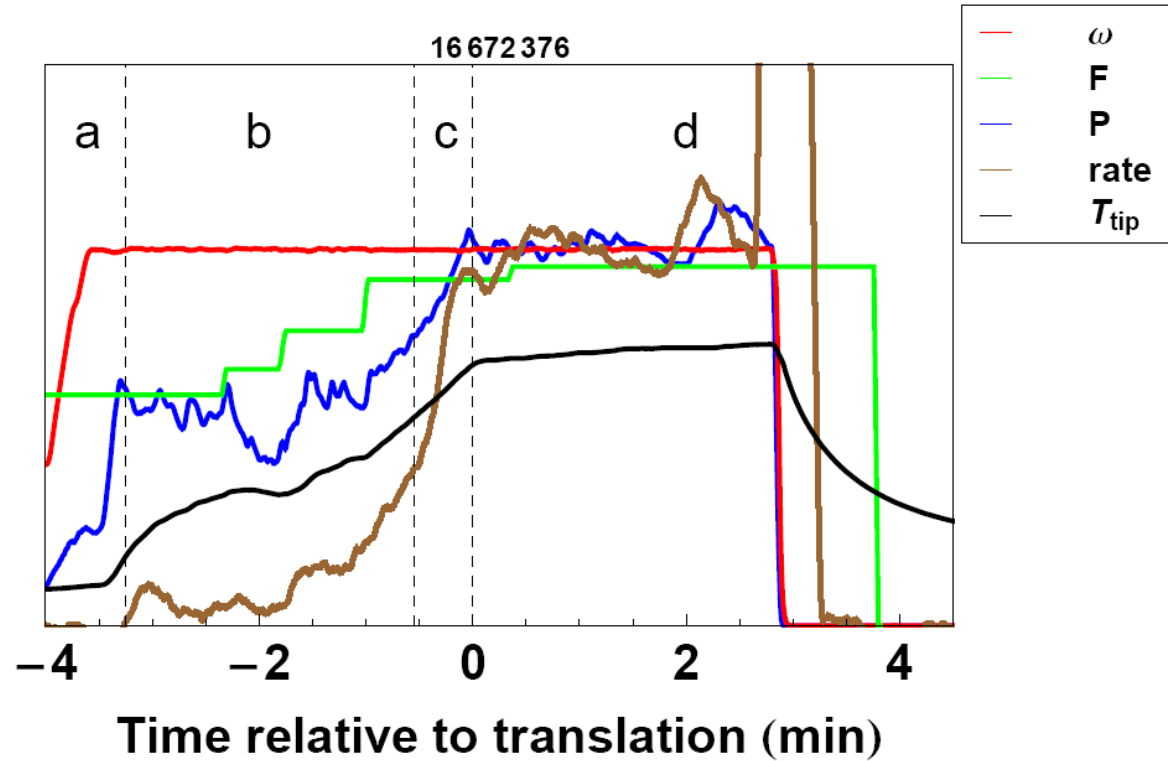


Figure 3.10 Four stages of fabrication process for an Al6061 run -- a. tool insertion, b. warm-up, c. bead formation, d. steady-state

The increase in contact area between the tool tip and the milled surface of the workpiece act to increase the power requirements of the system. The result is a plateau in the power to the system, or gradual increase in power with time. The increased thermal energy from the nub-to-workpiece friction and feedstock delivery cause the temperature of the tool tip to increase steadily during the warm-up period. Once the tip temperature reaches a critical value, bead formation begins.

### 3.2.3 Bead Formation

Bead formation begins once the tool tip reaches a critical temperature. Due to the intimate physical contact between the tool tip and the feedstock material in the center of the spindle, it is safe to assume that the tip temperature is a good indicator of the temperature of the feedstock at the moment of delivery. Once the feedstock reaches the critical temperature it begins to soften. The force on the feedstock push rod acts to supply adequate pressure to deform the tip of the feedstock, increasing the feedstock-to-workpiece contact area. An increase in contact area under conditions of constant rotational speed and constant interface pressure requires an increase in power. The additional power delivered to the system acts to further soften the feedstock material, allowing for further deformation. The temperature and

power therefore act to supply positive feedback to the system until the feedstock material completely fills the area under the tool shoulder. Once adequate material has been delivered such that the volume between the tool and workpiece has been filled, the power requirements and tip temperature level off to the steady-state values.

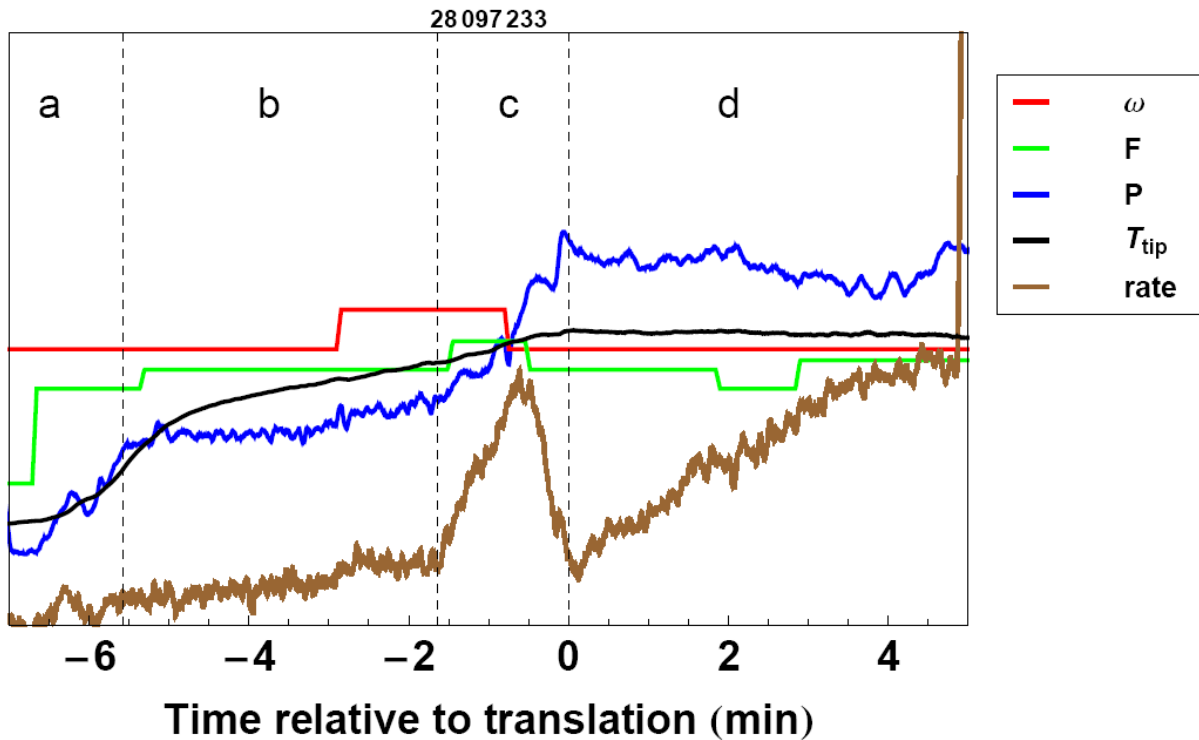


Figure 3.11 Four stages of fabrication run on Al5083 sample -- a. tool insertion, b. warm-up, c. bead formation, d. steady-state

The onset bead formation stage is therefore characterized by a sharp increase in feedstock delivery rate, motor power, and tip temperature. The end of the bead formation is characterized by a plateau in the power required to the system (stage c, Figure 3.11). Experimental data show that the bead begins to form at a tip temperature of approximately 225°C for the Al6061/Al6061 system, 170°C for the Al5083/Al5083 system, 275°C for the Al6061/Al5083 system, and 200°C for the Al5083/Al6061 system. The physical significance of the value of the critical temperature is not fully understood. The IR detection system for measuring tip temperature samples a finite cross-section of the sidewall of the tool tip. As such, the reflected value is an average of the area contained in the spot size of the focal point. Furthermore, the temperature profile within the tip itself cannot be measured. So, the temperature of the feedstock itself could vary somewhat from the temperatures reported by the IR detector.

The critical temperatures for the different material systems show that the value is not only a factor of the feedstock temperature, but also the temperature of the workpiece itself. The relationship between the critical temperature and the material system used for processing is not understood. The mechanism described above for a positive power-temperature feedback to the system would suggest critical temperatures that are much closer in value for Al6061 and Al5083.

### **3.2.4 Steady-State Operation**

In order for a friction stir fabrication run to be considered successful two criteria must be met. Firstly, the layer deposited by the tool must be continuous across the area of the surface corresponding to the shoulder of the tool. Secondly, the deposited layer should be intimately bound to the workpiece. While not quantitatively characterized in this work, the interface between a coating and the substrate appears good for all runs in which the tool nubs have been inserted into the workpiece surface. The achievement of a void-free coating on the surface of the workpiece is dependent on the processing parameters used for the run, as well as the interplay between the different parameters.

Ultimately, the success or failure of a run is depends on whether or not adequate material is delivered to the tool-workpiece interface. The Schultz-Creehan friction stir fabrication machine allows for user control of rotational speed, feedstock pushrod force, and tool translation speed. The rate of feedstock delivery and net horsepower delivered to the system are dependent upon the temperature of the material and the selected processing parameters. The instantaneous power delivered to the system is the simplest method for in-situ process monitoring. While the rate of material delivery relative to the amount required to maintain the bead is a more physically accurate method for gauging the success of a processing run, current equipment renders in-situ measurement of delivery rate impractical. Examination of the data after completion of a run shows the complex interrelation of the processing parameters, the material federate, and horsepower requirements.

#### **3.2.4.1 Rate of delivery of material for Al6061 versus Al5083**

As will be discussed subsequently, the instantaneous rate of material delivery depends on the force applied to the feedstock and the rotational frequency of the tool. The range of values for the average feedstock delivery depends on the material type of the feedstock and the workpiece. Figure 3.12 shows typical value ranges for delivery rate for different combinations of feedstock and workpiece material types. The data show that Al6061 stirred onto an Al6061 workpiece (Al6061/Al6061) allows for approximately 0.3 mm/sec of displacement of the pushrod, while Al5083 deposited onto an Al5083 substrate (Al5083/Al5083) results in an order of magnitude less displacement of the pushrod. For all of the runs shown in Figure 3.12, the tool tip is approximately the same temperature (~300°C). As

with the dependence of the critical temperatures on material type (see Section 3.2.3), the significance of the variance in rate is not understood. The average value of the feedrate for a material type dictates the maximum tool translation speed by restricting the total volume of material delivered to the system per unit time (see Section 3.2.4.2).

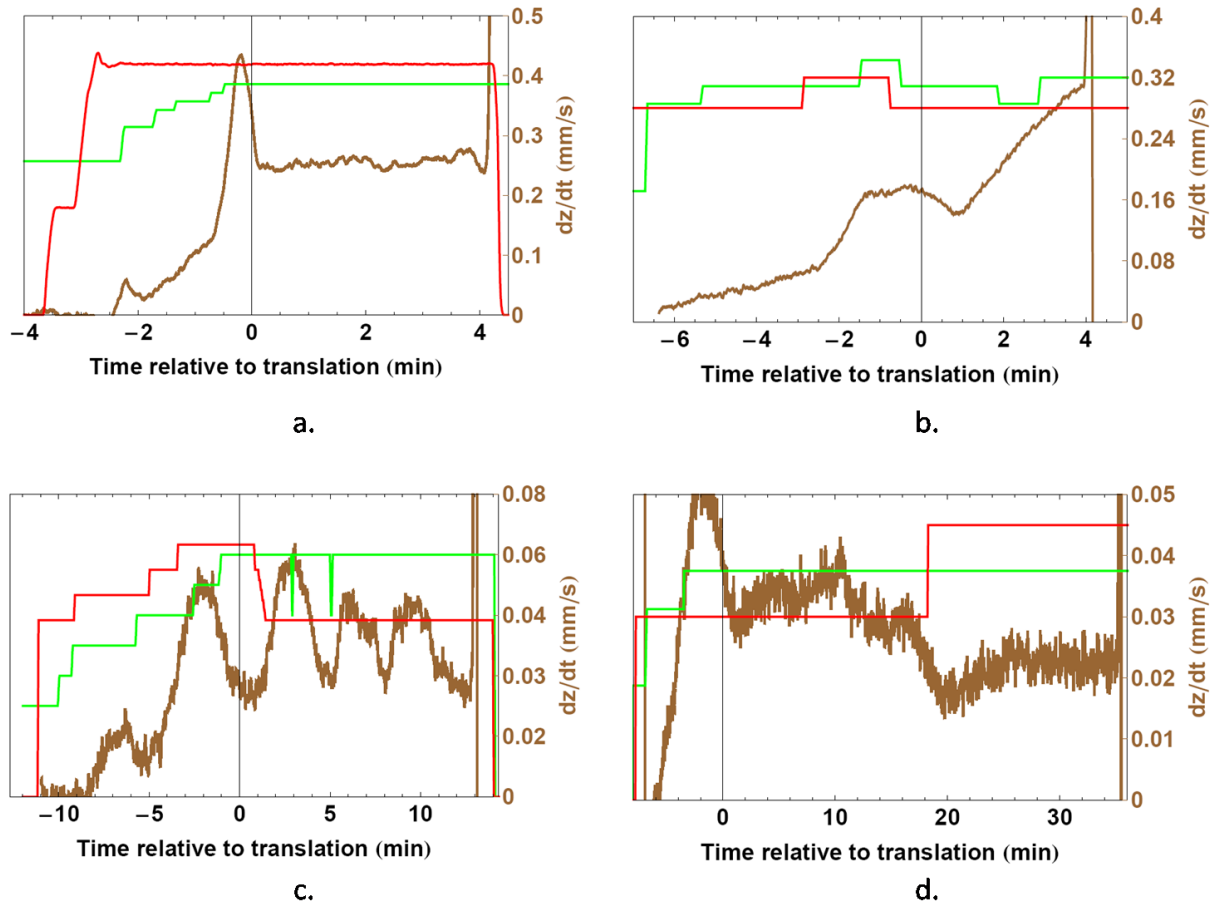
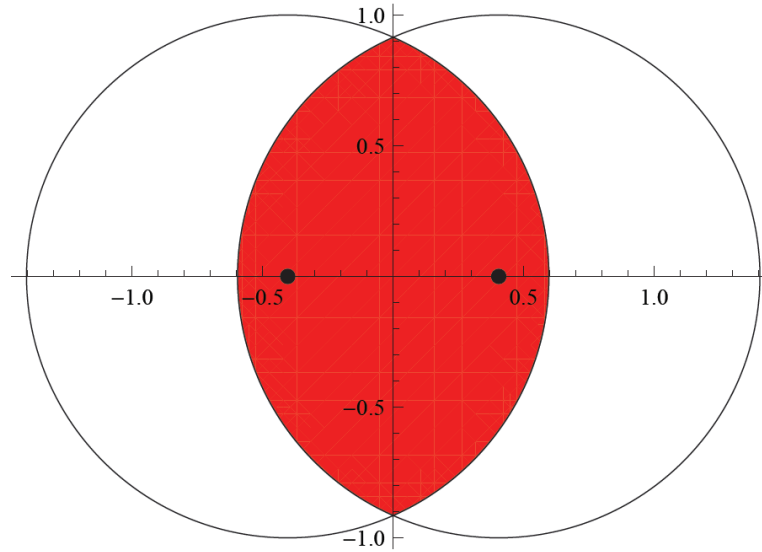


Figure 3.12 Typical absolute material delivery rate for a. Al6061/Al6061, b. Al6061/Al5083, c. Al5083/Al6061 and d. Al5083/Al5083

### 3.2.4.2 Volume of material required to maintain the bead

Since a successful run depends on adequate material delivery to the system, it is important to quantify the volumetric material delivery requirements during translation. As the tool is translated across the surface of the workpiece, a finite volume of material is required to fill the volume beneath the tool shoulder and the workpiece. The shape of material deposited during the process can be modeled as a series cylinders of radius equal to that of the tool separated by the distance traveled by the tool in time  $\Delta t$ . When the tool is translated at a constant speed  $v$  mm/sec in the x-direction, it will move  $v \Delta t$  mm in time  $\Delta t$ .



**Figure 3.13** Area of overlap of circles with centers separated by distance  $d$

The area of overlap of the two circles of radius  $r$  separated by distance  $d$  is defined as

$$A = 2r^2 \text{ArcCos} \left[ \frac{d}{2r} \right] - \frac{d}{2} \sqrt{4r^2 - d^2}$$

Therefore, the volume of material required to fill the volume beneath the tool in time  $\Delta t$  is

$$V_{req} = z_{eff} \left( \pi r^2 - 2r^2 \text{ArcCos} \left[ \frac{v\Delta t}{2r} \right] - \frac{v\Delta t}{2} \sqrt{4r^2 - (v\Delta t)^2} \right)$$

where  $z_{eff}$  is the effective depth of penetration of the feedstock material into the stirred zone.

The volume of material delivered to the interface through the feedstock is

$$V_{del} = \frac{\Delta z}{\Delta t} A_{cross}$$

where  $\Delta z/\Delta t$  is the measured rate of position change of the feedstock pushrod, and  $A_{cross}$  is the cross-sectional area of the feedstock itself ( $90.7 \text{ mm}^2$ ). When  $V_{del} = V_{req}$ , there is adequate material delivered to the tool-workpiece interface for the run to proceed successfully. To evaluate this equality, the value of  $z_{eff}$  must be determined. Process data for an Al5083/Al5083 process run in which the tool was translated at  $2.5 \text{ mm/min}$  is shown graphically in Figure 3.14.

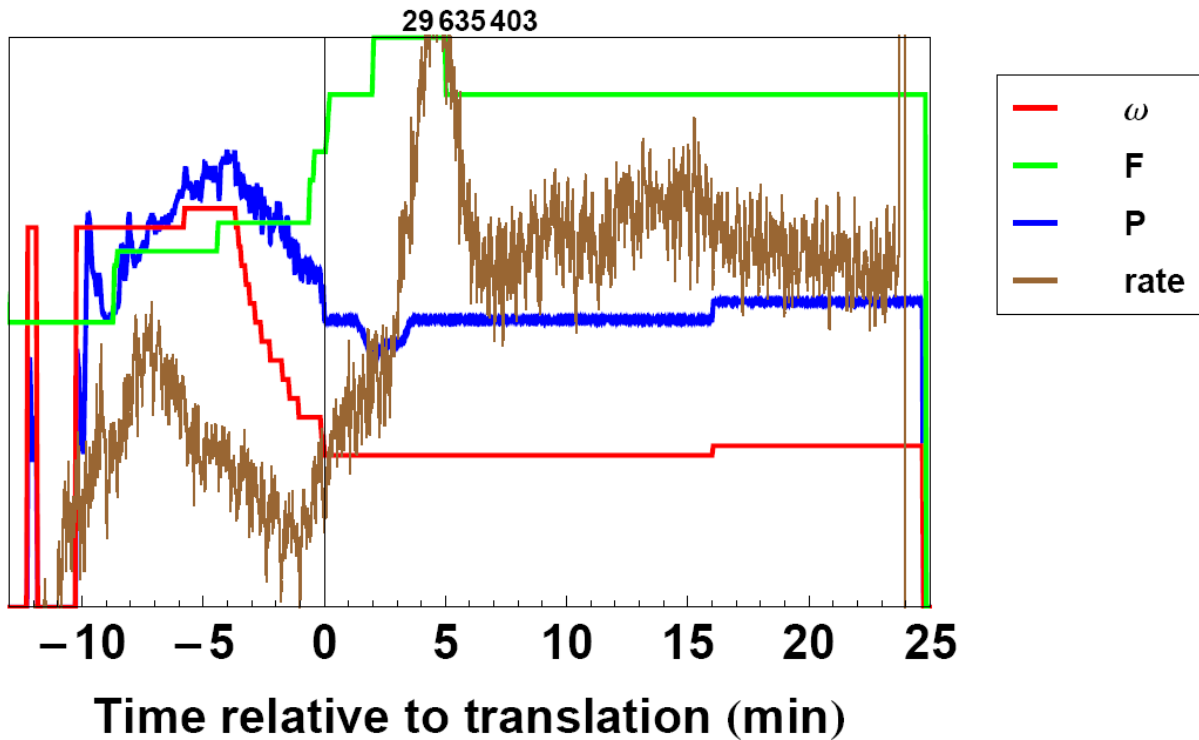


Figure 3.14 Process parameters for Al5083 run with  $v = 2.5\text{mm/min}$

The deposited track for the run shown in Figure 3.14 exhibited incomplete, shallow voids that did not penetrate the entire thickness of the deposition layer. The  $z_{\text{eff}}$  was calculated by equating the volume of material delivered to that required for a 2.5 mm/min translation speed. A value of 2.7 mm for  $z_{\text{eff}}$  yields values of  $V_{\text{del}}$  that are in close agreement with  $V_{\text{req}}$ . Figure 3.14 shows the normalized volume of material delivered to the bead using a  $z_{\text{eff}}$  value of 2.7 mm.

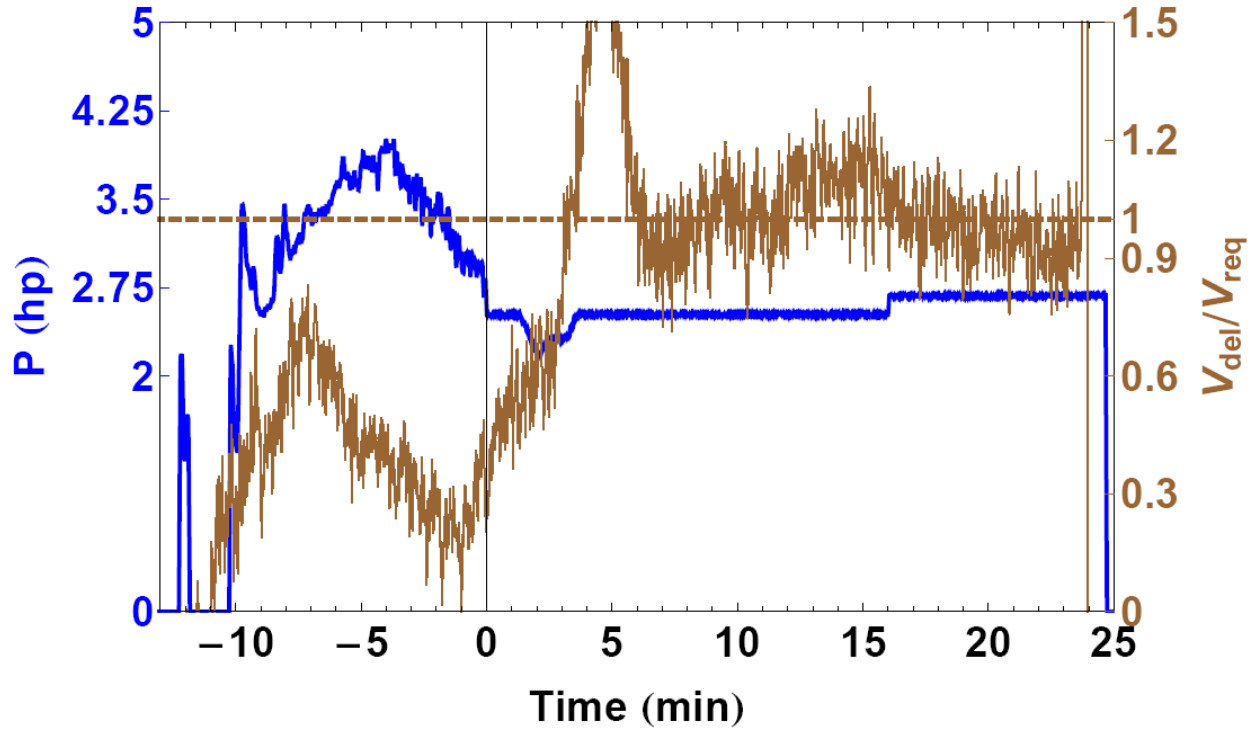


Figure 3.15 Volume of material delivered to bead normalized by effective depth of 2.7 mm for an Al5083/Al5083 process run with tool translation of 2.5 mm/min.

Since typical welds display mechanically affected zones on the order of 3 – 4 mm in depth (see Section 4.2.3), an effective feedstock penetration depth of 2.7 mm makes physical sense. Such a depth implies that the majority of the mechanically effected zone is material supplied from the feedstock, but that the workpiece material does play a role in supplying material to the stir zone. Normalization of empirical data from other runs shows that an estimate of 2.7 mm for  $z_{eff}$  of gives  $V_{del}/V_{req}$  ratios that are characteristics of the success of runs.

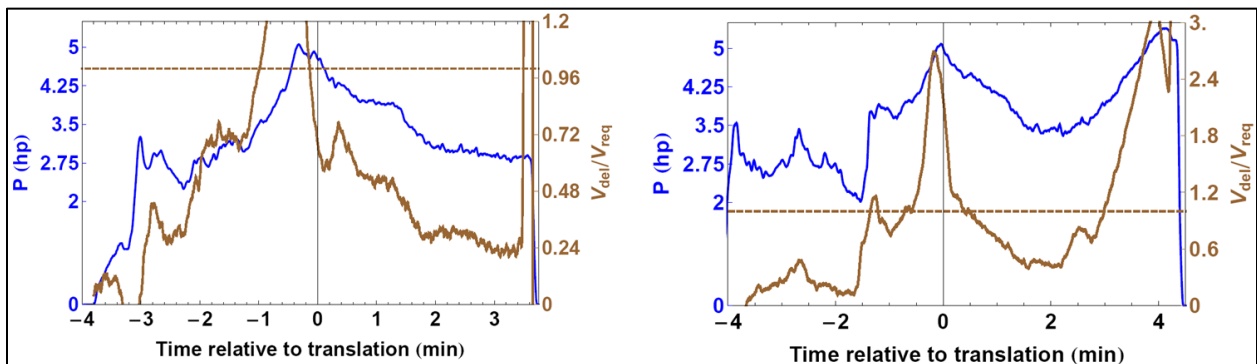


Figure 3.16 Examples of runs in which inadequate material was delivered to interface when  $z_{eff} = 2.7$ mm, resulting in incomplete deposition layers

The data in Figure 3.16 represent cases in which  $V_{del}/V_{req}$  was significantly less than unity with  $z_{eff} = 2.7$  mm. Neither of these runs exhibited continuous, void-free deposition layers. The

track in Figure 3.16b showed recovery after void formation towards the end of the run, corresponding to a value of  $V_{del}/V_{req}$  greater than unity. Contrast the data shown in Figure 3.17 for two successful runs to those in Figure 3.16. The  $V_{del}/V_{req}$  ratio remains greater than unity throughout the entire translation phase for both process runs shown in Figure 3.17.

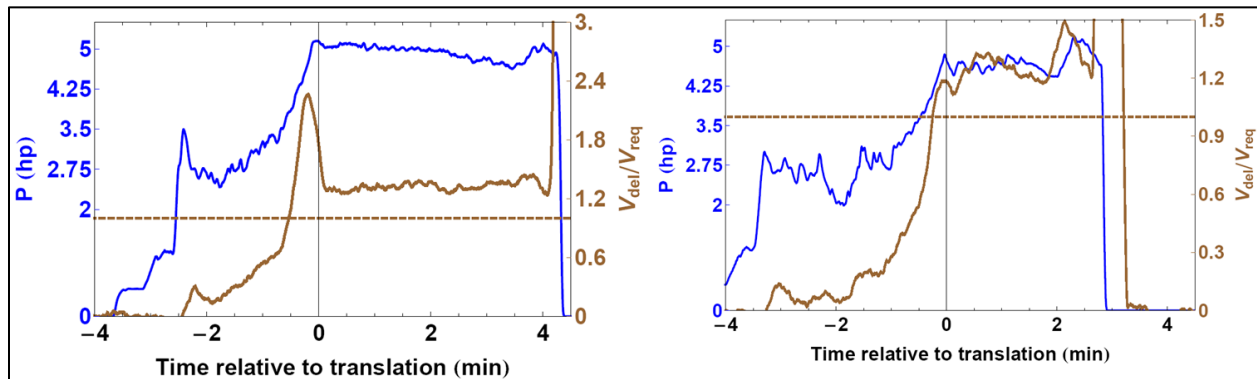


Figure 3.17 Examples of runs in which an excess of material was delivered to interface when  $z_{eff} = 2.7\text{mm}$ , resulting in successful depositions

### 3.2.4.3 Dependence of average steady-state horsepower on material

Under steady-state operation, assuming adequate material delivery to the interface, the average horsepower of the system depends on the properties of both the feedstock and the workpiece. Figure 3.18 shows typical steady-state horsepower delivered to the system for different feedstock/workpiece material combinations. Typically, an Al6061/Al6061 run requires approximately 4.5 – 5 hp, while an Al5083/Al5083 run requires  $\sim 3.15$  hp. A limited set of experiments was performed to explore horsepower requirements for mixed systems. It was found that the Al6061/Al5083 run required 3.85 hp and the Al5083/Al6061 run required slightly less power at 3.55 hp. The steady-state power requirements suggest that the properties of the feedstock material might influence the power requirements to a slightly higher degree than does the workpiece material. The dependence of horsepower on material type can be understood qualitatively by examining the energy required to deform the materials to fracture ( $36 \text{ J/m}^3$  for Al6061 vs.  $52 \text{ J/m}^3$  for Al5083). The toughness of a material acts to influence the amount of frictional heat required to maintain an adequate temperature in the bead material.

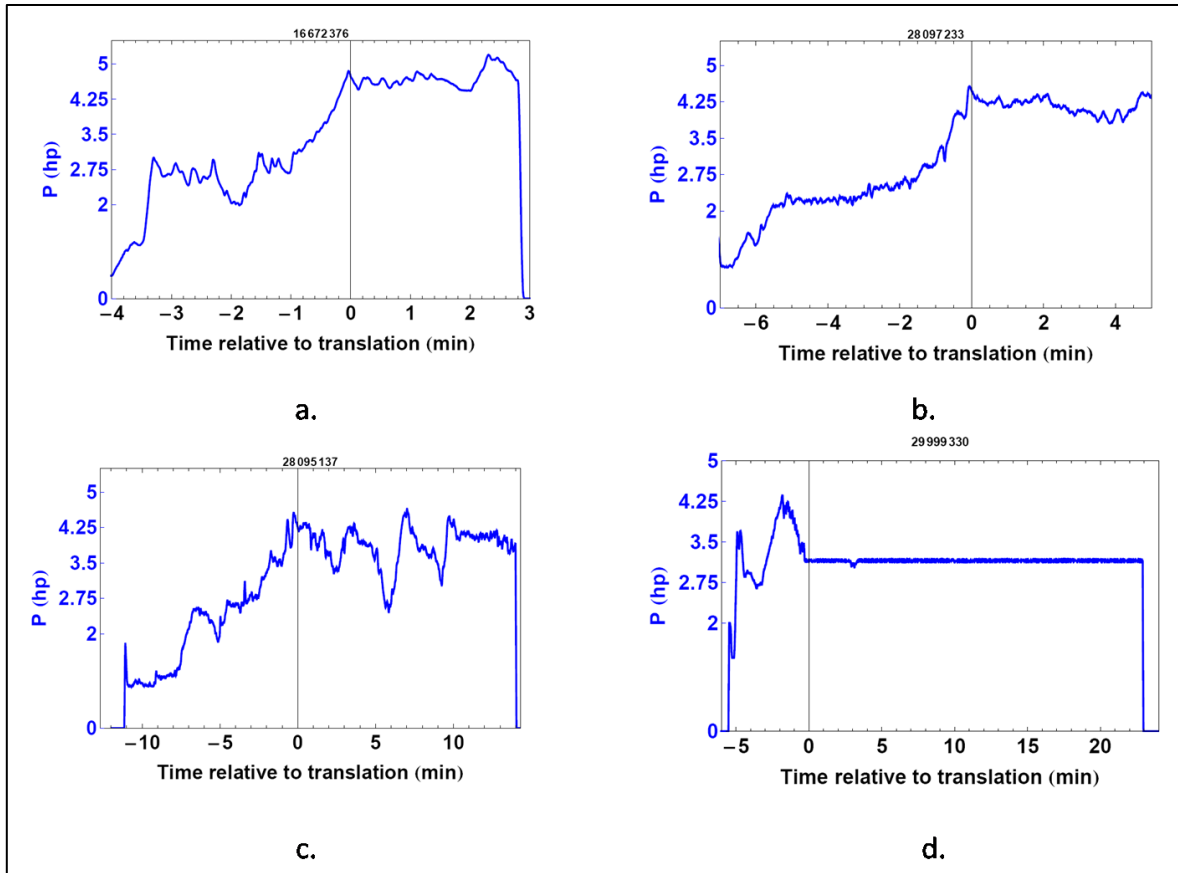


Figure 3.18 Graphs showing steady-state horsepower requirements for a. Al6061/Al6061, b. Al6061/Al5083, c. Al5083/Al6061, and d. Al5083/Al5083

### 3.2.4.4 Dependence of instantaneous horsepower on rate of feedstock delivery

While the average power required to maintain a bead depends on the material type, the instantaneous power depends predominantly on the rate of feedstock delivery. Figure 3.19 shows sample graphs from runs in which a change in the rate of material delivered to the bead resulted in changes in horsepower delivered to the system. In Figure 3.19a, the change in feedstock rate at  $t = 2$  min is followed closely by a sharp increase in horsepower of nearly the same shape. The slight lag in time between the change in rate and horsepower is a good illustration of the causal relationship between the two. Typically, changes in a  $V_{del}/V_{req}$  ratio much less than unity result in large swings in horsepower, while changes in  $V_{del}/V_{req}$  near unity have small changes in horsepower (compare Figure 3.19a to Figure 3.19b).

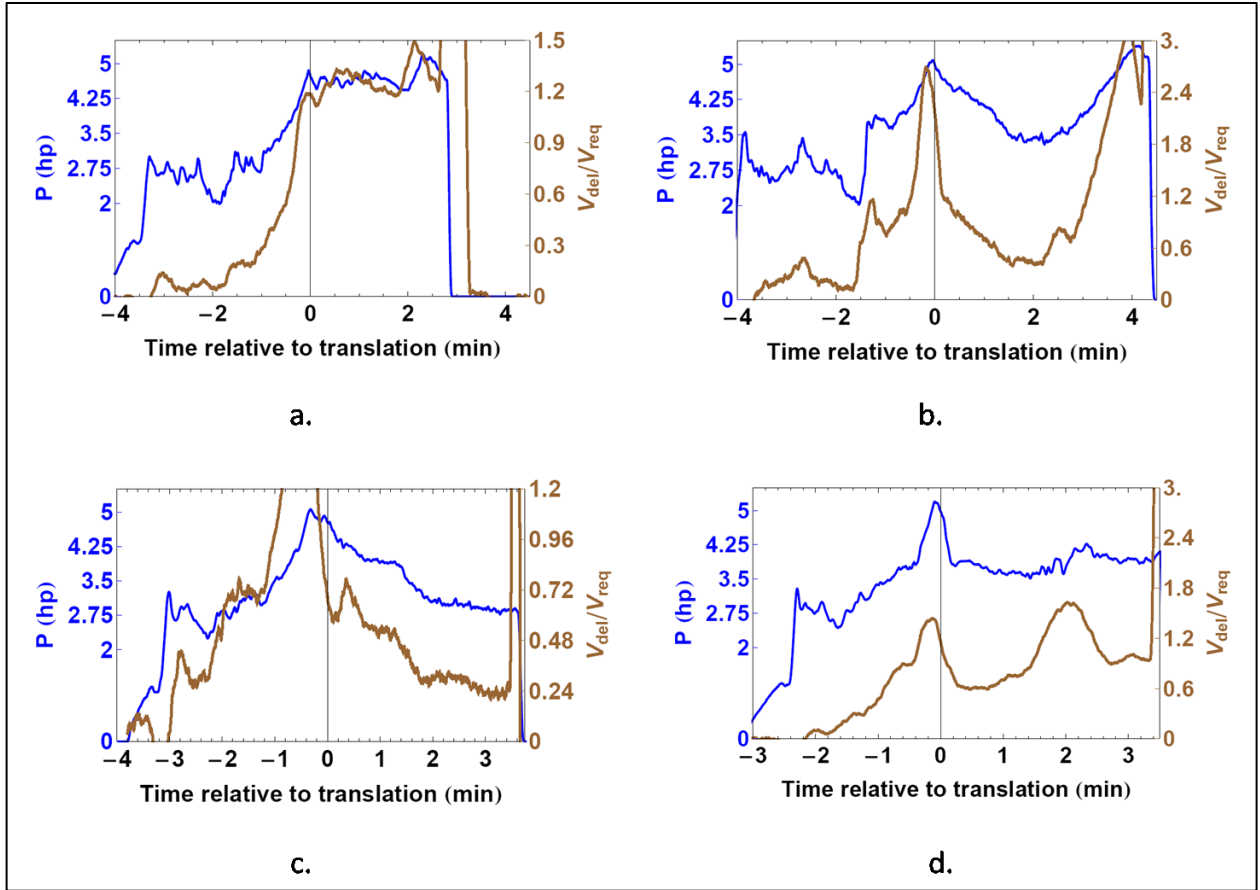


Figure 3.19 Graphs showing relationship between changes in feedstock delivery rate and instantaneous horsepower

### 3.2.4.5 Effect of feedstock force on material delivery

The rate of material delivery is, to a certain degree, dependent on the force applied to the backside of the feedstock. For the Al5083/Al5083 run shown in Figure 3.20, the tool was rotated at 3000 rpm and translated across the surface at 5 mm/min. Once the bead has formed ( $t = 0$ ), the material delivery rate is directly proportional to the force applied to the feedstock in the when the force exceeds 1100 N.

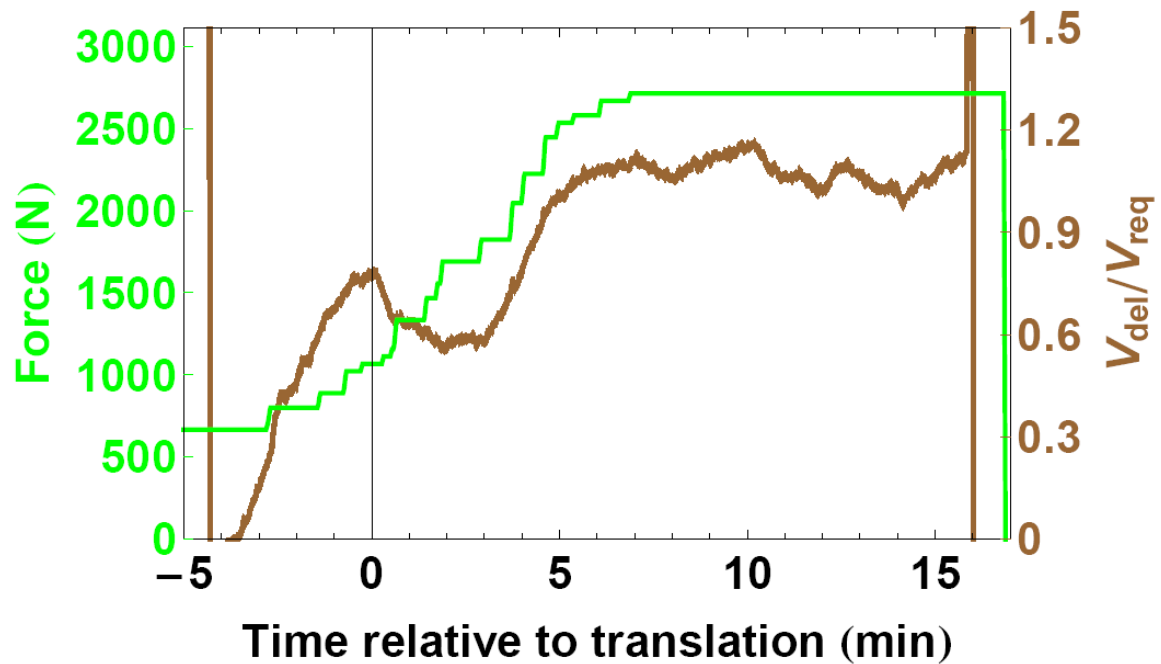


Figure 3.20 Force applied to feedstock and resulting material delivery rate

Figure 3.21 shows data curves for Al6061 stirred onto Al6061. The rotational frequency is included with the force and feedstock for the runs to exclude possible contributions of rotational rate on feedstock delivery. Figure 3.21 shows that the rate of material delivery is often very sensitive to the applied force. However, the data also show that changes in force do not always correspond to changes in delivery rate. There is a trend for a proportional relationship between force and rate, but the sometimes the system will either respond slowly or not at all to changes in force.

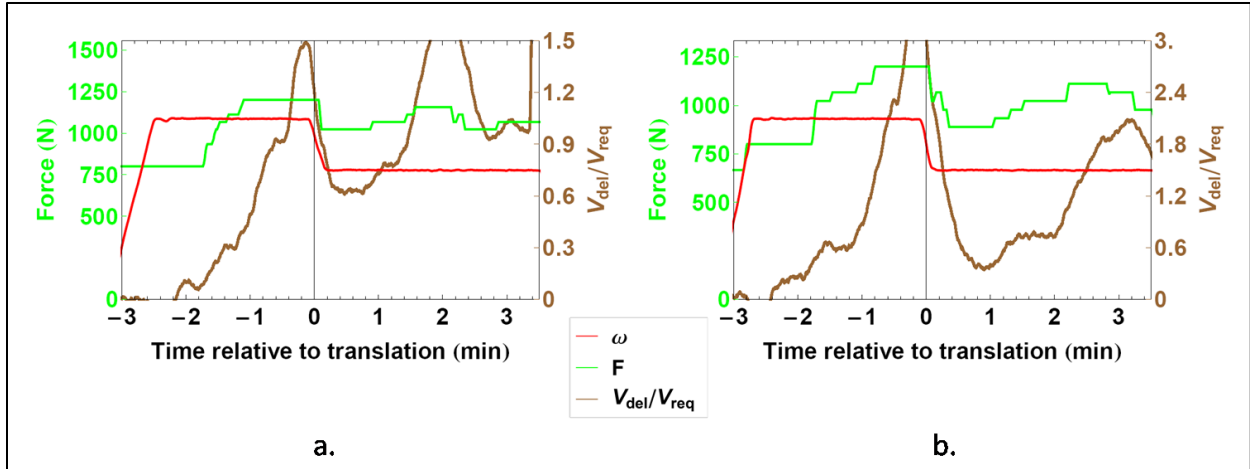


Figure 3.21 Graphs depicting dependence of feedstock rate on applied force at constant rotation

Two important deviations from the force to rate proportionality are insufficient force and sticking of the feedstock. Experiments have shown repetitively that the feedstock delivery system has a built-in resistance to motion. A force of less than 675 N applied to the feedstock pushrod will result in a failed process run regardless of the rotational or translational speed of the tool. The reason for the failure is demonstrated in Figure 3.22. Once the force drops to  $\sim 675$  N, the rate of material delivered drops off sharply. In Figure 3.22b, the data show that once the force is increased from 675 N to 890 N, the material delivery rate recovers, delivering more than adequate material to the bead.

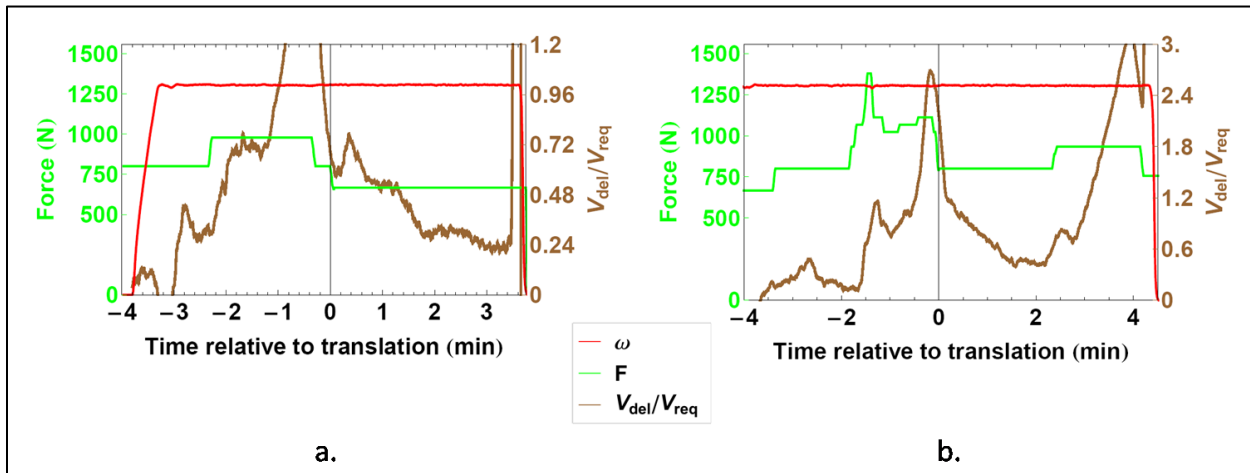


Figure 3.22 Process run data demonstrating feedstock built-in resistance to motion of  $\sim 675$  N

For the run presented in Figure 3.20, the feedrate increases proportionally with force for  $f > 900$  N. A more typical scenario when performing FSF depositions is shown in Figure 3.23. Typically an applied force of greater than 1500 N results in the stock binding within the spindle, as shown at time  $t > 1.6$  minutes in Figure 3.23a or  $t \cong 6$  minutes for Figure 3.23b. Application

of excess force to the stock without an outlet at the workpiece end of the tool causes the stock to deform inside the spindle. Instead of extrusion through the tip, there is compaction within the volume defined by the bead, the interior walls of the spindle, and the feedstock pushrod. To remove the stock from the tip, forces greater than those available to the pneumatic pushrod cylinder (~8800 N) are required.

The problems of built-in resistance to motion and feedstock binding could be overcome by changing the feedstock delivery system from a force-controlled drive to a position controlled drive with the capability to deliver much more force. Furthermore, by assuming an effective penetration of 2.7 mm, the feedrate could be coupled to the position of the feedstock pushrod to optimize the amount of material delivered to the system. The current force-driven system either delivers far too much feed (resulting in excess flash) or inadequate material to maintain a bead (resulting in a voided layer).

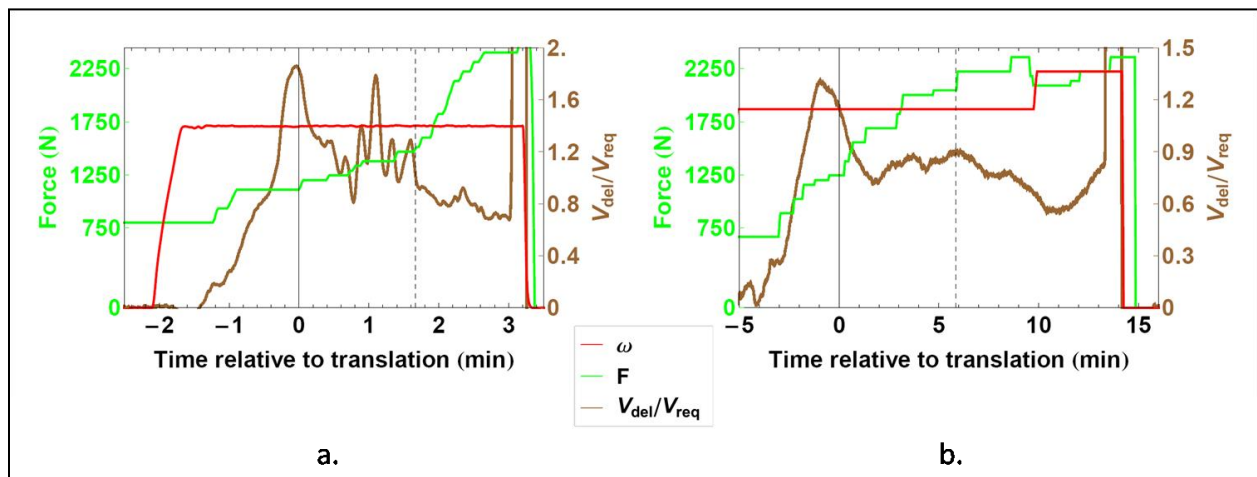


Figure 3.23 Decrease in feedrate with increasing force signifying stock stuck in spindle a. for Al6061/Al6061 run, and b. for Al5083/Al5083 run

### 3.2.4.6 Effect of rotational speed on system horsepower and feedrate

The instantaneous horsepower required by the system is most directly a function of the rate of material delivery. Applied feedstock force is the most direct parameter in terms of manipulation of the rate of material feed. The rotational frequency plays an important, albeit secondary, role in both the horsepower requirements of the system as well as the rate of material feed.

As discussed in Section 3.2.1, the rotational frequency effects the horsepower requirements prior to the bead formation. To explore the effect of horsepower on the steady-state phase of the process, a sample was processed without tool translation. The tool was inserted and the system driven through bead formation. The force on the feedstock was held constant at 1025 N throughout the duration of the run.

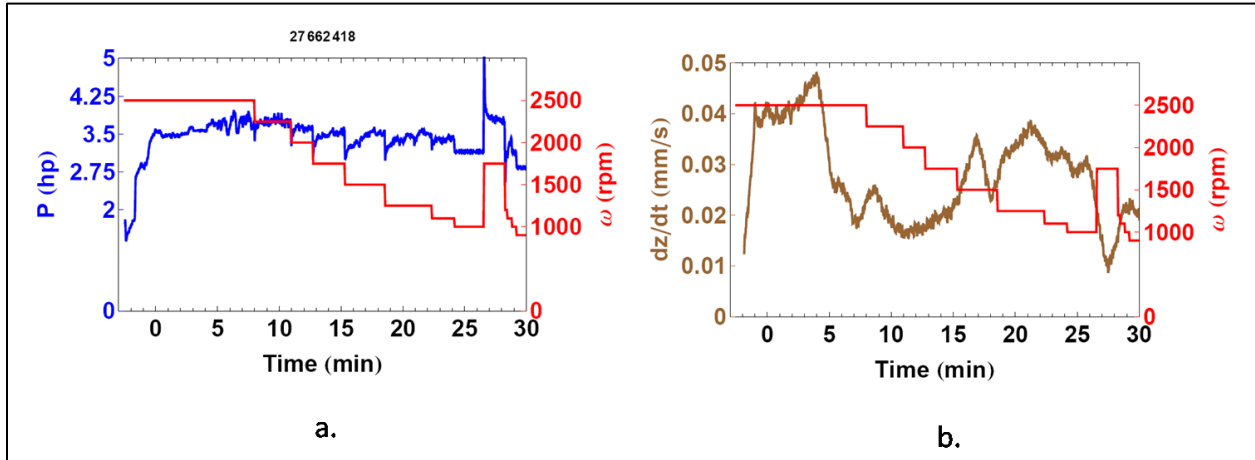


Figure 3.24 Horsepower and feedrate at various rotational frequencies without tool translation

Figure 3.24a shows an instantaneous change in horsepower requirements for changes in rotational frequency, suggesting an inverse dependence of power on  $\omega$ . Examination of the feedrate delivery for the same time period clouds the interpretation of the  $\omega$ -hp relationship. The fact that the step change in  $\omega$  results in an instantaneous change in power verifies that there is indeed a causal relationship, especially in light of the fact that a step change in  $\omega$  does not always result in a step change in material feedrate. A closer examination of the step change in  $\omega$  at time  $t = 26.5$  minutes (Figure 3.25) shows that the increase in  $\omega$  results in a gradual decrease in feedrate and a simultaneous increase power. Since power requirements depend on both rotational frequency and feedstock delivery rate, and since the magnitude of the effect of feedrate alone on power are not well understood, the magnitude of the effect of the rotational speed on power requirements is difficult to quantify.

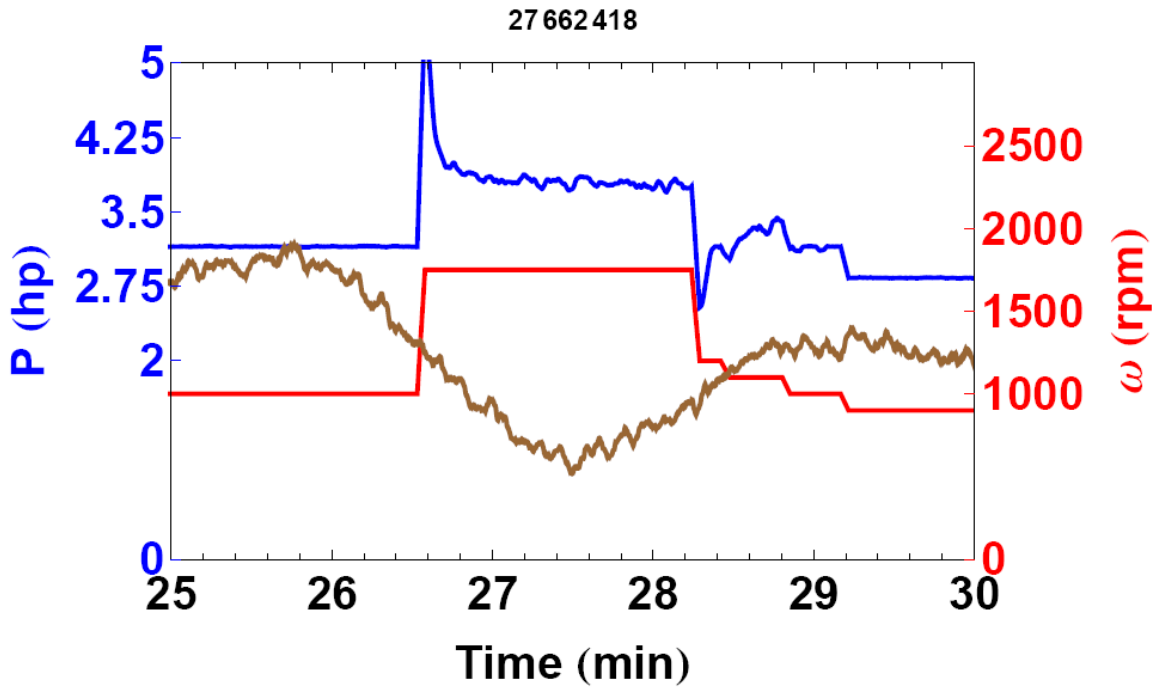


Figure 3.25 Focus on step change in  $\omega$  for stationary process run

The inverse relationship between rotational speed and material feed is illustrated in Figure 3.26. Both samples are Al5083/Al5083 runs in which the tool was translated at 2.5 mm/min. The steady-state rotational speed of Figure 3.26a is 1000 rpm while that of Figure 3.26b is 3000 rpm. The data show that at an  $\omega$  of 3000 rpm and force of 1470 N, the rate of feedstock delivery is less than half of a run at  $\omega$  of 1000 rpm and force of 1200 N.

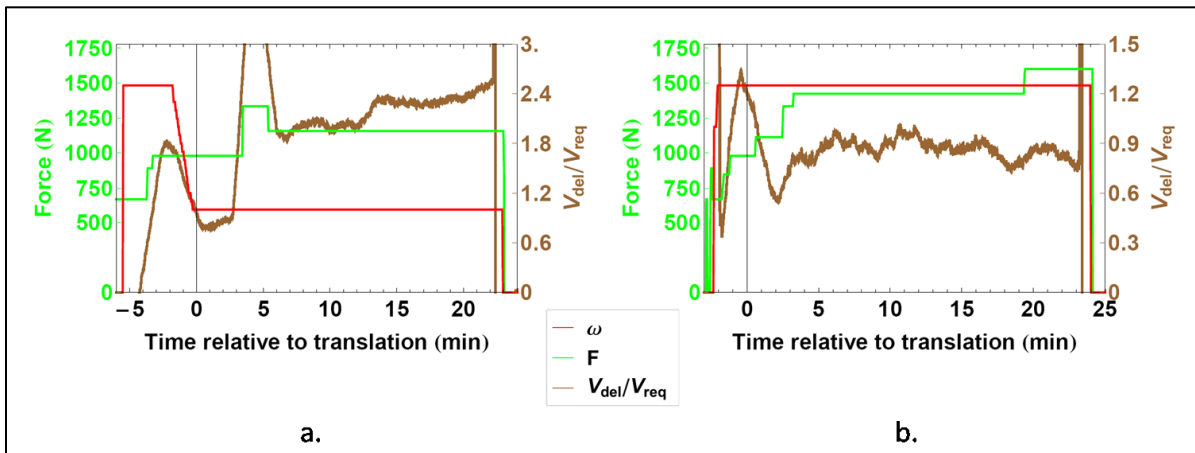


Figure 3.26 Comparison of feedrate of runs with different rotational frequencies

## 4 Effects of Processing Parameters on Microstructure and Hardness

### 4.1 General description of friction stir fabrication microstructures

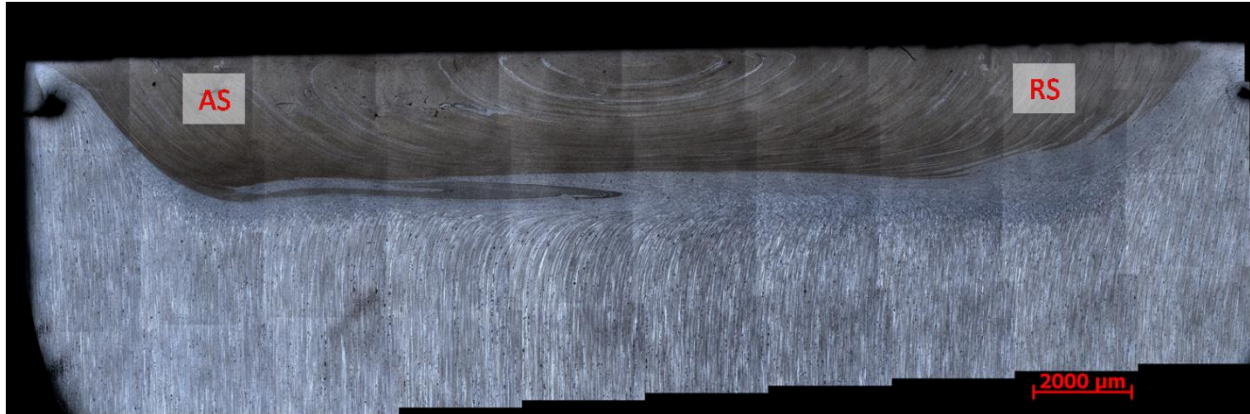
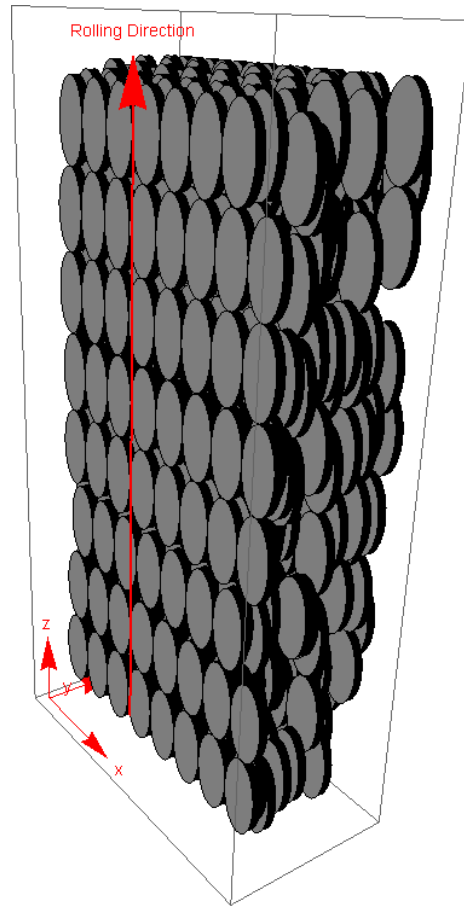


Figure 4.1 Cross sectional micrograph of a typical process run (Al5083/Al5083,  $\omega = 1200$  rpm,  $v = 2.5$  mm/min)

Figure 4.1 shows a micrograph of the cross section of a typical Al5083/Al5083 FSF sample. The sample in was processed with a rotation frequency of 1200 rpm and a translation rate of 2.5 mm/min. The micrograph shows the onion structure at the upper center portion of the weld. The onion structure is typical to FSW materials and corresponds to a dynamically recrystallized microstructure (see Section 1.1). Directly surrounding the weld nugget lies a halo of thermomechanically affected material, referred to as the. The remainder of the material in the workpiece lies in the HAZ, and while this material does not experience direct deformation from the tool or bead, FSF processing acts to significantly weaken the material (Section 4.3).



**Figure 4.2 Schematic representation of grain morphology in strain-hardened Al5083, as well as directions relative to FSF processing**

The Al5083 used as the workpiece material for the FSF experiments has undergone work hardening to achieve the correct temper. As such, there is an orientation to the grains within the alloy corresponding to the rolling direction of the strain-hardening process (Figure 4.2). All of the substrates used in the FSF experiments were oriented in the same direction. The direction of rolling of the as-received material is towards the top of the workpiece (tool/workpiece interface). A cross-sectional view of a processed piece will therefore display the narrow dimension of the grains (the y-z plane in Figure 4.2). This orientation of the workpiece facilitates visualization of the motion of the grains in the TMAZ halo surrounding the weld nugget.

#### 4.1.1 Description of the weld nugget

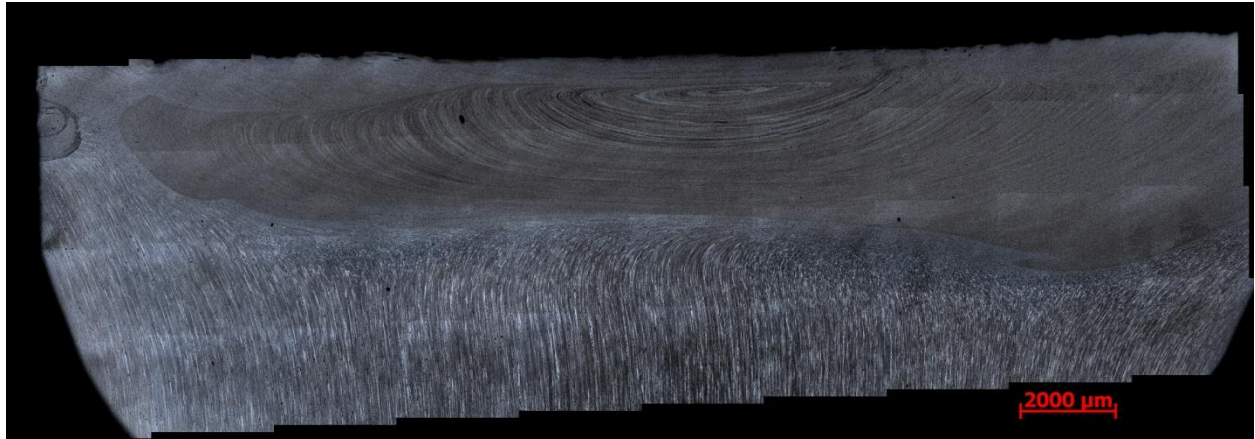


Figure 4.3 Micrograph of the cross section of a FSF workpiece (Al5083/Al5083,  $\omega = 1000$  rpm,  $v = 2.5$  mm/min)

Characteristic to all friction stirred materials is a region called the onion (see Figure 4.3). The onion shows strata of deposited material within the dynamically recrystallized zone. The cross-sectional view (Figure 4.3) coupled with a longitudinal view of the weld nugget (Figure 4.4) show that each layer of the onion is actually a series of shells deposited by the motion of the tool.

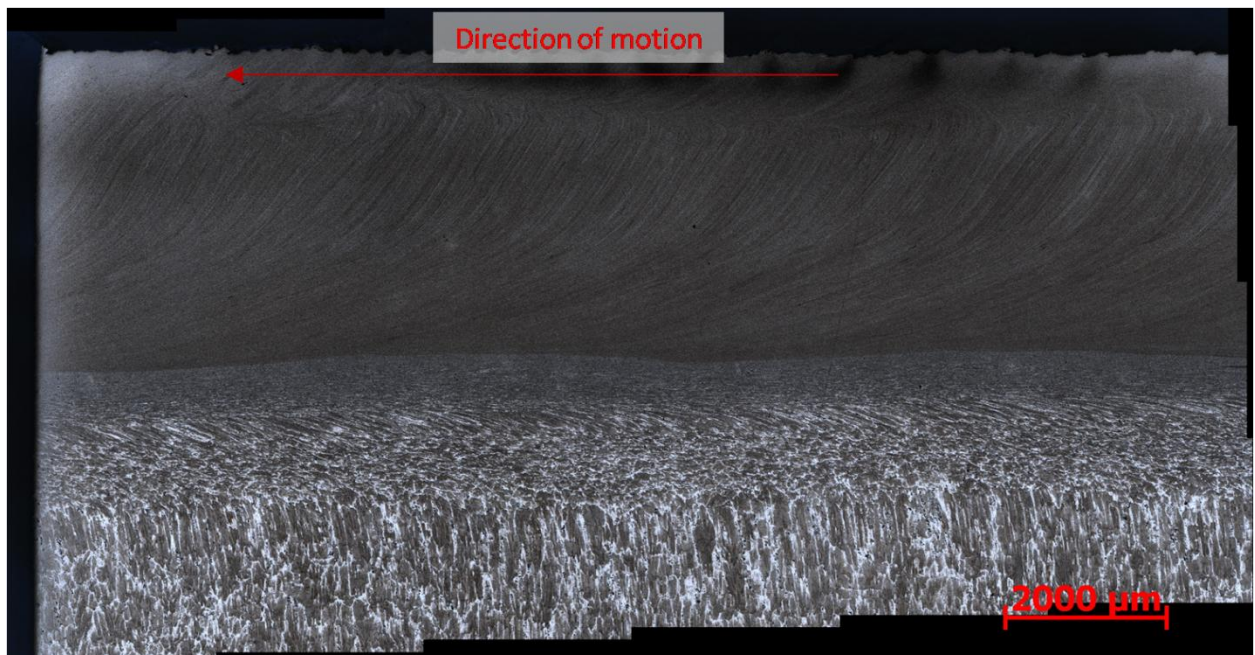
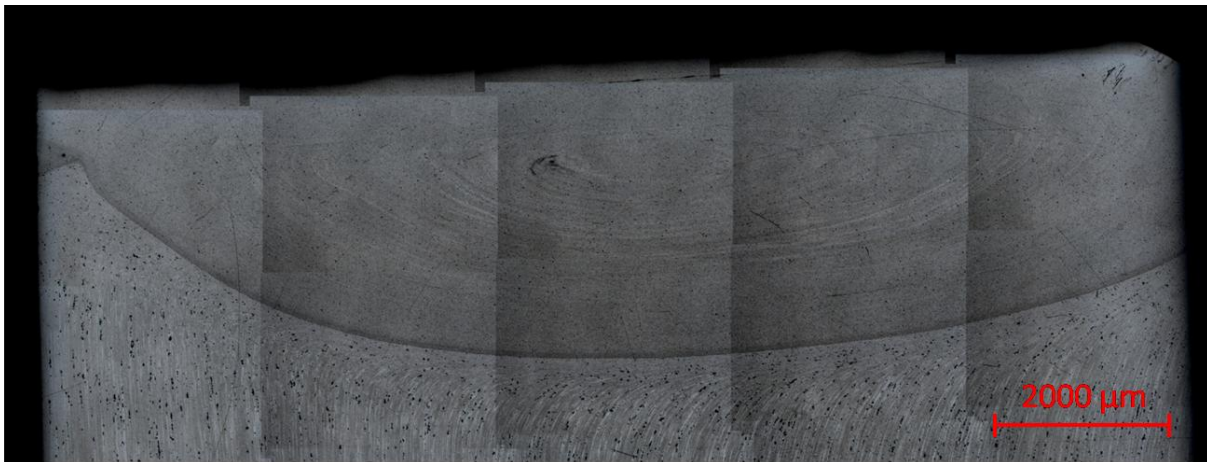


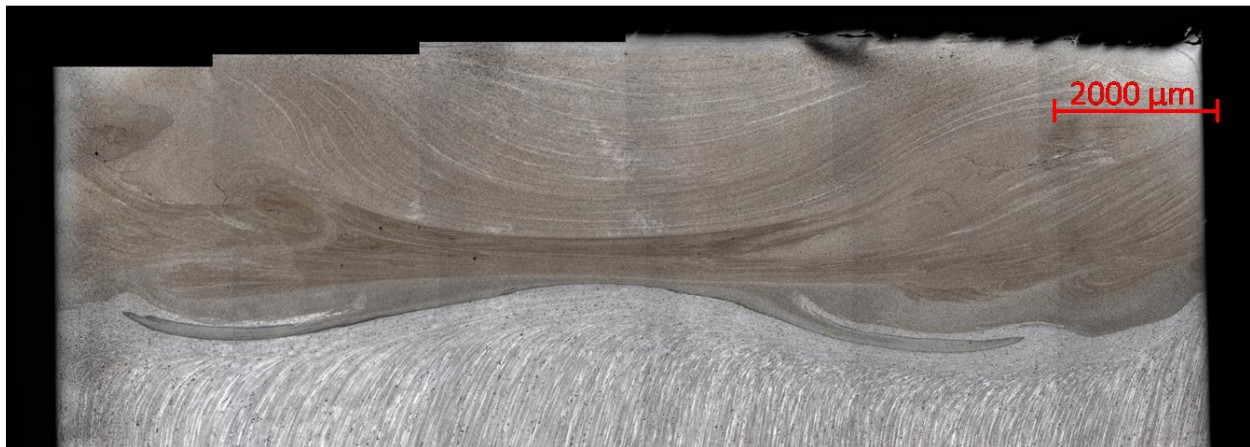
Figure 4.4 Longitudinal view of advancing side (AS) of weld (Al5083/Al5083,  $\omega = 1000$ ,  $v = 2.5$  mm/min)

As the tool rotates, material is moved from the front of the stir zone, around to the retreating side of the processed area, and finally to the advancing side of the tool. As the tool is

translated along the workpiece, successive shells of material are deposited. The actual shape of the material being moved by the weld at any given time is ellipsoidal in nature. A planar cross-section of the weld show materials deposited at different times. The outer layers of the weld union were deposited prior to those at the interior. Figure 4.5 shows a set of micrographs that show cross sections of only the earliest portions of the weld nuggets. Figure 4.5a shows a cross-section of a sample taken at a position such that only the very beginning of the onion formation is shown. Figure 4.5b shows a cross-section of a processed piece taken at a slightly later time so that the early part of the onion is shown along with material that was displaced during the initial formation of the onion.



a.



b.

Figure 4.5 Cross-sectional micrographs of FSF runs showing early, incomplete onion formation a. Al5083/Al5083,  $\omega = 1200$ ,  $v = 2.5\text{mm/min}$ , b. Al5083/Al5083,  $\omega = 1000$ ,  $v = 2.5\text{mm/min}$

During the deposition of each shell layer of the onion, the material within that layer experiences extreme plastic deformation and undergoes dynamic recrystallization. The result

of the mechanical deformation is a highly refined microstructure. Traditional metallographic etchants used for aluminum alloys were inadequate in resolving the grain structure of processed Al6061 or Al5083. Keller's etch, a two-step NaOH/HF etch, and a CrO<sub>3</sub> etch were evaluated as possible candidates for microstructural evaluation of the weld nugget. Figure 4.6 shows an optical micrograph of the interface between the stirred region (top of image) and the TMAZ (lower portion of the image) of an Al6061 sample. The sample was mounted, polished, and stained using Keller's etch. Neither the grains within the stir nor those within the TMAZ were visible optically.

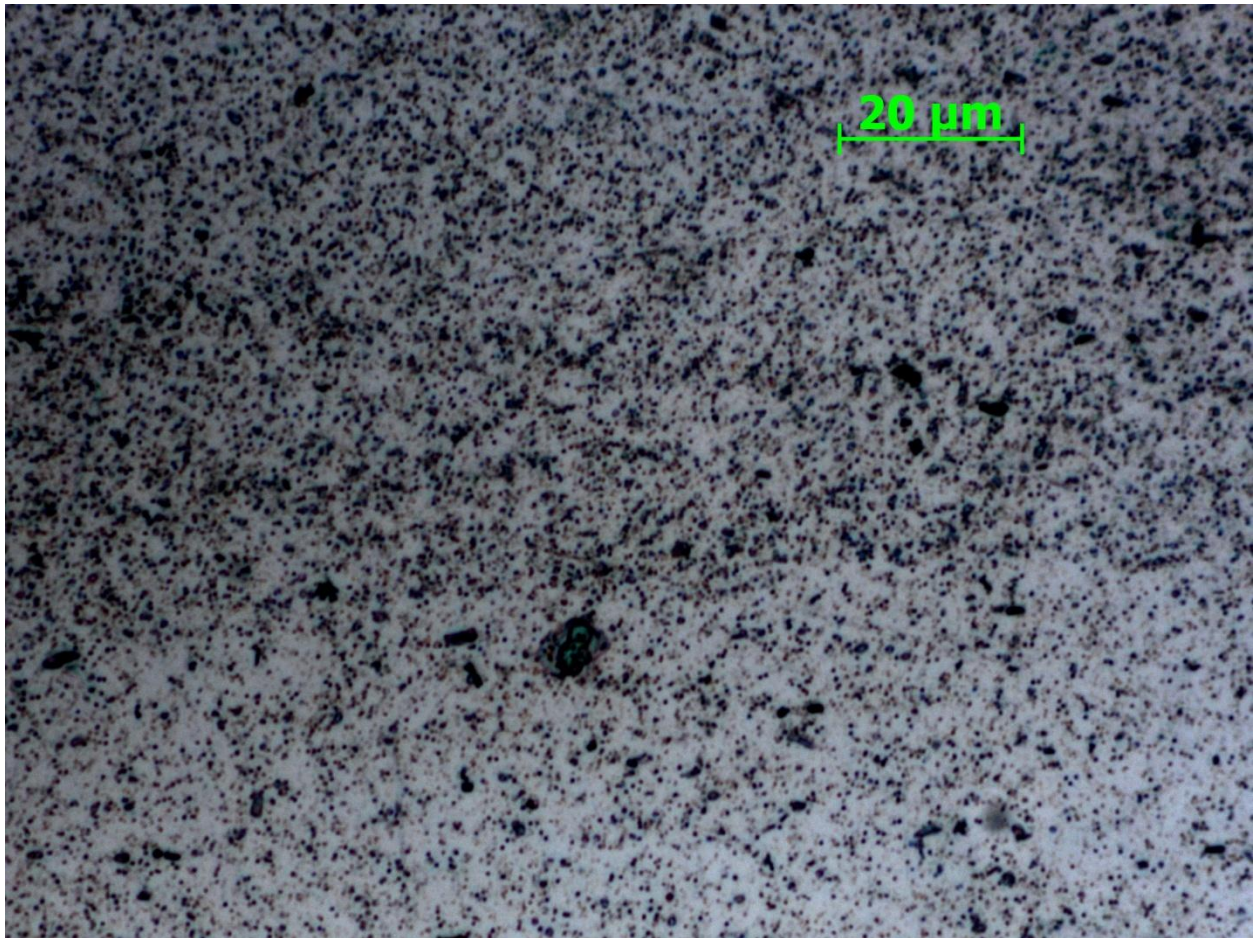


Figure 4.6 Optical micrograph of Al6061/Al6061 sample (2100 rpm, 25.4 mm/min) stained with NaOH

Scanning electron microscopy (SEM) was also used in an attempt to image grains within the sample. Figure 4.7 shows an SEM image of the interface between the DRZ and the TMAZ on the advancing wide of the weld nugget of an Al6061/Al6061 sample etched using a two step, NaOH/HF etch. While the grains bordering the DRZ are visible, the etchant is too aggressive in attacking the material within the stirred region. Since there is not adequate energy provided to the system subsequent to processing to anneal the damage incurred during the dynamic recrystallization, there is a great deal of residual strain and damage in the material of the

stirred zone. The strained state of the stirred region results in an increase in chemical reactivity of the material during etching. Furthermore, as the damage lies within the grains of the aluminum, the etch pits do not follow the grain boundaries, hindering microscopy.

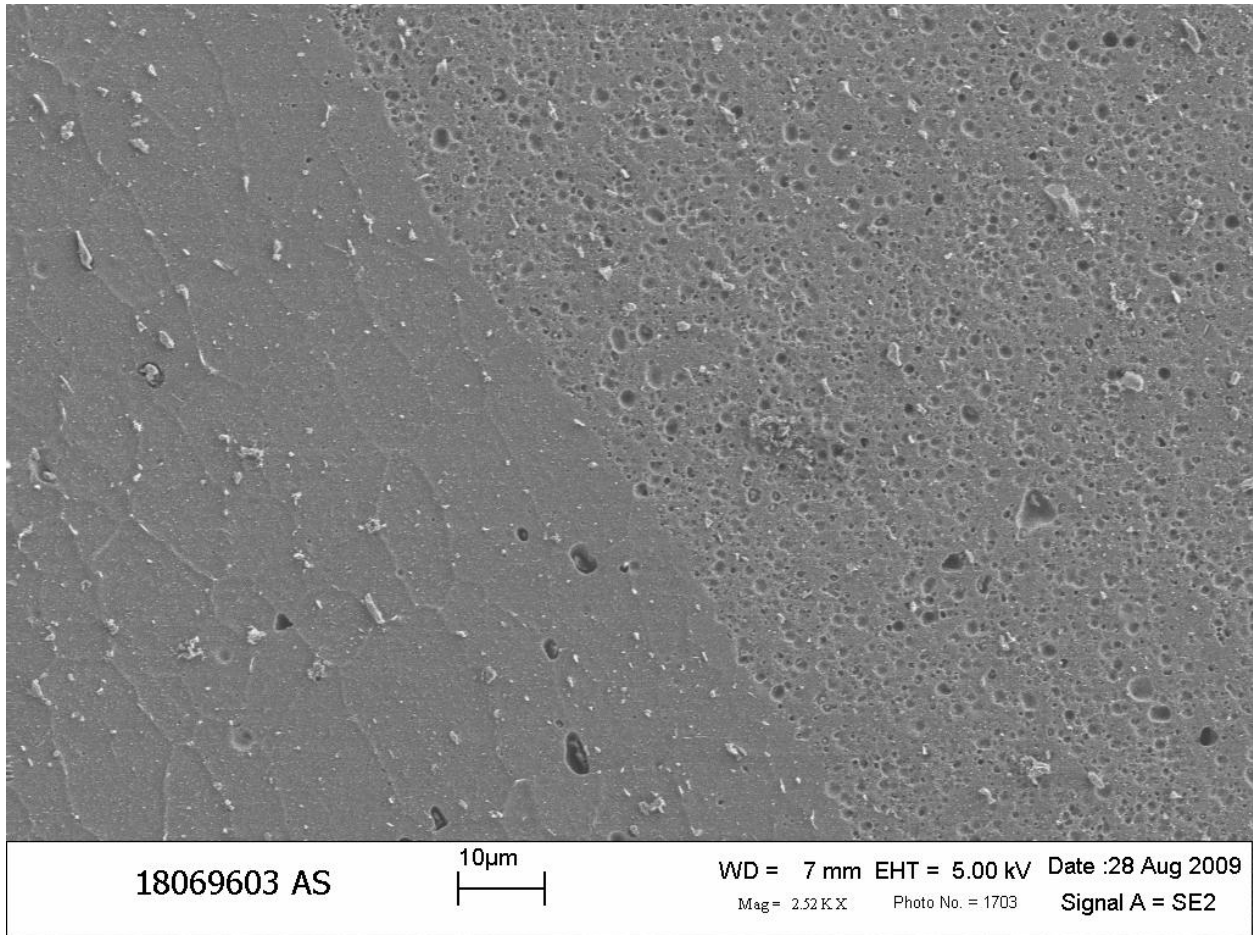


Figure 4.7 SEM image of advancing side nugget-to-TMAZ interface of sample (Al6061/Al6061,  $\omega = 2100$ ,  $v = 21$  mm/min) etched using two step NaOH/HF etch

Backscatter electron imaging (BSE) of the stirred region also proved ineffective. An Al5083/Al5083 sample was mounted and polished for EBSD analysis (with a final polish of 0.05  $\mu\text{m}$  colloidal silica on a vibrational polisher). Prior to EBSD analysis, backscattered electron analysis was performed in a field emission SEM. Figure 4.8 shows a BSE image of the region of the interface between the stirred region and the TMAZ region on the advancing side of the weld. Grains were not visible in any of the zones of the processed sample.

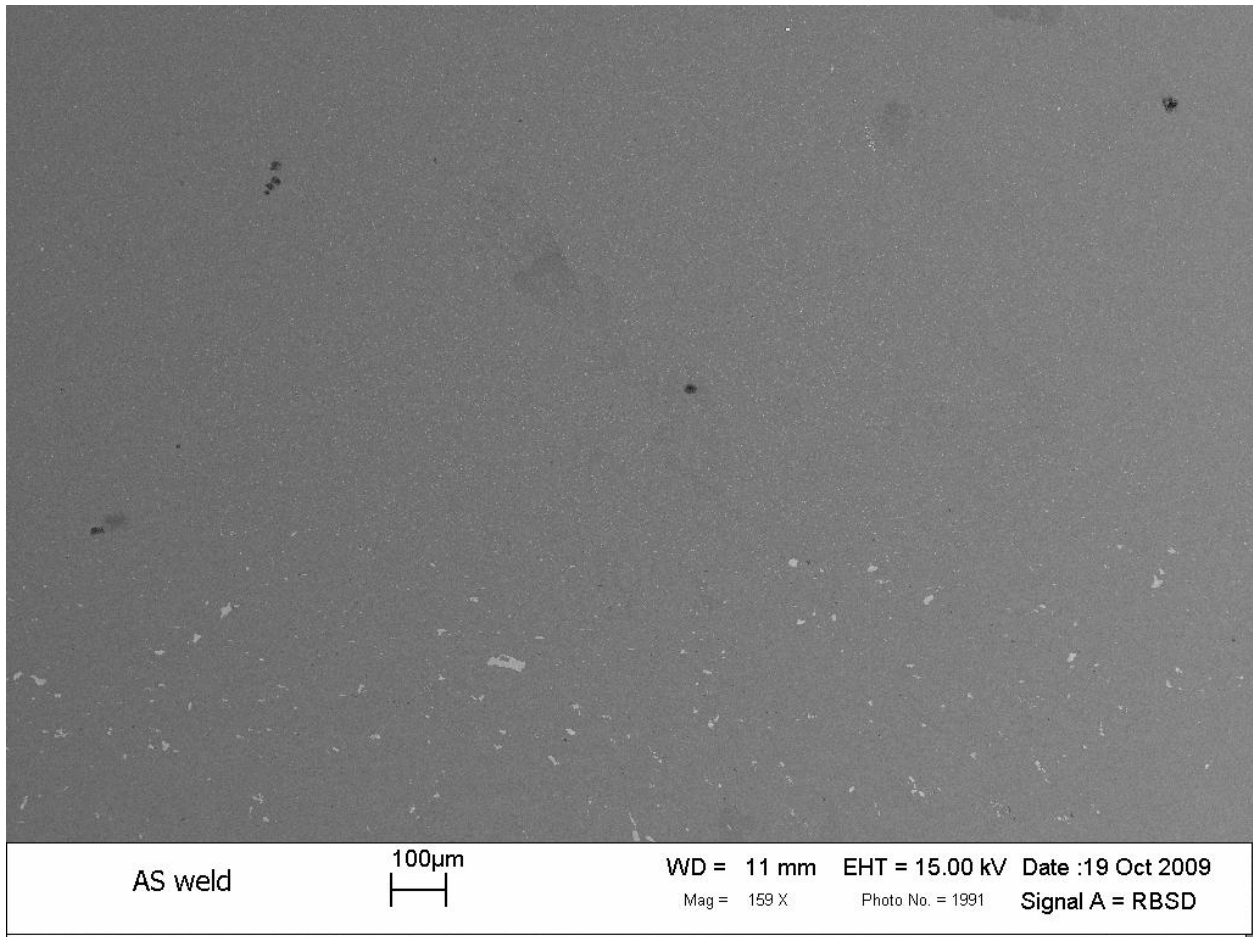


Figure 4.8 BSE image of the interface between the TMAZ and the DRZ of a FSF processed sample (Al5083/Al5083,  $\omega = 2500$  rpm,  $v = 2.5$  mm/min)

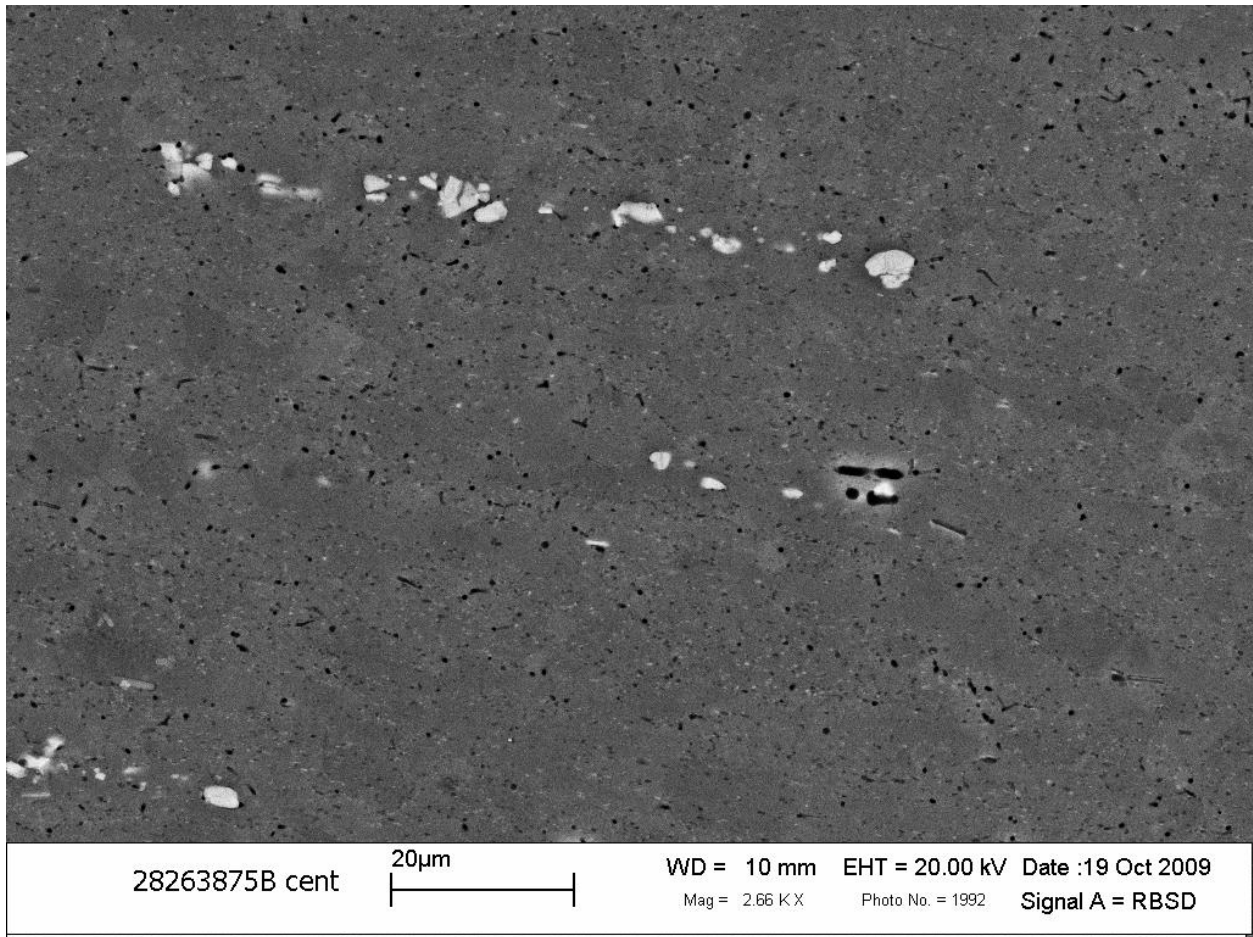


Figure 4.9 BSE image of Al5083/Al5083 sample etched with Keller's etch (Al5083/Al5083,  $\omega = 1000$  rpm,  $v = 3.56$  mm/min)

Figure 4.9 shows that after etching with Keller's etch, even grains within the TMAZ were extremely difficult to image. The image shows regions of different contrast that could highlight different grains within the aluminum.

While SEM imaging was not successful in resolving grains to allow for grain size determination in the different zones of the processed materials, it did allow for visualization of the effects of processing on the insoluble phases within the alloy. The as-received Al5083 shows long chains of insoluble intermetallic phases oriented in the direction of rolling (Figure 4.10). These chains can be seen to bend over to run parallel to the interface between the DRZ and the TMAZ (Figure 4.9). Not only are the chains disrupted within the weld nugget, but the insoluble particles are refined from large particles ( $\sim 5 \mu\text{m}$ ) to very fine particles ( $< 1 \mu\text{m}$ ) in the DRZ.

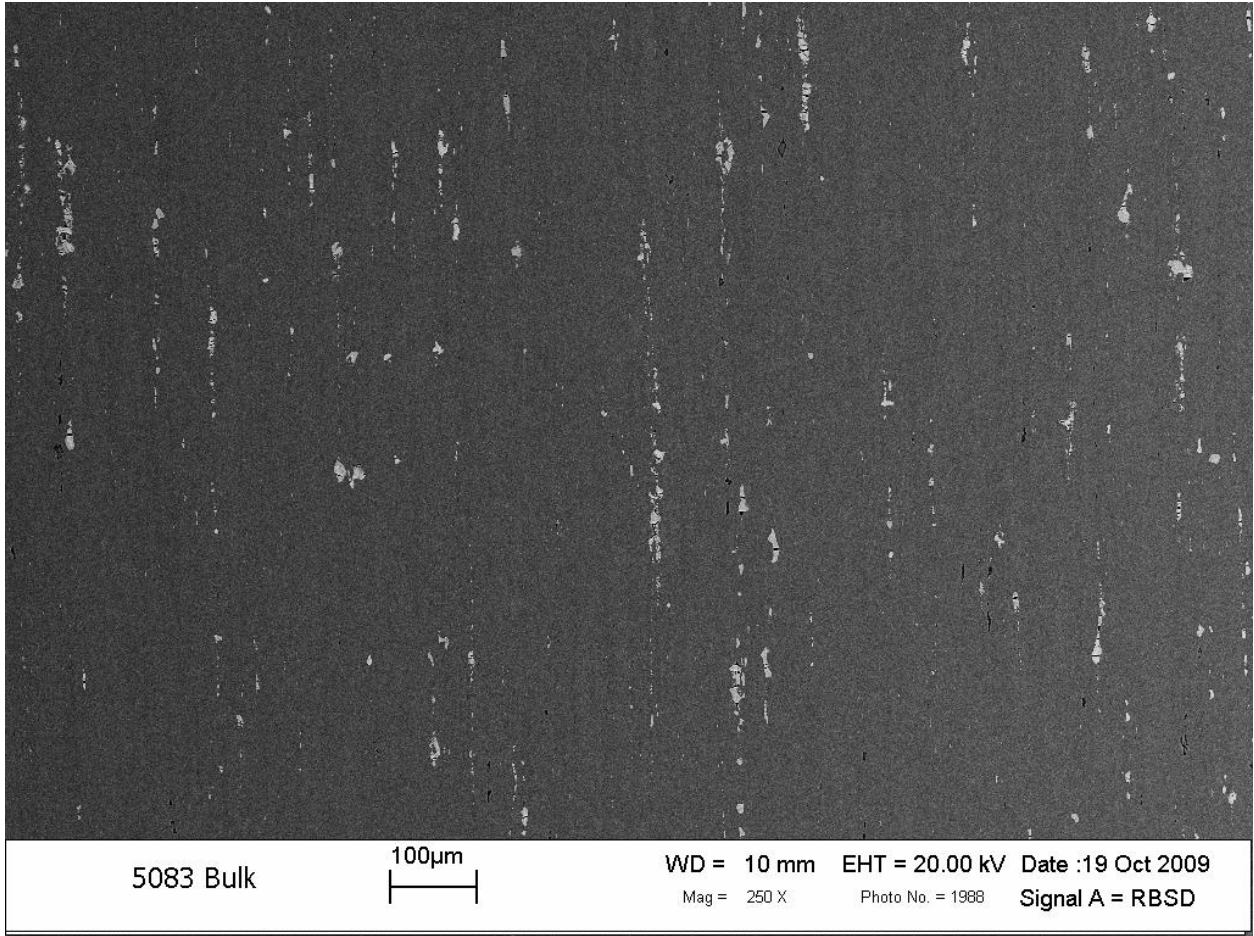
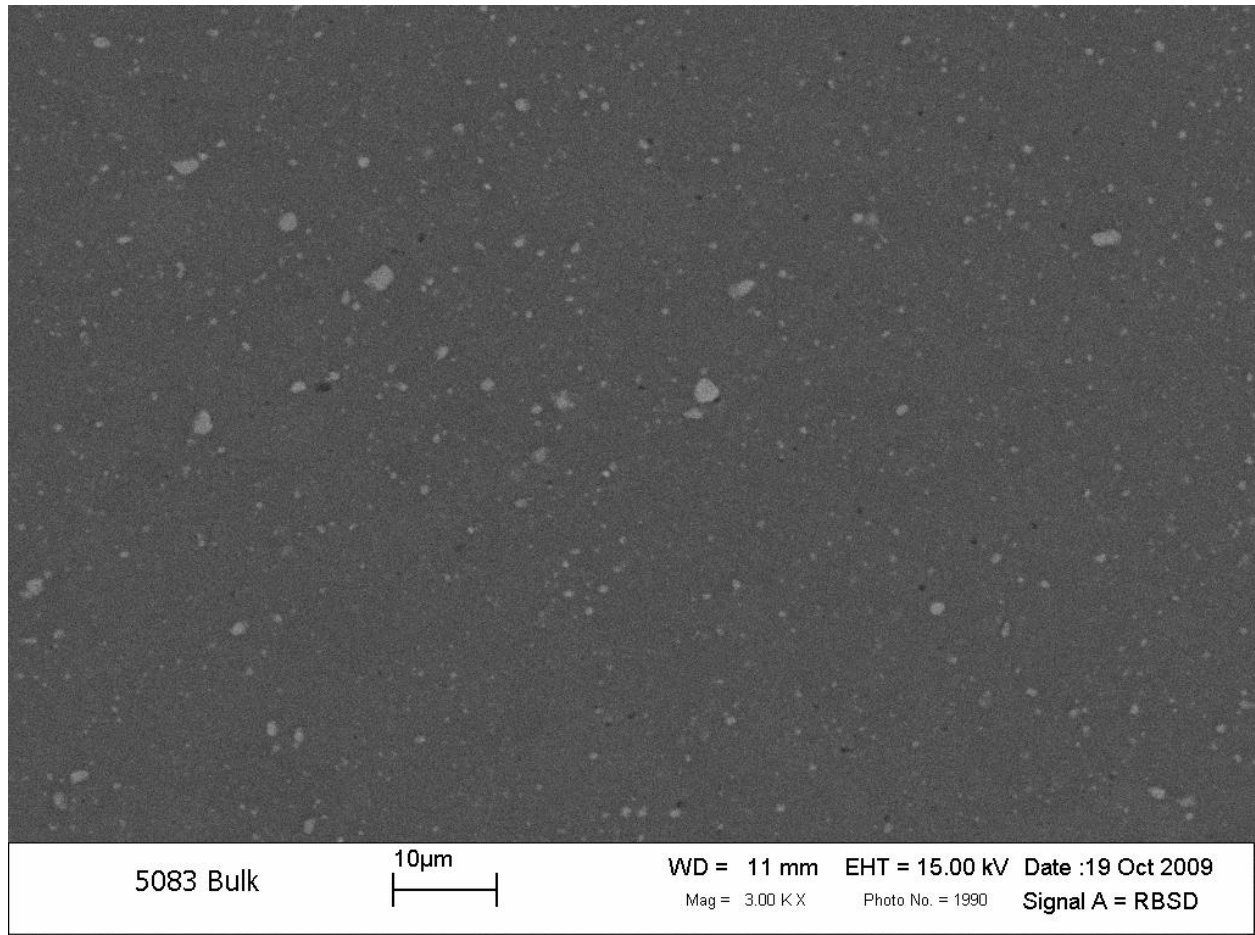
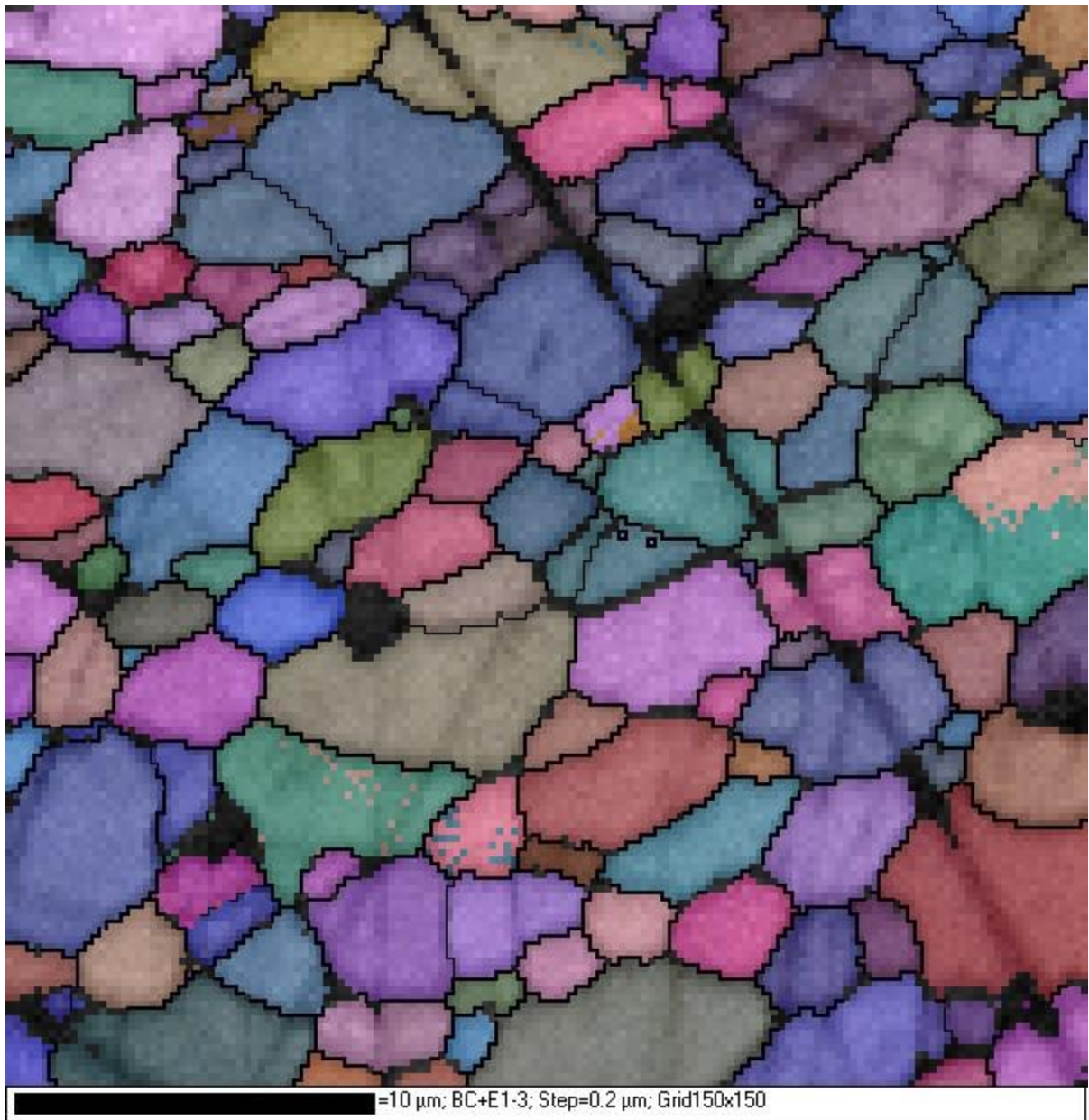


Figure 4.10 Backscatter image of Al5083 prior to processing showing insoluble precipitate chains oriented in the direction of rolling



**Figure 4.11** BSE image of stirred area in Al5083 sample showing refinement of insoluble intermetallic particles (Al5083/Al5083,  $\omega = 2500$  rpm,  $v = 2.5$  mm/min)

In order to resolve the grains within the stirred zone of the processed samples, electron backscattered diffraction (EBSD) was employed. Samples were prepared for EBSD via a rigorous polishing regime. Samples were loaded into a LEO Zeiss 1550 FESEM at 70 degrees to horizontal. SEM images were acquired at acceleration voltages of 20kV, and with working distances between 9 – 12 mm. For the EBSD patterns used in this work, five bands were used for matching with 35 reflectors and a Hough space of 50. Figure 4.12 shows an EBSD grain map from a region within the stirred region of an Al5083 sample ( $\omega = 1000$  rpm,  $v = 2.5$  mm/min). The thicker black lines separating the grains correspond to a difference in orientation between grains of  $10^\circ$ , while the fainter lines are a misorientation of  $2^\circ$ .



**Figure 4.12** EBSD image showing band contrast and Euler space coloring for a region within the advancing wide of a processed Al5083 sample (Al5083/Al5083,  $\omega = 1000$  rpm,  $v = 2.5$ mm/min).

For the sample shown in Figure 4.12, the grain statistics show an average grain size of approximately  $1 \mu\text{m}$ . While the EBSD imaging is an extremely powerful tool for grain size characterization, the time required for sample preparation and imaging make the process inappropriate for a survey of large number of samples with large areas of interest. As will be discussed subsequently (Section 4.3.1), the grain size within the various regions of the processed sample will be determined by correlating hardness values to reported grain sizes for Al5083.

#### 4.1.2 Description of the thermomechanically affected zone

Optical microscopy of processed samples reveals a layer of deformed material that surrounds the stirred area of the weld nugget (Figure 4.13). The halo of thermomechanically affected material extends approximately 1.5 mm into the workpiece beyond the edge of the dynamically recrystallized zone. The material in the TMAZ is subjected to elevated temperatures as well as plastic deformation. Deformation in the TMAZ is not directly due to the motion of the tool itself, but rather due to friction of the material contained in the weld bead. The material shows a gradient in both the orientation and the size of the grains from the bulk to the interface of the TMAZ and the DRZ. Generally, the grains in the bulk of the 5083 have an orientation parallel to the edges of the workpiece (Figure 4.13), with chains of precipitates that parallel the grains (Figure 4.10). The material in direct proximity to the DRZ-TMAZ interface shows grains oriented parallel to the tool/workpiece interface. Furthermore, the precipitate chains become less cohesive as the interface is approached (Figure 4.8).

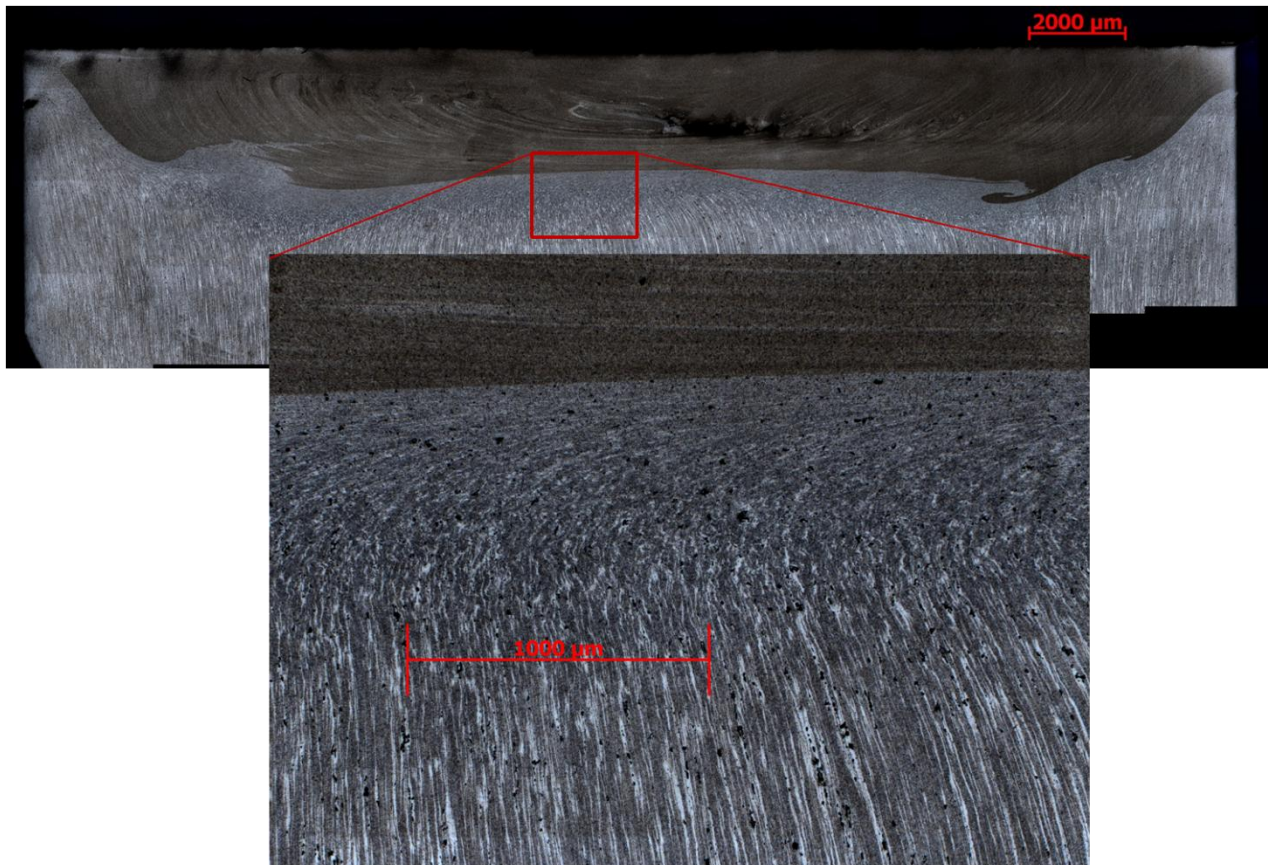


Figure 4.13 Micrograph of cross-section of processed sample with detail of TMAZ halo (Al5083/Al5083,  $\omega = 850$  rpm,  $v = 2.5$  mm/min) prepared with Keller's etch

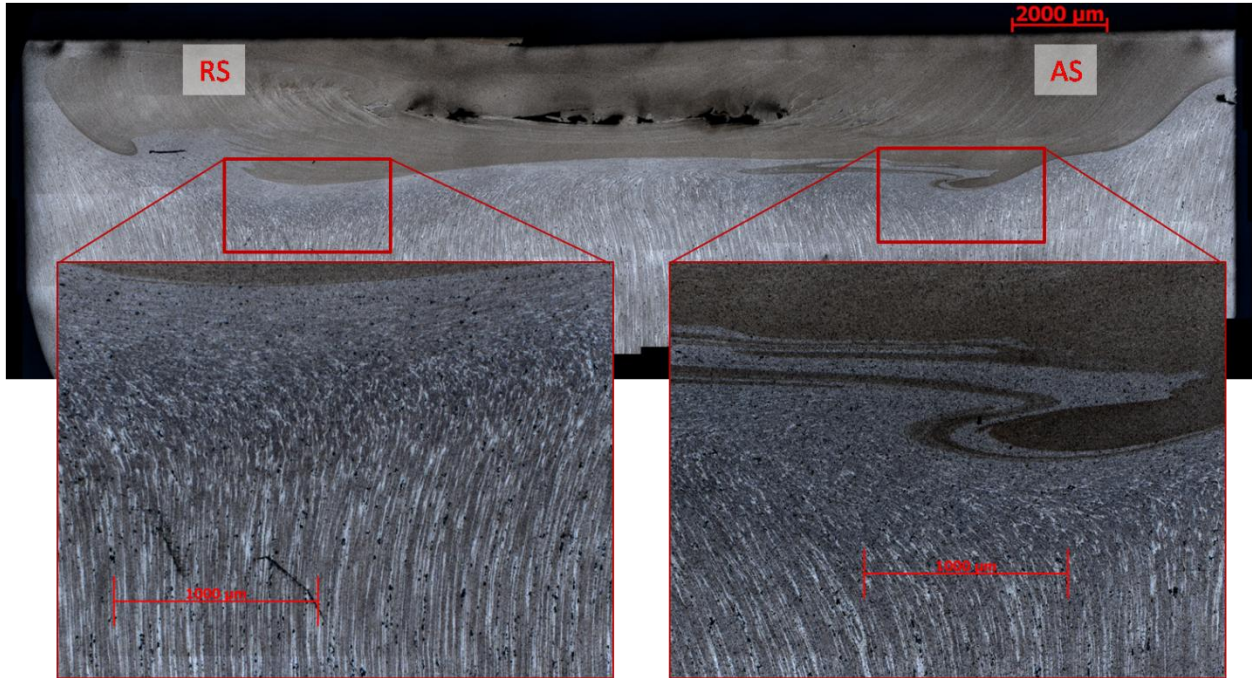


Figure 4.14 Detail of material in TMAZ directly under tool nubs (Al5083/Al5083,  $\omega = 800$  rpm,  $v = 2.5$  mm/min)

As shown in the detail insets in Figure 4.14, the material directly beneath the location corresponding to the tool nubs exhibits characteristic deformation. The material on the outside of the nubs is pushed towards the outside of the workpiece, while the material on the inner side of the nubs is forced towards the center of the workpiece. On the advancing side of the weld nugget, the motion of the tool acts to drive the material downwards in a screw-like motion. The material from the retreating side of the weld is moved towards the advancing side and collides with the material caught in the screw-motion and an advancing side swirl is formed.

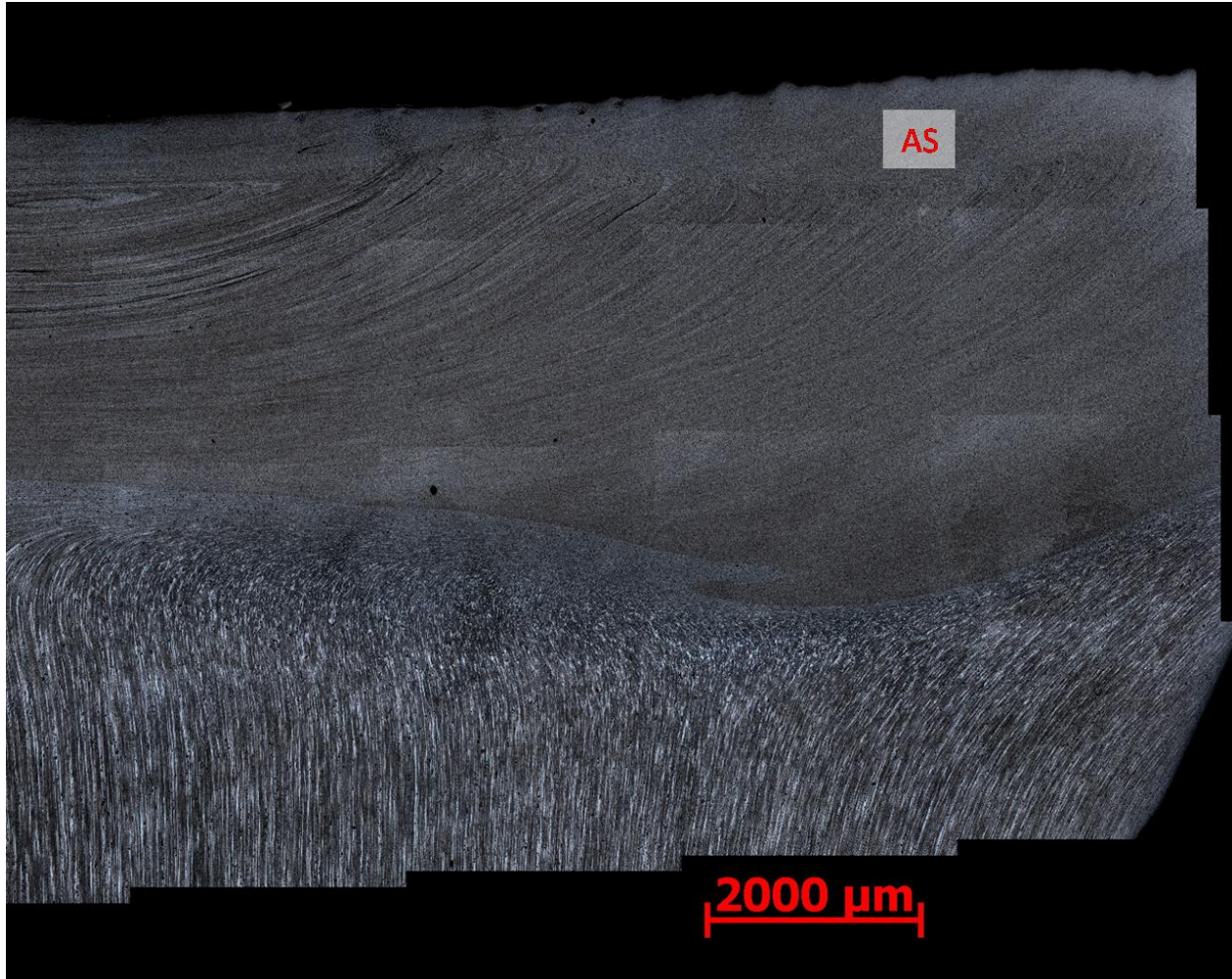


Figure 4.15 Detail of grain motion to accommodate screw motion of weld nugget (Al5083/Al5083,  $\omega = 1000$  rpm,  $v = 2.5$ mm/min)

Further evidence of the screw-like motion arising from the combination of the motion of the tool and movement of material from the retreating side of the weld to the advancing side is shown in Figure 4.15. The grains on the lower-right portion of the sample have been forced out of vertical alignment to accommodate extra material delivered from the weld nugget, while the DRZ extends much deeper into the workpiece on the advancing side than in the center of the weld. The accommodation of feedstock material through via deformation of the sidewall of the workpiece is typical for samples with an excess of feed delivery ( $V_{del}/V_{req} \gg 1$ ) (compare Figure 4.15 ( $V_{del}/V_{req} \cong 2.2$ ) to Figure 4.14 ( $V_{del}/V_{req} \cong 1.0$ )).



Figure 4.16 Longitudinal view of weld nugget and TMAZ underneath nub on retreating side of workpiece (Al5083/Al5083,  $\omega = 1000$  rpm,  $v = 2.5$  mm/min) prepared with Keller's etch

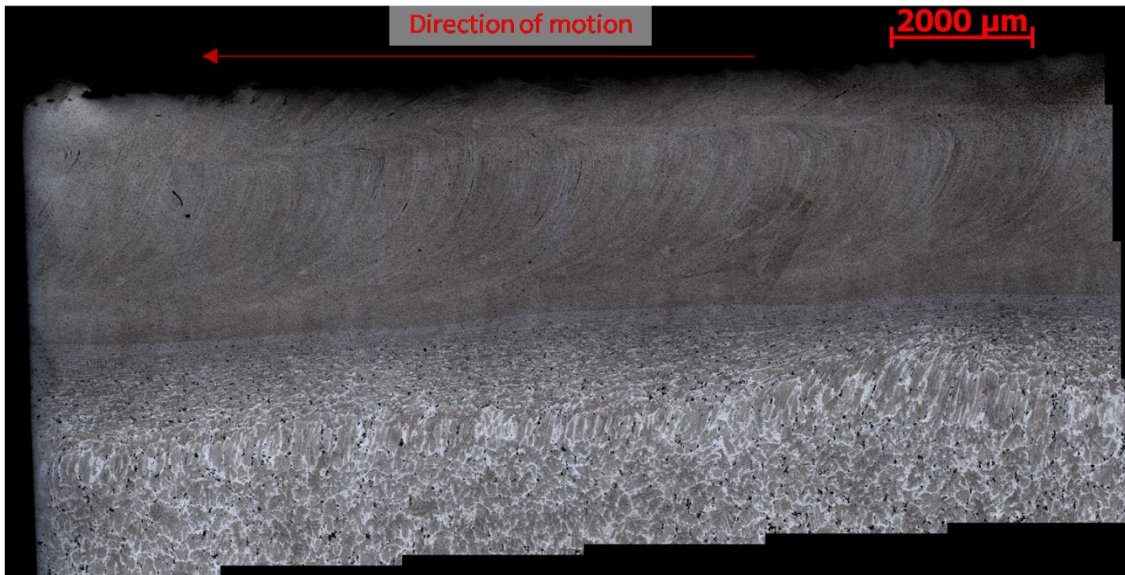


Figure 4.17 Longitudinal view of weld nugget and TMAZ along centerline of workpiece (Al5083/Al5083,  $\omega = 1000$  rpm,  $v = 2.5$  mm/min) prepared with Keller's etch



Figure 4.18 Longitudinal view of weld nugget and TMAZ underneath nub on advancing side of workpiece (Al5083/Al5083,  $\omega = 1000$  rpm,  $v = 2.5$  mm/min) prepared with Keller's etch

Micrographs taken along the length of the weld line (Figure 4.16, Figure 4.17, and Figure 4.18) show that the motion of the material in the TMAZ is complex. On the retreating side of the TMAZ (Figure 4.16), there is a gradual transition from the bulk to the weld nugget. It appears that there is little motion of the material in the longitudinal direction of the workpiece. Under the center and advancing side of the weld there appears a band of grains that have been stretched in the vertical direction. The micrograph of the advancing side of the TMAZ shows complex motion of the material in both the transverse and the longitudinal directions.

Although material in the TMAZ of Al6061 pieces responded well to metallographic etchants (Figure 4.7), grain size within the TMAZ of Al5083 samples proved difficult to image using optical techniques (Figure 4.8, Figure 4.9). In order to gauge the effect of processing on the grain size within the TMAZ, and to keep consistency with imaging done on the DRZ of the weld, the TMAZ was also examined using EBSD analysis.

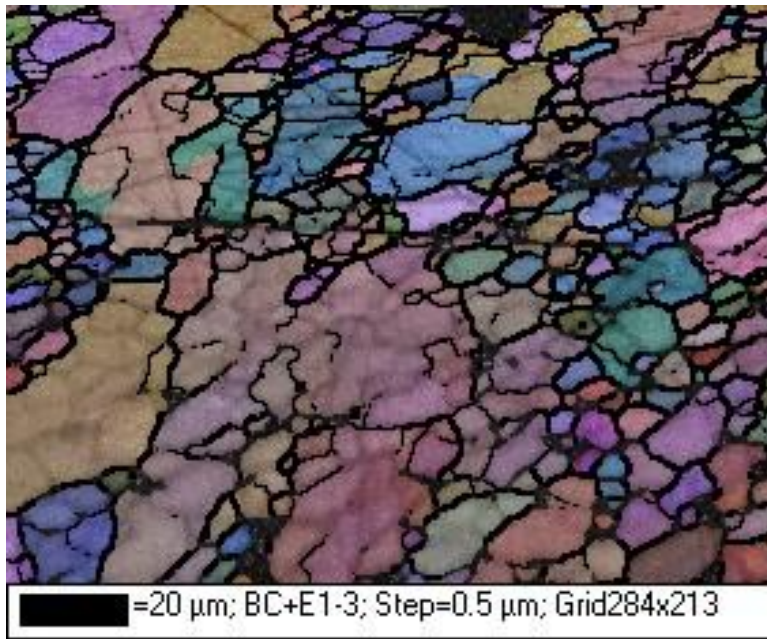


Figure 4.19 EBSD image of TMAZ of AS of weld of an Al5083 sample (Al5083/Al5083,  $\omega = 1000\text{rpm}$ ,  $v = 2.5\text{mm/min}$ )

The band contrast image shown in Figure 4.19 shows that the TMAZ is composed of a mixture of larger grains (tens of microns) and smaller grains ( $\sim 1$  micron), with a mean of  $2.76 \pm 3.55 \mu\text{m}$  (excluding grains on the border of the image). The EBSD image of Figure 4.19 was acquired on the same sample and under the same conditions as that of Figure 4.12.

A comparison of the grains in either the DRZ (Figure 4.12) or the TMAZ (Figure 4.19) with grains in HAZ shows that grains in both the DRZ and the TMAZ undergo significant refinement during processing. Figure 4.20 shows an EBSD image displaying the grain structure of the HAZ of the weld of an Al5083 sample. The grains in this zone have an average size of  $9.14 \pm 10.36 \mu\text{m}$ .

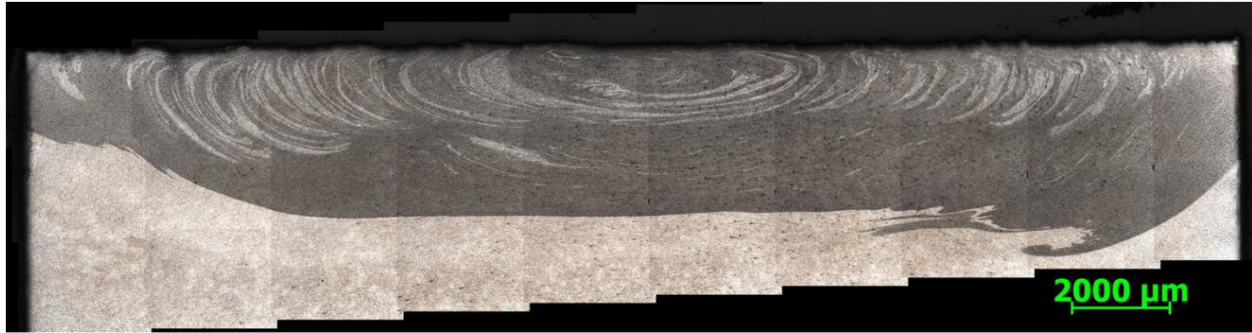


Figure 4.20 EBSD pattern of heat affected zone of Al5083 workpiece (Al5083/Al5083,  $\omega = 1000$  rpm,  $v = 2.5$  mm/min)

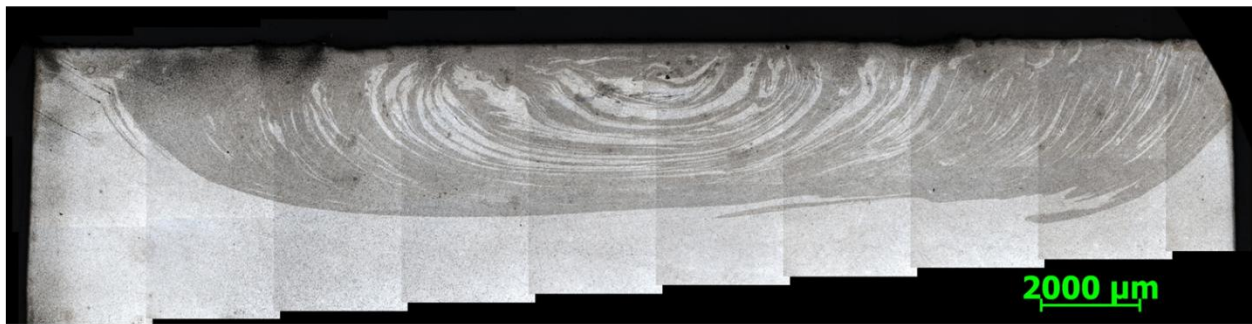
## 4.2 Effects of processing parameters on weld nugget macrostructure

### 4.2.1 Effect of $\omega/v$ ratio on weld nugget strata

Since each layer of the onion in the weld nugget is deposited by a single rotation of the tool, the thickness and spacing of the layers vary with the processing parameters. An increase in the rotational speed of the tool at a constant translational velocity should result in a reduction in the thickness and spacing of the onion layers. Conversely, an increase in the translational speed under constant rotational velocity should result in a thickening of the layers within the onion. It is therefore more illustrative to compare effects on the materials as a function of the  $\omega/v$  ratio.



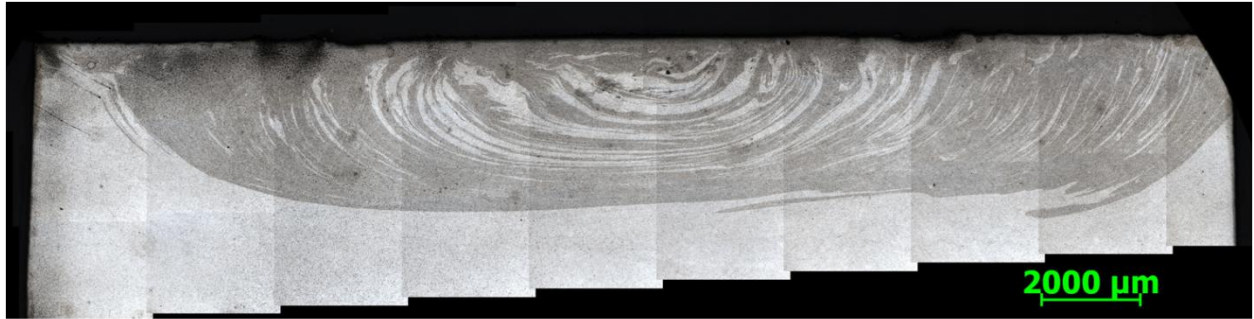
a.



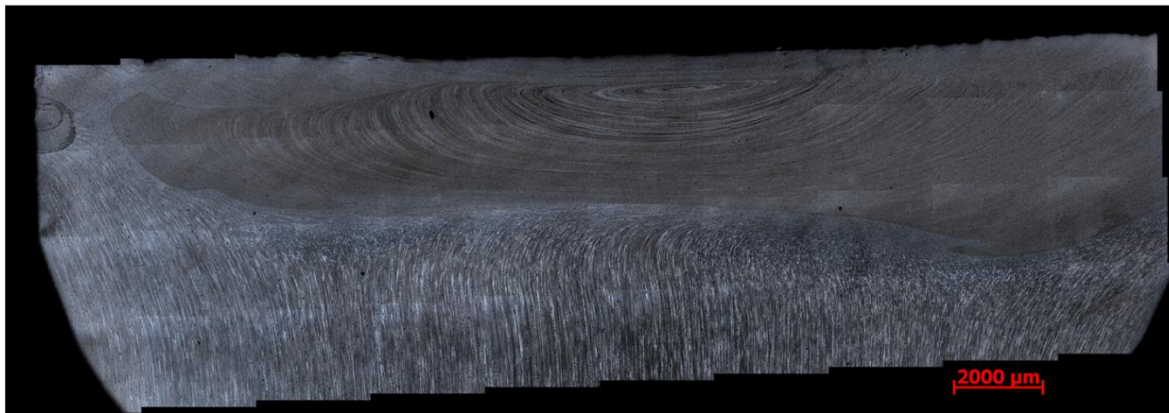
b.

Figure 4.21 Optical micrograph of two Al6061 samples showing difference in onion strata a.  $\omega/v = 207$  rev/mm, b.  $\omega/v = 83$  rev/mm

Examination of the onion in the weld nugget for samples processed at different  $\omega/v$  ratios Figure 4.21 shows that a decrease in the ratio (from 207 rev/mm to 83 rev/min) results in a thickening of the bands in the onion. A comparison between onion layers formed at a lower  $\omega/v$  ratio in Al6061 with those formed at a much higher ratio in Al5083 again show the dependence of the structure of the onion on the processing parameters (Figure 4.22).

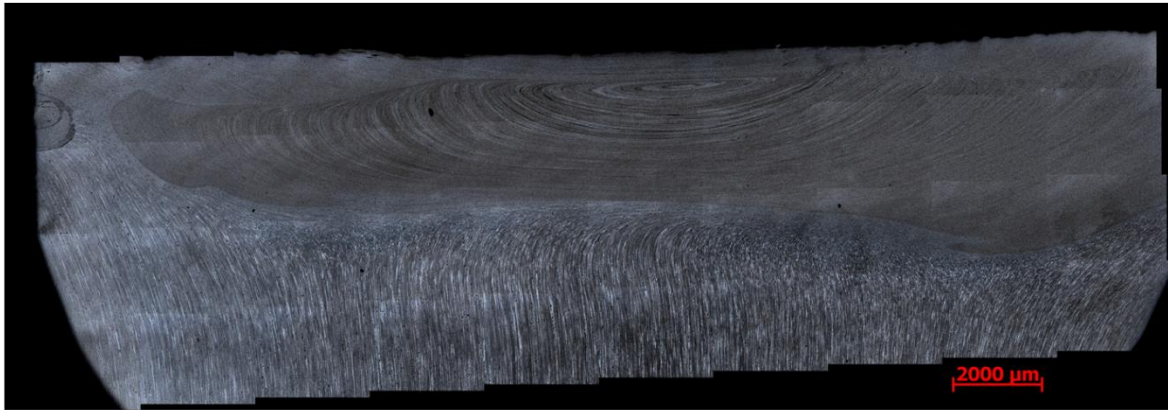


a.

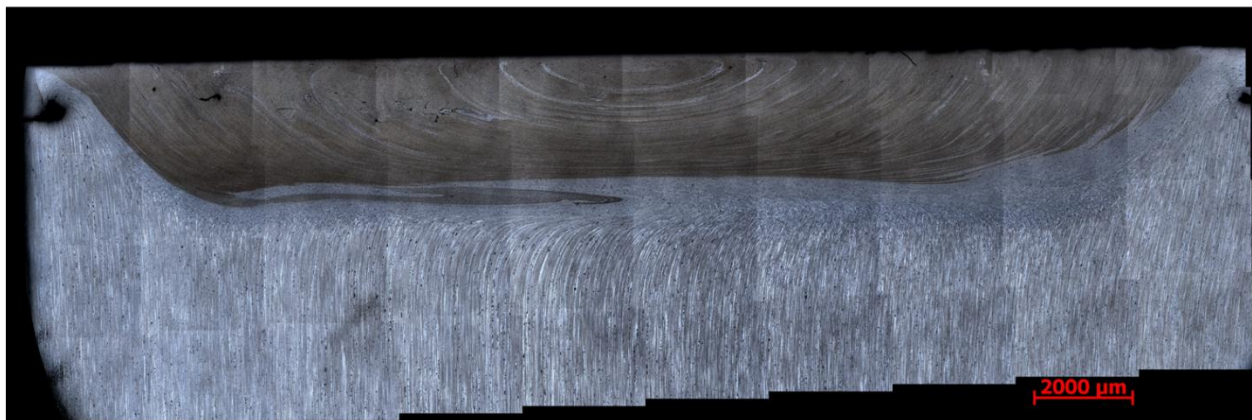


b.

Figure 4.22 Optical micrograph comparing onion layer thickness across material type a. Al6061/Al6061,  $\omega/v = 83$  rev/mm, b. Al5083/Al5083,  $\omega/v = 394$  rev/mm



a.



b.

Figure 4.23 Optical micrograph of two Al5083 samples showing difference in onion strata a.  $\omega/v = 394$  rev/mm, b.  $\omega/v = 472$  rev/mm

The trend in onion layer refinement does not continue once the  $\omega/v$  ratio is significantly greater than several hundred rev/mm (Figure 4.23). The strata within the onion do not appear to change shape significantly for samples fabricated in the Al5083/Al5083 material system. The  $\omega/v$  ratios possible during the Al5083 series of experiments was limited by the low maximum rate of feed delivery to the bead compared to the Al6061/Al6061 material system, and the limits in rotational frequency of the motor. The range of  $\omega/v$  values for the Al6061 system were from 83 to 207 rev/mm, while those of the Al5083 material system were restricted to the range of 281 – 984 rev/mm. As a comparison, ratios of  $\omega/v$  reported in the literature range from 0.025 rev/mm to 10 rev/mm[26].

#### 4.2.2 Effect of feedstock compaction in the tool tip on weld macrostructure

During a friction stir fabrication process run, material from the front of the advancing side of the tool is swept around with the motion of the tool to the retreating side of the weld. In friction stir welding, the tool shoulder is in intimate contact with the workpiece. For FSW, there is no volume to be filled by additional material. During a friction stir fabrication run

however, the tool shoulder rests at approximately 0.7 mm from the workpiece. As a FSF layer is deposited, the material from the workpiece is mixed with a new supply of material from the feedstock to fill the volume left between the tool and the workpiece. Without a supply of material from the center of the tool, material is swept from the advancing side of the weld line to the retreating side, but the volume of the deposited layer is not filled (Figure 4.24). Under such circumstances, the retreating side of the weld shows a typical onion structure, but the advancing side is eroded layer by layer resulting in a negative onion structure. The advancing side characteristic swirl is still present, signifying the presence of a TMAZ under the weld nugget.

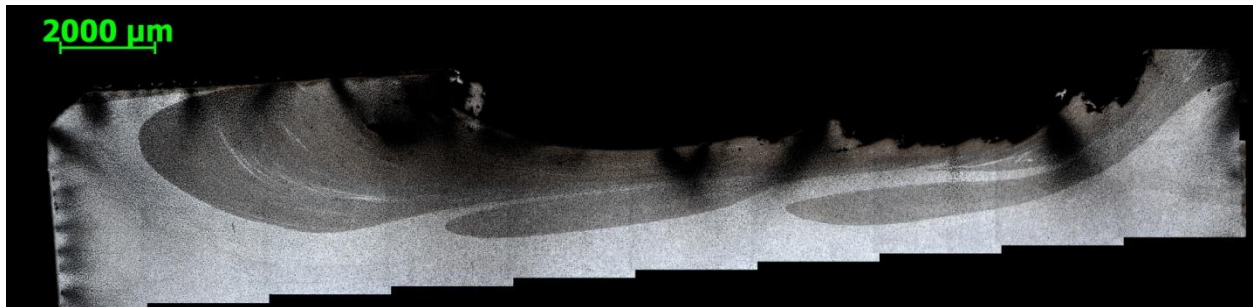
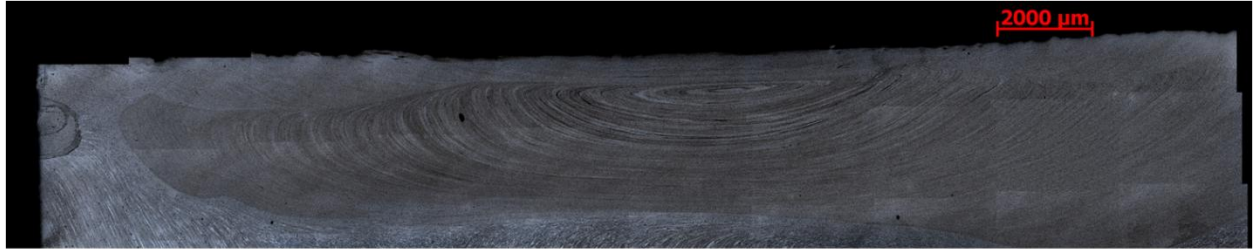


Figure 4.24 Micrograph of a FSF run without feedstock delivery (Al6061/Al6061,  $\omega = 2100$  rpm,  $v = 10.16$  mm/min)

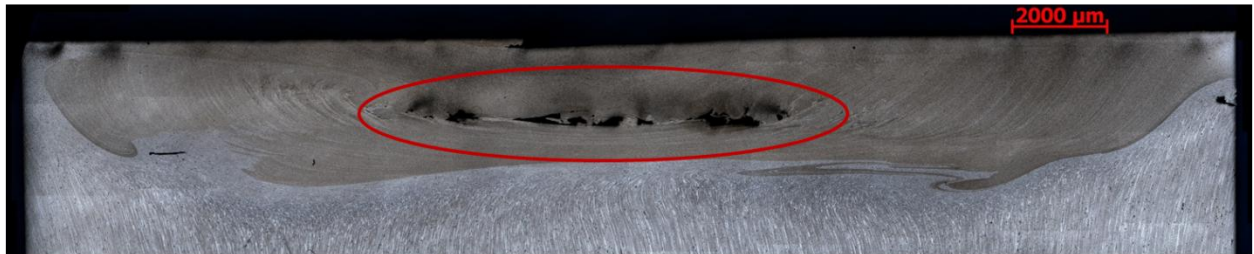
If adequate material is supplied from the feedstock, a complete weld nugget onion is formed. If for any reason there is not ample material from the workpiece and feedstock to feed the bead, the weld will begin to void. Since material motion begins at the advancing side of the weld, voids also initiate in the advancing side of the weld. Figure 4.25 shows various stages of void development within the weld nugget. Figure 4.25a shows a void-free cross-section. Figure 4.25b shows the beginning stage of a void formation. Note that the swirl on the left side of the TMAZ shows a tool rotation counter to Figure 4.25a and Figure 4.25c. The location of the void track starting to form in Figure 4.25b corresponds to the advancing side of the feed rod. In Figure 4.25c the void has traversed the entire length of the interface between the lower end of the feed rod and the weld nugget.



a.



b.



c.

Figure 4.25 Al5083 processed samples showing varying degrees of void in the onion a. no void, b. void initiation on AS of nugget, c. void across center of nugget

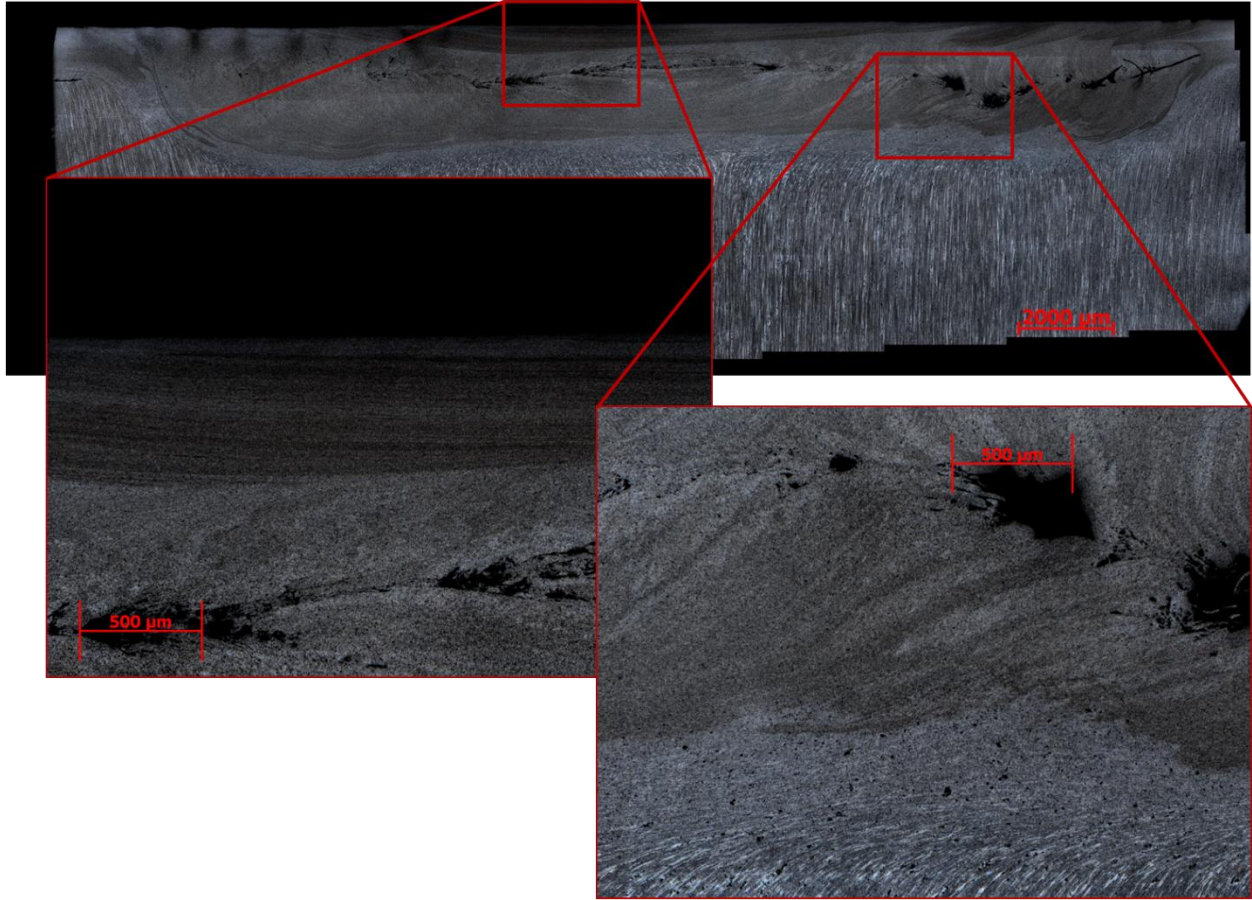


Figure 4.26 Detail of micrograph of void in Al5083 sample (Al5083/Al5083,  $\omega = 2500$  rpm,  $v = 2.54$  mm/min)

The structure of a voided weld nugget exhibits many different morphologies throughout the cross section. Figure 4.26 shows that onion-like strata are seen in the retreating side of the weld (left side of Figure 4.26), as well in portions of the nugget below the void (detail at right). When examining the void in the track, it is important to remember that the material at the edges of the workpiece was deposited prior to those at the center. Therefore, the void shown in Figure 4.26 undoubtedly shows material from either the further development or partial recovery of a void with time. Were a void to go to completion, the deposition would resemble that of Figure 4.25.

When the material supply through the feedstock is limited through binding of the feedstock material in the tool tip, the material below the void continues to be moved by the tool nubs (and corresponding workpiece material that is in the bead), resulting in the characteristic onion layers. The material above the void however is formed from continual motion of the end of the feedstock tip against the onion of the traditional weld nugget. The material in the region atop a partial or partially recovered void typically shows a more uniform morphology (Figure 4.27) with a finer grain structure than the rest of the sample (see Figure 4.38).

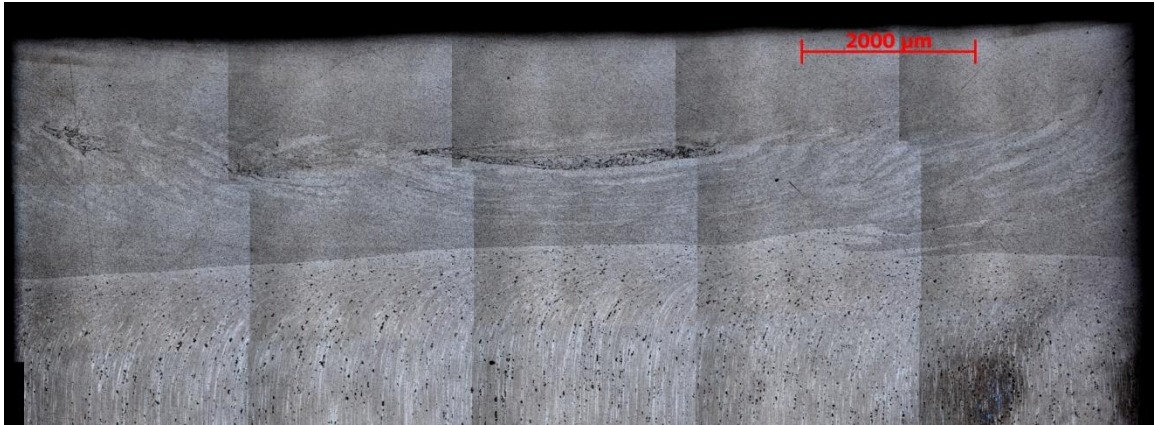
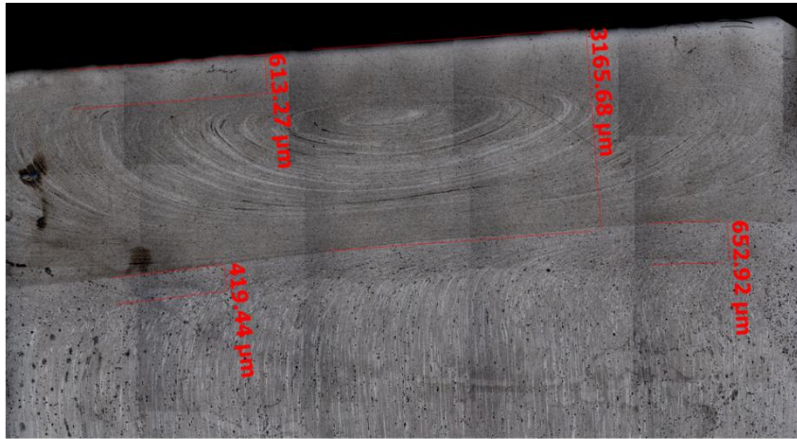


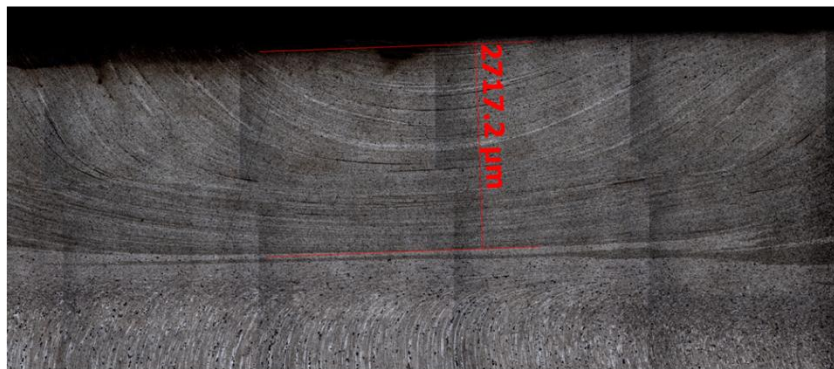
Figure 4.27 Incomplete void exhibiting a fully developed TMAZ and fine layer above the void line (Al5083/Al5083,  $\omega = 2250$  rpm,  $v = 2.54$  mm/min)

### 4.2.3 Effect of processing parameters on depth of DRZ

A survey of the micrographs of the processed samples shows that the general shape of the weld nugget is influenced by the processing parameters. Typically, the width of the processed area in the cross sectional view of the workpiece does not change with processing parameters, but is rather a factor of the geometry of the tool. The depth of the weld however appears to be determined by the relationships between the processing properties (Figure 4.28).



a.



b.

Figure 4.28 Comparison of depth of weld nugget for Al5083/Al5083 samples processed under different conditions a.  $\omega = 1200$  rpm,  $v = 3.56$  mm/min, depth = 3.167 mm b.  $\omega = 1000$  rpm,  $v = 3.56$  mm/min, depth = 2.717 mm

A comparison of the depths of the welds for various processing parameters shows that there is no clear trend of weld depth with feedstock force. A fit to the data gives a reciprocal relationship between feedstock force and weld depth (Figure 4.29), a result that is counter-intuitive. However, the low quality of the fit ( $r^2 = 0.373$ ) suggests that the relationship between force and depth suggested by the fit is statistically insignificant. The lack of direct influence of feedstock force on the weld depth may be explained by the fact that feedstock force is not directly proportional to feedstock delivery rate (see Section 3.2.4.5).

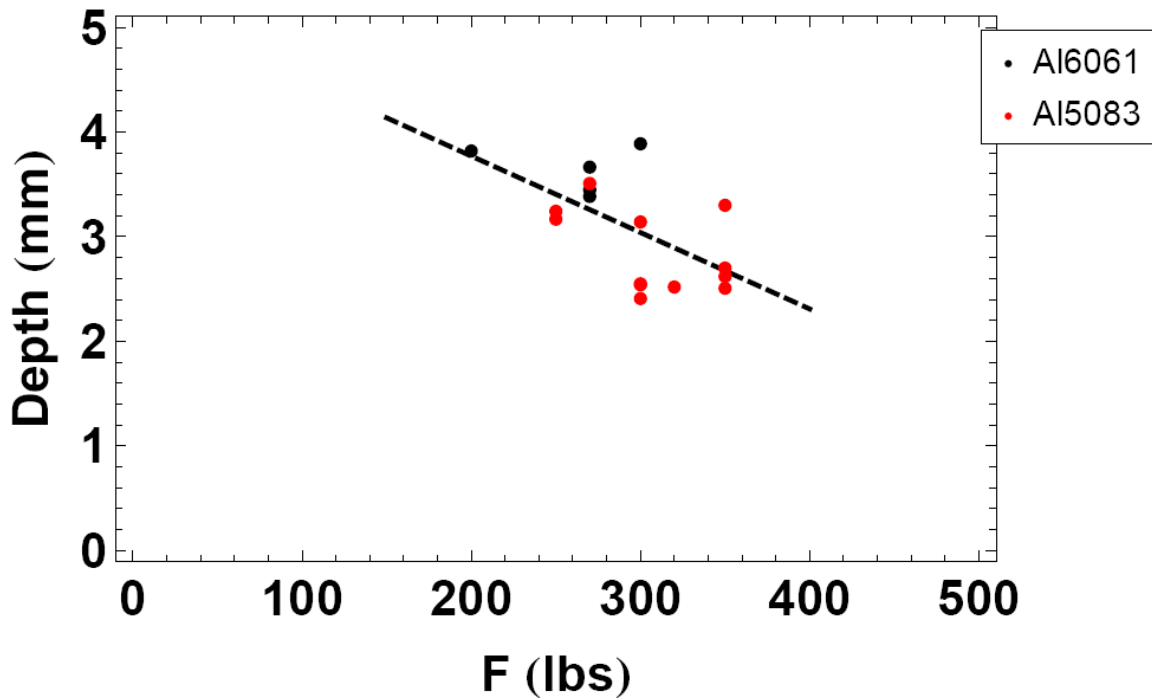
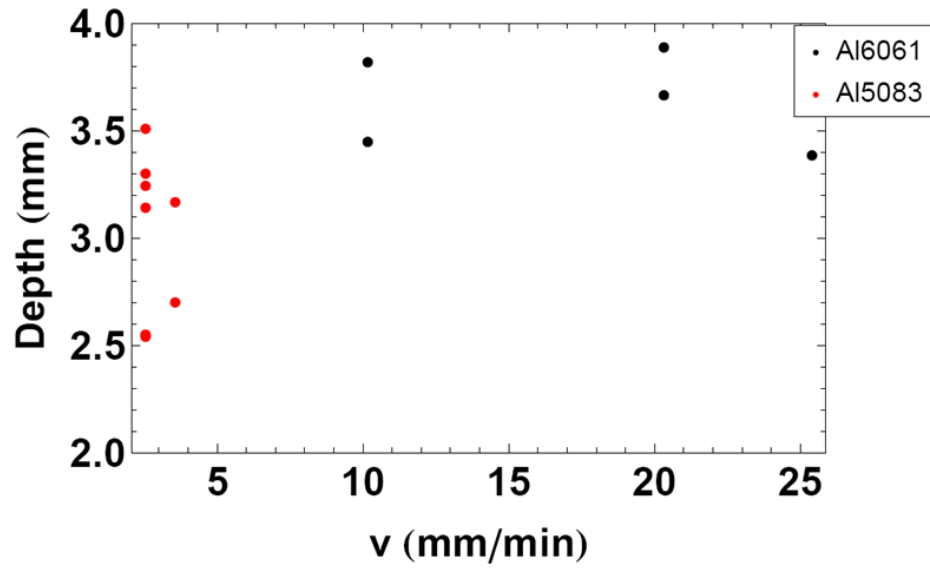
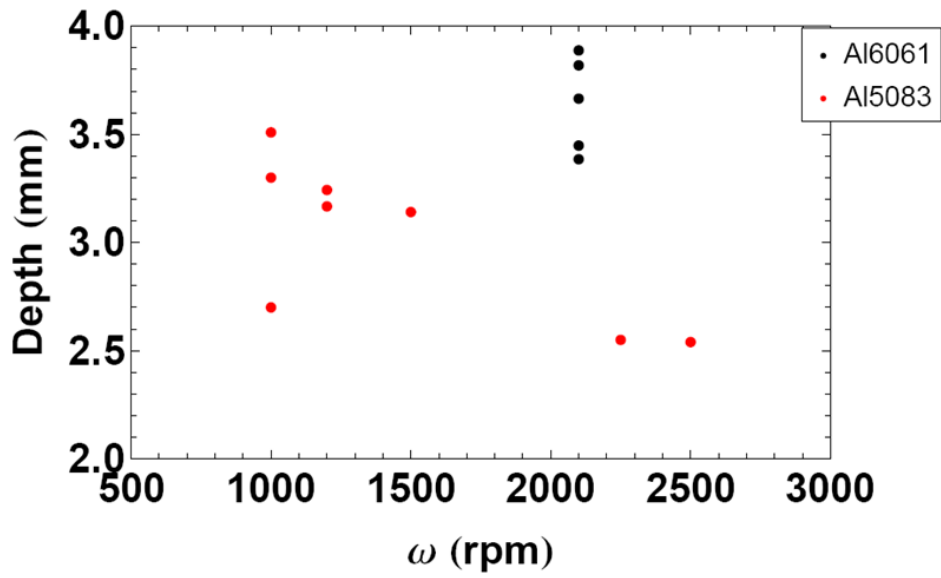


Figure 4.29 Weld depth versus feedstock force for Al6061 and Al5083 samples

The depth of the weld follows no clear trend when compared to translational velocity or rotational frequency (Figure 4.30). The Al6061 samples were all processed very early on as proof of concept samples. As such, variation in rotational velocity was not explored fully. Due to the limits of the friction stir fabrication machine, the translational velocity of the Al5083 samples is low, and there is little variation in speed between samples. Therefore, the Al6061 data show a relationship with velocity and the Al5083 data suggest a trend with rotational speed. As the tool translation rate decreases, there is more material motion and more thermal input per unit time. There should be therefore an increase in weld depth with decreasing velocity, a trend that is not evident in Figure 4.30a. As the tool rotation frequency increases, there is an increase in thermal energy to the system, but a decrease in availability of feedstock (Figure 3.25). The Al5083 data in Figure 4.30b suggest that an increase in rotational velocity tends to decrease the weld depth, but the trend is not echoed in the Al6061 data.



a.



b.

Figure 4.30 Depth of weld versus a. translational velocity and b. rotational frequency

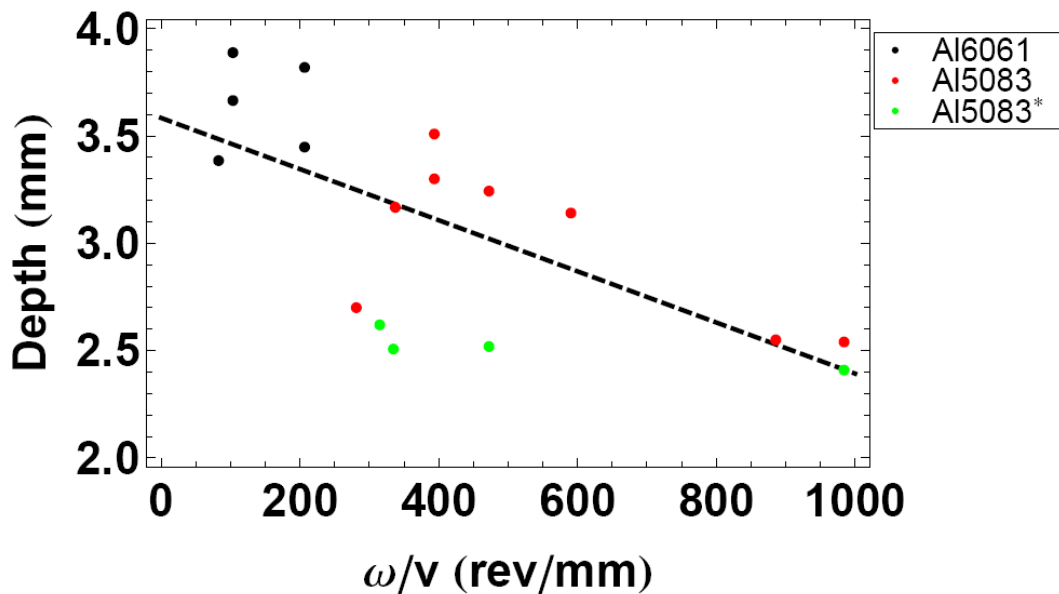


Figure 4.31 Depth of weld versus ratio of rotational frequency to translation speed including samples that show evidence of feedstock delivery problems

A comparison of weld depth with the ratio of rotational frequency to translation speed shows a trend. Figure 4.31 shows the depths of the welds for various  $\omega/v$  ratios for both the Al6061 and the Al5083 systems. The data suggest that there is an inverse relationship between the  $\omega/v$  ratio and the depth of the weld. The  $r^2$  value for the fit in Figure 4.31 is only 0.468, implying that the fit is of poor quality. However, several of the samples in this data set showed evidence of feedstock delivery problems (shown in green in Figure 4.31 – see Section 4.2.2). When the depth measurements for the problematic samples are excluded from the dataset (Figure 4.32), the  $r^2$  value of the fit is improved to 0.633.

While the exclusion of compacted feedstock samples improves the quality of the fit of depth versus  $\omega/v$  ratio, the low  $r^2$  value suggests that there is another variable influencing the depth of the weld. The fact that the delivery rate of feedstock material is not always constant under constant processing parameters (Figure 3.10) coupled with the lack of positional feedback from the gantry table means that it is not possible to quantify the rate of feed corresponding to a particular cross-sectional micrograph. In all likelihood, the rate of feed at any  $\omega/v$  ratio should influence the depth of the weld to a certain degree; however this work does not contain data to characterize such dependence.

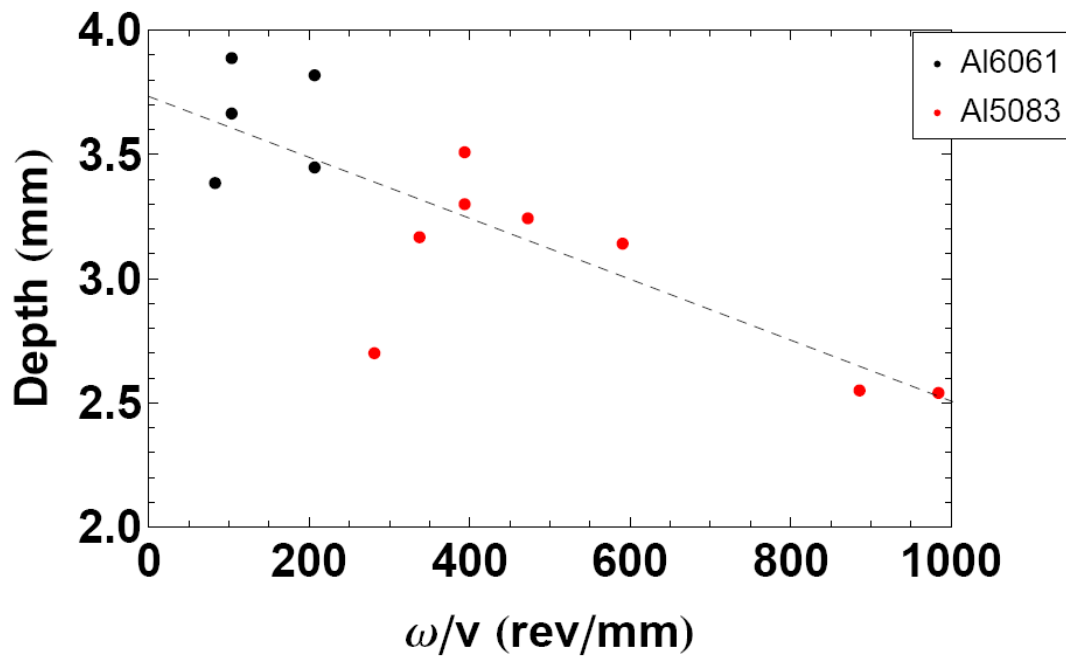


Figure 4.32 Depth versus  $\omega/v$  ratio excluding compacted stock samples

#### 4.2.3.1 Effect of depth of weld on system horsepower requirements

As mentioned in Section 3.2.4.3, the process monitor data suggests that the average horsepower required for steady state operation was mainly a function of the material system used (Al6061 vs. Al5083), particularly the material type of the feedstock. The survey performed to characterize the dependence of depth on processing parameters led to an examination of the variation in average horsepower requirements with a change in depth of weld. An increase in the depth of the weld should signify a proportional increase in the volume of material swept by a single rotation of the tool. However, as shown in Figure 4.33, the data show that there is no dependence of power requirements on depth. The data do reinforce the relationship between material type and horsepower requirements, albeit without taking into account the dependence of feedrate on the material type. The average, steady-state horsepower requirements are dependent on the  $\omega/v$  ratio as well as the rate of feedstock delivery, but are relatively independent of the depth of the weld nugget.

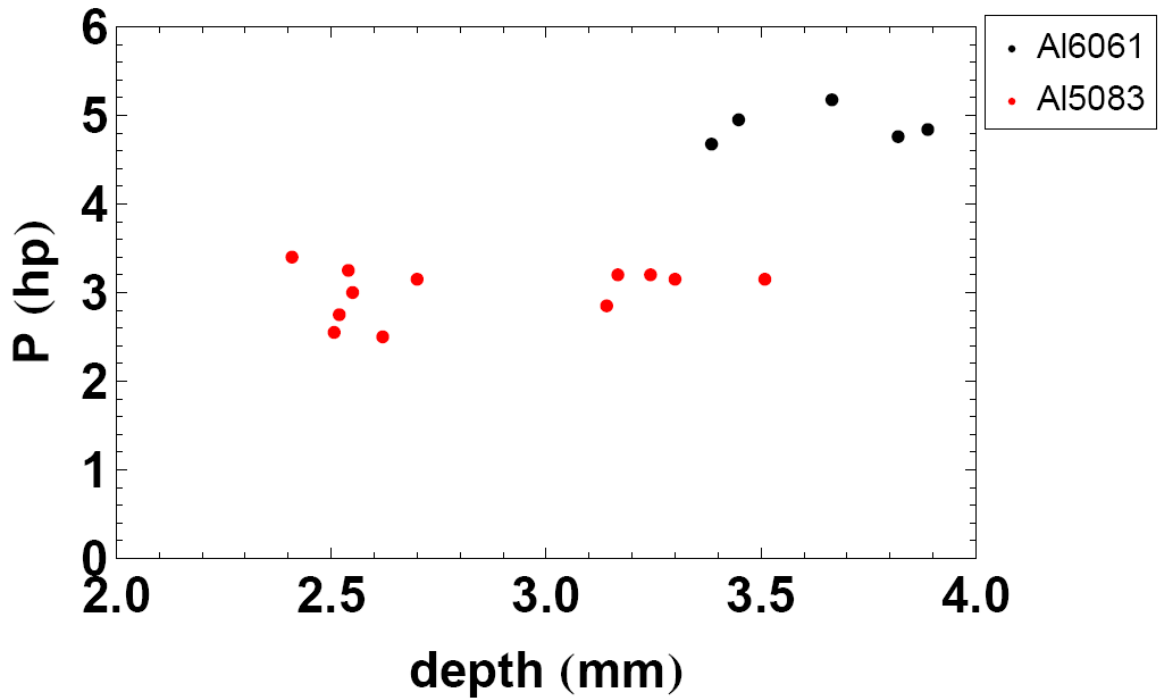


Figure 4.33 Average steady-state power versus depth of weld for Al6061/Al6061 and Al5083/Al5083 samples

### 4.3 Effects of processing parameters on grain size and hardness

Among the goals of this study are the characterization of the deposited layer as well as effects of the friction stir fabrication deposition technique on the underlying material. As discussed in 1.1, friction stir techniques typically tend to refine the grain structure of the material within the dynamically recrystallized zone while acting to soften the material in the HAZ through grain growth or precipitate reorganization. Characterization of the microstructure of the material within the various zones of the material can serve to elucidate the processes occurring during processing as well as to aid in prediction of mechanical properties of the sample.

The solid state aspect of the friction stir fabrication technique results in a microstructure that is plastically deformed at an elevated temperature. There is not however adequate energy provided during processing to allow for recovery of damage induced during the stirring process, neither is there a post-process annealing step to do so. The material in the mechanically affected zones of the workpiece therefore tends to exhibit high residual strains. As such, traditional chemical micrographic etchants proved unsuccessful in providing grains size contrast for optical microscopy (see discussion of Figure 4.6), decorating points of strain in the grains rather than grain boundaries. Backscatter electron detection was unable to provide grain size contrast in either polished or etched samples (Figure 4.7). While EBSD gave good results in grain size resolution (Figure 4.12, Figure 4.19, and Figure 4.20), the imaging time per

unit area renders this technique inappropriate for surveying large cross-sections of processed samples (typically on the order of 250 mm<sup>2</sup>/sample).

#### 4.3.1 Correlation of Vickers hardness to grain size

The relationship between Vickers hardness values and grain size for friction stir welded Al5083 has been reported previously in the literature [26]. Therefore, Vickers hardness measurements were employed as a time effective method for characterization of the grain size within the various zones of the samples while simultaneously provide feedback as to the hardness of the material. To conformity of our data with the trends reported in the literature, Vickers hardness measurements were made along the depth of a sample on which EBSD analysis had been performed. Hardness measurements were made with 1kgF and a 5 second dwell time. The area of the indents was measured using a calibrated optical microscope. The line scan of the hardness profile shown in Figure 4.34 shows that the material is harder within the weld nugget than in the TMAZ or the HAZ of the sample.

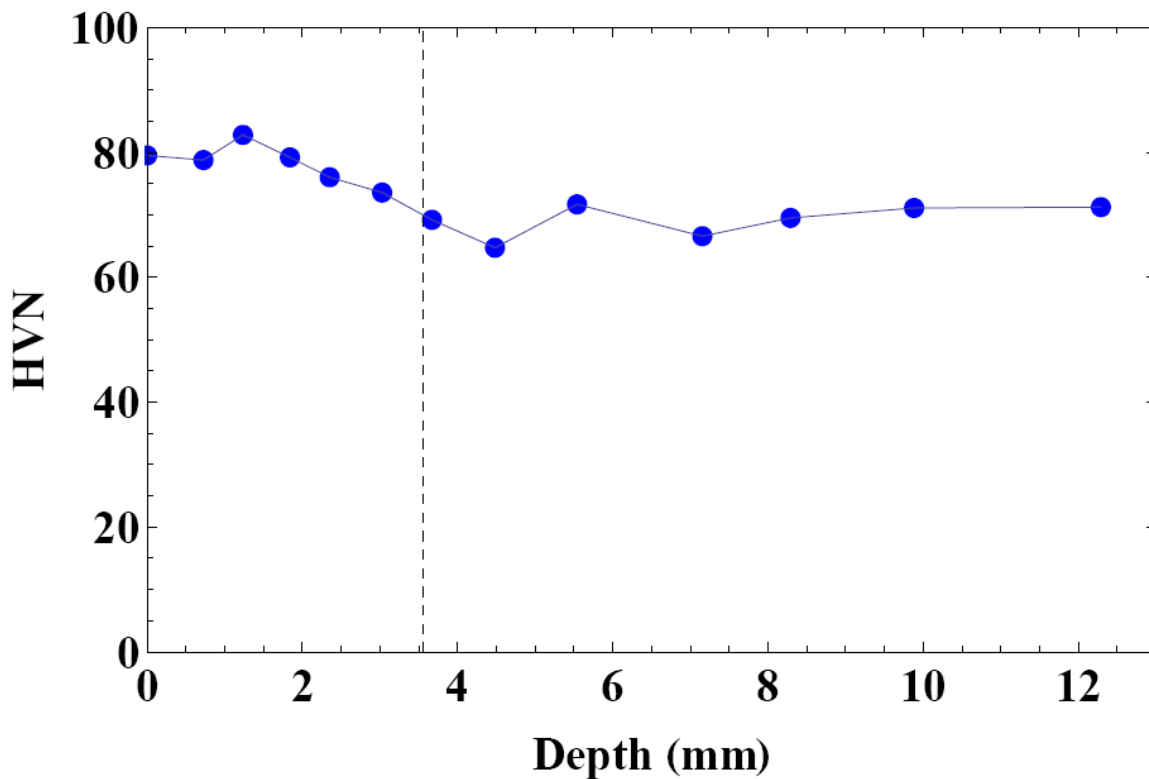


Figure 4.34 Depth profile of Vickers hardness of an Al5083/Al5083 sample ( $\omega = 1000$  rpm,  $v = 2.54$  mm/min), dashed line corresponds to the depth of the weld nugget

The data from the hardness profile combined with grain size measurements from EBSD analysis are plotted in Figure 4.35 along with values reported in the literature [26] for friction stir welded Al5083 samples. The figure shows that the relationship between hardness and grains size reported in the literature for friction stir processed Al5083 can be applied to the present study.

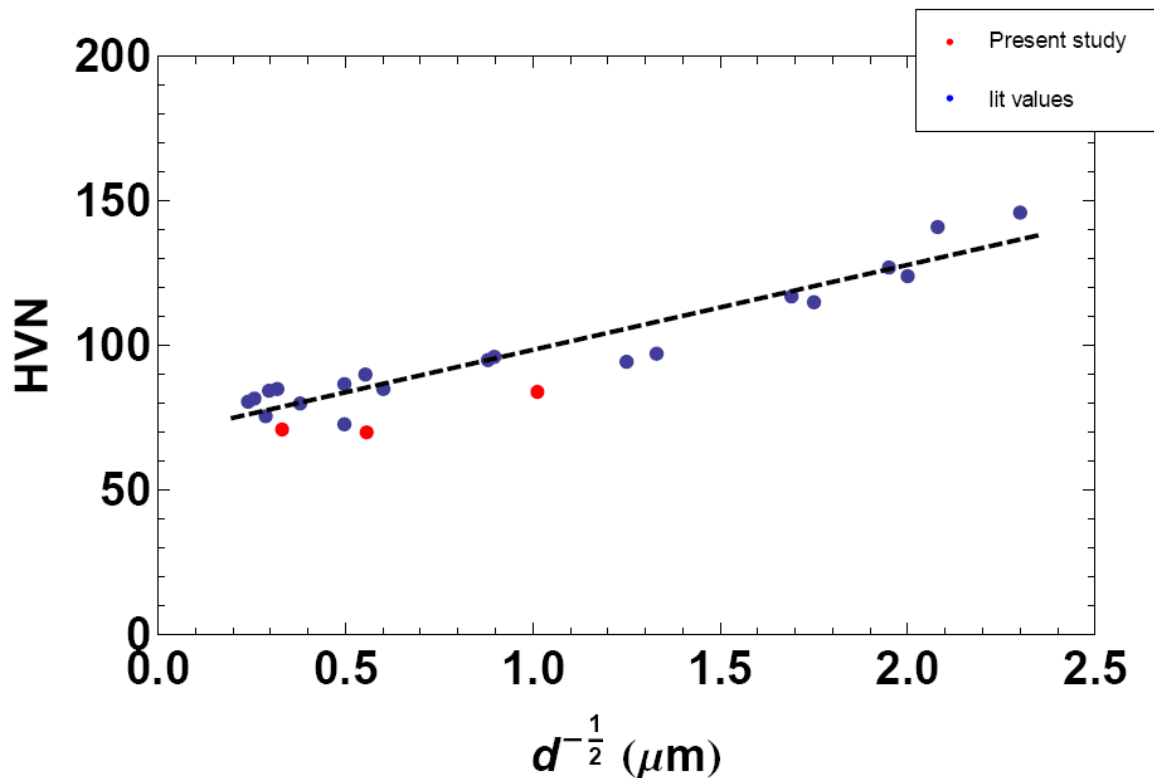


Figure 4.35 Hardness versus grain size relationship for friction stir processed Al5083 [26] (used with permission)

#### 4.3.2 Vickers hardness maps of processed samples

To characterize the effects of processing parameters on the grain size of processed samples, hardness maps were made on cross-sectional areas. Samples were sectioned using a high-speed, wet cut-off saw. Samples were mounted in a thermoset plastic and polished for microscopy. The samples were polished on a Buehler autopolisher with a final polish with a neutral pH, 0.05  $\mu\text{m}$  colloidal silica. Samples were then etched with Keller's etch for 30 seconds to allow for identification of stir zones. Indents were made on a Leco LV700AT hardness tester with 1kgF and a 5 second dwell time. The sample was manually positioned and indents made across the cross-section of samples along the interface of the DRZ and the TMAZ, as well as within the weld and the HAZ of the material. Mosaic micrographs of the cross-section of the

samples were then taken on a Zeiss optical microscope. Relative locations and areas of the indents were measured using microscope control software. The values of hardness measured were in good agreement with manual measurements made on the Leco indenter.

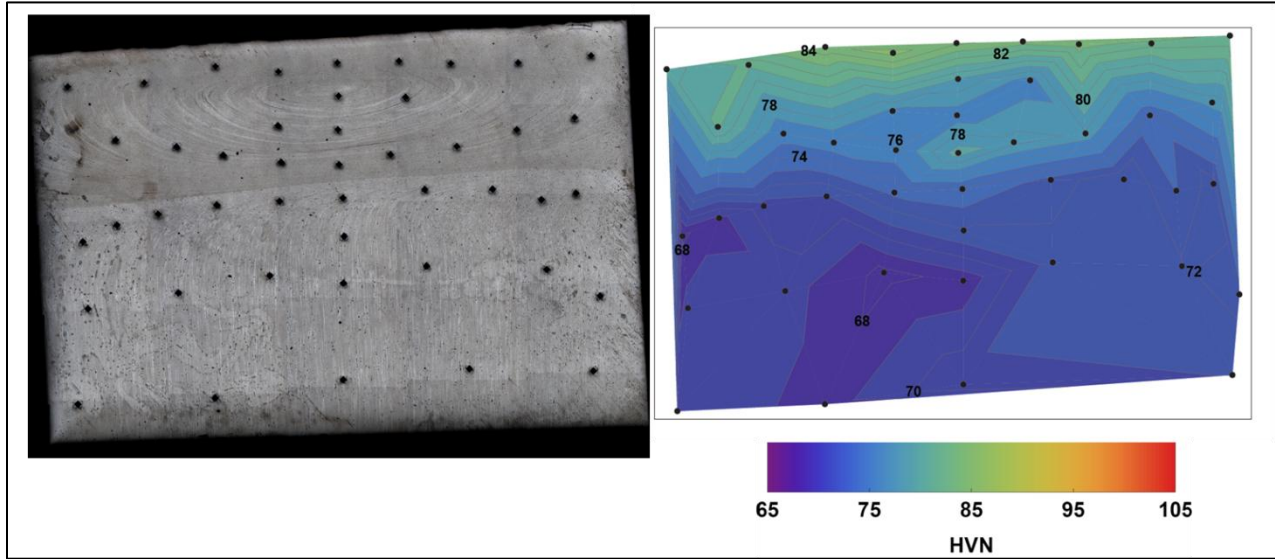


Figure 4.36 Optical micrograph showing location of hardness indents and corresponding hardness map (Al5083/Al5083,  $\omega = 1200$  rpm,  $v = 3.56$  mm/min)

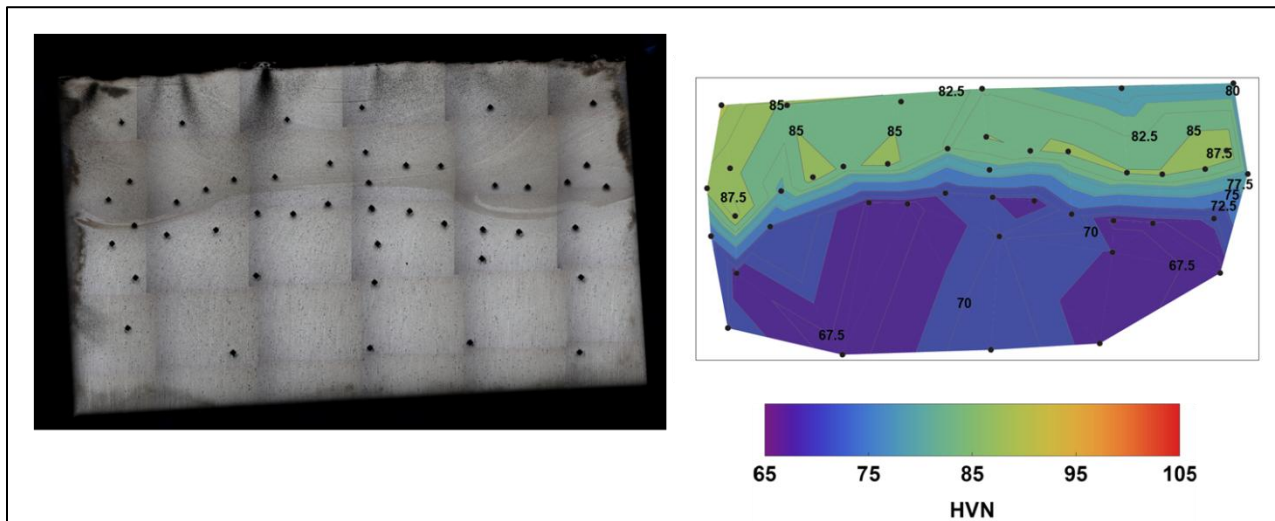


Figure 4.37 Optical micrograph showing location of hardness indents and corresponding hardness map (Al5083/Al5083,  $\omega = 1000$  rpm,  $v = 2.54$  mm/min)

Figure 4.36 and Figure 4.37 show mosaic optical micrographs of the etched samples showing the locations of the indents relative to the areas of interest of the weld. Also included in the images are contour maps of the hardness of the sample calculated from the area of the indents. The data show that the weld nugget is the hardest area of the sample. The material within the weld nugget shows relatively uniform hardness. There is a sharp transition from the

hardness of the weld nugget to that of the heat affected zone. The region of transition corresponds to the TMAZ of the processed piece.

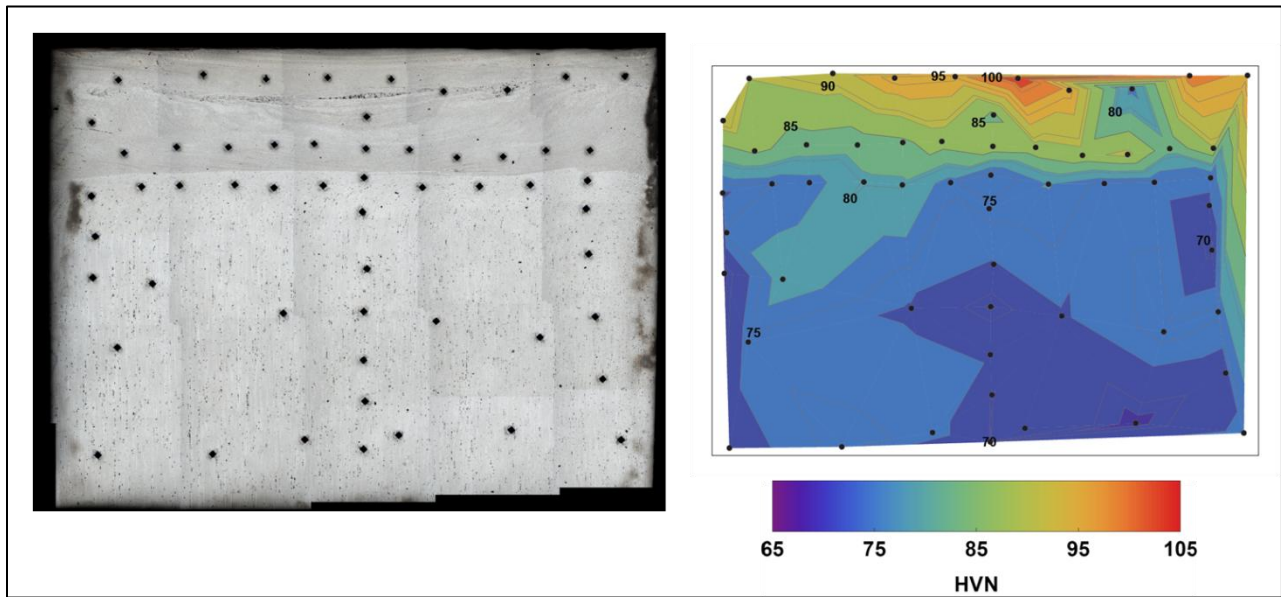


Figure 4.38 Optical micrograph showing location of hardness indents and corresponding hardness map (Al5083/Al5083,  $\omega = 2500$  rpm,  $v = 2.54$  mm/min)

The hardness map generated for a sample that shows the initial stages of void formation is presented in Figure 4.38. The region just below the void nucleus and the HAZ show properties similar to those of void-free samples (Figure 4.36 and Figure 4.37). The material above the void shows is much harder, signifying a more refined microstructure in this area than that of a typical weld nugget.

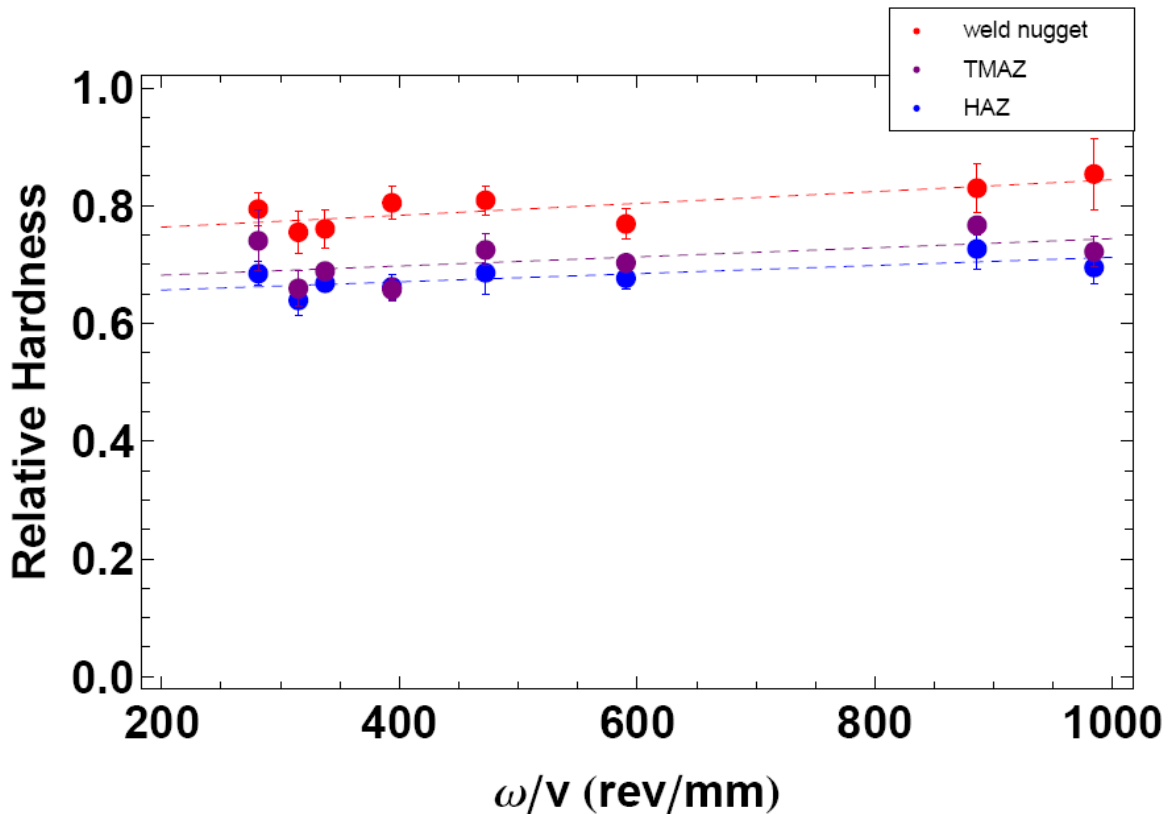


Figure 4.39 Relative hardness of sample with process parameters

A survey of the relative hardness versus processing parameters for the samples shows that the hardness of the various zones is relatively independent of the processing parameters (Figure 4.39). While the fit to the data does not show a statistical independence of hardness with respect to the  $\omega/v$  ratio at the 95% confidence level, the strength of the dependence is small (e.g.  $HVN = 10^{-4} \omega/v + 0.74$  for the material within the weld). The survey shows that the heat affected material in the processed samples loses 30% of the original strength. The loss of strength in the sample is due to the pressure applied to the piece ( $\sim 2.6$  MPa) at elevated temperature ( $\sim 400^\circ\text{C}$ ). During processing, the workpiece is oriented such that the direction of rolling is towards the tool shoulder. The narrow axis of the pancake-shaped grains is seen in a cross-sectional view of the material (Figure 4.23), while the larger axis of the grains is oriented parallel to the longitudinal view of the weld (Figure 4.16). The hardness of the as-received material therefore has an orientation as well. The as-received material has a hardness of  $104.67 \pm 2.47$  in the cross-sectional orientation and  $94.54 \pm 2.32$  in the longitudinal direction. The processed material however has a hardness of  $71.15 \pm 2.67$  in the cross-sectional orientation and  $74.55 \pm 4.30$  in the longitudinal direction. The pressure applied during processing counteracts the strain hardening of the original temper.

Figure 4.39 shows that material in the TMAZ is typically slightly harder than material in the HAZ, showing properties more closely related to those of the HAZ rather than the weld nugget. The complexity of the motion of material within the TMAZ makes correlations between hardness and microstructural refinement somewhat difficult. EBSD analysis suggests that microstructure in the TMAZ is a mixture of fine and coarse grains (Figure 4.19). The fine grains are most likely generated in the weld nugget, or in like manner (dynamically recrystallization). The larger grains however arise from a rotation of the as-received pancake-shape grains relative to the direction of welding. The strengthening effect of the recrystallized grains will be offset somewhat by the reorientation of the original grains.

Figure 4.39 shows that the material within the weld nugget is significantly harder than the rest of the workpiece ( $HVN = 83.42 \pm 3.62$ ). EBSD data (Figure 4.12) shows that the material in the weld nugget consists of small grains, as is reported for FSW materials [27]. Hardness measurements in the transverse and the longitudinal directions yield similar results ( $84.23 \pm 2.99$  and  $80.00 \pm 3.23$  respectively for  $\omega = 1000$  rpm,  $v = 2.56$  mm/min), suggesting isotropic grain size.

Since the grain in the weld nugget have no preferred orientation, the relationship between hardness and grain size reported in the literature (Figure 4.35) can be used to calculate the grain size in the weld from the hardness values measured.

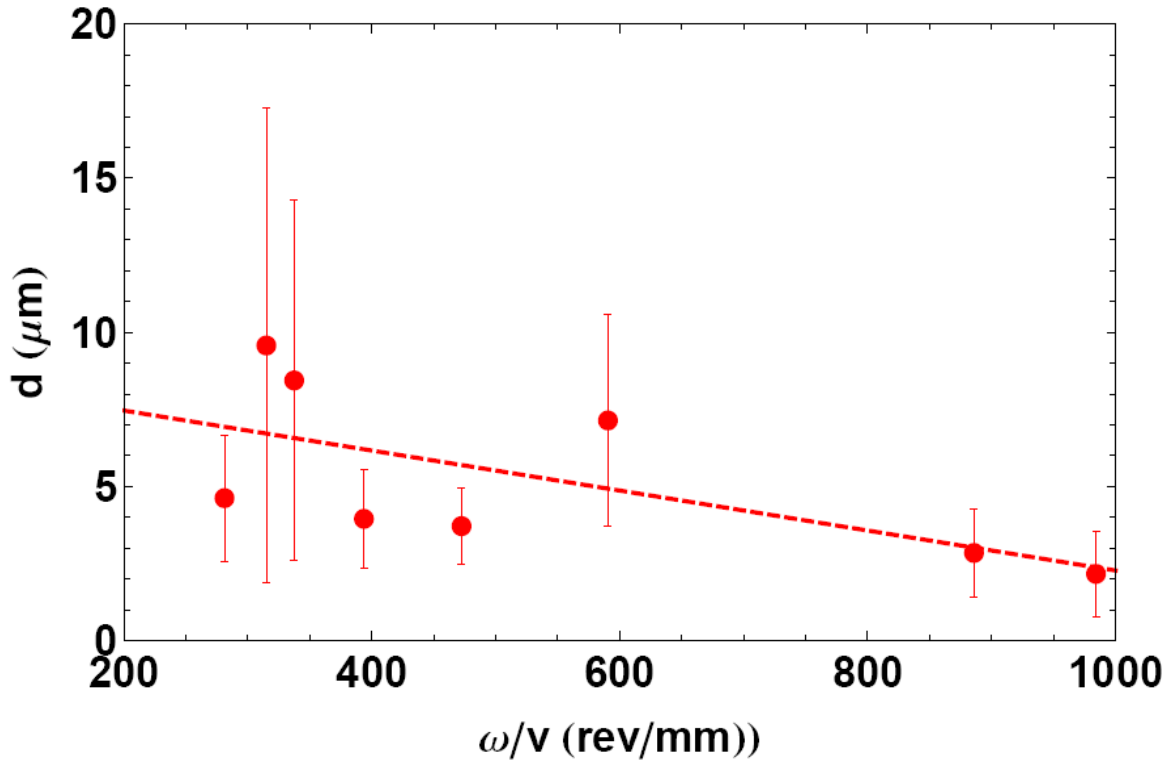


Figure 4.40 Calculated grain size for material in the weld nugget for different processing parameters

For the samples fabricated in the Al5083 system under the range of process parameters available to the system hardware, the average grain size is calculated to be  $8.75 \pm 1.885 \mu\text{m}$ . At the 95% confidence level, there is no dependence of grain size on processing parameters, as shown in Figure 4.40. A fit to the grain diameter versus  $\omega/v$  ratio yields

$$d = (8.75 \pm 1.885) - (0.006 \pm 0.0032) \frac{\omega}{v}$$

When the errors in the hardness measurements are propagated through to calculated values of grain size, it is apparent that some of the data in the statistical makeup of the set do not accurately represent the effects of processing parameters on the grain size within the weld (ref.  $\omega/v$  ratios of 315, 330, and 590 rev/mm in Figure 4.39). As a further example of the difficulty incurred due to the large variance in the data points in Figure 4.40, propagating the error in the hardness-to-grain size relationship shown in Figure 4.35 shows a much smaller standard deviation at all  $\omega/v$  ratios (Figure 4.41). The samples at  $\omega/v$  ratios of 315, 330, and 590 rev/mm correspond to samples in which a surface refinement was evident due to problems with stock delivery (as in Figure 4.38).

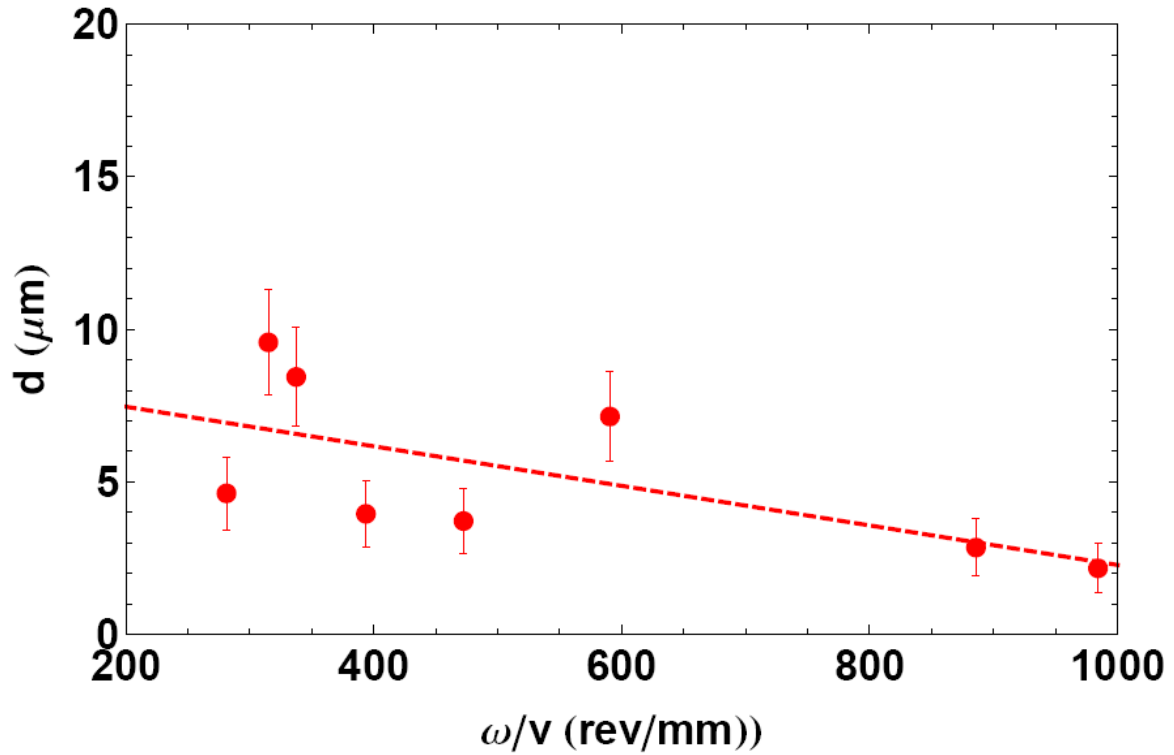


Figure 4.41 Calculated grain size for material in the weld nugget for different processing parameters with error in HVN-d propagation

The limits in rotational velocity of the synchronous motor and the translational speed due to the stock delivery system restrict the  $\omega/v$  ratio to a minimum value of roughly 200 rev/mm. In order to explore the effects of processing parameters on grain size more extensively, values of  $\omega/v$  of less than 10 rev/mm are necessary.

## 5 Conclusions and Future Work

### 5.1 Thermal Model Conclusions

We have created a three dimensional, implicit finite-difference model. The model approximates the solution to a dimensionless version of the partial differential heat equation for nodes within a user-defined mesh. The non-dimensionality of the model allows for portability across material types and scalability with respect to sample size. Our model assumes convection to room temperature (70°C) air at the top and side surfaces of the workpiece, with a heat transfer coefficient of 50 W/m<sup>2</sup>K. The model approximates the heat loss through the backside of the workpiece to a coolant block as a convective heat transfer to a fluid at 100°C with a heat transfer coefficient of 1000 W/m<sup>2</sup>K. The model predicts roughly 35% of the output power of the motor is converted from mechanical to thermal energy in the system. Using the effective thermal power calculated with the power conversion factor, the model shows excellent agreement with empirical measurements of temperatures from embedded thermocouples. The model also suggests that a conversion of the mechanism of heat loss through the backside to assume conduction across a resistance would increase the agreement of the model calculations with empirical data.

For simplicity, the current version of the model does not account for changes in material properties with temperature. Inclusion of temperature dependent property would add a dimension of complexity to the calculations required to arrive at solutions. Furthermore, conversion of temperature-dependent material parameters to allow for incorporation in the dimensionless model is not straightforward. Our model does not include a temperature dependence on the thermal energy, as suggested in the literature[16]. Although we initially proposed the inclusion of a step function-shaped form of the energy to represent the change in the coefficient of friction at melting temperatures, the agreement of our model with empirical data suggests that this is not a physically accurate assumption.

The single most important limitation of our model is that it exists as an *a posteriori* calculation tool rather than a predictive tool. The reason for the inability to predict temperature profiles lies in the lack of understanding of the effects of process parameters and material types on the heat provided to the system.

### 5.2 Thermal Model Future Work

In order for the model to predict the temperature profiles of a run from a set of process parameters, the relationship between those parameters and the thermal energy supplied to the system must be quantified. In particular, the effect of material toughness and material feedrate on energy must be understood. The limitations of the hardware as it exists now hindered research on the relationship between feedrate and horsepower.

Additionally, a second generation thermomechanical model should be developed, particularly for the Al5083/Al5083 system. Much work has been done previously on coupling thermal models to mechanical properties of Al6061 and other age-hardened alloys. It would be interesting to explore the effects of the temperature and pressure applied to the alloy during FSF, and coupling the change in mechanical properties to the orientation of the as-received Al5083 workpiece material. Inclusion of temperature dependent material properties would be important in prediction of final mechanical properties such as hardness.

### **5.3 Process Characterization Conclusions**

We have defined a four-stage friction stir process run; tool insertion, material warm-up, bead formation, and steady-state operation. The four stages can be characterized by changes in motor output power, feedstock delivery, and tool tip temperature. We have shown that the temperature of bead formation and the average steady-state system power requirements depend on the material properties of both the feedstock and workpiece. We have determined the volume of material delivery required to maintain a bead at a given translation rate, assuming an effective penetration depth 2.7 mm of the feedstock into the deposition layer. Since typical deposition layers are on the order of 3-4mm, the majority of the material in the weld nugget is supplied by the feedstock. Consequently, the properties of the feedstock material have greater effect on tip temperature at bead formation and steady-state temperature requirements.

We have shown that the instantaneous power delivered to the system is a function of the feedstock delivery rate and the tool rotational frequency. We have also shown that the material delivery rate is inversely proportional to rotational frequency at a constant force. The material delivery system for the friction stir fabrication machine is limited in that there is a built-in resistance to motion that controls the lower limit of feed rate. A more severe problem with the current system is that excessive force tends to cause the feedstock material to bind in the tool tip, resulting in void formation in the deposited layer. The material compaction problem limits the maximum delivery rate of material to the bead, and consequently limits the maximum translation speed of the tool.

### **5.4 Process Characterization Future Work**

The FSF system needs a complete redesign. In order to attain reliable deposition layers, the material feedrate must be made more reliable. We believe that changing the delivery method from a force control to positional control with a very large maximum force would ensure material delivery rates that would allow significant increases in translation speed. Also, the minimum possible rotational velocity of the tool must be lowered. The current system allows for 1000rpm, with some loss in torque. In order to fully explore the effects of rotational velocity, and the  $\omega/v$  ratio, the system must be capable of rotational velocities in the 400 rpm

range, and  $\omega/v$  ratios  $< 1$ . The system should also be updated to provide for control of the position of the tool on the surface of the workpiece. Inclusion of the position of the tool with respect to time during a process run would facilitate synchronization of process control variables.

Another venue of exploration in the process characterization would be to incorporate the constituents for the formation of *in-situ* metal matrix composites into the feedstock. The active FSF process characterization would require updating the system such that the feedrate could be controlled in order to ensure that the desired volume fraction of reinforcement was delivered to the bead. The change in mechanical properties due to the formation of ceramic reinforcing particles within the aluminum matrix should change the power requirements of the system. Characterization of both the change in mechanical properties and the resulting change in process power requirements should help to explain the material-dependent power requirements seen in this work.

## 5.5 Process effects on Microstructure Conclusions

The friction stir fabrication process results in a microstructure that resembles the microstructure seen in traditional friction stir welding and in friction stir fabrication. The processed material shows a dynamically recrystallized zone (DRZ), a thermomechanically affected zone (TMAZ), and a heat affected zone (HAZ). Residual strain in the DRZ rendered typical chemical etchants ineffective in delineating grains for grain size determination. While chemical etching shows grains in the TMAZ and HAZ of Al6061 samples, grains in Al5083 samples were not visible either optically or using electron imaging techniques.

The DRZ in FSF shows the characteristic friction stir onion structure. The onion is composed of layers of material extruded between previously deposited material and material currently contained in the weld bead. As such, the thickness of the layers in the onion shows an inverse dependence on the  $\omega/v$  ratio. Material in the DRZ shows a refined microstructure, with average grain size of  $\sim 1.5 \mu\text{m}$ . Over the range of  $\omega/v$  ratios available to the system, there appears to be no effect of process parameters on grain size. The width of the DRZ is defined by the width of the FSF tool tip, but the depth of the weld is proportional to the  $\omega/v$  ratio. SEM analysis showed the chains of insoluble phases in the as-received Al5083 were redistributed evenly throughout the DRZ. Furthermore, the average particle size of the precipitates was refined from  $\sim 5 \mu\text{m}$  to  $< 1 \mu\text{m}$  in the DRZ.

Material in the TMAZ shows a mixture of fine and coarse particles. Grains within the TMAZ are either refined due to dynamic recrystallization (as in the DRZ), or are moved into the zone from the HAZ through tangential friction with the weld nugget. Due to the grain structure in the TMAZ, the material here is significantly softer than material in the weld nugget.

The as-received Al5083 has an oriented grain structure due to a strain-hardening procedure. Hardness measurements performed on the as-received material shows a Vickers hardness of  $104.67 \pm 2.47$  in the transverse direction and  $94.54 \pm 2.31$  in the longitudinal direction. Hardness measurements of processed materials show a more isotropic material and that the material loses approximately 30% of its initial hardness. Given that Al5083 is not a heat-treatable alloy, the change to isotropic hardness, and the orientation of the workpiece, the applied pressure and elevated temperature act to counteract the original strain-hardening.

## 5.6 Process-Microstructure Future Work

Due to limitation in time it was not possible to fully map the grain size distribution across a section of a processed sample. Chemical etchants did not decorate grain boundaries to allow for optical microscopy of the samples to determine grain sizes. While electrolytic etchant might allow for mapping of the grains in all the zones of the weld, EBSD analysis would provide a greater volume of data. It would be advantageous to map the entire surface of a sample using EBSD and to characterize not only the grain size distribution, but also the misorientation between adjacent grains, and any texture that might exist in the strata of the weld onion.

The limitations of the FSF system did not allow for a complete characterization of the effects of the  $\omega/v$  ratio on the spacing of the onion strata nor on grain size distribution. It would be particularly interesting to explore the effects of low  $\omega/v$  ratios on the microstructure of the weld. The maximum translation speed of our system was  $\sim 25$  mm/min. Such a slow translation results in relatively uniform temperature profiles in the z-direction of the samples. A faster translation speed could act to reduce softening of the HAZ by reducing the maximum temperature attained therein.

It would also be illustrative to explore the effects of the addition of a hard phase into the weld in the *in-situ* MMC friction stir fabrication. Studies suggest that the dynamical recrystallization is affected by the relative hardness of the phases in the material[28]. While not only increasing the hardness of the material directly as a reinforcement, particles might also act to strengthen the material by further refining the grain in the DRZ. Deposition of *in-situ* MMC had originally been envisioned as a portion of this work. Due to the novelty of the process, characterization of the friction stir fabrication process required a large investment in time. Now that the process operation window has been outlined, and the limitations of the equipment exposed, work in an active, MMC system should be able to proceed at a rapid pace.

## 6 References

1. G. Liu, L.E.M., C-S Niou, J.C. McClure, F.R. Vega, *Microstructural Aspects of the Friction-Stir Welding of 6061-T6 Aluminum*. Scripta Materialia, 1997. **37**(3): p. 355-361.
2. R.S. Mishra, Z.Y.M., *Friction Stir Welding and Processing*. Material Science and Engineering,, 2005(R50): p. 1-78.
3. Jata, K.V. and S.L. Semiatin, *Continuous dynamic recrystallization during friction stir welding of high strength aluminum alloys*. Scripta Materialia, 2000. **43**: p. 743-749.
4. K. Tsuzaki, H.X., T. Maki, *Mechanism of Dynamic Continuous Recrystallization During Superplastic Deformation in a Microduplex Stainless Steel*. Acta Materialia, 1996. **44**(11): p. 4491-4499.
5. O.V. Flore, C.K., L.E. Murr, D. Brown, S. Pappas, B. Nowak, J.C. McClure, *Microstructural Issues in a Friction-Stir Welded Aluminum Alloy*. Scripta Materialia, 1998. **38**(5): p. 705-708.
6. C.G. Rhodes, e.a., *Effects of Friction Stir Welding on the Microstructure of 7075 Aluminum*. Scripta Materialia, 1997. **36**(1): p. 69-75.
7. Su, J.Q., et al., *Microstructural investigation of friction stir welded 7050-T651 aluminium*. Acta Materialia, 2003. **51**(3): p. 713-729.
8. J.Q. Su, T.W.N., R. Mishra, M. Mahoney, *Microstructural Investigation of Friction Stir Welded 7050-T651 Aluminum*. Acta Materialia, 2003. **51**: p. 713-729.
9. Johannes, L.B., et al., *Enhanced superplasticity through friction stir processing in continuous cast AA5083 aluminum*. Materials Science and Engineering: A, 2007. **464**(1-2): p. 351-357.
10. Peel, M., et al., *Microstructure, mechanical properties and residual stresses as a function of welding speed in aluminium AA5083 friction stir welds*. Acta Materialia, 2003. **51**(16): p. 4791-4801.
11. R.S. Mishra, M.W.M., S.X. McFadden, N.A. Mara, A.K. Mukherjee, Scripta Materialia, 2000: p. 163.
12. R.S. Mishra, M.W.M., mat. sci. forum, 2001. **357-359**: p. 507.
13. Myhr, O.R. and Ø. Grong, *Dimensionless maps for heat flow analyses in fusion welding*. Acta Metallurgica et Materialia, 1990. **38**(3): p. 449-460.
14. Myhr, O.R. and Ø. Grong, *Process modelling applied to 6082-T6 aluminium weldments--I. Reaction kinetics*. Acta Metallurgica et Materialia, 1991. **39**(11): p. 2693-2702.
15. Frigaard, Ø., Ø. Grong, and O. Midling, *A process model for friction stir welding of age hardening aluminum alloys*. Metallurgical and Materials Transactions A, 2001. **32**(5): p. 1189-1200.
16. Frigaard, O., *A process model for friction stir welding of age hardening aluminum alloys*, in *Department of Materials Technology and Electrochemistry*. 1999, The Norwegian University of Science and Technology: Trondheim. p. 235.
17. Song, M. and R. Kovacevic, *Thermal modeling of friction stir welding in a moving coordinate system and its validation*. International Journal of Machine Tools and Manufacture, 2003. **43**(6): p. 605-615.

18. Soundararajan, V., S. Zekovic, and R. Kovacevic, *Thermo-mechanical model with adaptive boundary conditions for friction stir welding of Al 6061*. International Journal of Machine Tools and Manufacture, 2005. **45**(14): p. 1577-1587.
19. Nandan, R., G. Roy, and T. Debroy, *Numerical simulation of three-dimensional heat transfer and plastic flow during friction stir welding*. Metallurgical and Materials Transactions A, 2006. **37**(4): p. 1247-1259.
20. Schmidt, H.B. and J.H. Hattel, *Thermal modelling of friction stir welding*. Scripta Materialia, 2008. **58**(5): p. 332-337.
21. Kamp, N., A. Sullivan, and J.D. Robson, *Modelling of friction stir welding of 7xxx aluminium alloys*. Materials Science and Engineering: A, 2007. **466**(1-2): p. 246-255.
22. Chen, C.M. and R. Kovacevic, *Finite element modeling of friction stir welding--thermal and thermomechanical analysis*. International Journal of Machine Tools and Manufacture, 2003. **43**(13): p. 1319-1326.
23. Heurtier, P., et al., *Mechanical and thermal modelling of Friction Stir Welding*. Journal of Materials Processing Technology, 2006. **171**(3): p. 348-357.
24. Myhr, O.R. and Ø. Grong, *Process modelling applied to 6082-T6 aluminium weldments--II. Applications of model*. Acta Metallurgica et Materialia, 1991. **39**(11): p. 2703-2708.
25. Incropera, F.P.a.D., David P., *Introduction to Heat Transfer*. Third Edition ed. 1996, New York: John Wiley and Sons.
26. Hirata, T., et al., *Influence of friction stir welding parameters on grain size and formability in 5083 aluminum alloy*. Materials Science and Engineering: A, 2007. **456**(1-2): p. 344-349.
27. Mishra, R.S. and Z.Y. Ma, *Friction stir welding and processing*. Materials Science and Engineering: R: Reports, 2005. **50**(1-2): p. 1-78.
28. Tsuzaki, K., X. Huang, and T. Maki, *Mechanism of dynamic continuous recrystallization during superplastic deformation in a microduplex stainless steel*. Acta Materialia, 1996. **44**(11): p. 4491-4499.

## Appendix A Conversion from dimensional to dimensionless form of the heat equation

The heat equation derived from Fourier's first law is written as

$$\frac{\partial T}{\partial t} = \alpha \nabla^2 T + q_r$$

where  $\alpha$  is the thermal diffusivity of the material in  $\text{m}^2/\text{s}$ , and  $q_r$  is the volumetric heat generation within the system in  $\text{K}/\text{s}$ . Using the thermal diffusivity, a characteristic temperature (here the melting temperature of the alloy) and a characteristic length (here the thickness of the sample), the parameters in the original heat equation can be normalized to dimensionless parameters, as described in Table 1.

Table 1 Summary of dimensional and dimensionless parameters

Parameter	Symbol	Units	Dimensionless Parameter	Conversion Equation
thermal diffusivity	$\alpha$	$\text{m}^2/\text{s}$	-	-
temperature	$T$	K	$\theta$	$\theta = T/T_m$
time	$t$	s	$\tau$	$\tau = t \alpha / L_z^2$
length	$x$	m	$u$	$u = x/L_z$
width	$y$	m	$v$	$v = y/L_z$
depth	$z$	m	$w$	$w = z/L_z$
volumetric heat	$q_r$	$\text{K}/\text{s}$	$Q$	$Q = q_r L_z^2 / (T_m \alpha)$
heat transfer coefficient	$h_r$	$\text{m}/\text{s}$	$\tilde{h}$	$\tilde{h} = h_r L_z^2 / \alpha$

Substituting

$$T = \theta T_m$$

and

$$q_r = Q \frac{T_m \alpha}{L_z^2}$$

into the one dimensional form of the heat equation yields

$$\frac{\partial}{\partial t} \theta T_m = \alpha \frac{\partial}{\partial x} \left( \frac{\partial}{\partial x} \theta T_m \right) + Q \frac{T_m \alpha}{L_z^2}$$

Wherefrom it follows that

$$T_m \frac{\partial \theta}{\partial t} = \alpha T_m \frac{\partial}{\partial x} \left( \frac{\partial \theta}{\partial x} \right) + Q \frac{T_m \alpha}{L_z^2}$$

$$T_m \frac{\partial \theta}{\partial \tau} \frac{\partial \tau}{\partial t} = \alpha T_m \frac{\partial}{\partial x} \left( \frac{\partial \theta}{\partial u} \frac{\partial u}{\partial x} \right) + Q \frac{T_m \alpha}{L_z^2}$$

$$T_m \frac{\partial \theta}{\partial \tau} \frac{\partial}{\partial t} \left( \frac{\alpha t}{L_z^2} \right) = \alpha T_m \frac{\partial}{\partial x} \left( \frac{\partial \theta}{\partial u} \frac{\partial}{\partial x} \left( \frac{x}{L_z} \right) \right) + Q \frac{T_m \alpha}{L_z^2}$$

$$\frac{T_m \alpha}{L_z^2} \frac{\partial \theta}{\partial \tau} = \frac{\alpha T_m}{L_z} \frac{\partial}{\partial x} \left( \frac{\partial \theta}{\partial u} \right) + Q \frac{T_m \alpha}{L_z^2}$$

$$\frac{T_m \alpha}{L_z^2} \frac{\partial \theta}{\partial \tau} = \frac{\alpha T_m}{L_z^2} \frac{\partial}{\partial u} \left( \frac{\partial \theta}{\partial u} \right) + Q \frac{T_m \alpha}{L_z^2}$$

and finally that

$$\frac{\partial \theta}{\partial \tau} = \nabla^2 \theta + Q$$

## Appendix B Derivation of Implicit, Dimensionless Boundary Conditions

### Interior Node

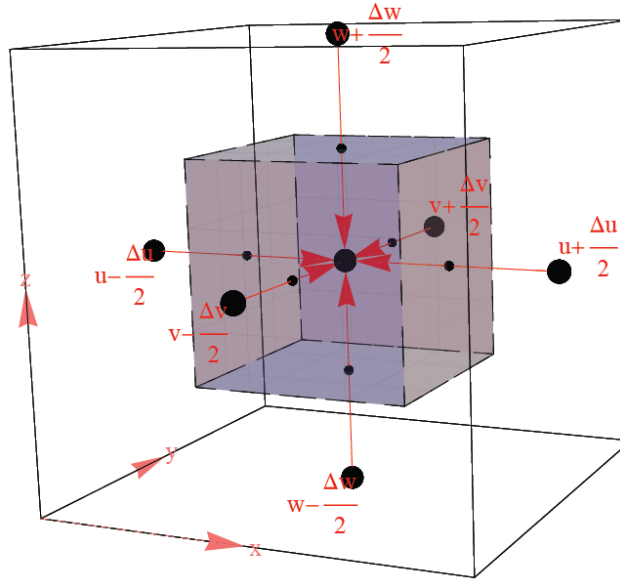


Figure B1 Schematic representation of internal node

As described in Section 2.2.1, for an internal node in the sample (Figure B1), the energy balance equation can be written as

$$\frac{1}{\Delta\tau}(\theta^P - \theta^0) = \frac{\theta^{u+1} - 2\theta^P + \theta^{u-1}}{\Delta u^2} + \frac{\theta^{v+1} - 2\theta^P + \theta^{v-1}}{\Delta v^2} + \frac{\theta^{w+1} - 2\theta^P + \theta^{w-1}}{\Delta w^2} + Q$$

where  $\theta^P$  is the dimensionless temperature at node P and time  $\tau + \Delta\tau$ .  $\theta^{u+1}$  is the dimensionless temperature at the neighboring node in the u-direction at time  $\tau + \Delta\tau$ .  $\theta^0$  is the temperature of node P at time  $\tau$ .  $\Delta u$ ,  $\Delta v$  and  $\Delta w$  are the dimensions of the mesh in the u, v, and w directions, respectively.

Solving for  $\theta^P$  yields

$$\alpha_B \theta^P = \Delta v^2 \Delta w^2 (\theta^{u+1} + \theta^{u-1}) + \Delta u^2 \Delta w^2 (\theta^{v+1} + \theta^{v-1}) + \Delta u^2 \Delta v^2 (\theta^{w+1} + \theta^{w-1}) + Q \Delta u^2 \Delta v^2 \Delta w^2 + \frac{\Delta u^2 \Delta v^2 \Delta w^2}{\Delta\tau} \theta^0$$

where

$$\alpha_B = \frac{\Delta u^2 \Delta v^2 \Delta w^2}{\Delta \tau} + 2\Delta v^2 \Delta w^2 + 2\Delta u^2 \Delta w^2 + 2\Delta u^2 \Delta v^2$$

and Q represents the dimensionless volumetric heat generation within the node.

**Node on a convective surface**

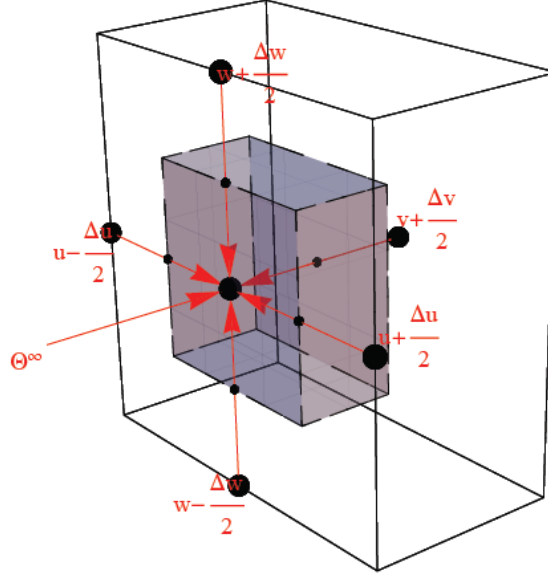


Figure B2 Schematic representation of a node at a convective surface

For the node at a convective surface depicted in Figure B2, the energy balance is given as

$$\frac{1}{\Delta \tau} (\theta^P - \theta^0) = \bar{h}(\theta^\infty - \theta^P) \Delta v \Delta w + \frac{\theta^{u+1} - \theta^P}{\Delta u^2} + \frac{\theta^{v+1} - 2\theta^P + \theta^{v-1}}{\Delta v^2} + \frac{\theta^{w+1} - 2\theta^P + \theta^{w-1}}{\Delta w^2} + Q$$

solving for  $\theta^P$  yields

$$\alpha_P \theta^P = \bar{h} \Delta u^2 \Delta v^3 \Delta w^3 (\theta^\infty) + \Delta v^2 \Delta w^2 (\theta^{u+1}) + \Delta u^2 \Delta w^2 (\theta^{v+1} + \theta^{v-1}) + \Delta u^2 \Delta v^2 (\theta^{w+1} + \theta^{w-1}) + Q \Delta u^2 \Delta v^2 \Delta w^2 + \frac{\Delta u^2 \Delta v^2 \Delta w^2}{\Delta \tau} \theta^0$$

where

$$\alpha_P = \frac{\Delta u^2 \Delta v^2 \Delta w^2}{\Delta \tau} + \bar{h} \Delta u^2 \Delta v^3 \Delta w^3 + \Delta v^2 \Delta w^2 + 2\Delta u^2 \Delta w^2 + 2\Delta u^2 \Delta v^2$$

where  $\bar{h}$  is the dimensionless convective heat transfer coefficient at the surface.

### Node at a convective edge

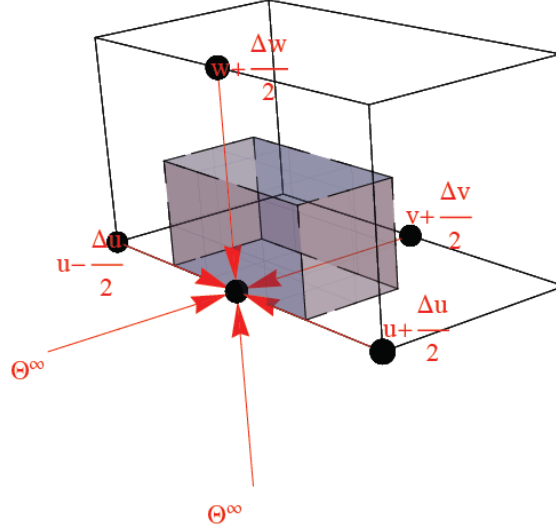


Figure B3 Schematic representation of a node at a convective edge

For a node on the edge of the workpiece, there are two half-planes of convection. The energy balance for the node shown in Figure B3 is therefore given as

$$\frac{1}{\Delta\tau}(\theta^P - \theta^0) = \frac{\bar{h}(\theta^\infty - \theta^P)\Delta v\Delta w}{2} + \frac{\theta^{u+1} - \theta^P}{\Delta u^2} + \frac{\theta^{v+1} - 2\theta^P + \theta^{v-1}}{\Delta v^2} + \frac{\bar{h}(\theta^\infty - \theta^P)\Delta u\Delta v}{2} + \frac{\theta^{w+1} - \theta^P}{\Delta w^2} + Q$$

solving for  $\theta^P$  yields

$$\alpha_E \theta^P = \left( \frac{\bar{h}\Delta u^2\Delta v^3\Delta w^3}{2} + \frac{\bar{h}\Delta u^3\Delta v^3\Delta w^2}{2} \right) (\theta^\infty) + \Delta v^2\Delta w^2(\theta^{u+1}) + \Delta u^2\Delta w^2(\theta^{v+1} + \theta^{v-1}) + \Delta u^2\Delta v^2(\theta^{w+1}) + Q\Delta u^2\Delta v^2\Delta w^2 + \frac{\Delta u^2\Delta v^2\Delta w^2}{\Delta\tau} \theta^0$$

with

$$\alpha_E = \frac{\Delta u^2\Delta v^2\Delta w^2}{\Delta\tau} + \frac{\bar{h}\Delta u^2\Delta v^3\Delta w^3}{2} + \Delta v^2\Delta w^2 + 2\Delta u^2\Delta w^2 + \frac{\bar{h}\Delta u^3\Delta v^3\Delta w^2}{2} + \Delta u^2\Delta v^2$$

In general, the  $\bar{h}$  terms should contain indexes corresponding to the surface of convective heat transfer. Generalizing the heat transfer coefficients is required in order to allow for different heat transfer mechanisms at the different boundary conditions. For our model, the top and four sides of the sample have identical boundary conditions (save the region within the radius of the tool on the top surface). The heat transfer to the backside of the workpiece is

different, representing the different mechanism and magnitude of transfer to the cooling block. Our boundary equations therefore have  $\bar{h}$  terms equivalent for the xy plane at  $z = 0$  and the yz and xz planes. For the xy plane at  $z = L_z$ , the  $\bar{h}$  term is changed to an  $\bar{h}_b$  term.

### Node at a convective corner

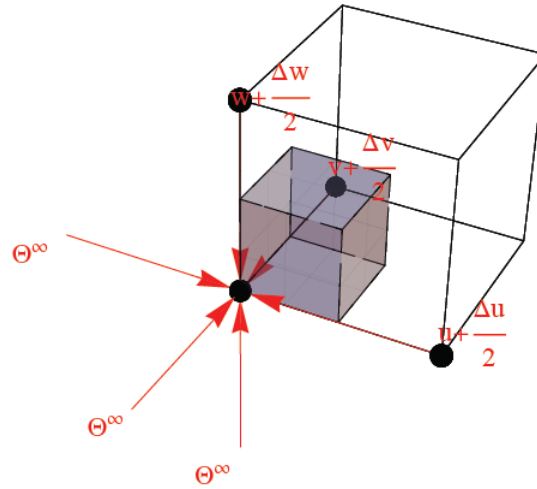


Figure B4 Schematic representation of a node at a convective corner

A node at a corner of the sample has three half-planes of convection, as shown in Figure B4. For the corner node, the energy balance can be written as

$$\frac{1}{\Delta\tau}(\theta^P - \theta^0) = \frac{\bar{h}(\theta^\infty - \theta^P)\Delta v\Delta w}{4} + \frac{\theta^{u+1} - \theta^P}{\Delta u^2} + \frac{\bar{h}(\theta^\infty - \theta^P)\Delta u\Delta w}{4} + \frac{\theta^{v-1} - \theta^P}{\Delta v^2} + \frac{\bar{h}(\theta^\infty - \theta^P)\Delta u\Delta v}{4} + \frac{\theta^{w+1} - \theta^P}{\Delta w^2} + Q$$

Solving for  $\theta^P$  yields

$$\alpha_C \theta^P = \left( \frac{\bar{h}\Delta u^2\Delta v^3\Delta w^3}{4} + \frac{\bar{h}\Delta u^3\Delta v^2\Delta w^3}{4} + \frac{\bar{h}\Delta u^3\Delta v^3\Delta w^2}{4} \right) (\theta^\infty) + \Delta v^2\Delta w^2(\theta^{u+1}) \\ + \Delta u^2\Delta w^2(\theta^{v-1}) + \Delta u^2\Delta v^2(\theta^{w+1}) + Q\Delta u^2\Delta v^2\Delta w^2 + \frac{\Delta u^2\Delta v^2\Delta w^2}{\Delta\tau} \theta^0$$

where

$$\alpha_C = \frac{\Delta u^2\Delta v^2\Delta w^2}{\Delta\tau} + \frac{\bar{h}\Delta u^2\Delta v^3\Delta w^3}{4} + \Delta v^2\Delta w^2 + \frac{\bar{h}\Delta u^3\Delta v^2\Delta w^3}{4} + \Delta u^2\Delta w^2 + \frac{\bar{h}\Delta u^3\Delta v^3\Delta w^2}{2} + \Delta u^2\Delta v^2$$

## Appendix C 3-D Implicit Model Mathematica® Code

```
(*Dimensionless Numerical method for FSF,
rectilinear mesh with uniform spacing along three
dimensions. Symmetry about y=
0 to reduce computational requirements*)

Clear["Global`*"]; Share[]; $RecursionLimit = 20000;

<< PlotLegends`

 $\Delta\tau = 10;$ 

trest = 3.25  $\times$  60 (*seconds*);
 $\tau$ rest = Round[trest  $\alpha$  / Lz / Lz];
trest2 = 3.25  $\times$  60 (*seconds*);
 $\tau$ rest2 = Round[trest2  $\alpha$  / Lz / Lz];
tnub = 120;
 $\tau$ nub = Round[tnub  $\alpha$  / Lz / Lz];

tadq = Round[ ((Lx - r) / vx + Max[trest, trest2]) ];

(*setup physicaldimensions of the mesh. Define nondimensional u,
v,w and set the grid spacing equal in each dimesnion.*)
Lx = 4  $\times$  25.4 / 1000; Ly = 1.25  $\times$  25.4 / 1000 / 2; Lz = .5  $\times$  25.4 / 1000;
Lu = Lx / Lz; Lv = Ly / Lz; Lw = Lz / Lz;
Mw = 5;  $\Delta w = Lw / Mw$ ;
Mu = 24 (*Round[Lu /  $\Delta w$ ]*); Mv = 5 (*Round[Lv /  $\Delta w$ ]*);
 $\Delta u = Lu / Mu$ ;  $\Delta v = Lv / Mv$ ;
 $\Delta V = \Delta u \Delta v \Delta w$ ;
 $\Delta x = \Delta u Lz$ ;  $\Delta y = \Delta v Lz$ ;
 $\Delta z = \Delta w Lz$ ;

Mu;
Mv;
Mw;
Mu Mv Mw;
```

```

(*define physical parameters of the system for scaling
and graphical representation*)
 $\alpha = 230 / (2702 \times 902)$  (*m2/s*);
Tm = 550 + 300 (*K*);
Tamb = 300; (*K*)
Tamb2 = 400;
 $\theta_{amb} = Tamb / Tm$ ;
 $\theta_{amb2} = Tamb2 / Tm$ ;
hr = h / (2702  $\times$  902) / ( $\Delta x \Delta y \Delta z$ ) (*m/s*);
h = 50 (*w/m2K*);
 $H = \frac{Lz^4}{\alpha} hr$ ;
hrb = hb / (2702  $\times$  902) / ( $\Delta x \Delta y \Delta z$ ) (*m/s*);
hb = 1200 (*w/m2K*);
 $Hb = \frac{Lz^4}{\alpha} hrb$ ;
ktherm = 230;  $\rho = 2702$ ;
cp = 902;

vx = 0.6  $\times$  25.4  $\times$  10-3 / 60 (*m/s*);
vy = 0 (*m/s*);
vu[n_] := vx  $\frac{Lz}{\alpha}$  /; n  $\Delta \tau \geq \tau_{rest}$ ;
vu[n_] := 0 /; n  $\Delta \tau < \tau_{rest}$ ;
vv[n_] := vy

r = .5  $\times$  25.4 / 1000;
R = r / Lz;

tadq = Round [ ((Lx - r) / vx + Max[trest, trest2]) ];
 $\tau_{adq} = Round [\tau_{adq} \alpha / Lz / Lz]$ ;
nadq = Round [ $\tau_{adq} / \Delta \tau$ ];

```

545

32

```

norm[i_, j_] := (i Δu - Lu/2)^2 + (j Δv - Lv/2)^2 /;
  (i Δu - Lu/2)^2 + (j Δv - Lv/2)^2 ≤ R^2;
norm[i_, j_] := 0 /; (i Δu - Lu/2)^2 + (j Δv - Lv/2)^2 > R^2;
nnorm =
  Total[Table[norm[i, j],
    {i, Mu/2 - Floor[R/Δu], Mu/2 + Floor[R/Δu]},
    {j, Mv/2 - Floor[R/Δv], Mv/2 + Floor[R/Δv]}], 2];
source = Table[norm[i, j] / nnorm,
  {i, Mu/2 - Floor[R/Δu], Mu/2 + Floor[R/Δu]},
  {j, Mv/2 - Floor[R/Δv], Mv/2 + Floor[R/Δv]}];
MatrixForm[source];

neg[i_, j_] := H /; (i Δu - Lu/2)^2 + (j Δv - Lv/2)^2 ≤ R^2;
neg[i_, j_] := 0 /; (i Δu - Lu/2)^2 + (j Δv - Lv/2)^2 > R^2;
negsource = Table[neg[i, j],
  {i, Mu/2 - Floor[R/Δu], Mu/2 + Floor[R/Δu]},
  {j, Mv/2 - Floor[R/Δv], Mv/2 + Floor[R/Δv]}];
MatrixForm[negsource];

x0 = (1) 25.4 / 1000;
y0 = 0;
u0 = x0 / Lz;
v0 = y0 / Lz;

pf = .35;
p1 = pf (5) 745 (*W*);
p2 = pf (2.5) 745;
qr1 =  $\frac{p2}{\rho \text{ cp } \Delta x \Delta y \Delta z}$ ;
qr =  $\frac{p1}{\rho \text{ cp } \Delta x \Delta y \Delta z}$  (*K/s*);
Qc[n_] := qr1  $\frac{Lz^2}{Tm \alpha}$  /; n Δτ ≤ τnub;
Qc[n_] :=
  qr1  $\frac{Lz^2}{Tm \alpha}$  + (qr - qr1)  $\frac{Lz^2}{Tm \alpha}$  / (τrest2 - τnub) (n - τnub / Δτ) Δτ /;
  And[n Δτ > τnub, n Δτ < τrest2];
Qc[n_] := qr  $\frac{Lz^2}{Tm \alpha}$  /; n Δτ ≥ τrest2;

```

```

Plot[Qc[n]/(Lz^2/Tm alpha)/qr, {n, 0, nadq}, PlotRange -> All,
  AxesOrigin -> {0, 0}];

facu[n_] := (vu[n] (n - Round[trrest/Delta tau] Delta tau + u0) / Delta u -
  Quotient[(vu[n] (n - Round[trrest/Delta tau] Delta tau + u0), Delta u]
qu[n_] := Quotient[vu[n] (n - Round[trrest/Delta tau] Delta tau + u0), Delta u]
facv[n_] := (vv[n] (n - Round[trrest/Delta tau] Delta tau + v0) / Delta v -
  Quotient[(vv[n] (n - Round[trrest/Delta tau] Delta tau + v0), Delta v]
qv[n_] := Quotient[vv[n] (n - Round[trrest/Delta tau] Delta tau + v0), Delta v]
cent3[n_] :=
  SparseArray[{{qu[n] + 1, qv[n] + 1} -> (1 - facu[n]) (1 - facv[n]),
    {qu[n] + 1, qv[n] + 2} -> (1 - facu[n]) (facv[n]),
    {qu[n] + 2, qv[n] + 1} -> facu[n] (1 - facv[n]),
    {qu[n] + 2, qv[n] + 2} -> facu[n] facv[n]}, {Mu + 1, Mv + 1}] /;
  And[Abs[qu[n]] <= Mu - 1, Abs[qv[n]] <= Mv - 1, qu[n] >= 0,
    qv[n] >= 0];
cent3[n_] := ConstantArray[0, {Mu + 1, Mv + 1}] /;
  Or[Abs[qu[n]] > Mu - 1, Abs[qv[n]] > Mv - 1, qu[n] < 0, qv[n] < 0]
S[n_] :=
  Qc[n] ListConvolve[source, cent3[n],
    {{(Dimensions[source][[1]] + 1) / 2,
      (Dimensions[source][[2]] + 1) / 2},
    {(Dimensions[source][[1]] + 1) / 2,
      (Dimensions[source][[2]] + 1) / 2}}, 0];
Htop[n_] := ListConvolve[negsource, cent3[n],
  {{(Dimensions[source][[1]] + 1) / 2,
    (Dimensions[source][[2]] + 1) / 2},
  {(Dimensions[source][[1]] + 1) / 2,
    (Dimensions[source][[2]] + 1) / 2}}, 0];

(*set coordinates of initial elevated temperature for
code testing*)
ic = Mu; jc = Mv;
kc = Mw;

```

```

(*setup initial conditions on dimensionless temperate  $\theta =$ 
  T/Tm. Also set one grid point to an elevated temp for
  testing*)
 $\theta_{init} = (300) / T_m;$ 
 $\theta_2 = (300) / T_m;$ 
 $\theta_{tab1} =$ 
  Flatten[Table[{i, j, k}, {i, 0, Mu}, {j, 0, Mv}, {k, 0, Mw}], 2];
 $\theta_d =$  Flatten[Table[ $\theta[i, j, k, 0] \rightarrow \theta_0[i, j, k]$ , {i, 0, Mu},
  {j, 0, Mv}, {k, 0, Mw}]];
 $\theta_d[[\text{Position}[\theta_{tab1}, \{ic, jc, kc\}][[1, 1]]]] = \theta[ic, jc, kc, 0] \rightarrow \theta_2;$ 
 $\theta_0[i_, j_, k_] = \theta_{init};$ 
 $sol[0] = \theta_d;$ 
(*sol[0]=
  Flatten[Table[T[i,j,k,0] $\rightarrow$ T0[i  $\Delta x$ , j  $\Delta y$ , k  $\Delta z$ ], {i,0,Mx},
  {j,0,My}, {k,0,Mz}]];*)
MatrixForm[sol[0]];

(*fixed boundary conditions*)
(* $\theta[0, j_, k_, n_] := 300/T_m;$ 
 $\theta[i_, 0, k_, n_] := 300/T_m;$ 
 $\theta[i_, j_, 0, n_] := 300/T_m;$ 
 $\theta[\mu, j_, k_, n_] := 300/T_m;$ 
 $\theta[i_, \nu, k_, n_] := 300/T_m;$ 
 $\theta[i_, j_, \nu, n_] := 300/T_m;*$ )

 $Q[i_, j_, k_, n_] := S[n][[i+1, j+1]] /; k == 0$ 
(*And[k=0, n<300/ $\Delta \tau$ ]*);
 $Q[i_, j_, k_, n_] := 0 /; k \neq 0;$ 
(*Q[i_, j_, k_, n_] := 0 /; n>50*)
(*define temporary zero heat input*)

```

(\*define  $\theta_p$  coefficients for grid equations\*)

(\*bulk\*)

$$\alpha_b = \frac{\Delta V^2}{\Delta \tau} + 2 \Delta v^2 \Delta w^2 + 2 \Delta u^2 \Delta w^2 + 2 \Delta u^2 \Delta v^2;$$

$$\alpha_{puw0} = \frac{\Delta V^2}{\Delta \tau} + 2 \Delta v^2 \Delta w^2 + 2 \Delta u^2 \Delta w^2 + 2 \Delta u^2 \Delta v^2;$$

(\*mirror on  $y=0$  plane\*)

(\*planes\*)

$$\alpha_{puv} [i_, j_, n_] := \frac{\Delta V^2}{\Delta \tau} + 2 \Delta v^2 \Delta w^2 + 2 \Delta u^2 \Delta w^2 + \Delta u^2 \Delta v^2 +$$
$$(H - H_{top}[n] [[i+1, j+1]]) \Delta u \Delta v \Delta V^2;$$

$$\alpha_{puvb} = \frac{\Delta V^2}{\Delta \tau} + 2 \Delta v^2 \Delta w^2 + 2 \Delta u^2 \Delta w^2 + \Delta u^2 \Delta v^2 + H_b \Delta u \Delta v \Delta V^2;$$

$$\alpha_{pvw} = \frac{\Delta V^2}{\Delta \tau} + \Delta v^2 \Delta w^2 + 2 \Delta u^2 \Delta w^2 + 2 \Delta u^2 \Delta v^2 + H \Delta v \Delta w \Delta V^2;$$

$$\alpha_{puw} = \frac{\Delta V^2}{\Delta \tau} + 2 \Delta v^2 \Delta w^2 + \Delta u^2 \Delta w^2 + 2 \Delta u^2 \Delta v^2 + H \Delta u \Delta w \Delta V^2;$$

$$\alpha_{eu0} = \frac{\Delta V^2}{\Delta \tau} + 2 \Delta v^2 \Delta w^2 + 2 \Delta u^2 \Delta w^2 + \Delta u^2 \Delta v^2 + H \Delta u \Delta v \Delta V^2;$$

(\* $y=0$  edge mirror, top convection\*)

$$\alpha_{eu0b} = \frac{\Delta V^2}{\Delta \tau} + 2 \Delta v^2 \Delta w^2 + 2 \Delta u^2 \Delta w^2 + \Delta u^2 \Delta v^2 + H_b \Delta u \Delta v \Delta V^2;$$

(\* $y=0$  edge mirror, bottom convection\*)

$$\alpha_{ew0} = \frac{\Delta V^2}{\Delta \tau} + \Delta v^2 \Delta w^2 + 2 \Delta u^2 \Delta w^2 + 2 \Delta u^2 \Delta v^2 + H \Delta v \Delta w \Delta V^2;$$

(\* $y=0$  edge mirror, top convection\*)

(\*edges\*)

$$\alpha_{eu} = \frac{\Delta V^2}{\Delta \tau} + 2 \Delta v^2 \Delta w^2 + \Delta u^2 \Delta w^2 + \Delta u^2 \Delta v^2 + \frac{H \Delta u \Delta v \Delta V^2}{2} + \frac{H \Delta u \Delta w \Delta V^2}{2};$$

$$\alpha_{eub} = \frac{\Delta V^2}{\Delta \tau} + 2 \Delta v^2 \Delta w^2 + \Delta u^2 \Delta w^2 + \Delta u^2 \Delta v^2 + \frac{H_b \Delta u \Delta v \Delta V^2}{2} + \frac{H \Delta u \Delta w \Delta V^2}{2};$$

$$\alpha_{ev} = \frac{\Delta V^2}{\Delta \tau} + \Delta v^2 \Delta w^2 + 2 \Delta u^2 \Delta w^2 + \Delta u^2 \Delta v^2 + \frac{H \Delta u \Delta v \Delta V^2}{2} + \frac{H \Delta v \Delta w \Delta V^2}{2};$$

$$\alpha_{evb} = \frac{\Delta V^2}{\Delta \tau} + \Delta v^2 \Delta w^2 + 2 \Delta u^2 \Delta w^2 + \Delta u^2 \Delta v^2 + \frac{H_b \Delta u \Delta v \Delta V^2}{2} + \frac{H \Delta v \Delta w \Delta V^2}{2};$$

$$\alpha_{ew} = \frac{\Delta V^2}{\Delta \tau} + \Delta v^2 \Delta w^2 + \Delta u^2 \Delta w^2 + 2 \Delta u^2 \Delta v^2 + \frac{H \Delta u \Delta w \Delta V^2}{2} + \frac{H \Delta v \Delta w \Delta V^2}{2};$$

```

sol[n_] := sol[n] =
Module[{vars, eqns},
(*define the variables*)

vars = Flatten[Table[ $\theta[i, j, k, n]$ , {i, 0, Mu}, {j, 0, Mv},
{k, 0, Mw}]];
eqns = Flatten[{

(*bulk*)
Table[
 $\theta[i, j, k, n] =$ 

$$\frac{1}{\alpha b} \left( \Delta v^2 \Delta w^2 (\theta[i+1, j, k, n] + \theta[i-1, j, k, n]) + \right.$$


$$\Delta u^2 \Delta w^2 (\theta[i, j+1, k, n] + \theta[i, j-1, k, n]) +$$


$$\Delta u^2 \Delta v^2 (\theta[i, j, k+1, n] + \theta[i, j, k-1, n]) +$$


$$\left. \frac{\Delta V^2}{\Delta \tau} \theta[i, j, k, n-1] + \Delta V^2 Q[i, j, k, n] \right), \{i, 1, Mu-1\},$$

{j, 1, Mv-1}, {k, 1, Mw-1}],

```

(\*planes\*)

$$\begin{aligned} & \text{Table[} \\ & \theta[0, j, k, n] = \\ & \frac{1}{\alpha_{pvw}} \\ & \left( \Delta v^2 \Delta w^2 (\theta[1, j, k, n]) + \right. \\ & \quad \Delta u^2 \Delta w^2 (\theta[0, j+1, k, n] + \theta[0, j-1, k, n]) + \\ & \quad \Delta u^2 \Delta v^2 (\theta[0, j, k+1, n] + \theta[0, j, k-1, n]) + H \Delta v \Delta w \Delta V^2 \theta_{amb} + \\ & \quad \left. \frac{\Delta V^2}{\Delta \tau} \theta[0, j, k, n-1] + \Delta V^2 Q[0, j, k, n] \right), \{j, 1, Mv-1\}, \\ & \left. \{k, 1, Mw-1\} \right], \end{aligned}$$

$$\begin{aligned} & \text{Table[} \\ & \theta[Mu, j, k, n] = \\ & \frac{1}{\alpha_{pvw}} \\ & \left( \Delta v^2 \Delta w^2 (\theta[Mu-1, j, k, n]) + \right. \\ & \quad \Delta u^2 \Delta w^2 (\theta[Mu, j+1, k, n] + \theta[Mu, j-1, k, n]) + \\ & \quad \Delta u^2 \Delta v^2 (\theta[Mu, j, k+1, n] + \theta[Mu, j, k-1, n]) + \\ & \quad \left. H \Delta v \Delta w \Delta V^2 \theta_{amb} + \frac{\Delta V^2}{\Delta \tau} \theta[Mu, j, k, n-1] + \Delta V^2 Q[Mu, j, k, n] \right), \\ & \left. \{j, 1, Mv-1\}, \{k, 1, Mw-1\} \right], \end{aligned}$$

$$\begin{aligned} & \text{Table[} \\ & \theta[i, 0, k, n] = \\ & \frac{1}{\alpha_{puw0}} \left( \Delta v^2 \Delta w^2 (\theta[i+1, 0, k, n] + \theta[i-1, 0, k, n]) + \right. \\ & \quad \Delta u^2 \Delta w^2 (\theta[i, 1, k, n] + \theta[i, 1, k, n]) + \\ & \quad \Delta u^2 \Delta v^2 (\theta[i, 0, k+1, n] + \theta[i, 0, k-1, n]) + \\ & \quad \left. \frac{\Delta V^2}{\Delta \tau} \theta[i, 0, k, n-1] + \Delta V^2 Q[i, 0, k, n] \right), \{i, 1, Mu-1\}, \\ & \left. \{k, 1, Mw-1\} \right], \end{aligned}$$

Table[

$$\theta[i, Mv, k, n] =$$

$$\frac{1}{\alpha_{puw}} \left( \Delta v^2 \Delta w^2 (\theta[i+1, Mv, k, n] + \theta[i-1, Mv, k, n]) + \Delta u^2 \Delta w^2 (\theta[i, Mv-1, k, n]) + \Delta u^2 \Delta v^2 (\theta[i, Mv, k+1, n] + \theta[i, Mv, k-1, n]) + H \Delta u \Delta w \Delta v^2 \theta_{amb} + \frac{\Delta V^2}{\Delta \tau} \theta[i, Mv, k, n-1] + \Delta V^2 Q[i, Mv, k, n] \right),$$

$$\{i, 1, Mu-1\}, \{k, 1, Mw-1\}],$$

Table[

$$\theta[i, j, 0, n] =$$

$$\frac{1}{\alpha_{puv}[i, j, n]} \left( \Delta v^2 \Delta w^2 (\theta[i+1, j, 0, n] + \theta[i-1, j, 0, n]) + \Delta u^2 \Delta w^2 (\theta[i, j+1, 0, n] + \theta[i, j-1, 0, n]) + \Delta u^2 \Delta v^2 (\theta[i, j, 1, n]) + (H - H_{top}[n][[i+1, j+1]]) \Delta u \Delta v \Delta v^2 \theta_{amb} + \frac{\Delta V^2}{\Delta \tau} \theta[i, j, 0, n-1] + \Delta V^2 Q[i, j, 0, n] \right), \{i, 1, Mu-1\}, \{j, 1, Mv-1\}],$$

Table[

$$\theta[i, j, Mw, n] =$$

$$\frac{1}{\alpha_{puvb}} \left( \Delta v^2 \Delta w^2 (\theta[i+1, j, Mw, n] + \theta[i-1, j, Mw, n]) + \Delta u^2 \Delta w^2 (\theta[i, j+1, Mw, n] + \theta[i, j-1, Mw, n]) + \Delta u^2 \Delta v^2 (\theta[i, j, Mw-1, n]) + H_b \Delta u \Delta v \Delta v^2 \theta_{amb2} + \frac{\Delta V^2}{\Delta \tau} \theta[i, j, Mw, n-1] + \Delta V^2 Q[i, j, Mw, n] \right), \{i, 1, Mu-1\}, \{j, 1, Mv-1\}],$$

(\*edges\*)

$$\begin{aligned} & \text{Table[} \\ & \theta[i, 0, 0, n] = \\ & \frac{1}{\alpha_{eu0}} \left( \Delta v^2 \Delta w^2 (\theta[i+1, 0, 0, n] + \theta[i-1, 0, 0, n]) + \right. \\ & \quad \Delta u^2 \Delta w^2 (\theta[i, 1, 0, n] + \theta[i, 1, 0, n]) + \Delta u^2 \Delta v^2 (\theta[i, 0, 1, n]) + \\ & \quad \left. H \Delta u \Delta v \Delta V^2 \theta_{amb} + \frac{\Delta V^2}{\Delta \tau} \theta[i, 0, 0, n-1] + \Delta V^2 Q[i, 0, 0, n] \right), \\ & \{i, 1, \text{Mu}-1\}], \end{aligned}$$

$$\begin{aligned} & \text{Table[} \\ & \theta[i, \text{Mv}, 0, n] = \\ & \frac{1}{\alpha_{eu}} \left( \Delta v^2 \Delta w^2 (\theta[i+1, \text{Mv}, 0, n] + \theta[i-1, \text{Mv}, 0, n]) + \right. \\ & \quad \Delta u^2 \Delta w^2 (\theta[i, \text{Mv}-1, 0, n]) + \Delta u^2 \Delta v^2 (\theta[i, \text{Mv}, 1, n]) + \\ & \quad \frac{H \Delta u \Delta w \Delta V^2}{2} \theta_{amb} + \frac{H \Delta u \Delta v \Delta V^2}{2} \theta_{amb} + \frac{\Delta V^2}{\Delta \tau} \theta[i, \text{Mv}, 0, n-1] + \\ & \quad \left. \Delta V^2 Q[i, \text{Mv}, 0, n] \right), \{i, 1, \text{Mu}-1\}], \end{aligned}$$

$$\begin{aligned} & \text{Table[} \\ & \theta[i, 0, \text{Mw}, n] = \\ & \frac{1}{\alpha_{eu0b}} \left( \Delta v^2 \Delta w^2 (\theta[i+1, 0, \text{Mw}, n] + \theta[i-1, 0, \text{Mw}, n]) + \right. \\ & \quad \Delta u^2 \Delta w^2 (\theta[i, 1, \text{Mw}, n] + \theta[i, 1, \text{Mw}, n]) + \\ & \quad \Delta u^2 \Delta v^2 (\theta[i, 0, \text{Mw}-1, n]) + H_b \Delta u \Delta v \Delta V^2 \theta_{amb} + \\ & \quad \left. \frac{\Delta V^2}{\Delta \tau} \theta[i, 0, \text{Mw}, n-1] + \Delta V^2 Q[i, 0, \text{Mw}, n] \right), \{i, 1, \text{Mu}-1\}], \end{aligned}$$

Table $\left[\theta[i, Mv, Mw, n] =$

$$\frac{1}{\alpha_{eub}} \left( \Delta v^2 \Delta w^2 (\theta[i+1, Mv, Mw, n] + \theta[i-1, Mv, Mw, n]) + \Delta u^2 \Delta w^2 (\theta[i, Mv-1, Mw, n]) + \Delta u^2 \Delta v^2 (\theta[i, Mv, Mw-1, n]) + \frac{H \Delta u \Delta w \Delta V^2}{2} \theta_{amb} + \frac{Hb \Delta u \Delta v \Delta V^2}{2} \theta_{amb} + \frac{\Delta V^2}{\Delta \tau} \theta[i, Mv, Mw, n-1] + \Delta V^2 Q[i, Mv, Mw, n] \right), \{i, 1, Mu-1\},$$

Table $\left[$

$\theta[0, j, 0, n] =$

$$\frac{1}{\alpha_{ev}} \left( \Delta v^2 \Delta w^2 (\theta[1, j, 0, n]) + \Delta u^2 \Delta w^2 (\theta[0, j+1, 0, n] + \theta[0, j-1, 0, n]) + \Delta u^2 \Delta v^2 (\theta[0, j, 1, n]) + \frac{H \Delta u \Delta v \Delta V^2}{2} \theta_{amb} + \frac{H \Delta v \Delta w \Delta V^2}{2} \theta_{amb} + \frac{\Delta V^2}{\Delta \tau} \theta[0, j, 0, n-1] + \Delta V^2 Q[0, j, 0, n] \right), \{j, 1, Mv-1\},$$

Table $\left[$

$\theta[Mu, j, 0, n] =$

$$\frac{1}{\alpha_{ev}} \left( \Delta v^2 \Delta w^2 (\theta[Mu-1, j, 0, n]) + \Delta u^2 \Delta w^2 (\theta[Mu, j+1, 0, n] + \theta[Mu, j-1, 0, n]) + \Delta u^2 \Delta v^2 (\theta[Mu, j, 1, n]) + \frac{H \Delta u \Delta v \Delta V^2}{2} \theta_{amb} + \frac{H \Delta v \Delta w \Delta V^2}{2} \theta_{amb} + \frac{\Delta V^2}{\Delta \tau} \theta[Mu, j, 0, n-1] + \Delta V^2 Q[Mu, j, 0, n] \right), \{j, 1, Mv-1\},$$

$$\begin{aligned}
& \text{Table} [ \\
& \theta[0, j, Mw, n] = \\
& \frac{1}{\alpha evb} \\
& \left( \Delta v^2 \Delta w^2 (\theta[1, j, Mw, n]) + \right. \\
& \quad \Delta u^2 \Delta w^2 (\theta[0, j+1, Mw, n] + \theta[0, j-1, Mw, n]) + \\
& \quad \Delta u^2 \Delta v^2 (\theta[0, j, Mw-1, n]) + \frac{Hb \Delta u \Delta v \Delta V^2}{2} \theta_{amb} + \\
& \quad \left. \frac{H \Delta v \Delta w \Delta V^2}{2} \theta_{amb} + \frac{\Delta V^2}{\Delta \tau} \theta[0, j, Mw, n-1] + \Delta V^2 Q[0, j, Mw, n] \right), \\
& \{j, 1, Mv-1\} ],
\end{aligned}$$

$$\begin{aligned}
& \text{Table} [\theta[Mu, j, Mw, n] = \\
& \frac{1}{\alpha evb} \\
& \left( \Delta v^2 \Delta w^2 (\theta[Mu-1, j, Mw, n]) + \right. \\
& \quad \Delta u^2 \Delta w^2 (\theta[Mu, j+1, Mw, n] + \theta[Mu, j-1, Mw, n]) + \\
& \quad \Delta u^2 \Delta v^2 (\theta[Mu, j, Mw-1, n]) + \frac{Hb \Delta u \Delta v \Delta V^2}{2} \theta_{amb} + \\
& \quad \left. \frac{H \Delta v \Delta w \Delta V^2}{2} \theta_{amb} + \frac{\Delta V^2}{\Delta \tau} \theta[Mu, j, Mw, n-1] + \Delta V^2 Q[Mu, j, Mw, n] \right), \\
& \{j, 1, Mv-1\} ],
\end{aligned}$$

$$\begin{aligned}
& \text{Table} [ \\
& \theta[0, 0, k, n] = \\
& \frac{1}{\alpha ew0} \\
& \left( \Delta v^2 \Delta w^2 (\theta[1, 0, k, n]) + \Delta u^2 \Delta w^2 (\theta[0, 1, k, n] + \theta[0, 1, k, n]) + \right. \\
& \quad \Delta u^2 \Delta v^2 (\theta[0, 0, k+1, n] + \theta[0, 0, k-1, n]) + H \Delta v \Delta w \Delta V^2 \theta_{amb} + \\
& \quad \left. \frac{\Delta V^2}{\Delta \tau} \theta[0, 0, k, n-1] + \Delta V^2 Q[0, 0, k, n] \right), \{k, 1, Mw-1\} ],
\end{aligned}$$

$$\begin{aligned}
& \text{Table} \left[ \right. \\
& \quad \theta[\text{Mu}, 0, k, n] = \\
& \quad \frac{1}{\alpha_{ew0}} \\
& \quad \left( \Delta v^2 \Delta w^2 (\theta[\text{Mu} - 1, 0, k, n]) + \right. \\
& \quad \quad \Delta u^2 \Delta w^2 (\theta[\text{Mu}, 1, k, n] + \theta[\text{Mu}, 1, k, n]) + \\
& \quad \quad \Delta u^2 \Delta v^2 (\theta[\text{Mu}, 0, k + 1, n] + \theta[\text{Mu}, 0, k - 1, n]) + \\
& \quad \quad \left. H \Delta v \Delta w \Delta V^2 \theta_{amb} + \frac{\Delta V^2}{\Delta \tau} \theta[\text{Mu}, 0, k, n - 1] + \Delta V^2 Q[\text{Mu}, 0, k, n] \right), \\
& \quad \left. \{k, 1, M_w - 1\} \right],
\end{aligned}$$

$$\begin{aligned}
& \text{Table} \left[ \right. \\
& \quad \theta[0, M_v, k, n] = \\
& \quad \frac{1}{\alpha_{ew}} \left( \Delta v^2 \Delta w^2 (\theta[1, M_v, k, n]) + \Delta u^2 \Delta w^2 (\theta[0, M_v - 1, k, n]) + \right. \\
& \quad \quad \Delta u^2 \Delta v^2 (\theta[0, M_v, k + 1, n] + \theta[0, M_v, k - 1, n]) + \\
& \quad \quad \frac{H \Delta u \Delta w \Delta V^2}{2} \theta_{amb} + \frac{H \Delta v \Delta w \Delta V^2}{2} \theta_{amb} + \frac{\Delta V^2}{\Delta \tau} \theta[0, M_v, k, n - 1] + \\
& \quad \quad \left. \Delta V^2 Q[0, M_v, k, n] \right), \{k, 1, M_w - 1\} \right],
\end{aligned}$$

$$\begin{aligned}
& \text{Table} \left[ \theta[\text{Mu}, M_v, k, n] = \right. \\
& \quad \frac{1}{\alpha_{ew}} \left( \Delta v^2 \Delta w^2 (\theta[\text{Mu} - 1, M_v, k, n]) + \Delta u^2 \Delta w^2 (\theta[\text{Mu}, M_v - 1, k, n]) + \right. \\
& \quad \quad \Delta u^2 \Delta v^2 (\theta[\text{Mu}, M_v, k + 1, n] + \theta[\text{Mu}, M_v, k - 1, n]) + \\
& \quad \quad \frac{H \Delta u \Delta w \Delta V^2}{2} \theta_{amb} + \frac{H \Delta v \Delta w \Delta V^2}{2} \theta_{amb} + \frac{\Delta V^2}{\Delta \tau} \theta[\text{Mu}, M_v, k, n - 1] + \\
& \quad \quad \left. \Delta V^2 Q[\text{Mu}, M_v, k, n] \right), \{k, 1, M_w - 1\} \right],
\end{aligned}$$

(\*corners\*)

$$\theta[0, Mv, 0, n] =$$

$$\frac{1}{\alpha c} \left( \Delta v^2 \Delta w^2 (\theta[1, Mv, 0, n]) + \Delta u^2 \Delta w^2 (\theta[0, Mv - 1, 0, n]) + \right. \\ \left. \Delta u^2 \Delta v^2 (\theta[0, Mv, 1, n]) + \frac{H \Delta v \Delta w \Delta V^2}{4} \theta_{amb} + \frac{H \Delta u \Delta w \Delta V^2}{4} \theta_{amb} + \right. \\ \left. \frac{H \Delta u \Delta v \Delta V^2}{4} \theta_{amb} + \frac{\Delta V^2}{\Delta \tau} \theta[0, Mv, 0, n - 1] + \Delta V^2 Q[0, Mv, 0, n] \right),$$

$$\theta[Mu, Mv, 0, n] =$$

$$\frac{1}{\alpha c} \left( \Delta v^2 \Delta w^2 (\theta[Mu - 1, Mv, 0, n]) + \Delta u^2 \Delta w^2 (\theta[Mu, Mv - 1, 0, n]) + \right. \\ \left. \Delta u^2 \Delta v^2 (\theta[Mu, Mv, 1, n]) + \frac{H \Delta v \Delta w \Delta V^2}{4} \theta_{amb} + \frac{H \Delta u \Delta w \Delta V^2}{4} \theta_{amb} + \right. \\ \left. \frac{H \Delta u \Delta v \Delta V^2}{4} \theta_{amb} + \frac{\Delta V^2}{\Delta \tau} \theta[Mu, Mv, 0, n - 1] + \Delta V^2 Q[Mu, Mv, 0, n] \right),$$

$$\theta[Mu, Mv, Mw, n] =$$

$$\frac{1}{\alpha c b} \left( \Delta v^2 \Delta w^2 (\theta[Mu - 1, Mv, Mw, n]) + \Delta u^2 \Delta w^2 (\theta[Mu, Mv - 1, Mw, n]) + \right. \\ \left. \Delta u^2 \Delta v^2 (\theta[Mu, Mv, Mw - 1, n]) + \frac{H \Delta v \Delta w \Delta V^2}{4} \theta_{amb} + \right. \\ \left. \frac{H \Delta u \Delta w \Delta V^2}{4} \theta_{amb} + \frac{H b \Delta u \Delta v \Delta V^2}{4} \theta_{amb} + \frac{\Delta V^2}{\Delta \tau} \theta[Mu, Mv, Mw, n - 1] + \right. \\ \left. \Delta V^2 Q[Mu, Mv, Mw, n] \right),$$

$$\begin{aligned}
\theta[0, Mv, Mw, n] = & \\
& \frac{1}{\alpha cb} \left( \Delta v^2 \Delta w^2 (\theta[1, Mv, Mw, n]) + \Delta u^2 \Delta w^2 (\theta[0, Mv - 1, Mw, n]) + \right. \\
& \Delta u^2 \Delta v^2 (\theta[0, Mv, Mw - 1, n]) + \frac{H \Delta v \Delta w \Delta V^2}{4} \theta_{amb} + \\
& \frac{H \Delta u \Delta w \Delta V^2}{4} \theta_{amb} + \frac{Hb \Delta u \Delta v \Delta V^2}{4} \theta_{amb} + \frac{\Delta V^2}{\Delta \tau} \theta[0, Mv, Mw, n - 1] + \\
& \left. \Delta V^2 Q[0, Mv, Mw, n] \right),
\end{aligned}$$

$$\begin{aligned}
\theta[0, 0, 0, n] = & \\
& \frac{1}{\alpha cv0} \\
& \left( \Delta v^2 \Delta w^2 (\theta[1, 0, 0, n]) + \Delta u^2 \Delta w^2 (\theta[0, 1, 0, n] + \theta[0, 1, 0, n]) + \right. \\
& \Delta u^2 \Delta v^2 (\theta[0, 0, 1, n]) + \frac{H \Delta u \Delta v \Delta V^2}{2} \theta_{amb} + \frac{H \Delta v \Delta w \Delta V^2}{2} \theta_{amb} + \\
& \left. \frac{\Delta V^2}{\Delta \tau} \theta[0, 0, 0, n - 1] + \Delta V^2 Q[0, 0, 0, n] \right),
\end{aligned}$$

$$\begin{aligned}
\theta[Mu, 0, 0, n] = & \\
& \frac{1}{\alpha cv0} \\
& \left( \Delta v^2 \Delta w^2 (\theta[Mu - 1, 0, 0, n]) + \right. \\
& \Delta u^2 \Delta w^2 (\theta[Mu, 1, 0, n] + \theta[Mu, 1, 0, n]) + \\
& \Delta u^2 \Delta v^2 (\theta[Mu, 0, 1, n]) + \frac{H \Delta u \Delta v \Delta V^2}{2} \theta_{amb} + \frac{H \Delta v \Delta w \Delta V^2}{2} \theta_{amb} + \\
& \left. \frac{\Delta V^2}{\Delta \tau} \theta[Mu, 0, 0, n - 1] + \Delta V^2 Q[Mu, 0, 0, n] \right),
\end{aligned}$$

```


$$\theta[0, 0, Mw, n] = \frac{1}{\alpha cv0b} \left( \Delta v^2 \Delta w^2 (\theta[1, 0, Mw, n]) + \Delta u^2 \Delta w^2 (\theta[0, 1, Mw, n] + \theta[0, 1, Mw, n]) + \Delta u^2 \Delta v^2 (\theta[0, 0, Mw - 1, n]) + \frac{Hb \Delta u \Delta v \Delta V^2}{2} \theta_{amb} + \frac{H \Delta v \Delta w \Delta V^2}{2} \theta_{amb} + \frac{\Delta V^2}{\Delta \tau} \theta[0, 0, Mw, n - 1] + \Delta V^2 Q[0, 0, Mw, n] \right),$$


$$\theta[Mu, 0, Mw, n] = \frac{1}{\alpha cv0b} \left( \Delta v^2 \Delta w^2 (\theta[Mu - 1, 0, Mw, n]) + \Delta u^2 \Delta w^2 (\theta[Mu, 1, Mw, n] + \theta[Mu, 1, Mw, n]) + \Delta u^2 \Delta v^2 (\theta[Mu, 0, Mw - 1, n]) + \frac{Hb \Delta u \Delta v \Delta V^2}{2} \theta_{amb} + \frac{H \Delta v \Delta w \Delta V^2}{2} \theta_{amb} + \frac{\Delta V^2}{\Delta \tau} \theta[Mu, 0, Mw, n - 1] + \Delta V^2 Q[Mu, 0, Mw, n] \right)$$

}} /. sol[n - 1];
(*solve the equations *)
Solve[eqns, vars][[1]]

```

```

DateString[]
utime = Timing[sol[1];][[1]]
DateString[]

```

6.303

Tue 13 Oct 2009 11:02:45

```

DateString[]
DatePlus[Date[], {utime (nadq - 1), "Second"}];
Print["Projected " DateString[%]]
Timing[sol[nadq];];
Print["Actual " DateString[]]

```

Tue 13 Oct 2009 11:02:46

Projected Tue 13 Oct 2009 11:06:01

Actual Tue 13 Oct 2009 11:06:07

$$\text{tc1mod} = \left\{ \text{Round} \left[ \frac{.5 \times 25.4}{1000 \text{ Lz } \Delta u} \right] \Delta x * 1000 / 25.4, \right. \\ \left. \text{Round} \left[ \frac{0 \times 25.4}{1000 \text{ Lz } \Delta v} \right] \Delta y * 1000 / 25.4, \right. \\ \left. \left( \text{Round} \left[ \frac{.25 \times 25.4}{1000 \text{ Lz } \Delta w} \right] \right) \Delta z * 1000 / 25.4 \right\}$$

$$\text{tc2mod} = \left\{ \text{Round} \left[ \frac{2 \times 25.4}{1000 \text{ Lz } \Delta u} \right] \Delta x * 1000 / 25.4, \right. \\ \left. \text{Round} \left[ \frac{0 \times 25.4}{1000 \text{ Lz } \Delta v} \right] \Delta y * 1000 / 25.4, \right. \\ \left. \text{Round} \left[ \frac{.25 \times 25.4}{1000 \text{ Lz } \Delta w} \right] \Delta z * 1000 / 25.4 \right\}$$

$$\text{tc3mod} = \left\{ \text{Round} \left[ \frac{2.5 \times 25.4}{1000 \text{ Lz } \Delta u} \right] \Delta x * 1000 / 25.4, \right. \\ \left. \text{Round} \left[ \frac{0 \times 25.4}{1000 \text{ Lz } \Delta v} \right] \Delta y * 1000 / 25.4, \right. \\ \left. \text{Round} \left[ \frac{.25 \times 25.4}{1000 \text{ Lz } \Delta w} \right] \Delta z * 1000 / 25.4 \right\}$$

$$\text{tc4mod} = \left\{ \text{Round} \left[ \frac{1 \times 25.4}{1000 \text{ Lz } \Delta u} \right] \Delta x * 1000 / 25.4, \right. \\ \left. \text{Round} \left[ \frac{(0) 25.4}{1000 \text{ Lz } \Delta v} \right] \Delta y * 1000 / 25.4, \right. \\ \left. \left( \text{Round} \left[ \frac{.25 \times 25.4}{1000 \text{ Lz } \Delta w} \right] + 1 \right) \Delta z * 1000 / 25.4 \right\}$$

{0.5, 0, 0.2}

{2., 0, 0.2}

{2.5, 0, 0.2}

{1., 0, 0.3}

```

tothist[t_] :=
ListPlot[
{Table[{Round[n α / Lz / Lz / Δτ] Δτ Lz Lz / α / 60 - trest / 60,
Tm θ [Round[ $\frac{1 \times 25.4}{1000 \text{ Lz } \Delta u}$ ], Round[ $\frac{0 \times 25.4}{1000 \text{ Lz } \Delta v}$ ], Round[ $\frac{.25 \times 25.4}{1000 \text{ Lz } \Delta w}$ ],
Round[n α / Lz / Lz / Δτ] ] - 273 /.
sol[Round[n α / Lz / Lz / Δτ]]}, {n, 0, t}],
Table[{Round[n α / Lz / Lz / Δτ] Δτ Lz Lz / α / 60 - trest / 60,
Tm θ [Round[ $\frac{2 \times 25.4}{1000 \text{ Lz } \Delta u}$ ], Round[ $\frac{0 \times 25.4}{1000 \text{ Lz } \Delta v}$ ], Round[ $\frac{.25 \times 25.4}{1000 \text{ Lz } \Delta w}$ ],
Round[n α / Lz / Lz / Δτ] ] - 273 /.
sol[Round[n α / Lz / Lz / Δτ]]}, {n, 0, t}],
Table[{Round[n α / Lz / Lz / Δτ] Δτ Lz Lz / α / 60 - trest / 60,
Tm θ [Round[ $\frac{3 \times 25.4}{1000 \text{ Lz } \Delta u}$ ], Round[ $\frac{0 \times 25.4}{1000 \text{ Lz } \Delta v}$ ], Round[ $\frac{.25 \times 25.4}{1000 \text{ Lz } \Delta w}$ ],
Round[n α / Lz / Lz / Δτ] ] - 273 /.
sol[Round[n α / Lz / Lz / Δτ]]}, {n, 0, t}],
Table[{Round[n α / Lz / Lz / Δτ] Δτ Lz Lz / α / 60 - trest / 60,
Tm θ [Round[ $\frac{1.5 \times 25.4}{1000 \text{ Lz } \Delta u}$ ], Round[ $\frac{(1.25 / 4) 25.4}{1000 \text{ Lz } \Delta v}$ ],
(Round[ $\frac{.36 \times 25.4}{1000 \text{ Lz } \Delta w}$ ] - 1), Round[n α / Lz / Lz / Δτ] ] - 273 /.
sol[Round[n α / Lz / Lz / Δτ]]}, {n, 0, t}],
Table[{Round[n α / Lz / Lz / Δτ] Δτ Lz Lz / α / 60 - trest / 60,
Tm Total[cent3[Round[n α / Lz / Lz / Δτ]]
Table[θ[i, j, 0, Round[n α / Lz / Lz / Δτ]] /.
sol[Round[n α / Lz / Lz / Δτ]], {i, 0, Mu}, {j, 0, Mv}],
2] - 273 /. sol[Round[n α / Lz / Lz / Δτ]]}, {n, 0, t}],
PlotRange → {{-1.2 (trest2) / 60, Automatic}, {000, 600}},
Joined → True, FrameLabel → {"Time (min)", None, "Temp (C)"},
PlotStyle → {Red, Green, Blue, Brown, Black},
AxesOrigin → {-trest / 60, 000},
PlotLabel → StringJoin["pin = ", ToString[pl / 746],
" Hp, h = ", ToString[h], ", Hb = ", ToString[hb],
", v = ", ToString[vx 1000 / 25.4 × 60], " in/min"],
Frame → True]

```

```

tothistadq[t_] :=
ListPlot[
{
Table[{
(Round[n  $\alpha$  / Lz / Lz /  $\Delta\tau$ ]  $\Delta\tau$  Lz Lz /  $\alpha$  / 60 - trest / 60) / tadq,
Tm  $\theta$  [Round[ $\frac{1 \times 25.4}{1000 \text{ Lz } \Delta u}$ ], Round[ $\frac{0 \times 25.4}{1000 \text{ Lz } \Delta v}$ ], Round[ $\frac{.25 \times 25.4}{1000 \text{ Lz } \Delta w}$ ],
Round[n  $\alpha$  / Lz / Lz /  $\Delta\tau$ ]] - 273 /.
sol[Round[n  $\alpha$  / Lz / Lz /  $\Delta\tau$ ]]}, {n, 0, t}],
Table[{
(Round[n  $\alpha$  / Lz / Lz /  $\Delta\tau$ ]  $\Delta\tau$  Lz Lz /  $\alpha$  / 60 - trest / 60) / tadq,
Tm  $\theta$  [Round[ $\frac{2 \times 25.4}{1000 \text{ Lz } \Delta u}$ ], Round[ $\frac{0 \times 25.4}{1000 \text{ Lz } \Delta v}$ ], Round[ $\frac{.25 \times 25.4}{1000 \text{ Lz } \Delta w}$ ],
Round[n  $\alpha$  / Lz / Lz /  $\Delta\tau$ ]] - 273 /.
sol[Round[n  $\alpha$  / Lz / Lz /  $\Delta\tau$ ]]}, {n, 0, t}],
Table[{
(Round[n  $\alpha$  / Lz / Lz /  $\Delta\tau$ ]  $\Delta\tau$  Lz Lz /  $\alpha$  / 60 - trest / 60) / tadq,
Tm  $\theta$  [Round[ $\frac{3 \times 25.4}{1000 \text{ Lz } \Delta u}$ ], Round[ $\frac{0 \times 25.4}{1000 \text{ Lz } \Delta v}$ ], Round[ $\frac{.25 \times 25.4}{1000 \text{ Lz } \Delta w}$ ],
Round[n  $\alpha$  / Lz / Lz /  $\Delta\tau$ ]] - 273 /.
sol[Round[n  $\alpha$  / Lz / Lz /  $\Delta\tau$ ]]}, {n, 0, t}],
Table[{
(Round[n  $\alpha$  / Lz / Lz /  $\Delta\tau$ ]  $\Delta\tau$  Lz Lz /  $\alpha$  / 60 - trest / 60) / tadq,
Tm  $\theta$  [Round[ $\frac{1.5 \times 25.4}{1000 \text{ Lz } \Delta u}$ ], Round[ $\frac{(1.25 / 4) 25.4}{1000 \text{ Lz } \Delta v}$ ],
(Round[ $\frac{.36 \times 25.4}{1000 \text{ Lz } \Delta w}$ ] - 1), Round[n  $\alpha$  / Lz / Lz /  $\Delta\tau$ ]] - 273 /.
sol[Round[n  $\alpha$  / Lz / Lz /  $\Delta\tau$ ]]}, {n, 0, t}],
Table[{
(Round[n  $\alpha$  / Lz / Lz /  $\Delta\tau$ ]  $\Delta\tau$  Lz Lz /  $\alpha$  / 60 - trest / 60) / tadq,
Tm Total[cent3[Round[n  $\alpha$  / Lz / Lz /  $\Delta\tau$ ]]
Table[ $\theta$ [i, j, 0, Round[n  $\alpha$  / Lz / Lz /  $\Delta\tau$ ]] /.
sol[Round[n  $\alpha$  / Lz / Lz /  $\Delta\tau$ ]], {i, 0, Mu}, {j, 0, Mv}],
2] - 273 /. sol[Round[n  $\alpha$  / Lz / Lz /  $\Delta\tau$ ]]}, {n, 0, t}],
PlotRange  $\rightarrow$  All, Joined  $\rightarrow$  True,
FrameLabel  $\rightarrow$  {"Time (min)", None, "Temp (C)"},
PlotStyle  $\rightarrow$  {Red, Green, Blue, Brown, Black},
AxesOrigin  $\rightarrow$  Automatic,
PlotLabel  $\rightarrow$  StringJoin["pin = ", ToString[pl / 746],
" Hp, h = ", ToString[h], ", Hb = ", ToString[hb],
", v = ", ToString[vx 1000 / 25.4  $\times$  60], " in/min"],
Frame  $\rightarrow$  True]

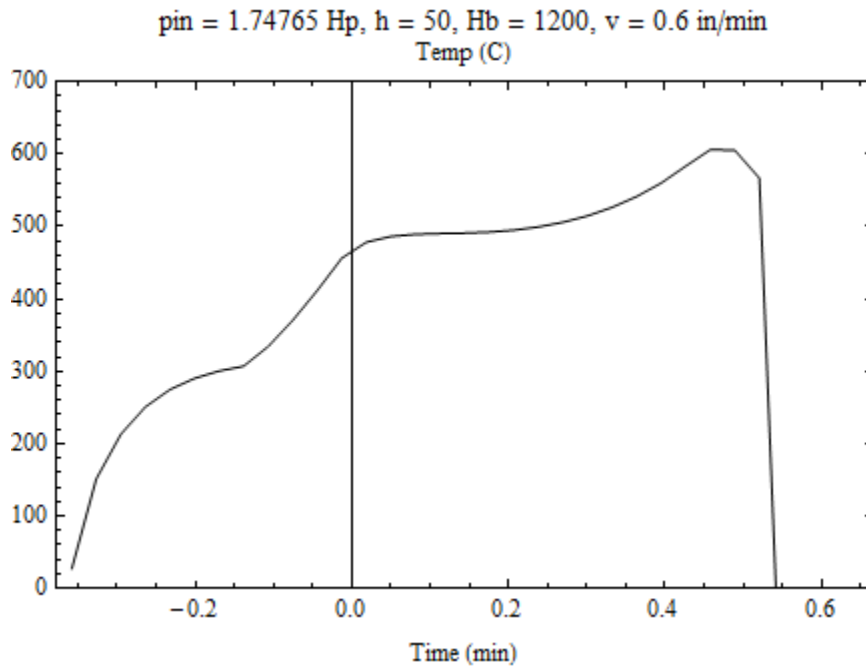
```

```

surfadqnorm[t_] :=
ListPlot[
Table[{(Round[n  $\alpha$  / Lz / Lz /  $\Delta\tau$ ]  $\Delta\tau$  Lz Lz /  $\alpha$  - trest) / tadq,
Tm Total[cent3[Round[n  $\alpha$  / Lz / Lz /  $\Delta\tau$ ]]
Table[ $\theta$ [i, j, 0, Round[n  $\alpha$  / Lz / Lz /  $\Delta\tau$ ]] /.
sol[Round[n  $\alpha$  / Lz / Lz /  $\Delta\tau$ ]], {i, 0, Mu}, {j, 0, Mv}], 2] -
273 /. sol[Round[n  $\alpha$  / Lz / Lz /  $\Delta\tau$ ]], {n, 0, t, 10}],
PlotRange  $\rightarrow$  {All, {0, 700}}, Joined  $\rightarrow$  True,
FrameLabel  $\rightarrow$  {"Time (min)", None, "Temp (C)"},
PlotStyle  $\rightarrow$  {Red, Green, Blue, Brown, Black},
AxesOrigin  $\rightarrow$  Automatic,
PlotLabel  $\rightarrow$  StringJoin["pin = ", ToString[p1 / 746],
" Hp, h = ", ToString[h], ", Hb = ", ToString[hb],
", v = ", ToString[vx 1000 / 25.4  $\times$  60], " in/min"],
Frame  $\rightarrow$  True]

```

```
surfadqnorm[tadq]
```



```

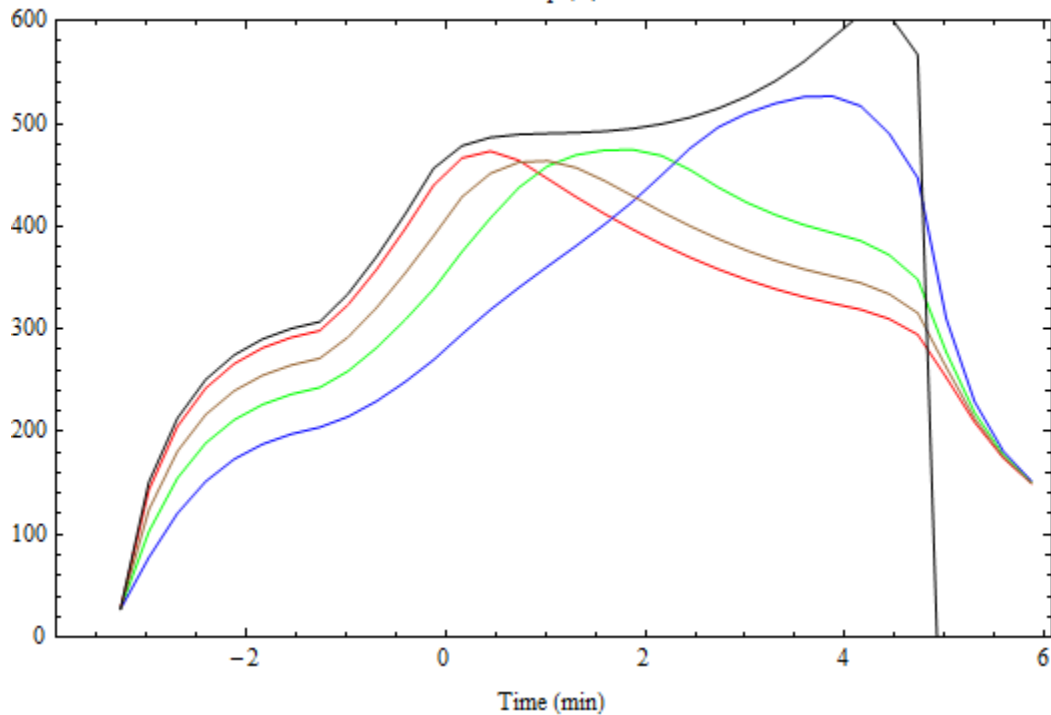
tothistnorm[t_] :=
ListPlot[
{Table[{Round[n α / Lz / Lz / Δτ] Δτ Lz Lz / α / 60 - trest / 60,
ϑ[Round[ $\frac{1 \times 25.4}{1000 Lz \Delta u}$ ], Round[ $\frac{0 \times 25.4}{1000 Lz \Delta v}$ ], Round[ $\frac{.25 \times 25.4}{1000 Lz \Delta w}$ ],
Round[n α / Lz / Lz / Δτ] ] /. sol[Round[n α / Lz / Lz / Δτ]]},
{n, 0, t}],
Table[{Round[n α / Lz / Lz / Δτ] Δτ Lz Lz / α / 60 - trest / 60,
ϑ[Round[ $\frac{2 \times 25.4}{1000 Lz \Delta u}$ ], Round[ $\frac{0 \times 25.4}{1000 Lz \Delta v}$ ], Round[ $\frac{.25 \times 25.4}{1000 Lz \Delta w}$ ],
Round[n α / Lz / Lz / Δτ] ] /. sol[Round[n α / Lz / Lz / Δτ]]},
{n, 0, t}],
Table[{Round[n α / Lz / Lz / Δτ] Δτ Lz Lz / α / 60 - trest / 60,
ϑ[Round[ $\frac{3 \times 25.4}{1000 Lz \Delta u}$ ], Round[ $\frac{0 \times 25.4}{1000 Lz \Delta v}$ ], Round[ $\frac{.25 \times 25.4}{1000 Lz \Delta w}$ ],
Round[n α / Lz / Lz / Δτ] ] /. sol[Round[n α / Lz / Lz / Δτ]]},
{n, 0, t}],
Table[{Round[n α / Lz / Lz / Δτ] Δτ Lz Lz / α / 60 - trest / 60,
ϑ[Round[ $\frac{1.5 \times 25.4}{1000 Lz \Delta u}$ ], Round[ $\frac{(1.25 / 4) 25.4}{1000 Lz \Delta v}$ ],
Round[ $\frac{.36 \times 25.4}{1000 Lz \Delta w}$ ], Round[n α / Lz / Lz / Δτ] ] /.
sol[Round[n α / Lz / Lz / Δτ]]}, {n, 0, t}],
Table[{Round[n α / Lz / Lz / Δτ] Δτ Lz Lz / α / 60 - trest / 60,
Total[cent3[Round[n α / Lz / Lz / Δτ]]
Table[ϑ[i, j, 0, Round[n α / Lz / Lz / Δτ]] /.
sol[Round[n α / Lz / Lz / Δτ]], {i, 0, Mu}, {j, 0, Mv}], 2] /.
sol[Round[n α / Lz / Lz / Δτ]]}, {n, 0, t}],
PlotRange → {{-1.2 (trest2) / 60, Automatic}, {000, 1.2}},
Joined → True, AxesLabel → {"Time (min)", "Temp (C/C)"},
PlotStyle → {Red, Green, Blue, Brown, Black},
AxesOrigin → {0, 000},
PlotLabel → StringJoin["pin = ", ToString[pl / 746],
", h = ", ToString[h], ", Hb = ", ToString[hb]]]

```

```
(*tothistnorm[300]*)
```

```
tothist[tadq]
```

pin = 1.74765 Hp, h = 50, Hb = 1200, v = 0.6 in/min  
Temp (C)



```
t34hist[t_] :=
```

```
ListPlot[  
  {Table[{Round[n  $\alpha$  / Lz / Lz /  $\Delta\tau$ ]  $\Delta\tau$  Lz Lz /  $\alpha$  / 60 - trest2 / 60,  
    Tm  $\theta$  [Round[ $\frac{2 \times 25.4}{1000 \text{ Lz } \Delta u}$ ], Round[ $\frac{0 \times 25.4}{1000 \text{ Lz } \Delta v}$ ], Round[ $\frac{.25 \times 25.4}{1000 \text{ Lz } \Delta w}$ ],  
    Round[n  $\alpha$  / Lz / Lz /  $\Delta\tau$ ]}] - 273 /.  
    sol[Round[n  $\alpha$  / Lz / Lz /  $\Delta\tau$ ]], {n, 0, t}],  
  Table[{Round[n  $\alpha$  / Lz / Lz /  $\Delta\tau$ ]  $\Delta\tau$  Lz Lz /  $\alpha$  / 60 - trest / 60,  
    Tm  $\theta$  [Round[ $\frac{2 \times 25.4}{1000 \text{ Lz } \Delta u}$ ], Round[ $\frac{0 \times 25.4}{1000 \text{ Lz } \Delta v}$ ], Round[ $\frac{.5 \times 25.4}{1000 \text{ Lz } \Delta w}$ ],  
    Round[n  $\alpha$  / Lz / Lz /  $\Delta\tau$ ]}] - 273 /.  
    sol[Round[n  $\alpha$  / Lz / Lz /  $\Delta\tau$ ]], {n, 0, t}}],  
  PlotRange  $\rightarrow$  {{-1.2 (trest2) / 60, Automatic}, {300, 500}},  
  Joined  $\rightarrow$  True, AxesLabel  $\rightarrow$  {"Time (min)", "Temp (C)"},  
  PlotStyle  $\rightarrow$  {Green, Brown}, AxesOrigin  $\rightarrow$  {0, 0}]
```

```
(*t34hist[tadq]*)
```

```
sgraph[n_] :=
```

```
Flatten[
```

```
{Table[{i Δu Lz, j Δv Lz, S[n][[i+1, j+1]]}, {i, 1, Mu},  
  {j, 0, Mv}], Table[{i Δu Lz, -j Δv Lz, S[n][[i+1, j+1]]},  
  {i, 1, Mu}, {j, 0, Mv}]}, 2]
```

```
sourmax = qr  $\frac{Lz^2}{Tm \alpha}$  Max[source];
```

```
sourplot[n_] := ListContourPlot[sgraph[n],  
  ColorFunction → Function[{z}, Hue[.6 (1 - z / (sourmax))]],  
  ColorFunctionScaling → False, AspectRatio → 2 Ly / Lx,  
  InterpolationOrder → 1, PlotRange → All]
```

```

xyplane[w_, n_] :=
ListDensityPlot[
  Flatten[
    {Table[{i Δu Lz 1000/25.4, j Δv Lz 1000/25.4,
      Tm θ[i, j, w, Round[n α/Lz/Lz/Δτ]] /.
      sol[Round[n α/Lz/Lz/Δτ]]}, {i, 0, Mu}, {j, 0, Mv}],
    Table[{i Δu Lz 1000/25.4, -j Δv Lz 1000/25.4,
      Tm θ[i, j, w, Round[n α/Lz/Lz/Δτ]] /.
      sol[Round[n α/Lz/Lz/Δτ]]}, {i, 0, Mu}, {j, 0, Mv}]}, 2],
  InterpolationOrder → 3, AspectRatio → 2 Ly/Lx,
  PlotLabel → Round[n α/Lz/Lz/Δτ] Δτ Lz Lz / α "seconds",
  FrameLabel → {"x (m)", "y (m)"}]

```

```

xzplane[v_, n_] :=
ListDensityPlot[
  Flatten[Table[{i Δu Lz 1000/25.4, -k Δw Lz 1000/25.4,
    Tm θ[i, v, k, Round[n α/Lz/Lz/Δτ]] /.
    sol[Round[n α/Lz/Lz/Δτ]]}, {i, 0, Mu}, {k, 0, Mw}], 1],
  InterpolationOrder → 3, AspectRatio → Lz/Lx,
  PlotLabel → Round[n α/Lz/Lz/Δτ] Δτ Lz Lz / α "seconds"]

```

```

yzplane[u_, n_] :=
ListDensityPlot[
  Flatten[
    {Table[{j Δv Lz 1000/25.4, -k Δw Lz 1000/25.4,
      Tm θ[u, j, k, Round[n α/Lz/Lz/Δτ]] /.
      sol[Round[n α/Lz/Lz/Δτ]]}, {j, 0, Mv}, {k, 0, Mw}],
    Table[{-j Δv Lz 1000/25.4, -k Δw Lz 1000/25.4,
      Tm θ[u, j, k, Round[n α/Lz/Lz/Δτ]] /.
      sol[Round[n α/Lz/Lz/Δτ]]}, {j, 0, Mv}, {k, 0, Mw}]}, 2],
  InterpolationOrder → 3, AspectRatio → Lz/2/Ly,
  PlotLabel → Round[n α/Lz/Lz/Δτ] Δτ Lz Lz / α "seconds"]

```

```

thist[x_, y_, z_, t_] :=
ListPlot[
Table[{Round[n  $\alpha$  / Lz / Lz /  $\Delta\tau$ ]  $\Delta\tau$  Lz Lz /  $\alpha$  / 60,
Tm  $\theta$  [Round[ $\frac{x \ 25.4}{1000 \ Lz \ \Delta u}$ ], Round[ $\frac{y \ 25.4}{1000 \ Lz \ \Delta v}$ ], Round[ $\frac{z \ 25.4}{1000 \ Lz \ \Delta w}$ ],
Round[n  $\alpha$  / Lz / Lz /  $\Delta\tau$ ]] - 273 /. sol[Round[n  $\alpha$  / Lz / Lz /  $\Delta\tau$ ]]},
{n, 0, t}], PlotRange  $\rightarrow$  {All, {0, 700}}, Joined  $\rightarrow$  True,
AxesLabel  $\rightarrow$  {"Time (sec)", "Temp (C)"}]

```

```

(*thist[.5,0,.25,385]
thist[2,0,.25,385]
thist[3.5,0,.25,385]*)

```

```

xyplane2[w_, n_] :=
ListPlot3D[
Flatten[
{Table[{i  $\Delta u$  Lz 1000 / 25.4, j  $\Delta v$  Lz 1000 / 25.4,
Tm  $\theta$  [i, j, w, Round[n  $\alpha$  / Lz / Lz /  $\Delta\tau$ ]] - 273 /.
sol[Round[n  $\alpha$  / Lz / Lz /  $\Delta\tau$ ]]}, {i, 0, Mu}, {j, 0, Mv}},
Table[{i  $\Delta u$  Lz 1000 / 25.4, -j  $\Delta v$  Lz 1000 / 25.4,
Tm  $\theta$  [i, j, w, Round[n  $\alpha$  / Lz / Lz /  $\Delta\tau$ ]] - 273 /.
sol[Round[n  $\alpha$  / Lz / Lz /  $\Delta\tau$ ]]}, {i, 0, Mu}, {j, 0, Mv}}], 2],
InterpolationOrder  $\rightarrow$  3, BoxRatios  $\rightarrow$  {1, 2 Ly / Lx, .25},
PlotLabel  $\rightarrow$  Round[n  $\alpha$  / Lz / Lz /  $\Delta\tau$ ]  $\Delta\tau$  Lz Lz /  $\alpha$  "seconds",
AxesLabel  $\rightarrow$  {"x (m)", "y (m)", "T"},
PlotRange  $\rightarrow$  {All, All, {0, 750}}]

```

```

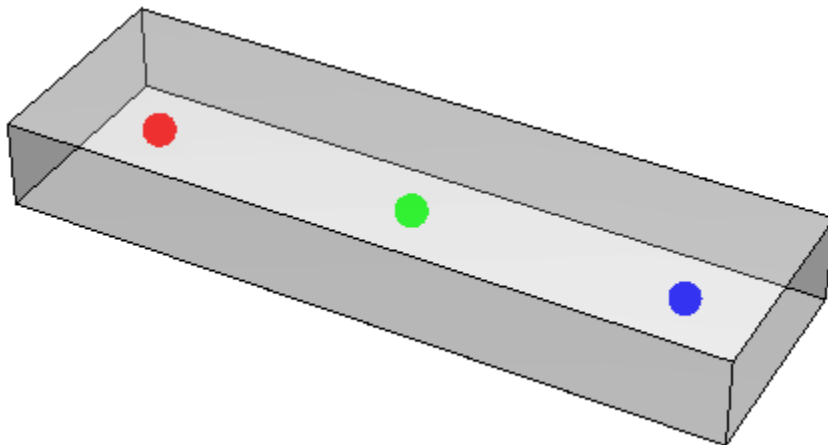
(*ListAnimate[Table[xyplane2[0,i],{i,0,385,10}]]*)

```

```

tcp1 = ListPointPlot3D[{{.5×25.4, 1.25/2×25.4, .25×25.4}},
  PlotStyle → {{PointSize[.04], Red}}];
tcp2 = ListPointPlot3D[{{2×25.4, 1.25/2×25.4, .25×25.4}},
  PlotStyle → {{PointSize[.04], Green}}];
tcp3 = ListPointPlot3D[{{3.5×25.4, 1.25/2×25.4, .25×25.4}},
  PlotStyle → {{PointSize[.04], Blue}}];
tcp4 = ListPointPlot3D[
  {{1.5×25.4, 1/4×2.5/2×25.4, (.5 - .36) 25.4}},
  PlotStyle → {{PointSize[.04], Brown}}];
Heat =
  Graphics3D[{Red, Opacity[.21],
    Cylinder[{{1×25.4, 1.25/2×25.4, .5×25.4},
      {1×25.4, 1.25/2×25.4, .51×25.4}}, .5×25.4]};
wpiece = Graphics3D[{Specularity[White, 10], Opacity[.25],
  Gray, Cuboid[{{0, 0, 0}, {4×25.4, 1.25×25.4, .5×25.4}}]},
  Lighting → {"Directional", White, {{0, 0, 1}, {0, 0, 0}})];
Show[wpiece, tcp1, tcp2, tcp3, Boxed → False,
  Lighting → {"Directional", White, {{0, 0, 1}, {0, 0, 0}})];
Show[tcp1, tcp2, tcp3, tcp4,
  PlotRange → {{0, 4×25.4}, {0, 1.25×25.4}, {0, .5×25.4}},
  BoxRatios → {1, 1.25/4, .5/4}];
Show[wpiece, Heat, tcp1, tcp2, tcp3];

```



```

SetDirectory["C:\phd\onr"];
SetDirectory["run data"];
Directory[]
dat = Import["16608477 corr.csv", "csv"];
torque = 15;
runnum = dat[[1, 2]];
tend = Length[dat]; start = 1;
 $\omega$  = Table[dat[[i, 4]], {i, start, tend}];
t = Table[dat[[i, 3]], {i, start, tend}];
tip = Table[dat[[i, 7]], {i, start, tend}];
tc1 = Table[dat[[i, 8]], {i, start, tend}];
tc2 = Table[dat[[i, 9]], {i, start, tend}];
tc3 = Table[dat[[i, 10]], {i, start, tend}];
torq = Table[dat[[i, 6]], {i, start, tend}];
f = Table[dat[[i, 11]], {i, start, tend}];
cur = Table[dat[[i, 5]], {i, start, tend}];
hp = Table[dat[[i, 4]] * dat[[i, 6]] 15 / 5252, {i, start, tend}];
 $\omega$ max = 3000;
tmax = Max[t];
tipmax = Max[tip];
tc1max = Max[tc1];
tc2max = Max[tc2];
tc3max = Max[tc3];
torqmax = 100;
fmax = 700;
currmax = Max[cur];
hpmax = Max[hp];
maxtemp = Max[tc1max, tc2max, tc3max, tipmax];
tstart = t[[Position[tc1, Max[tc1]][[1, 1]]]] / 60;
tr = ListPlot[{{tstart, -1000}, {tstart, 3000}}, Joined  $\rightarrow$  True,
  PlotStyle  $\rightarrow$  Directive[Dashed, Black]];
tc1start = tc1[[Position[tc1, Max[tc1]][[1, 1]]]];
tc2start = tc2[[Position[tc1, Max[tc1]][[1, 1]]]];
tc3start = tc3[[Position[tc1, Max[tc1]][[1, 1]]]];
tipstart = tip[[Position[tc1, Max[tc1]][[1, 1]]]];

```

C:\phd\onr\run data

```

tc1plot =
  ListPlot[Table[{t[[i]] / 60 - tstart, tc1[[i]] / maxtemp},
    {i, 1, Length[t], 5}], Joined → True, AxesOrigin → {0, 0},
    LabelStyle → Directive[Bold, FontFamily → "Arial"],
    AxesLabel → {"Time (min)", "Temp °C"}, PlotStyle → Red];
tc2plot =
  ListPlot[Table[{t[[i]] / 60 - tstart, tc2[[i]] / maxtemp},
    {i, 1, Length[t], 5}], Joined → True,
    AxesLabel → {"Time (min)", "Temp"}, PlotStyle → Green];
tc3plot =
  ListPlot[Table[{t[[i]] / 60 - tstart, tc3[[i]] / maxtemp},
    {i, 1, Length[t], 5}], Joined → True,
    AxesLabel → {"Time (min)", "Temp"}, PlotStyle → Blue];

tc1plotabs =
  ListPlot[Table[{t[[i]] / 60 - tstart, tc1[[i]]},
    {i, 1, Length[t], 150}], Joined → False, AxesOrigin → {0, 0},
    LabelStyle → Directive[Bold, FontFamily → "Arial"],
    AxesLabel → {"Time (min)", "Temp °C"}, PlotStyle → Red];
tc2plotabs =
  ListPlot[Table[{t[[i]] / 60 - tstart, tc2[[i]]},
    {i, 1, Length[t], 150}], Joined → False,
    AxesLabel → {"Time (min)", "Temp"}, PlotStyle → Green];
tc3plotabs =
  ListPlot[Table[{t[[i]] / 60 - tstart, tc3[[i]]},
    {i, 1, Length[t], 150}], Joined → False,
    AxesLabel → {"Time (min)", "Temp"}, PlotStyle → Blue];

therm = Show[tc1plot, tc2plot, tc3plot,
  PlotLabel → "Normalized Temp vs Time",
  PlotRange → {{60, Automatic}, {0, 1}}, Frame → True,
  FrameLabel → {"Time (min)", "Temp"}];
ShowLegend[therm,
  {{{Graphics[{Directive[Red], Line[{{0, 10}, {16, 10}}]}]},
    Style["TC1", FontFamily → "Arial"]},
  {Graphics[{Green, Line[{{0, 10}, {16, 10}}]}]},
    Style["TC2", FontFamily → "Arial"]},
  {Graphics[{Blue, Line[{{0, 10}, {16, 10}}]}]},
    Style["TC3", FontFamily → "Arial"]},
  {Graphics[{Brown, Line[{{0, 10}, {16, 10}}]}]},
    Style["TC4", FontFamily → "Arial"]}}, LegendSize → {.25, 0.4},
  LegendShadow → {0, 0}, LegendTextSpace → 0.8,
  LegendPosition → {.7, -.40}];
tipplot =
  ListPlot[Table[{t[[i]] / 60 - tstart, tip[[i]] / maxtemp},
    {i, 1, Length[t]}], Joined → True,
    AxesLabel → {"Time (min)", "Tip Temp"}, PlotStyle → {Black}];
tipplot2 =

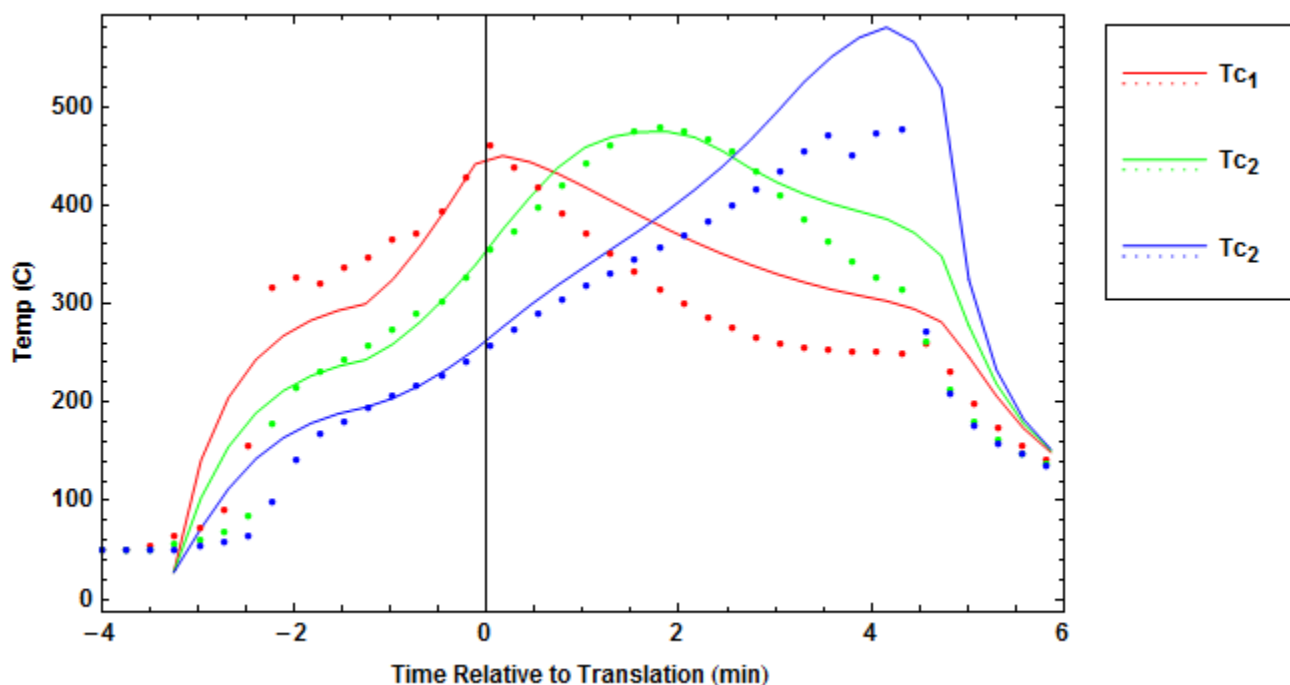
```

```

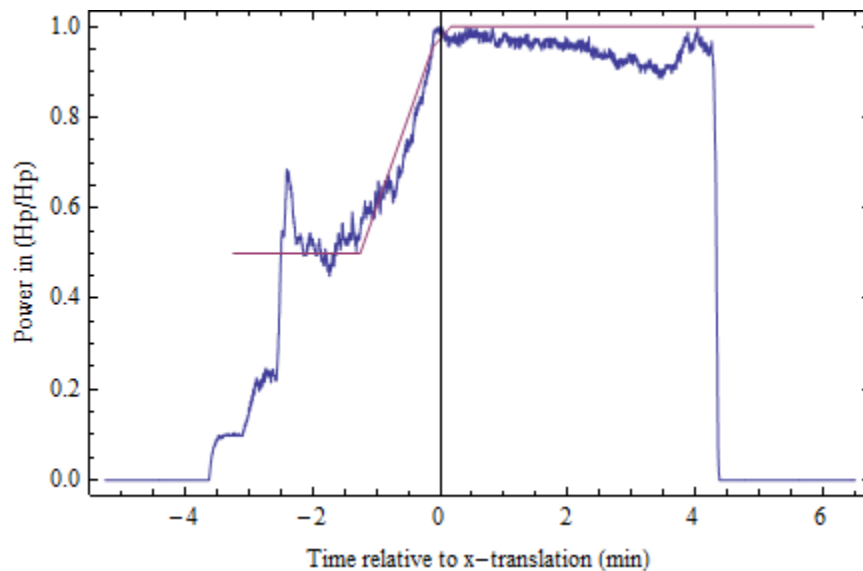
theo =
ListPlot[
{Table[{Round[n  $\alpha$  / Lz / Lz /  $\Delta\tau$ ]  $\Delta\tau$  Lz Lz /  $\alpha$  / 60 - trest / 60,
Tm  $\theta$  [Round[ $\frac{.5 \times 25.4}{1000 \text{ Lz } \Delta u}$ ], Round[ $\frac{0 \times 25.4}{1000 \text{ Lz } \Delta v}$ ], Round[ $\frac{.25 \times 25.4}{1000 \text{ Lz } \Delta w}$ ],
Round[n  $\alpha$  / Lz / Lz /  $\Delta\tau$ ]}] - 273 /.
sol[Round[n  $\alpha$  / Lz / Lz /  $\Delta\tau$ ]], {n, 0, tadq}],
Table[{Round[n  $\alpha$  / Lz / Lz /  $\Delta\tau$ ]  $\Delta\tau$  Lz Lz /  $\alpha$  / 60 - trest / 60,
Tm  $\theta$  [Round[ $\frac{2 \times 25.4}{1000 \text{ Lz } \Delta u}$ ], Round[ $\frac{0 \times 25.4}{1000 \text{ Lz } \Delta v}$ ], Round[ $\frac{.25 \times 25.4}{1000 \text{ Lz } \Delta w}$ ],
Round[n  $\alpha$  / Lz / Lz /  $\Delta\tau$ ]}] - 273 /.
sol[Round[n  $\alpha$  / Lz / Lz /  $\Delta\tau$ ]], {n, 0, tadq}],
Table[{Round[n  $\alpha$  / Lz / Lz /  $\Delta\tau$ ]  $\Delta\tau$  Lz Lz /  $\alpha$  / 60 - trest / 60,
Tm  $\theta$  [Round[ $\frac{3.5 \times 25.4}{1000 \text{ Lz } \Delta u}$ ], Round[ $\frac{0 \times 25.4}{1000 \text{ Lz } \Delta v}$ ], Round[ $\frac{.25 \times 25.4}{1000 \text{ Lz } \Delta w}$ ],
Round[n  $\alpha$  / Lz / Lz /  $\Delta\tau$ ]}] - 273 /.
sol[Round[n  $\alpha$  / Lz / Lz /  $\Delta\tau$ ]], {n, 0, tadq}]]],
PlotStyle  $\rightarrow$  {Red, Green, Blue, Brown}, Joined  $\rightarrow$  True,
Frame  $\rightarrow$  True,
FrameLabel  $\rightarrow$  {"Time Relative to Translation (min)", "Temp (C)"},
LabelStyle  $\rightarrow$  {Bold, FontFamily  $\rightarrow$  "Arial"}];
complot = Show[{theo, tc1plotabs, tc2plotabs, tc3plotabs},
PlotLabel  $\rightarrow$  StringJoin["pin = ", ToString[p1 / 746],
" Hp, h = ", ToString[h], ", Hb = ", ToString[hb],
", v = ", ToString[vx 1000 / 25.4  $\times$  60], " in/min"],
Frame  $\rightarrow$  True, PlotRange  $\rightarrow$  {All, {0, 600}},
LabelStyle  $\rightarrow$  {Bold, FontFamily  $\rightarrow$  "Arial"},
FrameLabel  $\rightarrow$  {"Time Relative to Translation (min)", "Temp (C)"},
LabelStyle  $\rightarrow$  {Bold, FontFamily  $\rightarrow$  "Arial"}];
complot = Show[{theo, tc1plotabs, tc2plotabs, tc3plotabs},
PlotRange  $\rightarrow$  {{-4, 6}, All}];

```

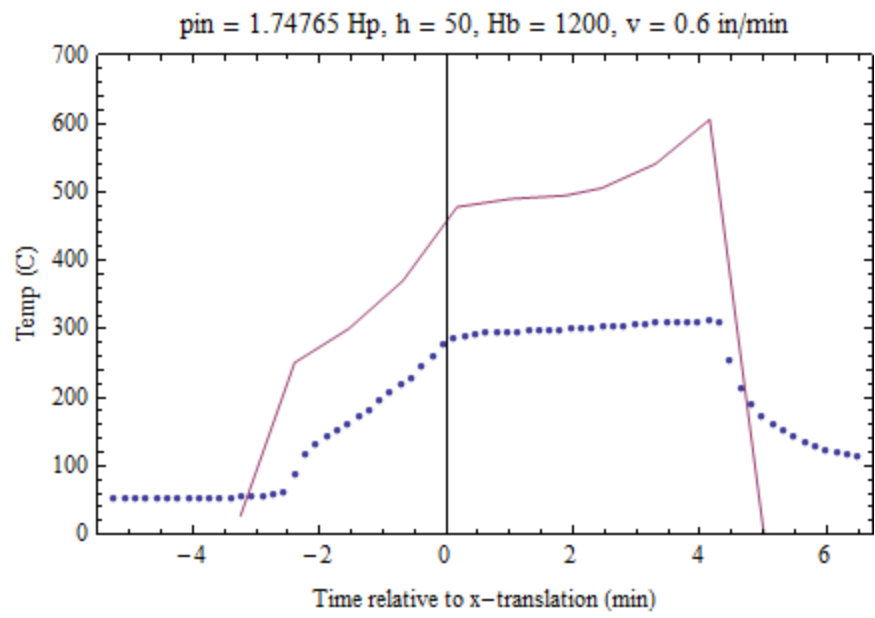
```
ShowLegend[complot,
{{{Graphics[{Directive[White], Line[{{0, 10}, {16, 10}}]},
  Directive[Red], Line[{{0, 17}, {16, 17}}]},
  Directive[Red, Dotted], Line[{{0, 15}, {16, 15}}]}]},
Style["Tc1", FontFamily -> "Arial", Bold]},
{Graphics[{Directive[White], Line[{{0, 10}, {16, 10}}]},
  Directive[Green], Line[{{0, 17}, {16, 17}}]},
  Directive[Green, Dotted], Line[{{0, 15}, {16, 15}}]}]},
Style["Tc2", FontFamily -> "Arial", Bold]},
{Graphics[{Directive[White], Line[{{0, 10}, {16, 10}}]},
  Directive[Blue], Line[{{0, 17}, {16, 17}}]},
  Directive[Blue, Dotted], Line[{{0, 15}, {16, 15}}]}]},
Style["Tc2", FontFamily -> "Arial", Bold]}],
LegendSize -> {.35, 0.5}, LegendShadow -> {0, 0},
LegendTextSpace -> 0.8, LegendPosition -> {1, .10}]}
```



```
Show[
ListPlot[
{Table[{t[[i]]/60 - tstart, hp[[i]]/hpmax}, {i, 1, Length[t]}],
Table[{n Δτ Lz Lz / α / 60 - trest / 60, Qc[n] / (qr  $\frac{Lz^2}{Tm \alpha}$ )},
{n, 0, nadq}]], Joined → True, Frame → True,
FrameLabel → {"Time relative to x-translation (min)",
"Power in (Hp/Hp)"}]]
```



```
Show[
ListPlot[
{Table[{t[[i]]/60 - tstart, tip[[i]]}, {i, 1, Length[t], 100}],
Table[{Round[n α / Lz / Lz / Δτ] Δτ Lz Lz / α / 60 - trest / 60,
Total[cent3[Round[n α / Lz / Lz / Δτ]]
Table[Tm θ[i, j, 0, Round[n α / Lz / Lz / Δτ]] - 273 /.
sol[Round[n α / Lz / Lz / Δτ]], {i, 0, Mu}, {j, 0, Mv}], 2] /.
sol[Round[n α / Lz / Lz / Δτ]]}, {n, 0, tadq, 50}]},
Joined → {False, True}, Frame → True,
FrameLabel → {"Time relative to x-translation (min)",
"Temp (C)"}, PlotRange → {All, {0, 700}}],
PlotLabel → StringJoin["pin = ", ToString[p1/746],
" Hp, h = ", ToString[h], ", Hb = ", ToString[hb],
", v = ", ToString[vx 1000 / 25.4 × 60], " in/min"],
Frame → True]
```



 Created with Wolfram Mathematica 7.0

## Appendix D 3-D Explicit Finite Difference Model Mathematica® Code

```
<< PlotLegends`

(*Define all the Constants*)
 $\alpha = 9.7 \times 10^{-5};$  (*m2/s*)
ktherm = 230; (*W/mk*)
h = 300; (*W/m^2k*)
 $\rho_{cp} = 2702 \star 902$  (*W s/m3 K*);

(*Define the inputs to the system*)
v = 1 * 25.4 / 60 / 1000 (*m/s*)
r = .012 (*m*);
 $\omega = 3000 / 60$  (*rev/sec*);
press = 1000 / 3 * 1 000 000 (*Pa*);
 $\mu = 1;$ 

0.000423333

(*Define the mesh and the workpiece dimensions*)
(*need to ensure no problems with dimy/2 being noninteger*)
dimx = .1; (*m*)
dimy = .1; (*m*)
dimz = .025; (*m*)
(* $\delta x = .005;$  (*m*)*)
 $\delta y = .005;$  (*m*)
 $\delta z = .005;$  (*m*)
nx = dimx /  $\delta x + 1$ 
  ny = dimy / 2 /  $\delta y + 1$ 
  nz = dimz /  $\delta z + 1$ *)
nx = 21;
ny = (nx + 1) / 2 + 1
nz = 6;
 $\delta x = \text{dimx} / (\text{nx} - 1)$ 
 $\delta y = \text{dimy} / (2 * (\text{ny} - 1))$ 
 $\delta z = \text{dimz} / (\text{nz} - 1)$ 
r /  $\delta x;$ 

12

0.005
```

0.00454545

0.005

```
(*determine the starting position for the tool
  center. the starting point is (xstart,0,0) by
  default. The tool moves along the y=0, z=0 line.*)
resx = dimx / (nx - 1);
resy = dimy / (ny - 1);
xstart = -dimx / 2 + 1.2 r(*m*);
xroun = If[OddQ[nx], Round[xstart /  $\delta x$ ]  $\delta x$ ,
  Round[xstart /  $\delta x$ ]  $\delta x$ ];
```

(\*using the mesh size,  
calculate the maximum time step that will ensure  
stability in the model\*)

```
Clear[δt]
stab1 = Solve[1 -  $\frac{2 k_{\text{therm}} \delta t}{\rho c p} \left( \frac{1}{\delta x^2} + \frac{1}{\delta y^2} + \frac{1}{\delta z^2} \right) == 0, \delta t]$ ;
stab2 = Solve[1 -  $\frac{h \delta t}{\rho c p \delta x} - \frac{k_{\text{therm}} \delta t}{\rho c p} \left( \frac{1}{\delta x^2} + \frac{1}{\delta y^2} + \frac{1}{\delta z^2} \right) == 0, \delta t]$ ;
stab3 = Solve[1 -  $\frac{h \delta t}{\rho c p \delta y} - \frac{k_{\text{therm}} \delta t}{\rho c p} \left( \frac{1}{\delta x^2} + \frac{1}{\delta y^2} + \frac{1}{\delta z^2} \right) == 0, \delta t]$ ;
stab4 = Solve[1 -  $\frac{h \delta t}{\rho c p \delta z} - \frac{k_{\text{therm}} \delta t}{\rho c p} \left( \frac{1}{\delta x^2} + \frac{1}{\delta y^2} + \frac{1}{\delta z^2} \right) == 0, \delta t]$ ;
stab5 =
  Solve[1 -  $\frac{h \delta t}{2 \rho c p \delta x} \left( \frac{1}{\delta x} + \frac{1}{\delta y} \right) - \frac{k_{\text{therm}} \delta t}{2 \rho c p} \left( \frac{1}{\delta x^2} + \frac{1}{\delta y^2} + \frac{1}{\delta z^2} \right) == 0,$ 
    δt];
stab6 =
  Solve[1 -  $\frac{h \delta t}{2 \rho c p \delta x} \left( \frac{1}{\delta x} + \frac{1}{\delta z} \right) - \frac{k_{\text{therm}} \delta t}{2 \rho c p} \left( \frac{1}{\delta x^2} + \frac{1}{\delta y^2} + \frac{1}{\delta z^2} \right) == 0,$ 
    δt];
stab7 =
  Solve[1 -  $\frac{h \delta t}{2 \rho c p \delta x} \left( \frac{1}{\delta y} + \frac{1}{\delta z} \right) - \frac{k_{\text{therm}} \delta t}{2 \rho c p} \left( \frac{1}{\delta x^2} + \frac{1}{\delta y^2} + \frac{1}{\delta z^2} \right) == 0,$ 
    δt];
stab8 =
  Solve[
    1 -  $\frac{h \delta t}{4 \rho c p \delta x} \left( \frac{1}{\delta x} + \frac{1}{\delta y} + \frac{1}{\delta z} \right) - \frac{k_{\text{therm}} \delta t}{4 \rho c p} \left( \frac{1}{\delta x^2} + \frac{1}{\delta y^2} + \frac{1}{\delta z^2} \right) == 0,$ 
    δt];
stab1 = stab1[[1, 1, 2]];
stab2 = stab2[[1, 1, 2]];
stab3 = stab3[[1, 1, 2]];
stab4 = stab4[[1, 1, 2]];
stab5 = stab5[[1, 1, 2]];
stab6 = stab6[[1, 1, 2]];
stab7 = stab7[[1, 1, 2]];
stab8 = stab8[[1, 1, 2]];

δtmax = Min[stab1, stab2, stab3, stab4, stab5, stab6,
  stab7, stab8];
Print["Maximum time step = ", Style[δtmax, Red],
  " seconds"]
```

Maximum time step = 0.0412638 seconds

```
(*set the time step to something lower than  $\delta t_{max}$ . also,
set tmax*)
 $\delta t = 1.4 (*\delta t_{max} / 2*)$ ;
If[ $\delta t > \delta t_{max}$ ,  $\delta t = .999 \delta t_{max}$ ,  $\delta t = \delta t$ ];
tmax = Round[6 /  $\delta t$ ]  $\delta t$ ;
tpre = Round[3 /  $\delta t$ ]  $\delta t$ ;
Print["Timestep of ", Style[ $\delta t$ , Red],
" seconds, total time of ", Style[tmax, Red], " seconds (",
Style[tmax /  $\delta t$ , Red], ") iterations."]
```

Timestep of 0.0412225 seconds, total time of  
6.01849 seconds (146.) iterations.

```
(*set the initial temperature of the workpiece and
set the room temperature for convection*)
tinit = 300; (*K*)
tamb = 300 (*K*);
```

```
(*initialize the temperature matrix to be filled in
during future calculations*)
init = Table[{i, j, k, tinit, 1}, {1, 1, tmax /  $\delta t$ },
  {i, -dimx / 2, dimx / 2,  $\delta x$ }, {j, 0, dimy / 2,  $\delta y$ },
  {k, 0, dimz,  $\delta z$ }]
```

```
sizepre = Dimensions[init];
size = sizepre [[1]] sizepre [[2]] sizepre [[3]] sizepre [[4]];
Print["Total of ", Style[size, Red], " matrix entries"]
```

Total of 220752 matrix entries

```

(*(*Define Δx and Δy. The following allows for a non-
linear mesh distribution,
whereas the source matrix calculation (later) will
not function unless the mesh is rectilinear*)
Δx[l_,i_,j_,k_]:=
If[i==1,Abs[(init[[l,i+1,j,k,1]]-init[[l,i,j,k,1]])],
  If[i==nx,Abs[(init[[l,i-1,j,k,1]]-init[[l,i,j,k,1]])],
    Abs[(init[[l,i+1,j,k,1]]-init[[l,i,j,k,1]])]/2+
    Abs[(init[[l,i,j,k,1]]-init[[l,i-1,j,k,1]])]/2]];
Δy[l_,i_,j_,k_]:=
If[j==1,Abs[(init[[l,i,j+1,k,2]]-init[[l,i,j,k,2]])],
  If[j==ny,Abs[(init[[l,i,j-1,k,2]]-init[[l,i,j,k,2]])],
    Abs[(init[[l,i,j+1,k,2]]-init[[l,i,j,k,2]])]/2+
    Abs[(init[[l,i,j,k,2]]-init[[l,i,j-1,k,2]])]/2]];
Δz[l_,i_,j_,k_]:=
If[k==1,Abs[(init[[l,i,j,k+1,3]]-init[[l,i,j,k,3]])],
  If[k==nz,Abs[(init[[l,i,j,k-1,3]]-init[[l,i,j,k,3]])],
    Abs[(init[[l,i,j,k+1,3]]-init[[l,i,j,k,3]])]/2+
    Abs[(init[[l,i,j,k,3]]-init[[l,i,j,k-1,3]])]/2]];*)

(*input the position of the center of the heat source
as a function of time. The following assumes a fixed-
velocity linear translation along the y=
0 line with a preheat time, tpre*)
qc = Table[If[l < tpre , {l, xroun, 0},
  {l, Round[(xroun + v (l - tpre)) / δx] δx, 0}],
  {l, 0, tmax, δt}];

(*initialize the source matrix*)
qtool = Table[{i, j, 0, 1}, {l, 0, tmax, δt},
  {i, -dimx/2, dimx/2, δx}, {j, 0, dimy/2, δy}];

```

```

(*determine the input energy flux by using the radius
of the source and the mesh size*)
dimx2 = dimy2 = 2.2 r;
init2 = Table[{i, j}, {i, -dimx2/2, dimx2/2,  $\delta x$ },
  {j, -dimy2/2, dimy2/2,  $\delta y$ ]];
qint1 =
  Table[If[Sqrt[init2[[i, j, 1]]^2 + init2[[i, j, 2]]^2] > r,
    0, Ceiling[ $\frac{\sqrt{\text{init2}[[i, j, 1]]^2 + \text{init2}[[i, j, 2]]^2}}{\sqrt{\delta x^2 + \delta y^2}}$ ]],
  {i, 1, dimx2 /  $\delta x$  + 1}, {j, 1, dimy2 /  $\delta y$  + 1}];
MatrixForm[qint1];

(*determine total heat input*)
qtesttotal = 4 / 3 Pi^2 r^3 press  $\omega \mu$ ;
qtesttotalhp = qtesttotal .001341;
Print["Total input power = ", qtesttotal, " watts (",
  qtesttotalhp, " hp)."]

Total input power = 378993. watts (508.229 hp).

```

(\*fill the heat matrix by determining whether the gridpoint (i,j,0) is within the radius of the tool\*)

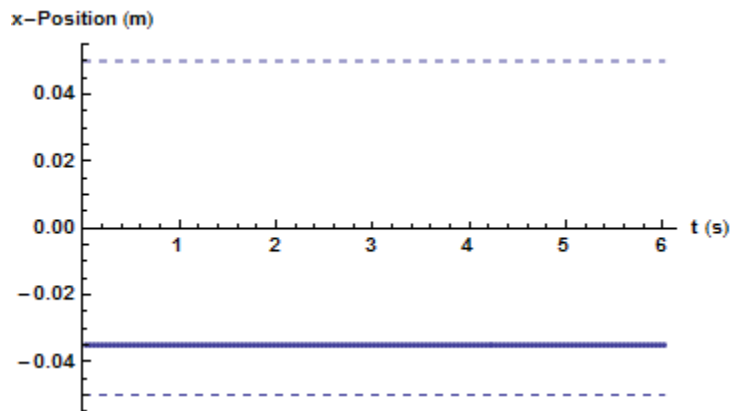
```

Table[
  If[
    Sqrt[(init[[1, i, j, 1, 1]] - qc[[1, 2]])^2 +
      (init[[1, i, j, 1, 2]] - qc[[1, 3]])^2] > r,
    qtool[[1, i, j, 3]] = 0,
    qtool[[1, i, j, 3]] =
      4/3 π^2 μ press ω
      (Round[Sqrt[(init[[1, i, j, 1, 1]] - qc[[1, 2]])^2 +
        2 + (init[[1, i, j, 1, 2]] - qc[[1, 3]])^2]/
        (√δx^2 + δy^2)] √δx^2 + δy^2)^3 -
      (Round[1/√δx^2 + δy^2 Sqrt[
        (init[[1, i, j, 1, 1]] - qc[[1, 2]])^2 +
        (init[[1, i, j, 1, 2]] - qc[[1, 3]])^2] - 1]
        √δx^2 + δy^2)^3)/
    Count[qint1,
      Round[
        Sqrt[(init[[1, i, j, 1, 1]] - qc[[1, 2]])^2 +
          (init[[1, i, j, 1, 2]] - qc[[1, 3]])^2]/
          (√δx^2 + δy^2)], 2]], {1, 1, tmax/δt},
    {i, 1, dimx/δx + 1}, {j, 1, dimy/2/δy + 1}];

```

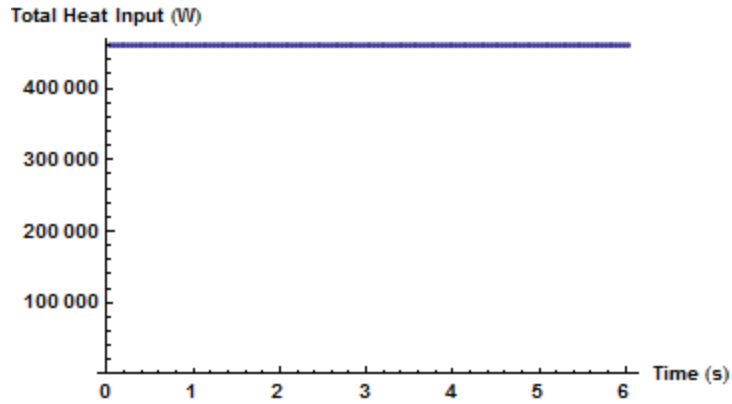
(\*plot the location of the center of the heat source to gauge when the heat source enters and leaves the workpiece\*)

```
bound1 = ListPlot[{{0, dimx/2}, {tmax, dimx/2}},
  Joined → True, PlotStyle → {Dashed}];
bound2 = ListPlot[{{0, -dimx/2}, {tmax, -dimx/2}},
  Joined → True, PlotStyle → {Dashed}];
cent = ListPlot[Table[{i δt, qc[[i, 2]]}, {i, 1, tmax/δt}],
  AxesLabel → {"t (s)", "x-Position (m)"},
  PlotRange → {{0, All}, {-1.1 dimx/2, 1.1 dimx/2}},
  (*PlotLabel→"heat source center",*)
  LabelStyle → Directive[Bold, FontFamily → "Arial"]];
Show[cent, bound1, bound2]
```



(\*Calculate and plot the total power input into the system as a function of time\*)

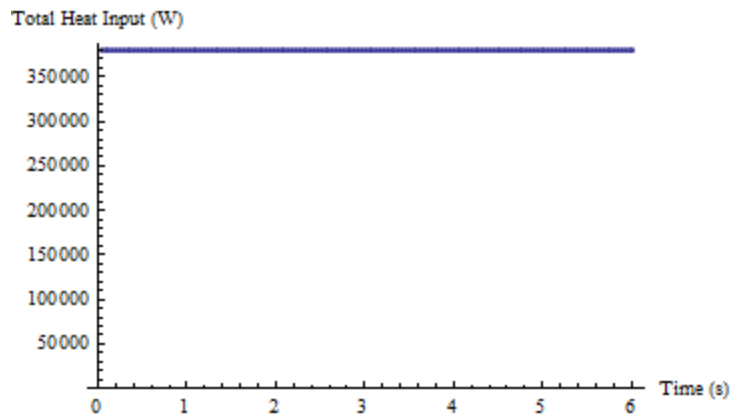
```
qcalc[x_] :=
  2 Sum[qtool[{x, i, j, 3}], {i, 1, dimx/δx}, {j, 1, ny}];
ListPlot[Table[{x δt, qcalc[x]}, {x, 1, tmax/δt}],
  PlotRange → {All, {0, Automatic}},
  AxesLabel → {"Time (s)", "Total Heat Input (W)"},
  LabelStyle → Directive[Bold, FontFamily → "Arial"]]
```



```
qal = qtesttotal/qcalc[Round[2/δt]];
Table[qtool[[1, i, j, 3]] = qtool[[1, i, j, 3]] qal,
  {1, 1, tmax/δt}, {i, 1, dimx/δx + 1}, {j, 1, dimy/2/δy + 1}];
```

(\*Calculate and plot the total power input into the system as a function of time\*)

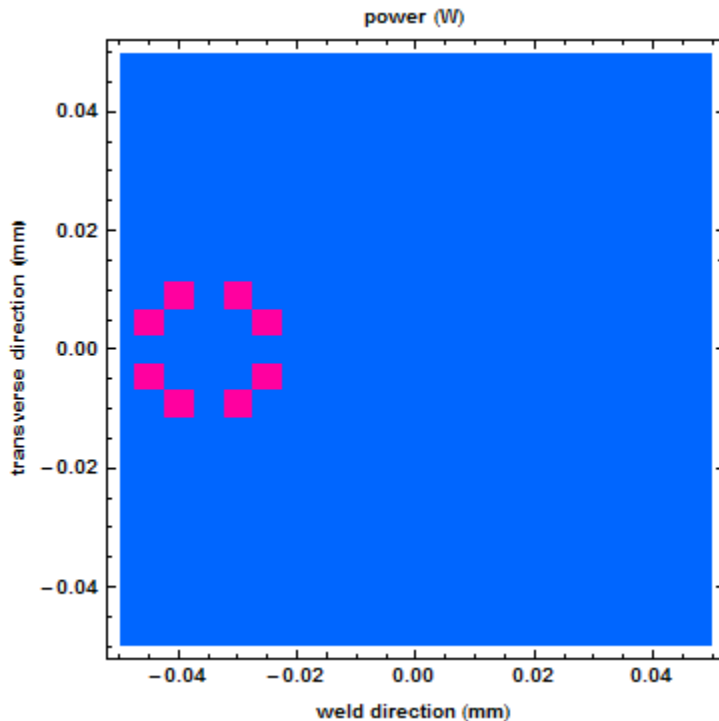
```
qcalc[x_] :=
  2 Sum[qtool[[x, i, j, 3]], {i, 1, dimx/δx}, {j, 1, ny}];
ListPlot[Table[{x δt, qcalc[x]}, {x, 1, tmax/δt}],
  PlotRange → {All, {0, Automatic}},
  AxesLabel → {"Time (s)", "Total Heat Input (W)"}]
```



```
(*Generate and plot the heat input in a 3D format to
illustrate the moving heat source*)
```

```
qplot1[x_] :=
  Flatten[
    Table[{qtool[[x, i, j, 1]], qtool[[x, i, j, 2]],
      qtool[[x, i, j, 3]]}, {i, 1, nx}, {j, 1, ny}], 1];
qplot2[x_] :=
  Flatten[
    Table[{qtool[[x, i, j, 1]], -qtool[[x, i, j, 2]],
      qtool[[x, i, j, 3]]}, {i, 1, nx}, {j, 1, ny}], 1];
qplot[x_] := Join[qplot1[x], qplot2[x]]
```

```
ListContourPlot[qplot[Round[3/δt]],
  ColorFunction → Function[{z}, Hue[.6 (1 - z/100)]],
  ColorFunctionScaling → False,
  FrameLabel → {"weld direction (mm)",
    "transverse direction (mm)", "power (W)"},
  LabelStyle → Directive[Bold, FontFamily → "Arial"],
  InterpolationOrder → 0]
```



```
pmax = Max[qplot[2]]
```

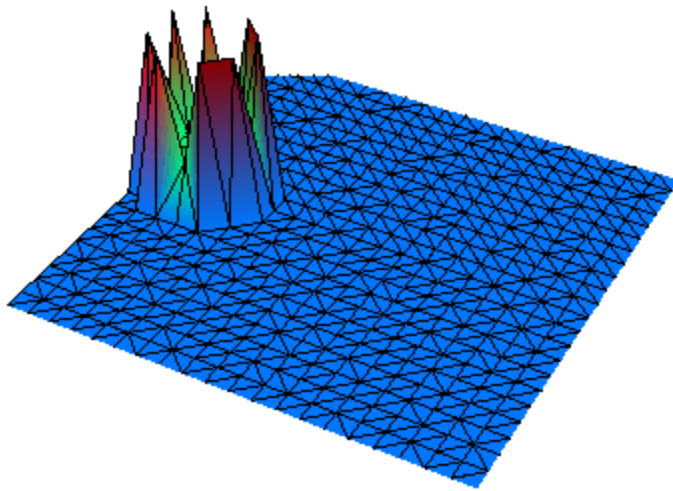
```
27 901.3
```

```

range2 = .6;
NewColor2[r_] := Hue[range2 (1 - r)];
pmin = 00;
LinearScale2 = Table[ $\frac{pmax - pmin}{100} i + pmin$ , {i, 0, 100}];
ScaleGradient2 = Table[Hue[range2 (1 -  $\frac{i}{101}$ )],
  {i, 0, Length[LinearScale2]}];
GradientScale2 =
  Table[{ScaleGradient2[[i]], PointSize[0.14],
    Point[{LinearScale2[[i]], .025}]},
  {i, 1, Length[LinearScale2]}];
ScaleLabel2 = Plot[0, {x, pmin, pmax},
  PlotRange -> {{0, pmax}, All}, AxesOrigin -> {-1, 1},
  Axes -> {True, False}, Frame -> True,
  FrameStyle -> {RGBColor[0, 0, 0], RGBColor[1, 1, 1],
    RGBColor[1, 1, 1], RGBColor[1, 1, 1]},
  FrameTicks -> {Automatic, None, None, None},
  FrameLabel -> {"Power, W", ""}, ImageSize -> {300, 10},
  AspectRatio -> .25, DisplayFunction -> Identity];
scale2 = Show[ScaleLabel2, Graphics[{GradientScale2}],
  DisplayFunction -> Identity, ImageSize -> {300, 100},
  LabelStyle -> Directive[Bold, FontFamily -> "Arial"]];

ListPlot3D[qqplot[Round[3 / dt]],
  ColorFunction -> Function[{x, y, z}, Hue[.6 (1 - z)]],
  ColorFunctionScaling -> True,
  PlotRange -> {{-dimx / 2, dimx / 2}, {-dimy / 2, dimy / 2},
  Automatic}, Mesh -> All, Axes -> False, Boxed -> False,
  PlotStyle -> Opacity[1],
  LabelStyle -> Directive[Bold, FontFamily -> "Arial"]
Show[scale2]

```



0      5000      10000      15000      20000      25000  
 Power, W

```
qgen = 0;
tsolid = 933;
feed[l_, i_, j_, k_] :=
  If[init[[l-1, i, j, k, 4]] < tsolid, 1, 0]
```

(\*using the initial temperature of the plate, tinit,  
 calculate the temperature at each node for each time  
 step. If any of the indices are equal to 1 or N,  
 calculate temperatures using boundary conditions,  
 i.e. convection, conduction, etc.\*)

Table[

```
(*CORNERS*) If [And[i == 1, j == 1, k == 1],
init[[l, i, j, k, 4]] =
init[[l - 1, i, j, k, 4]]
   $\left(1 - \frac{k_{\text{therm}} \delta t}{2 \rho_{\text{cp}}} \left(\frac{1}{\delta x^2} + \frac{1}{\delta y^2} + \frac{1}{\delta z^2}\right) - \frac{h \delta t}{2 \rho_{\text{cp}}} \left(\frac{1}{\delta x} + \frac{1}{\delta z}\right)\right) +$ 
   $\text{tamb} \frac{h \delta t}{2 \rho_{\text{cp}}} \left(\frac{1}{\delta x} + \frac{1}{\delta z}\right) +$ 
   $\frac{k_{\text{therm}} \delta t}{\rho_{\text{cp}}}$ 
   $\left(\frac{1}{2 \delta x^2} \text{init}[[l - 1, i + 1, j, k, 4]] +$ 
     $\frac{1}{2 \delta y^2} \text{init}[[l - 1, i, j + 1, k, 4]] +$ 
     $\frac{1}{2 \delta z^2} \text{init}[[l - 1, i, j, k + 1, 4]]\right) +$ 
   $\frac{\delta t}{\rho_{\text{cp}} \delta x \delta y \delta z} (\text{qgen} + \text{feed}[l, i, j, k] \text{qtool}[[l, i, j, 3]]),$ 
```

```
If [And[i == 1, j == 1, k == nz],
init[[l, i, j, k, 4]] =
init[[l - 1, i, j, k, 4]]
   $\left(1 - \frac{k_{\text{therm}} \delta t}{2 \rho_{\text{cp}}} \left(\frac{1}{\delta x^2} + \frac{1}{\delta y^2} + \frac{1}{\delta z^2}\right) - \frac{h \delta t}{2 \rho_{\text{cp}}} \left(\frac{1}{\delta x} + \frac{1}{\delta z}\right)\right) +$ 
   $\text{tamb} \frac{h \delta t}{2 \rho_{\text{cp}}} \left(\frac{1}{\delta x} + \frac{1}{\delta z}\right) +$ 
   $\frac{k_{\text{therm}} \delta t}{\rho_{\text{cp}}}$ 
   $\left(\frac{1}{2 \delta x^2} \text{init}[[l - 1, i + 1, j, k, 4]] +$ 
     $\frac{1}{2 \delta y^2} \text{init}[[l - 1, i, j + 1, k, 4]] +$ 
     $\frac{1}{2 \delta z^2} \text{init}[[l - 1, i, j, k - 1, 4]]\right),$ 
```

```

If [And[i == 1, j == ny, k == 1],
  init[[l, i, j, k, 4]] =
  init[[l - 1, i, j, k, 4]]
  (1 -  $\frac{k_{therm} \delta t}{4 \rho c p} \left( \frac{1}{\delta x^2} + \frac{1}{\delta y^2} + \frac{1}{\delta z^2} \right) - \frac{h \delta t}{4 \rho c p} \left( \frac{1}{\delta x} + \frac{1}{\delta y} + \frac{1}{\delta z} \right)) +$ 
  tamb  $\frac{h \delta t}{4 \rho c p} \left( \frac{1}{\delta x} + \frac{1}{\delta y} + \frac{1}{\delta z} \right) +$ 
   $\frac{k_{therm} \delta t}{4 \rho c p}$ 
  (  $\frac{1}{\delta x^2}$  init[[l - 1, i + 1, j, k, 4]] +
     $\frac{1}{\delta y^2}$  init[[l - 1, i, j - 1, k, 4]] +
     $\frac{1}{\delta z^2}$  init[[l - 1, i, j, k + 1, 4]] ) +
   $\frac{\delta t}{\rho c p \delta x \delta y \delta z}$  (qgen + feed[l, i, j, k] qtool[[l, i, j, 3]]),

```

```

If [And[i == 1, j == ny, k == nz],
  init[[l, i, j, k, 4]] =
  init[[l - 1, i, j, k, 4]]
  (1 -  $\frac{k_{therm} \delta t}{4 \rho c p} \left( \frac{1}{\delta x^2} + \frac{1}{\delta y^2} + \frac{1}{\delta z^2} \right) - \frac{h \delta t}{4 \rho c p} \left( \frac{1}{\delta x} + \frac{1}{\delta y} + \frac{1}{\delta z} \right)) +$ 
  tamb  $\frac{h \delta t}{4 \rho c p} \left( \frac{1}{\delta x} + \frac{1}{\delta y} + \frac{1}{\delta z} \right) +$ 
   $\frac{k_{therm} \delta t}{4 \rho c p}$ 
  (  $\frac{1}{\delta x^2}$  init[[l - 1, i + 1, j, k, 4]] +
     $\frac{1}{\delta y^2}$  init[[l - 1, i, j - 1, k, 4]] +
     $\frac{1}{\delta z^2}$  init[[l - 1, i, j, k - 1, 4]] ),

```

```

If [And[i == nx, j == 1, k == 1],
  init[[l, i, j, k, 4]] =
  init[[l - 1, i, j, k, 4]]
  \left(1 - \frac{k_{\text{therm}} \delta t}{2 \rho_{\text{cp}}} \left(\frac{1}{\delta x^2} + \frac{1}{\delta y^2} + \frac{1}{\delta z^2}\right) - \frac{h \delta t}{2 \rho_{\text{cp}}} \left(\frac{1}{\delta x} + \frac{1}{\delta z}\right)\right) +
  \text{tamb} \frac{h \delta t}{2 \rho_{\text{cp}}} \left(\frac{1}{\delta x} + \frac{1}{\delta z}\right) +
  \frac{k_{\text{therm}} \delta t}{\rho_{\text{cp}}}
  \left(\frac{1}{2 \delta x^2} \text{init}[[l - 1, i - 1, j, k, 4]] +
  \frac{1}{2 \delta y^2} \text{init}[[l - 1, i, j + 1, k, 4]] +
  \frac{1}{2 \delta z^2} \text{init}[[l - 1, i, j, k + 1, 4]]\right) +
  \frac{\delta t}{\rho_{\text{cp}} \delta x \delta y \delta z} (\text{qgen} + \text{feed}[l, i, j, k] \text{qtool}[[l, i, j, 3]]),

```

```

If [And[i == nx, j == 1, k == nz],
  init[[l, i, j, k, 4]] =
  init[[l - 1, i, j, k, 4]]
  \left(1 - \frac{k_{\text{therm}} \delta t}{2 \rho_{\text{cp}}} \left(\frac{1}{\delta x^2} + \frac{1}{\delta y^2} + \frac{1}{\delta z^2}\right) - \frac{h \delta t}{2 \rho_{\text{cp}}} \left(\frac{1}{\delta x} + \frac{1}{\delta z}\right)\right) +
  \text{tamb} \frac{h \delta t}{2 \rho_{\text{cp}}} \left(\frac{1}{\delta x} + \frac{1}{\delta z}\right) +
  \frac{k_{\text{therm}} \delta t}{\rho_{\text{cp}}}
  \left(\frac{1}{2 \delta x^2} \text{init}[[l - 1, i - 1, j, k, 4]] +
  \frac{1}{2 \delta y^2} \text{init}[[l - 1, i, j + 1, k, 4]] +
  \frac{1}{2 \delta z^2} \text{init}[[l - 1, i, j, k - 1, 4]]\right),

```

```

If [And[i == nx, j == ny, k == 1],
  init[[l, i, j, k, 4]] =
  init[[l - 1, i, j, k, 4]]
  (1 -  $\frac{k_{\text{therm}} \delta t}{4 \rho c p} \left( \frac{1}{\delta x^2} + \frac{1}{\delta y^2} + \frac{1}{\delta z^2} \right) - \frac{h \delta t}{4 \rho c p} \left( \frac{1}{\delta x} + \frac{1}{\delta y} + \frac{1}{\delta z} \right)) +$ 
  tamb  $\frac{h \delta t}{4 \rho c p} \left( \frac{1}{\delta x} + \frac{1}{\delta y} + \frac{1}{\delta z} \right) +$ 
   $\frac{k_{\text{therm}} \delta t}{4 \rho c p}$ 
  (  $\frac{1}{\delta x^2}$  init[[l - 1, i - 1, j, k, 4]] +
     $\frac{1}{\delta y^2}$  init[[l - 1, i, j - 1, k, 4]] +
     $\frac{1}{\delta z^2}$  init[[l - 1, i, j, k + 1, 4]] ) +
   $\frac{\delta t}{\rho c p \delta x \delta y \delta z}$  (qgen + feed[l, i, j, k] qtool[[l, i, j, 3]]),

```

```

If [And[i == nx, j == ny, k == nz],
  init[[l, i, j, k, 4]] =
  init[[l - 1, i, j, k, 4]]
  (1 -  $\frac{k_{\text{therm}} \delta t}{4 \rho c p} \left( \frac{1}{\delta x^2} + \frac{1}{\delta y^2} + \frac{1}{\delta z^2} \right) - \frac{h \delta t}{4 \rho c p} \left( \frac{1}{\delta x} + \frac{1}{\delta y} + \frac{1}{\delta z} \right)) +$ 
  tamb  $\frac{h \delta t}{4 \rho c p} \left( \frac{1}{\delta x} + \frac{1}{\delta y} + \frac{1}{\delta z} \right) +$ 
   $\frac{k_{\text{therm}} \delta t}{4 \rho c p}$ 
  (  $\frac{1}{\delta x^2}$  init[[l - 1, i - 1, j, k, 4]] +
     $\frac{1}{\delta y^2}$  init[[l - 1, i, j - 1, k, 4]] +
     $\frac{1}{\delta z^2}$  init[[l - 1, i, j, k - 1, 4]] ),

```

```

(*edges*)
If [And[i == 1, j == 1],
  init[[1, i, j, k, 4]] =
  init[[1 - 1, i, j, k, 4]]
  
$$\left(1 - \frac{k_{\text{therm}} \delta t}{\rho c p} \left(\frac{1}{\delta x^2} + \frac{1}{\delta y^2} + \frac{1}{\delta z^2}\right) - \frac{h \delta t}{\rho c p} \left(\frac{1}{\delta x}\right)\right) +$$

  
$$\text{tamb} \frac{h \delta t}{\rho c p} \left(\frac{1}{\delta x}\right) +$$

  
$$\frac{k_{\text{therm}} \delta t}{\rho c p}$$

  
$$\left(\frac{1}{\delta x^2} \text{init}[[1 - 1, i + 1, j, k, 4]] +$$

  
$$\frac{1}{\delta y^2} \text{init}[[1 - 1, i, j + 1, k, 4]] +$$

  
$$\frac{1}{2 \delta z^2} (\text{init}[[1 - 1, i, j, k - 1, 4]] +$$

  
$$\text{init}[[1 - 1, i, j, k + 1, 4]])\right),$$


If [And[i == 1, j == ny],
  init[[1, i, j, k, 4]] =
  init[[1 - 1, i, j, k, 4]]
  
$$\left(1 - \frac{k_{\text{therm}} \delta t}{2 \rho c p} \left(\frac{1}{\delta x^2} + \frac{1}{\delta y^2} + \frac{1}{\delta z^2}\right) - \frac{h \delta t}{2 \rho c p} \left(\frac{1}{\delta x} + \frac{1}{\delta y}\right)\right) +$$

  
$$\text{tamb} \frac{h \delta t}{2 \rho c p} \left(\frac{1}{\delta x} + \frac{1}{\delta y}\right) +$$

  
$$\frac{k_{\text{therm}} \delta t}{\rho c p}$$

  
$$\left(\frac{1}{2 \delta x^2} \text{init}[[1 - 1, i + 1, j, k, 4]] +$$

  
$$\frac{1}{2 \delta y^2} \text{init}[[1 - 1, i, j - 1, k, 4]] +$$

  
$$\frac{1}{4 \delta z^2} (\text{init}[[1 - 1, i, j, k - 1, 4]] +$$

  
$$\text{init}[[1 - 1, i, j, k + 1, 4]])\right),$$


```

```

If [And[i == nx, j == 1],
  init[[l, i, j, k, 4]] =
  init[[l - 1, i, j, k, 4]]
  (1 -  $\frac{k_{\text{therm}} \delta t}{\rho c p} \left( \frac{1}{\delta x^2} + \frac{1}{\delta y^2} + \frac{1}{\delta z^2} \right) - \frac{h \delta t}{\rho c p} \left( \frac{1}{\delta x} \right) +$ 
   $\text{tamb} \frac{h \delta t}{\rho c p} \left( \frac{1}{\delta x} \right) +$ 
   $\frac{k_{\text{therm}} \delta t}{\rho c p}$ 
  (  $\frac{1}{\delta x^2}$  init[[l - 1, i - 1, j, k, 4]] +
     $\frac{1}{\delta y^2}$  init[[l - 1, i, j + 1, k, 4]] +
     $\frac{1}{2 \delta z^2}$  (init[[l - 1, i, j, k - 1, 4]] +
      init[[l - 1, i, j, k + 1, 4]])) ,

```

```

If [And[i == nx, j == ny],
  init[[l, i, j, k, 4]] =
  init[[l - 1, i, j, k, 4]]
  (1 -  $\frac{k_{\text{therm}} \delta t}{2 \rho c p} \left( \frac{1}{\delta x^2} + \frac{1}{\delta y^2} + \frac{1}{\delta z^2} \right) - \frac{h \delta t}{2 \rho c p} \left( \frac{1}{\delta x} + \frac{1}{\delta y} \right) +$ 
   $\text{tamb} \frac{h \delta t}{2 \rho c p} \left( \frac{1}{\delta x} + \frac{1}{\delta y} \right) +$ 
   $\frac{k_{\text{therm}} \delta t}{\rho c p}$ 
  (  $\frac{1}{2 \delta x^2}$  init[[l - 1, i - 1, j, k, 4]] +
     $\frac{1}{2 \delta y^2}$  init[[l - 1, i, j - 1, k, 4]] +
     $\frac{1}{4 \delta z^2}$  (init[[l - 1, i, j, k - 1, 4]] +
      init[[l - 1, i, j, k + 1, 4]])) ,

```

```

If [And[i == 1, k == 1],
  init[[l, i, j, k, 4]] =
  init[[l - 1, i, j, k, 4]]
  (1 -  $\frac{k_{\text{therm}} \delta t}{2 \rho_{\text{cp}}} \left( \frac{1}{\delta x^2} + \frac{1}{\delta y^2} + \frac{1}{\delta z^2} \right) - \frac{h \delta t}{2 \rho_{\text{cp}}} \left( \frac{1}{\delta x} + \frac{1}{\delta z} \right)) +$ 
  tamb  $\frac{h \delta t}{2 \rho_{\text{cp}}} \left( \frac{1}{\delta x} + \frac{1}{\delta z} \right) +$ 
   $\frac{k_{\text{therm}} \delta t}{\rho_{\text{cp}}}$ 
  (  $\frac{1}{2 \delta x^2}$  init[[l - 1, i + 1, j, k, 4]] +
     $\frac{1}{4 \delta y^2}$  (init[[l - 1, i, j - 1, k, 4]] +
      init[[l - 1, i, j + 1, k, 4]]) +
     $\frac{1}{2 \delta z^2}$  init[[l - 1, i, j, k + 1, 4]] ) +
   $\frac{\delta t}{\rho_{\text{cp}} \delta x \delta y \delta z}$  (qgen + feed[l, i, j, k] qtool[[l, i, j, 3]]),

```

```

If [And[i == 1, k == nz],
  init[[l, i, j, k, 4]] =
  init[[l - 1, i, j, k, 4]]
  (1 -  $\frac{k_{\text{therm}} \delta t}{2 \rho_{\text{cp}}} \left( \frac{1}{\delta x^2} + \frac{1}{\delta y^2} + \frac{1}{\delta z^2} \right) - \frac{h \delta t}{2 \rho_{\text{cp}}} \left( \frac{1}{\delta x} + \frac{1}{\delta z} \right)) +$ 
  tamb  $\frac{h \delta t}{2 \rho_{\text{cp}}} \left( \frac{1}{\delta x} + \frac{1}{\delta z} \right) +$ 
   $\frac{k_{\text{therm}} \delta t}{\rho_{\text{cp}}}$ 
  (  $\frac{1}{2 \delta x^2}$  init[[l - 1, i + 1, j, k, 4]] +
     $\frac{1}{4 \delta y^2}$  (init[[l - 1, i, j - 1, k, 4]] +
      init[[l - 1, i, j + 1, k, 4]]) +
     $\frac{1}{2 \delta z^2}$  init[[l - 1, i, j, k - 1, 4]] ),

```

```

If [And[i == nx, k == 1],
  init[[l, i, j, k, 4]] =
  init[[l - 1, i, j, k, 4]]
   $\left(1 - \frac{k_{\text{therm}} \delta t}{2 \rho_{\text{cp}}} \left(\frac{1}{\delta x^2} + \frac{1}{\delta y^2} + \frac{1}{\delta z^2}\right) - \frac{h \delta t}{2 \rho_{\text{cp}}} \left(\frac{1}{\delta x} + \frac{1}{\delta z}\right)\right) +$ 
   $\text{tamb} \frac{h \delta t}{2 \rho_{\text{cp}}} \left(\frac{1}{\delta x} + \frac{1}{\delta z}\right) +$ 
   $\frac{k_{\text{therm}} \delta t}{\rho_{\text{cp}}}$ 
   $\left(\frac{1}{2 \delta x^2} \text{init}[[l - 1, i - 1, j, k, 4]] +$ 
   $\frac{1}{4 \delta y^2} (\text{init}[[l - 1, i, j - 1, k, 4]] +$ 
   $\text{init}[[l - 1, i, j + 1, k, 4]]) +$ 
   $\frac{1}{2 \delta z^2} \text{init}[[l - 1, i, j, k + 1, 4]]\right) +$ 
   $\frac{\delta t}{\rho_{\text{cp}} \delta x \delta y \delta z} (\text{qgen} + \text{feed}[l, i, j, k] \text{qtool}[[l, i, j, 3]]),$ 

```

```

If [And[i == nx, k == nz],
  init[[l, i, j, k, 4]] =
  init[[l - 1, i, j, k, 4]]
   $\left(1 - \frac{k_{\text{therm}} \delta t}{2 \rho_{\text{cp}}} \left(\frac{1}{\delta x^2} + \frac{1}{\delta y^2} + \frac{1}{\delta z^2}\right) - \frac{h \delta t}{2 \rho_{\text{cp}}} \left(\frac{1}{\delta x} + \frac{1}{\delta z}\right)\right) +$ 
   $\text{tamb} \frac{h \delta t}{2 \rho_{\text{cp}}} \left(\frac{1}{\delta x} + \frac{1}{\delta z}\right) +$ 
   $\frac{k_{\text{therm}} \delta t}{\rho_{\text{cp}}}$ 
   $\left(\frac{1}{2 \delta x^2} \text{init}[[l - 1, i - 1, j, k, 4]] +$ 
   $\frac{1}{4 \delta y^2} (\text{init}[[l - 1, i, j - 1, k, 4]] +$ 
   $\text{init}[[l - 1, i, j + 1, k, 4]]) +$ 
   $\frac{1}{2 \delta z^2} \text{init}[[l - 1, i, j, k - 1, 4]]\right),$ 

```

```

If [And[j == 1, k == 1],
  init[[l, i, j, k, 4]] =
  init[[l - 1, i, j, k, 4]]
   $\left(1 - \frac{k_{\text{therm}} \delta t}{\rho_{\text{cp}}} \left(\frac{1}{\delta x^2} + \frac{1}{\delta y^2} + \frac{1}{\delta z^2}\right) - \frac{h \delta t}{\rho_{\text{cp}}} \left(\frac{1}{\delta z}\right)\right) +$ 
   $\text{tamb} \frac{h \delta t}{\rho_{\text{cp}}} \left(\frac{1}{\delta z}\right) +$ 
   $\frac{k_{\text{therm}} \delta t}{\rho_{\text{cp}}}$ 
   $\left(\frac{1}{2 \delta x^2} (\text{init}[[l - 1, i + 1, j, k, 4]] +$ 
     $\text{init}[[l - 1, i - 1, j, k, 4]]) +$ 
     $\frac{1}{\delta y^2} \text{init}[[l - 1, i, j + 1, k, 4]] +$ 
     $\frac{1}{\delta z^2} \text{init}[[l - 1, i, j, k + 1, 4]]) +$ 
   $\frac{\delta t}{\rho_{\text{cp}} \delta x \delta y \delta z} (\text{qgen} + \text{feed}[l, i, j, k] \text{qtool}[[l, i, j, 3]]),$ 

```

```

If [And[j == 1, k == nz],
  init[[l, i, j, k, 4]] =
  init[[l - 1, i, j, k, 4]]
   $\left(1 - \frac{k_{\text{therm}} \delta t}{\rho_{\text{cp}}} \left(\frac{1}{\delta x^2} + \frac{1}{\delta y^2} + \frac{1}{\delta z^2}\right) - \frac{h \delta t}{\rho_{\text{cp}}} \left(\frac{1}{\delta z}\right)\right) +$ 
   $\text{tamb} \frac{h \delta t}{\rho_{\text{cp}}} \left(\frac{1}{\delta z}\right) +$ 
   $\frac{k_{\text{therm}} \delta t}{\rho_{\text{cp}}}$ 
   $\left(\frac{1}{2 \delta x^2} (\text{init}[[l - 1, i + 1, j, k, 4]] +$ 
     $\text{init}[[l - 1, i - 1, j, k, 4]]) +$ 
     $\frac{1}{\delta y^2} \text{init}[[l - 1, i, j + 1, k, 4]] +$ 
     $\frac{1}{\delta z^2} \text{init}[[l - 1, i, j, k - 1, 4]]) ,$ 

```

```

If [And[j == ny, k == 1],
  init[[l, i, j, k, 4]] =
  init[[l - 1, i, j, k, 4]]
  
$$\left(1 - \frac{k_{\text{therm}} \delta t}{2 \rho c p} \left(\frac{1}{\delta x^2} + \frac{1}{\delta y^2} + \frac{1}{\delta z^2}\right) - \frac{h \delta t}{2 \rho c p} \left(\frac{1}{\delta y} + \frac{1}{\delta z}\right)\right) +$$

  tamb  $\frac{h \delta t}{2 \rho c p} \left(\frac{1}{\delta y} + \frac{1}{\delta z}\right) +$ 
  
$$\frac{k_{\text{therm}} \delta t}{\rho c p}$$

  
$$\left(\frac{1}{4 \delta x^2} (\text{init}[[l - 1, i - 1, j, k, 4]] +$$

    init[[l - 1, i + 1, j, k, 4]]) +
  
$$\frac{1}{2 \delta y^2} \text{init}[[l - 1, i, j - 1, k, 4]] +$$

  
$$\frac{1}{2 \delta z^2} \text{init}[[l - 1, i, j, k + 1, 4]]) +$$

  
$$\frac{\delta t}{\rho c p \delta x \delta y \delta z} (\text{qgen} + \text{feed}[l, i, j, k] \text{qtool}[[l, i, j, 3]]),$$


```

```

If [And[j == ny, k == nz],
  init[[l, i, j, k, 4]] =
  init[[l - 1, i, j, k, 4]]
  
$$\left(1 - \frac{k_{\text{therm}} \delta t}{2 \rho c p} \left(\frac{1}{\delta x^2} + \frac{1}{\delta y^2} + \frac{1}{\delta z^2}\right) - \frac{h \delta t}{2 \rho c p} \left(\frac{1}{\delta y} + \frac{1}{\delta z}\right)\right) +$$

  tamb  $\frac{h \delta t}{2 \rho c p} \left(\frac{1}{\delta y} + \frac{1}{\delta z}\right) +$ 
  
$$\frac{k_{\text{therm}} \delta t}{\rho c p}$$

  
$$\left(\frac{1}{4 \delta x^2} (\text{init}[[l - 1, i - 1, j, k, 4]] +$$

    init[[l - 1, i + 1, j, k, 4]]) +
  
$$\frac{1}{2 \delta y^2} \text{init}[[l - 1, i, j - 1, k, 4]] +$$

  
$$\frac{1}{2 \delta z^2} \text{init}[[l - 1, i, j, k - 1, 4]]\right),$$


```

(\*planes\*)

$$\begin{aligned} \text{If } [i == 1, \text{init}[[l, i, j, k, 4]] = \\ & \text{init}[[l-1, i, j, k, 4]] \\ & \left( 1 - \frac{k_{\text{therm}} \delta t}{\rho c p} \left( \frac{1}{\delta x^2} + \frac{1}{\delta y^2} + \frac{1}{\delta z^2} \right) - \frac{h \delta t}{\rho c p} \left( \frac{1}{\delta x} \right) \right) + \\ & \text{tamb} \frac{h \delta t}{\rho c p} \frac{1}{\delta x} + \\ & \frac{k_{\text{therm}} \delta t}{\rho c p} \\ & \left( \frac{1}{\delta x^2} \text{init}[[l-1, i+1, j, k, 4]] + \right. \\ & \quad \frac{1}{2 \delta y^2} (\text{init}[[l-1, i, j-1, k, 4]] + \\ & \quad \quad \text{init}[[l-1, i, j+1, k, 4]]) + \\ & \quad \frac{1}{2 \delta z^2} (\text{init}[[l-1, i, j, k-1, 4]] + \\ & \quad \quad \left. \text{init}[[l-1, i, j, k+1, 4]]) \right), \end{aligned}$$

$$\begin{aligned} \text{If } [i == nx, \text{init}[[l, i, j, k, 4]] = \\ & \text{init}[[l-1, i, j, k, 4]] \\ & \left( 1 - \frac{k_{\text{therm}} \delta t}{\rho c p} \left( \frac{1}{\delta x^2} + \frac{1}{\delta y^2} + \frac{1}{\delta z^2} \right) - \frac{h \delta t}{\rho c p} \left( \frac{1}{\delta x} \right) \right) + \\ & \text{tamb} \frac{h \delta t}{\rho c p} \frac{1}{\delta x} + \\ & \frac{k_{\text{therm}} \delta t}{\rho c p} \\ & \left( \frac{1}{\delta x^2} \text{init}[[l-1, i-1, j, k, 4]] + \right. \\ & \quad \frac{1}{2 \delta y^2} (\text{init}[[l-1, i, j-1, k, 4]] + \\ & \quad \quad \text{init}[[l-1, i, j+1, k, 4]]) + \\ & \quad \frac{1}{2 \delta z^2} (\text{init}[[l-1, i, j, k-1, 4]] + \\ & \quad \quad \left. \text{init}[[l-1, i, j, k+1, 4]]) \right), \end{aligned}$$

$$\begin{aligned}
& \text{If } [j == 1, \text{init}[[1, i, j, k, 4]] = \\
& \text{init}[[1 - 1, i, j, k, 4]] \left( 1 - \frac{2 \text{ktherm } \delta t}{\rho c p} \left( \frac{1}{\delta x^2} + \frac{1}{\delta y^2} + \frac{1}{\delta z^2} \right) \right) + \\
& \frac{\text{ktherm } \delta t}{\rho c p} \\
& \left( \frac{1}{\delta x^2} (\text{init}[[1 - 1, i - 1, j, k, 4]] + \right. \\
& \quad \left. \text{init}[[1 - 1, i + 1, j, k, 4]]) + \right. \\
& \frac{1}{\delta y^2} (\text{init}[[1 - 1, i, j + 1, k, 4]] + \\
& \quad \left. \text{init}[[1 - 1, i, j - 1, k, 4]]) + \right. \\
& \frac{1}{\delta z^2} (\text{init}[[1 - 1, i, j, k - 1, 4]] + \\
& \quad \left. \text{init}[[1 - 1, i, j, k + 1, 4]]) \right),
\end{aligned}$$

$$\begin{aligned}
& \text{If } [j == n_y, \text{init}[[1, i, j, k, 4]] = \\
& \text{init}[[1 - 1, i, j, k, 4]] \\
& \left( 1 - \frac{\text{ktherm } \delta t}{\rho c p} \left( \frac{1}{\delta x^2} + \frac{1}{\delta y^2} + \frac{1}{\delta z^2} \right) - \frac{h \delta t}{\rho c p} \left( \frac{1}{\delta y} \right) \right) + \\
& \text{tamb } \frac{h \delta t}{\rho c p} \frac{1}{\delta y} + \\
& \frac{\text{ktherm } \delta t}{\rho c p} \\
& \left( \frac{1}{2 \delta x^2} (\text{init}[[1 - 1, i - 1, j, k, 4]] + \right. \\
& \quad \left. \text{init}[[1 - 1, i + 1, j, k, 4]]) + \right. \\
& \frac{1}{\delta y^2} \text{init}[[1 - 1, i, j - 1, k, 4]] + \\
& \frac{1}{2 \delta z^2} (\text{init}[[1 - 1, i, j, k - 1, 4]] + \\
& \quad \left. \text{init}[[1 - 1, i, j, k + 1, 4]]) \right),
\end{aligned}$$

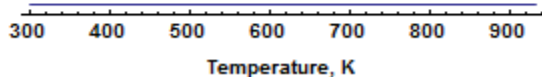
$$\begin{aligned}
& \text{If } [k == 1, \text{init}[[l, i, j, k, 4]] = \\
& \text{init}[[l-1, i, j, k, 4]] \\
& \left( 1 - \frac{k_{\text{therm}} \delta t}{\rho c_p} \left( \frac{1}{\delta x^2} + \frac{1}{\delta y^2} + \frac{1}{\delta z^2} \right) - \frac{h \delta t}{\rho c_p} \left( \frac{1}{\delta z} \right) \right) + \\
& \text{tamb} \frac{h \delta t}{\rho c_p} \frac{1}{\delta z} + \\
& \frac{k_{\text{therm}} \delta t}{\rho c_p} \\
& \left( \frac{1}{2 \delta x^2} (\text{init}[[l-1, i-1, j, k, 4]] + \right. \\
& \quad \left. \text{init}[[l-1, i+1, j, k, 4]]) + \right. \\
& \frac{1}{2 \delta y^2} (\text{init}[[l-1, i, j-1, k, 4]] + \\
& \quad \left. \text{init}[[l-1, i, j+1, k, 4]]) + \right. \\
& \left. \frac{1}{\delta z^2} \text{init}[[l-1, i, j, k+1, 4]] \right) + \\
& \frac{\delta t}{\rho c_p \delta x \delta y \delta z} (\text{qgen} + \text{feed}[l, i, j, k] \text{qtool}[[l, i, j, 3]]),
\end{aligned}$$



```

range = 1 - (300 / tsolid);
NewColor[r_] := Hue[range (1 - 300 / tsolid) (1 - r)];
Tmax = tsolid;
Tmin = 300;
LinearScale = Table[ $\frac{T_{max} - T_{min}}{100} i + T_{min}$ , {i, 0, 100}];
ScaleGradient = Table[Hue[range (1 -  $\frac{i}{101}$ )],
  {i, 0, Length[LinearScale]}];
GradientScale =
  Table[{ScaleGradient[[i]], PointSize[0.14],
    Point[{LinearScale[[i]], .025}]},
  {i, 1, Length[LinearScale]}];
ScaleLabel = Plot[0, {x, Tmin, Tmax}, PlotRange -> {All, All},
  AxesOrigin -> {-1, 1}, Axes -> {True, False}, Frame -> True,
  FrameStyle -> {RGBColor[0, 0, 0], RGBColor[1, 1, 1],
    RGBColor[1, 1, 1], RGBColor[1, 1, 1]},
  FrameTicks -> {Automatic, None, None, None},
  FrameLabel -> {"Temperature, K", "", ImageSize -> {300, 10},
  AspectRatio -> .25, DisplayFunction -> Identity];
scale = Show[ScaleLabel, Graphics[{GradientScale}],
  DisplayFunction -> Identity, ImageSize -> {300, 100},
  LabelStyle -> Directive[Bold, FontFamily -> "Arial"]

```

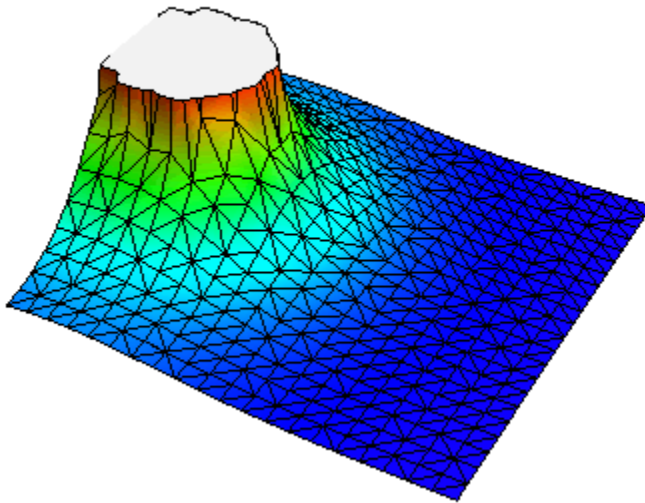


```

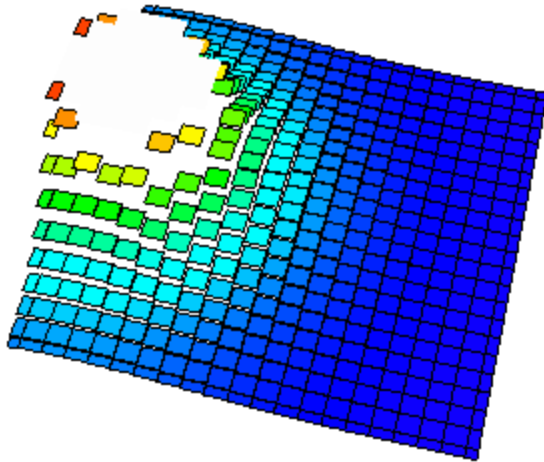
(*generate a 3D plot table of the temperature of the
workpiece as a function of time*)
plotxy1[x_, y_] :=
  Flatten[
    Table[{init[[x, i, j, y, 1]], init[[x, i, j, y, 2]],
      init[[x, i, j, y, 4]]}, {i, 1, nx}, {j, 1, ny}], 1];
plotxy2[x_, y_] :=
  Flatten[
    Table[{init[[x, i, j, y, 1]], -init[[x, i, j, y, 2]],
      init[[x, i, j, y, 4]]}, {i, 1, nx}, {j, 1, ny}], 1];
plotxy[x_, y_] := Join[plotxy1[x, y], plotxy2[x, y]]

```

```
ListPlot3D[plotxy[Round[6/δt], 1],
PlotRange → {All, All, {300, 900}},
ColorFunction → Function[{x, y, z}, Hue[(1 - z/tsolid)]],
ColorFunctionScaling → False,
(*AxesLabel → {"weld direction", "transverse direction",
"Temperatur (K)"}*)
PlotRange → {{-dimx/2, dimx/2}, {-dimy/2, dimy/2},
Automatic}, Mesh → All, PlotStyle -> Opacity[1],
Boxed → False, Axes → False, InterpolationOrder → 1]
```



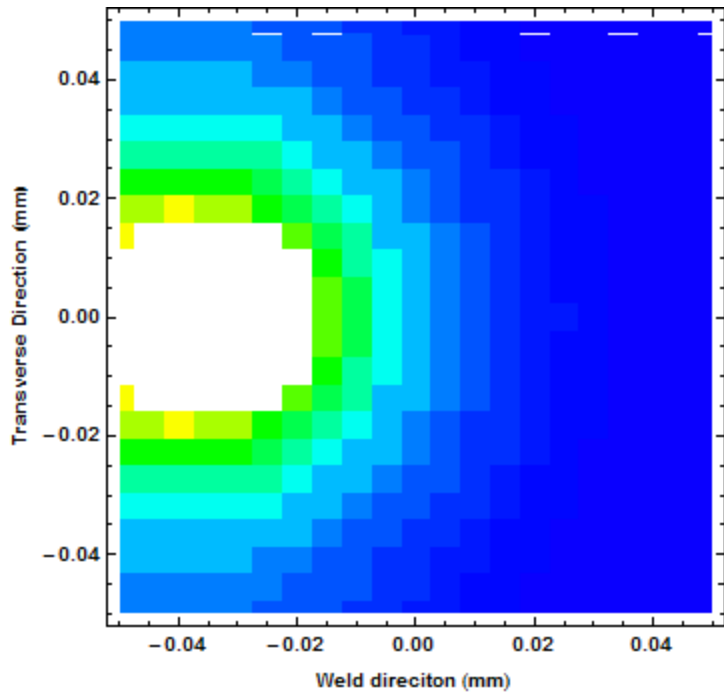
```
ListPlot3D[plotxy[Round[6/δt], 1],
PlotRange → {All, All, {300, 900}},
ColorFunction → Function[{x, y, z}, Hue[(1 - z/tsolid)]],
ColorFunctionScaling → False,
(*AxesLabel → {"weld direction", "transverse direction",
"Temperatur (K)"}*)
PlotRange → {{-dimx/2, dimx/2}, {-dimy/2, dimy/2},
Automatic}, Mesh → All, PlotStyle -> Opacity[1],
Boxed → False, Axes → False, InterpolationOrder → 0]
```



```

topo1 = ListContourPlot[plotxy[Round[6 /  $\delta t$ ], 1],
  Contours  $\rightarrow$  {300, 310, 320, 330, 350, 375, 400, 450, 500,
    550, 600, 650, 700, 750, 800, 850}, PlotRange  $\rightarrow$  {300, 800},
  ContourLabels  $\rightarrow$  Automatic,
  ColorFunction  $\rightarrow$  Function[{z}, Hue[(1 - z / (tsolid))]],
  ColorFunctionScaling  $\rightarrow$  False,
  FrameLabel  $\rightarrow$  {"Weld direction (mm)",
    "Transverse Direction (mm)"},
  LabelStyle  $\rightarrow$  Directive[Bold, FontFamily  $\rightarrow$  "Arial"],
  InterpolationOrder  $\rightarrow$  0]

```



```
(*j2=Table[ListContourPlot[plotxy[Round[i/δt],1],
  Contours→{300,310,320,330,350,375,400,450,500,550,
    600,650,700,750,800,850},PlotRange→{300,800},
  ContourLabels→Automatic,
  ColorFunction→Function[{z},Hue[(1-z/(tsolid))]],
  ColorFunctionScaling→False,
  FrameLabel→{"Weld direciton (mm)",
    "Transverse Direction (mm)"},
  LabelStyle→Directive[Bold,FontFamily→"Arial"],
  InterpolationOrder→0],{i,1,Round[tmax],5}];*)

(*movie1=ListAnimate[j2]*)

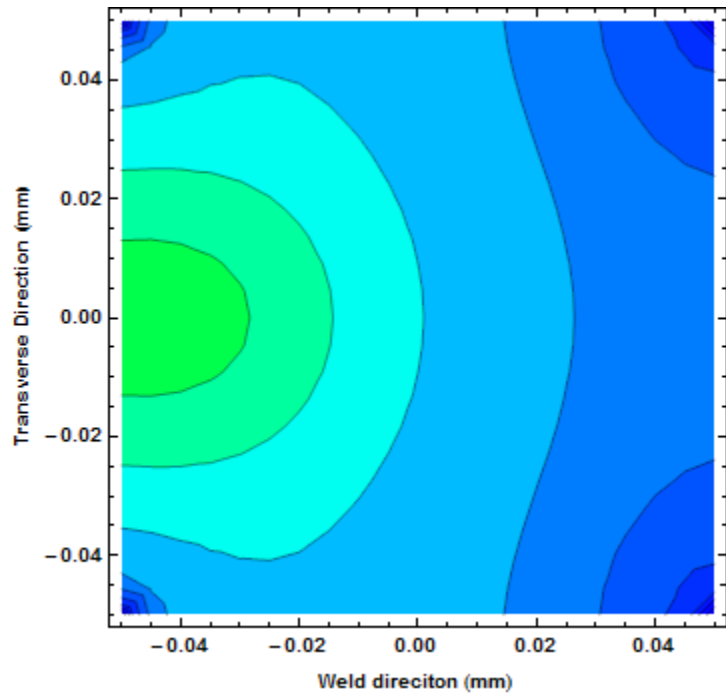
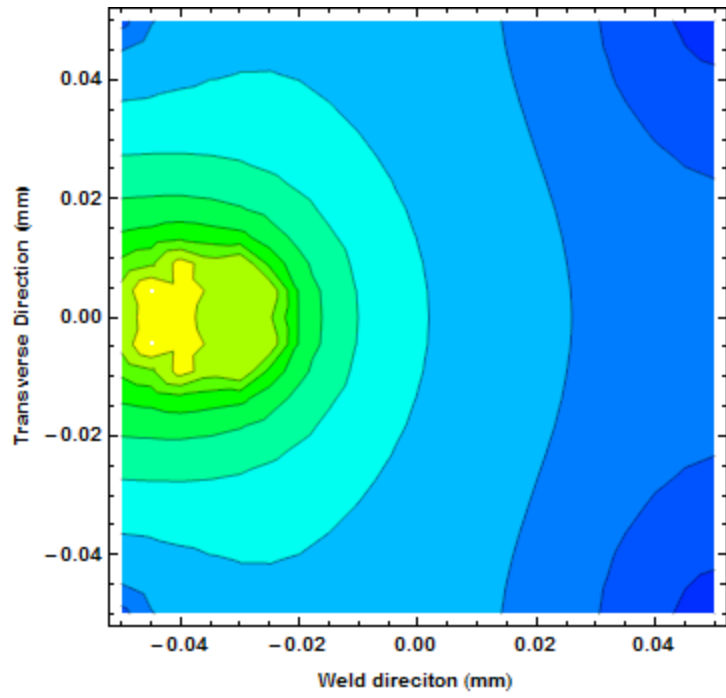
(*Export["movie120sec_1in_per_min.avi",movie1,"AVI"]*)
```

```

ListContourPlot[plotxy[Round[6/δt], 1],
  Contours → {300, 310, 320, 330, 350, 375, 400, 450, 500,
    550, 600, 650, 700, 750, 800, 850}, PlotRange → {300, 800},
  ContourLabels → Automatic,
  ColorFunction → Function[{z}, Hue[(1 - z/tsolid)]],
  ColorFunctionScaling → False,
  FrameLabel → {"Weld direciton (mm)",
    "Transverse Direction (mm)"},
  LabelStyle → Directive[Bold, FontFamily → "Arial"]]
ListContourPlot[plotxy[Round[6/δt], dimz/δz],
  Contours → {300, 310, 320, 330, 350, 375, 400, 450, 500,
    550, 600, 650, 700, 750, 800, 850}, PlotRange → {300, 800},
  ContourLabels → Automatic,
  ColorFunction → Function[{z}, Hue[(1 - z/tsolid)]],
  ColorFunctionScaling → False,
  FrameLabel → {"Weld direciton (mm)",
    "Transverse Direction (mm)"},
  LabelStyle → Directive[Bold, FontFamily → "Arial"]]

ListContourPlot[plotxy[Round[60/δt], 1], ContourLabels → None,
  Contours → {300, 310, 320, 330, 350, 375, 400, 450, 500,
    550, 600, 650, 700, 750, 800, 850}, PlotRange → {300, 800},
  ContourLabels → Automatic,
  ColorFunction → Function[{z}, Hue[(1 - z/tsolid)]],
  ColorFunctionScaling → False,
  FrameLabel → {"Weld direciton (mm)",
    "Transverse Direction (mm)"},
  LabelStyle → Directive[Bold, FontFamily → "Arial"]]
ListContourPlot[plotxy[Round[60/δt], dimz/δz],
  ContourLabels → None,
  Contours → {300, 310, 320, 330, 350, 375, 400, 450, 500,
    550, 600, 650, 700, 750, 800, 850}, PlotRange → {300, 800},
  ContourLabels → Automatic,
  ColorFunction → Function[{z}, Hue[(1 - z/tsolid)]],
  ColorFunctionScaling → False,
  FrameLabel → {"Weld direciton (mm)",
    "Transverse Direction (mm)"},
  LabelStyle → Directive[Bold, FontFamily → "Arial"]]

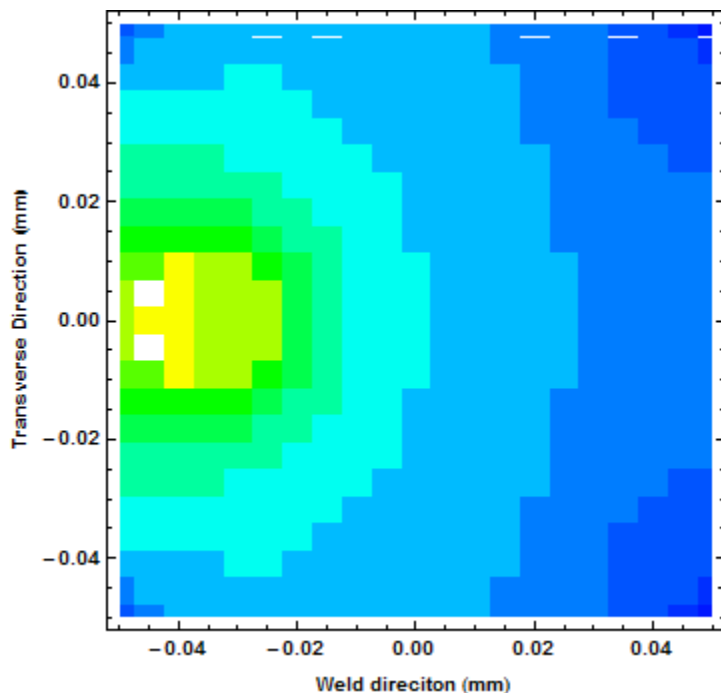
```

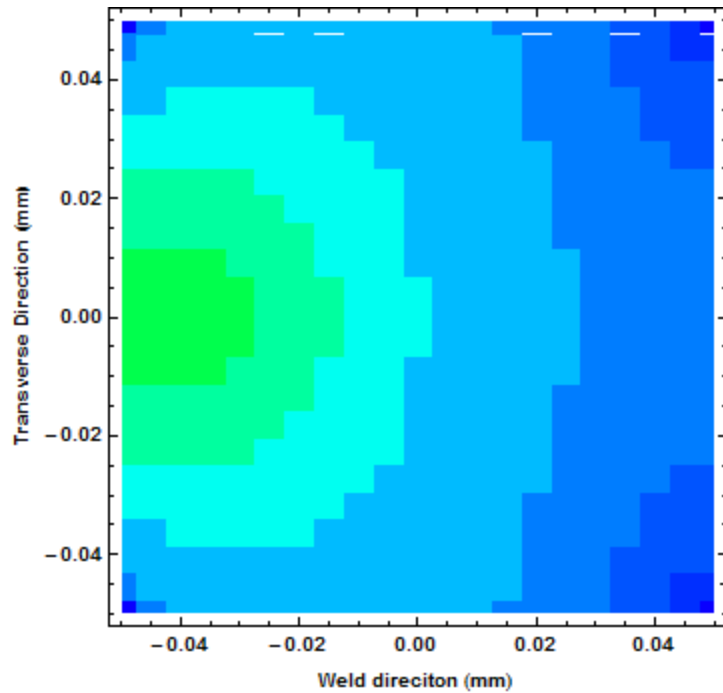


```

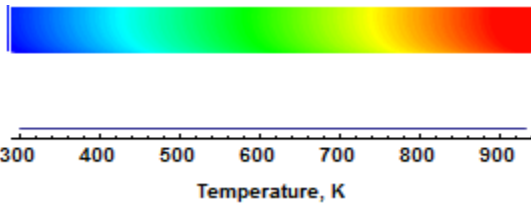
ListContourPlot[plotxy[Round[60 /  $\delta t$ ], 1], ContourLabels  $\rightarrow$  None,
  InterpolationOrder  $\rightarrow$  0,
  Contours  $\rightarrow$  {300, 310, 320, 330, 350, 375, 400, 450, 500,
    550, 600, 650, 700, 750, 800, 850}, PlotRange  $\rightarrow$  {300, 800},
  ContourLabels  $\rightarrow$  Automatic,
  ColorFunction  $\rightarrow$  Function[{z}, Hue[(1 - z / tsolid)]],
  ColorFunctionScaling  $\rightarrow$  False,
  FrameLabel  $\rightarrow$  {"Weld direciton (mm)",
    "Transverse Direction (mm)"},
  LabelStyle  $\rightarrow$  Directive[Bold, FontFamily  $\rightarrow$  "Arial"]]
ListContourPlot[plotxy[Round[60 /  $\delta t$ ], dimz /  $\delta z$ ],
  ContourLabels  $\rightarrow$  None, InterpolationOrder  $\rightarrow$  0,
  Contours  $\rightarrow$  {300, 310, 320, 330, 350, 375, 400, 450, 500,
    550, 600, 650, 700, 750, 800, 850}, PlotRange  $\rightarrow$  {300, 800},
  ContourLabels  $\rightarrow$  Automatic,
  ColorFunction  $\rightarrow$  Function[{z}, Hue[(1 - z / tsolid)]],
  ColorFunctionScaling  $\rightarrow$  False,
  FrameLabel  $\rightarrow$  {"Weld direciton (mm)",
    "Transverse Direction (mm)"},
  LabelStyle  $\rightarrow$  Directive[Bold, FontFamily  $\rightarrow$  "Arial"]]

```





Show [scale]

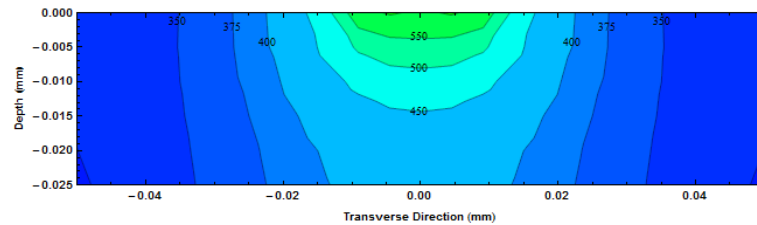


```

plotyz1[x_, y_] :=
  Flatten[
    Table[{init[[x, y, j, k, 2]], -init[[x, y, j, k, 3]],
          init[[x, y, j, k, 4]]}, {j, 1, ny}, {k, 1, nz}], 1];
plotyz2[x_, y_] :=
  Flatten[
    Table[{-init[[x, y, j, k, 2]], -init[[x, y, j, k, 3]],
          init[[x, y, j, k, 4]]}, {j, 1, ny}, {k, 1, nz}], 1];
plotyz[x_, y_] := Join[plotyz1[x, y], plotyz2[x, y]]

```

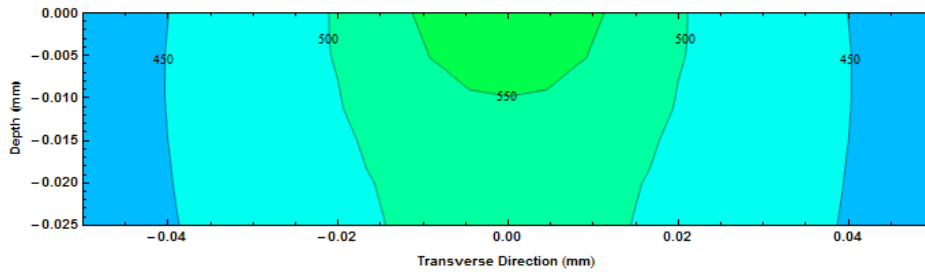
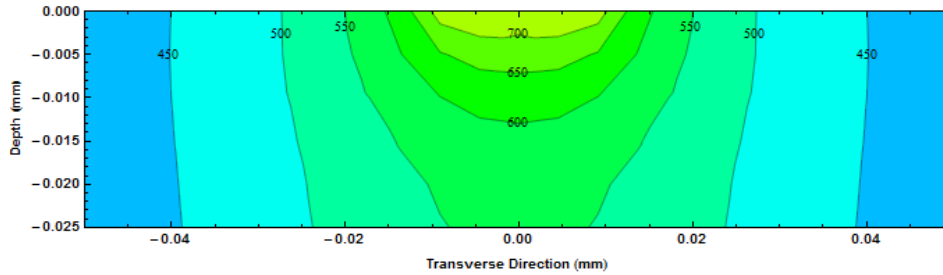
```
ListContourPlot[plotyz[Round[10 /  $\delta t$ ], 4],
  Contours  $\rightarrow$  {300, 310, 320, 330, 350, 375, 400, 450, 500,
    550, 600, 650, 700, 750, 800, 850},
  PlotRange  $\rightarrow$  {{-dimy / 2, dimy / 2}, {0, -dimz}, {300, 800}},
  ContourLabels  $\rightarrow$  Automatic, AspectRatio  $\rightarrow$  dimz / dimy,
  ColorFunction  $\rightarrow$  Function[{z}, Hue[(1 - z / tsolid)]],
  ColorFunctionScaling  $\rightarrow$  False,
  FrameLabel  $\rightarrow$  {"Transverse Direction (mm)", "Depth (mm)"},
  LabelStyle  $\rightarrow$  Directive[Bold, FontFamily  $\rightarrow$  "Arial"]]
```



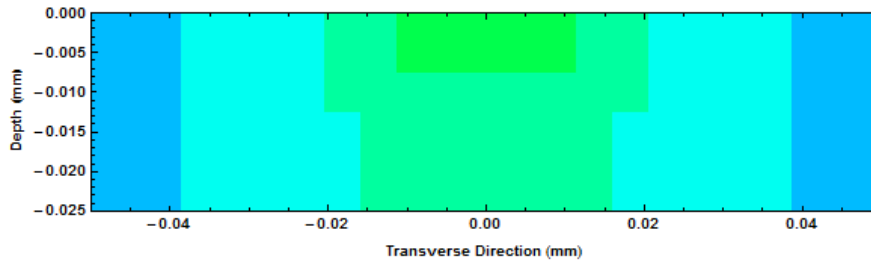
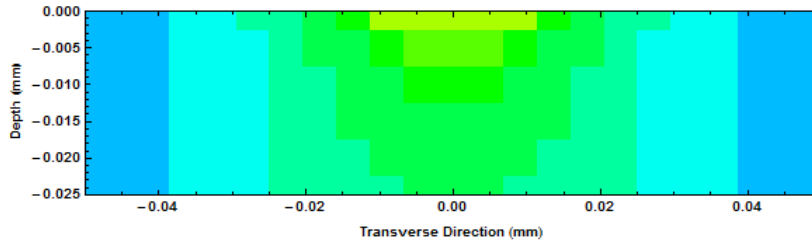
```
plotqyz[L_] := If[Abs[qc[[L, 2]] /  $\delta x$ ] > (nx + 1) / 2,
  plotyz[1, 1], plotyz[L, Round[(nx + 1) / 2 + qc[[L, 2]] /  $\delta x$ ]]]
plotqfrontyz[L_] := If[Abs[qc[[L, 2]] /  $\delta x$ ] > (nx + 1) / 2,
  plotyz[1, 1],
  plotyz[L, Round[(nx + 1) / 2 + qc[[L, 2]] /  $\delta x$ ] +
    Round[(r + .002) /  $\delta x$ ]]]
```

```
ListContourPlot[plotqyz[Round[60 /  $\delta t$ ]],
  Contours  $\rightarrow$  {300, 310, 320, 330, 350, 375, 400, 450, 500,
    550, 600, 650, 700, 750, 800, 850},
  PlotRange  $\rightarrow$  {{-dimy / 2, dimy / 2}, {0, -dimz}, {300, 800}},
  ContourLabels  $\rightarrow$  Automatic,
  (*PlotLabel $\rightarrow$ "Temperature (K) Under the Tool",*)
  ColorFunction  $\rightarrow$  Function[{z}, Hue[(1 - z / tsolid)]],
  ColorFunctionScaling  $\rightarrow$  False, AspectRatio  $\rightarrow$  dimz / dimy,
  FrameLabel  $\rightarrow$  {"Transverse Direction (mm)", "Depth (mm)"},
  LabelStyle  $\rightarrow$  Directive[Bold, FontFamily  $\rightarrow$  "Arial"]]
```

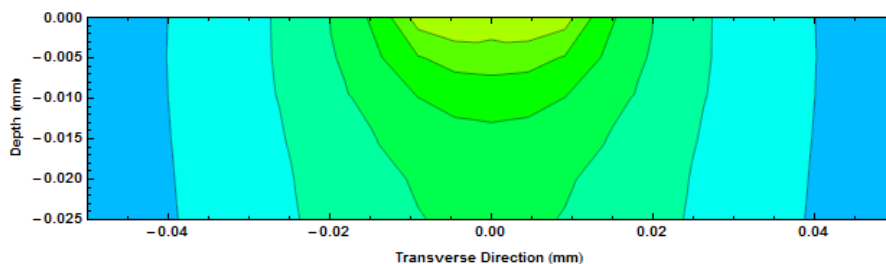
```
ListContourPlot[plotqfrontyz[Round[60 /  $\delta t$ ]],
  Contours  $\rightarrow$  {300, 310, 320, 330, 350, 375, 400, 450, 500,
    550, 600, 650, 700, 750, 800, 850},
  PlotRange  $\rightarrow$  {{-dimy / 2, dimy / 2}, {0, -dimz}, {300, 800}},
  ContourLabels  $\rightarrow$  Automatic(*,
  PlotLabel $\rightarrow$ "Temperature (K) Under the Tool + 2mm"*) ,
  ColorFunction  $\rightarrow$  Function[{z}, Hue[(1 - z / tsolid)]],
  ColorFunctionScaling  $\rightarrow$  False, AspectRatio  $\rightarrow$  dimz / dimy,
  FrameLabel  $\rightarrow$  {"Transverse Direction (mm)", "Depth (mm)"},
  LabelStyle  $\rightarrow$  Directive[Bold, FontFamily  $\rightarrow$  "Arial"]]
```

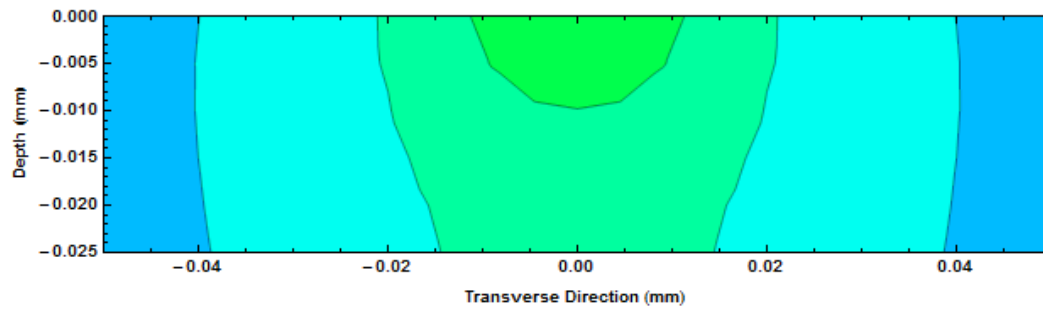


```
ListContourPlot[plotqyz[Round[60 /  $\delta t$ ]],
  Contours  $\rightarrow$  {300, 310, 320, 330, 350, 375, 400, 450, 500,
    550, 600, 650, 700, 750, 800, 850},
  PlotRange  $\rightarrow$  {{-dimy / 2, dimy / 2}, {0, -dimz}, {300, 800}},
  ContourLabels  $\rightarrow$  Automatic,
  (*PlotLabel $\rightarrow$ "Temperature (K) Under the Tool",*)
  ColorFunction  $\rightarrow$  Function[{z}, Hue[(1 - z / tsolid)]],
  ColorFunctionScaling  $\rightarrow$  False, AspectRatio  $\rightarrow$  dimz / dimy,
  FrameLabel  $\rightarrow$  {"Transverse Direction (mm)", "Depth (mm)"},
  LabelStyle  $\rightarrow$  Directive[Bold, FontFamily  $\rightarrow$  "Arial"],
  InterpolationOrder  $\rightarrow$  0]
ListContourPlot[plotqfrontyz[Round[60 /  $\delta t$ ]],
  Contours  $\rightarrow$  {300, 310, 320, 330, 350, 375, 400, 450, 500,
    550, 600, 650, 700, 750, 800, 850},
  PlotRange  $\rightarrow$  {{-dimy / 2, dimy / 2}, {0, -dimz}, {300, 800}},
  ContourLabels  $\rightarrow$  Automatic(*,
  PlotLabel $\rightarrow$ "Temperature (K) Under the Tool + 2mm"*) ,
  ColorFunction  $\rightarrow$  Function[{z}, Hue[(1 - z / tsolid)]],
  ColorFunctionScaling  $\rightarrow$  False, AspectRatio  $\rightarrow$  dimz / dimy,
  FrameLabel  $\rightarrow$  {"Transverse Direction (mm)", "Depth (mm)"},
  LabelStyle  $\rightarrow$  Directive[Bold, FontFamily  $\rightarrow$  "Arial"],
  InterpolationOrder  $\rightarrow$  0]
```



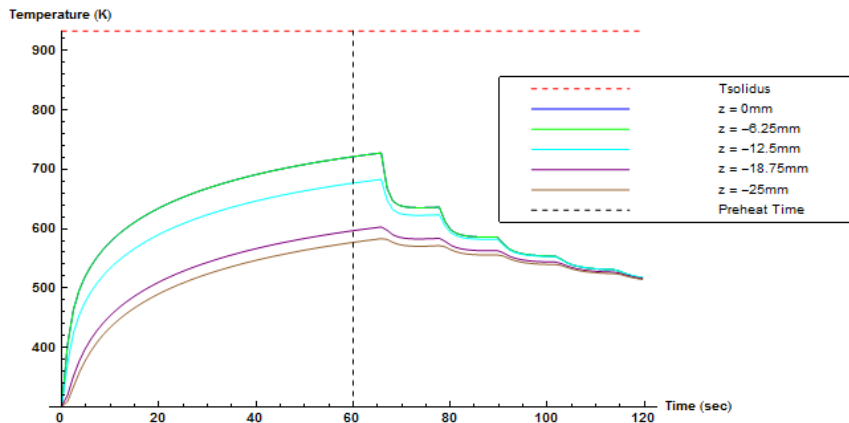
```
ListContourPlot[plotqyz[Round[60 /  $\delta t$ ]], ContourLabels  $\rightarrow$  None,
  Contours  $\rightarrow$  {300, 310, 320, 330, 350, 375, 400, 450, 500,
    550, 600, 650, 700, 750, 800, 850},
  PlotRange  $\rightarrow$  {{-dimy / 2, dimy / 2}, {0, -dimz}, {300, 800}},
  ContourLabels  $\rightarrow$  Automatic,
  (*PlotLabel  $\rightarrow$  "Temperature (K) Under the Tool", *)
  ColorFunction  $\rightarrow$  Function[{z}, Hue[(1 - z / tsolid)]],
  ColorFunctionScaling  $\rightarrow$  False, AspectRatio  $\rightarrow$  dimz / dimy,
  FrameLabel  $\rightarrow$  {"Transverse Direction (mm)", "Depth (mm)"},
  LabelStyle  $\rightarrow$  Directive[Bold, FontFamily  $\rightarrow$  "Arial"]]
ListContourPlot[plotqfrontyz[Round[60 /  $\delta t$ ]],
  ContourLabels  $\rightarrow$  None,
  Contours  $\rightarrow$  {300, 310, 320, 330, 350, 375, 400, 450, 500,
    550, 600, 650, 700, 750, 800, 850},
  PlotRange  $\rightarrow$  {{-dimy / 2, dimy / 2}, {0, -dimz}, {300, 800}},
  ContourLabels  $\rightarrow$  Automatic (*,
  PlotLabel  $\rightarrow$  "Temperature (K) Under the Tool + 2mm" *),
  ColorFunction  $\rightarrow$  Function[{z}, Hue[(1 - z / tsolid)]],
  ColorFunctionScaling  $\rightarrow$  False, AspectRatio  $\rightarrow$  dimz / dimy,
  FrameLabel  $\rightarrow$  {"Transverse Direction (mm)", "Depth (mm)"},
  LabelStyle  $\rightarrow$  Directive[Bold, FontFamily  $\rightarrow$  "Arial"]]
```



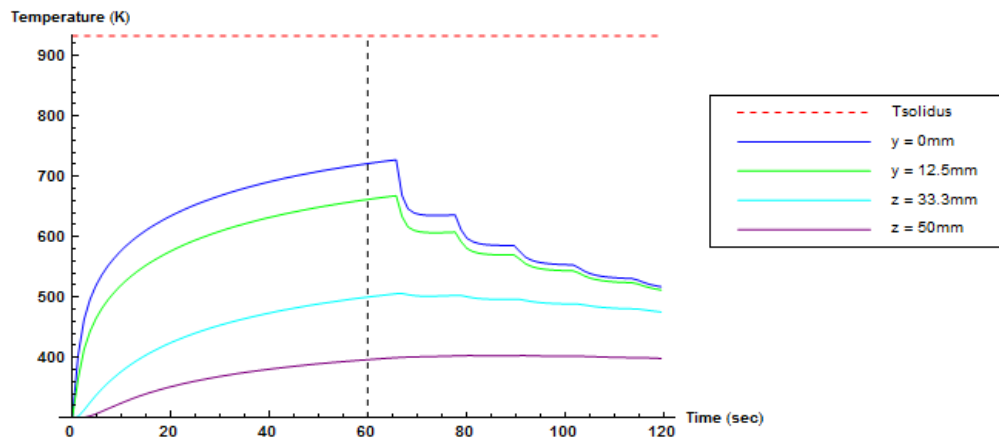


```
pointarb[x_, y_, z_] :=
Table[
  {1  $\delta t$ , init[{1, If[Round[x /  $\delta x$ ] + (nx + 1) / 2 == 0, 1,
    Round[x /  $\delta x$ ] + (nx + 1) / 2],
    If[y > 0, Round[y /  $\delta y$ ], If[y == 0, 1, Round[y /  $\delta y$ ]]],
    If[z == 0, 1, Round[z /  $\delta z$ ]], 4]}],
  {1, 1, tmax /  $\delta t$ , Round[tmax /  $\delta t$  / 100]}]
```

```
ShowLegend[
ListPlot[{pointarb[-dimx/2, 0, .0],
  pointarb[-dimx/2, 0, dimz/4],
  pointarb[-dimx/2, 0, dimz/2],
  pointarb[-dimx/2, 0, 3 dimz/4], pointarb[-dimx/2, 0, dimz],
  {{0, tsolid}, {tmax, tsolid}}, {{tpre, 0}, {tpre, tsolid}}},
LabelStyle → Directive[Bold, FontFamily → "Arial"],
AxesLabel → {"Time (sec)", "Temperature (K)"},
(*PlotLabel→"Thermal History of Point x,y,z",*)
Joined → True, PlotRange → {All, {300, tsolid}},
PlotStyle → {Blue, Green, Cyan, Purple, Brown,
  Directive[Dashed, Red], Directive[Dashed, Black]}},
{{{Graphics[{Directive[Dashed, Red],
  Line[{{0, 0}, {16, 0}]}]},
  Style["Tsolidus", FontFamily → "Arial"]},
{Graphics[{Blue, Line[{{0, 0}, {16, 0}]}]},
  Style["z = 0mm", FontFamily → "Arial"]},
{Graphics[{Green, Line[{{0, 0}, {16, 0}]}]},
  Style["z = -6.25mm", FontFamily → "Arial"]},
{Graphics[{Cyan, Line[{{0, 0}, {16, 0}]}]},
  Style["z = -12.5mm", FontFamily → "Arial"]},
{Graphics[{Purple, Line[{{0, 0}, {16, 0}]}]},
  Style["z = -18.75mm", FontFamily → "Arial"]},
{Graphics[{Brown, Line[{{0, 0}, {16, 0}]}]},
  Style["z = -25mm", FontFamily → "Arial"]},
{Graphics[{Directive[Dashed, Black],
  Line[{{0, 0}, {16, 0}]}]},
  Style["Preheat Time", FontFamily → "Arial"]}},
LegendSize → {1, 0.4}, LegendShadow → {0, 0},
LegendTextSpace → 0.8, LegendPosition → {.35, -0.05}]]
```



```
ShowLegend[
ListPlot[{pointarb[-dimx/2, 0, .0], pointarb[-dimx/2, r, 0],
  pointarb[-dimx/2, 2 dimy / 6, 0],
  pointarb[-dimx/2, dimy / 2, 0],
  {{0, tsolid}, {tmax, tsolid}}, {{tpre, 0}, {tpre, tsolid}}},
LabelStyle → Directive[Bold, FontFamily → "Arial"],
AxesLabel → {"Time (sec)", "Temperature (K)"},
(*PlotLabel → "Thermal History of Point x,y,z",*)
Joined → True, PlotRange → {All, {300, tsolid}},
PlotStyle → {Blue, Green, Cyan, Purple,
  Directive[Dashed, Red], Directive[Dashed, Black]}},
{{{Graphics[{Directive[Dashed, Red],
  Line[{{0, 0}, {16, 0}]}]},
  Style["Tsolidus", FontFamily → "Arial"]},
{Graphics[{Blue, Line[{{0, 0}, {16, 0}]}]},
  Style["y = 0mm", FontFamily → "Arial"]},
{Graphics[{Green, Line[{{0, 0}, {16, 0}]}]},
  Style["y = 12.5mm", FontFamily → "Arial"]},
{Graphics[{Cyan, Line[{{0, 0}, {16, 0}]}]},
  Style["z = 33.3mm", FontFamily → "Arial"]},
{Graphics[{Purple, Line[{{0, 0}, {16, 0}]}]},
  Style["z = 50mm", FontFamily → "Arial"]}},
LegendSize → {.8, 0.4}, LegendShadow → {0, 0},
LegendTextSpace → 0.8, LegendPosition → {.85, -0.1}]]
```

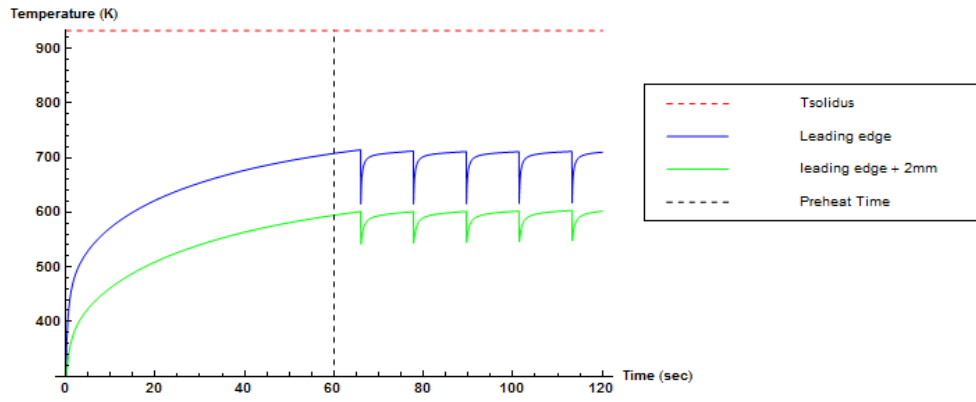


```

pointunder =
Table[
  {1  $\delta t$ , init[[1, If[Abs[qc[[1, 2]] /  $\delta x$ ]  $\geq$  (nx + 1) / 2,
    1, If[Abs[qc[[1, 2]] /  $\delta x$  + Round[r /  $\delta x$ ]]  $\geq$  (nx + 1) / 2,
    1, Round[(nx + 1) / 2 + qc[[1, 2]] /  $\delta x$  + Round[r /  $\delta x$ ]]]],
  1, 1, 4]], {1, 1, tmax /  $\delta t$ };
pointunder2 =
Table[
  {1  $\delta t$ , init[[1, If[Abs[qc[[1, 2]] /  $\delta x$ ]  $\geq$  (nx + 1) / 2,
    1, If[Abs[qc[[1, 2]] /  $\delta x$  + Round[(r + .002) /  $\delta x$ ]]  $\geq$ 
    (nx + 1) / 2, 1,
    Round[(nx + 1) / 2 + qc[[1, 2]] /  $\delta x$  +
    Round[(r + .002) /  $\delta x$ ]]]], 1, 1, 4]], {1, 1, tmax /  $\delta t$ };

ShowLegend[
ListPlot[{pointunder, pointunder2,
  {{0, tsolid}, {tmax, tsolid}}, {{tpre, 0}, {tpre, tsolid}}},
LabelStyle  $\rightarrow$  Directive[Bold, FontFamily  $\rightarrow$  "Arial"],
AxesLabel  $\rightarrow$  {"Time (sec)", "Temperature (K)"},
(*PlotLabel  $\rightarrow$  "Thermal History of Point x,y,z",*)
Joined  $\rightarrow$  True, PlotRange  $\rightarrow$  {All, {300, tsolid}},
PlotStyle  $\rightarrow$  {Blue, Green, Directive[Dashed, Red],
  Directive[Dashed, Black]}},
{{{Graphics[{Directive[Dashed, Red], Line[{{0, 0}, {5, 0}}]}]},
  Style["Tsolidus", FontFamily  $\rightarrow$  "Arial"]},
{Graphics[{Blue, Line[{{0, 0}, {5, 0}}]}]},
  Style["Leading edge", FontFamily  $\rightarrow$  "Arial"]},
{Graphics[{Green, Line[{{0, 0}, {5, 0}}]}]},
  Style["leading edge + 2mm", FontFamily  $\rightarrow$  "Arial"]},
{Graphics[{Directive[Dashed, Black],
  Line[{{0, 0}, {5, 0}}]}]},
  Style["Preheat Time", FontFamily  $\rightarrow$  "Arial"]}},
LegendSize  $\rightarrow$  {1, 0.4}, LegendShadow  $\rightarrow$  {0, 0},
LegendTextSpace  $\rightarrow$  1.5, LegendPosition  $\rightarrow$  {.85, -0.1}}]

```



 Created with Wolfram Mathematica 7.0